Study of solvated molecular ion stability in the gas-phase : cooling and irradiation

Paul Bertier

To cite this version:

Paul Bertier. Study of solvated molecular ion stability in the gas-phase : cooling and irradiation. Nuclear Experiment [nucl-ex]. Université de Lyon, 2017. English. NNT : 2017LYSE1207 . tel-01710261

HAL Id: tel-01710261
https://theses.hal.science/tel-01710261
Submitted on 15 Feb 2018

N°d'ordre NNT : xxx

THESE de DOCTORAT DE L'UNIVERSITE DE LYON
Opérée au sein de
L'Université Claude Bernard Lyon 1

Ecole Doctorale N° 52
Ecole doctorale de Physique et d'Astrophysique (PHAST)

Spécialité de doctorat : **Physique**

Soutenue prévue le 23/10/2017, par :
Paul BERTIER

Study of solvated molecular ion stability in the gas-phase: cooling and irradiation.

Devant le jury composé de :

ROUSSEAU, Patrick	Maître de conférences - HDR	Université Caen Normandie	Rapporteur
SCHMIDT, Henning	Professeur	Université de Stockholm	Rapporteur
AUGIER, Corinne	Professeure	Université Lyon I	Examinatrice
AZUMA, Toshiyuki	Chief Scientist	RIKEN	Examinateur
CALVO, Florent	Directeur de recherche CNRS	Université Grenoble Alpes	Examinateur
FARIZON, Bernadette	Directeur de recherche CNRS	Université Lyon I	Examinatrice
VERNHET, Dominique	Directrice de recherche CNRS	Université Paris 6	Examinatrice

N°d'ordre NNT : xxx

THESE de DOCTORAT DE L'UNIVERSITE DE LYON

Opérée au sein de
L'Université Claude Bernard Lyon 1

Ecole Doctorale N° 52
Ecole doctorale de Physique et d'Astrophysique (PHAST)

Spécialité de doctorat : Physique

Soutenue prévue le 23/10/2017, par :
Paul BERTIER

Directeur de thèse :
Michel FARIZON

Co-directeur de thèse :
Hassan ABDOUL-CARIME

Study of solvated molecular ion stability in the gas-phase: cooling and irradiation.

Devant le jury composé de :

ROUSSEAU, Patrick	Maître de conférences - HDR	Université Caen Normandie	Rapporteur
SCHMIDT, Henning	Professeur	Université de Stockholm	Rapporteur
AUGIER, Corinne	Professeure	Université Lyon I	Examinatrice
AZUMA, Toshiyuki	Chief Scientist	RIKEN	Examinateur
CALVO, Florent	Directeur de recherche CNRS	Université Grenoble Alpes	Examinateur
FARIZON, Bernadette	Directeur de recherche CNRS	Université Lyon I	Examinatrice
VERNHET, Dominique	Directrice de recherche CNRS	Université Paris 6	Examinatrice

Acknowledgement

I am very glad that I could do my PhD research in collaboration between two laboratories: I had the opportunity to work in RIKEN, in Japan in the AMO laboratory and in IPNL in France in the IPM laboratory.

I would first like to thank Toshiyuki Azuma for accepting me into his AMO laboratory and for his advice & help all the way through my PhD. I would also like to thank him for accepting to be one of the referees for my thesis and for attending my PhD defense. He has helped me pursue my PhD goals and in creating the collaboration.

I would also like to thank Bernadette Farizon for accepting me into the IPM laboratory and for accepting to be one of the referees for my thesis. She constantly helped me find and apply to scholarships which allowed me to go through my PhD project. She did a lot for the collaboration between both laboratories and went up to Korea to attend conferences and present the results of the collaboration.

I would specially like to thank Michel Farizon for his continuous help during my PhD and for being my advisor. He taught me how to be very rigorous in my research and I learnt a lot from him. He was very mindful to follow my research in Japan and gave me the opportunity to do experiments with him in France. I am very grateful for all the results I got with his help both in my research done in France and in Japan. We had many deep and interesting conversations which kept me motivated to pursue my research.

I would like to thank Hassan Abdoul-Carime for all his advice and for being my co-advisor. His advices help me to make sure I understand everything about what I am doing and to study all part of my results.

I would like to thank Patrick Rousseau and Henning Schmidt for both accepting to be referees of my thesis as well as writing a report on it.

I would like to thank both Corinne Augier and Dominique Vernhet for accepting to be referees of my thesis.

I would like to thank Florent Calvo for his calculations and for being a referee of my thesis.

I would like to thank Sebastian Menk and all the members of the AMO laboratory for teaching me and helping me in the laboratory work. Sebastian was working with me every day on the design of the apparatus in RIKEN. He taught me how to design, build and test an experimental set-up. He was very passionate and a great teacher.

I would like to thank Linda Feketeová, Thibaud Salbaing and all the members of the IPM group for their help and support.

I would like to thank all the member of the PHAST graduate school for accepting me and for their help with the administrative work.

Last but not least, I would like to thank my friends and family: my parents, my brothers and my rugby team mates for supporting me throughout writing this thesis and my life in general.

Résumé

Les radiations peuvent endommager notre environnement biologique mais elles peuvent aussi être bienfaisantes si elles sont contrôlées. L'action initiale des radiations à l'échelle microscopique consiste en une excitation électronique dans une molécule. L'observation de la redistribution de l'énergie dans l'environnement de cette molécule excitée est primordiale à la compréhension et à la description de l'effet des rayonnements dans les systèmes biomoléculaires. Les agrégats de molécules isolés en phase gazeuse constituent des systèmes modèles prometteurs pour étudier les interactions entre molécules sous irradiation.

La première partie de ce travail décrit la construction et la validation d'une ligne de faisceau permettant la production de paquets d'agrégats moléculaires froid injectables dans l'anneau de stockage RICE à RIKEN. La ligne de faisceau est composée d'une source electrospray, d'un filtre en masse quadripolaire, de guides d'ions d'un tube d'accélération, la pièce centrale étant un piège à ions cryogénique refroidi à 4 K. Le paquet d'ions froids, dont les ions ont été sélectionnés en masse et accélérés jusqu'à 20 keV, a été sondé avec un laser. La ligne a été validée par la mesure d'un spectre d'action du bleu de méthylène.

La seconde partie de ce travail s'appuie sur les expériences réalisées auprès du dispositif d'irradiation d'agrégats moléculaires (DIAM-IPNL). La méthode COINTOF-VMI permet la mesure de la distribution de vitesse des molécules d'eau évaporées à partir d'un agrégat après collision à haute vitesse avec un atome d'argon. Les distributions de vitesse mesurées pour des agrégats mixtes pyridine protonée et eau présentent deux composantes : une partie à basse vitesse qui correspond à une évaporation après redistribution de l'énergie dans l'agrégat, et une partie à haute vitesse où la molécule d'eau est évaporée avant redistribution de l'énergie. La comparaison des résultats avec les distributions calculées par dynamique moléculaire statistique montre que la partie basse vitesse peut être interprétée comme la contribution des deux possibilités d'excitation induites par la collision : l'excitation de la pyridine protonée ou l'excitation d'une des molécules d'eau.

Abstract

Radiation can damage our biological environment, but it can also be beneficial under certain controlled conditions. Initial action at microscopic scale consists of electronic excitation in molecules. The redistribution of this excitation energy to the environment is the primary process to be understood to describe the radiation effect on biomolecular system. Isolated molecular clusters in gas-phase are a promising model system to study the molecular interaction under radiation.

The first part of this work describes the construction and the validation of a beamline which can produce bunches of cold molecular cluster ions to be injected in the RIKEN cryogenic electrostatic (RICE) storage ring. The beamline is composed of an electrospray ion source, a quadrupole mass filter, ion guides and an acceleration tube; with the main part being a cryogenic ion trap cool down to 5K. The cold ion bunches, in which the ions have been mass selected and accelerated to 20keV, was probed with a laser. The beamline was successfully taken into operation and a measurement of the methylene blue action spectrum in gas-phase was carried out.

The second part of this work rely on experiment realized with the dispositif d'irradiation d'agrégats moléculaires (DIAM-IPNL). The COINTOF-VMI method allows the measurement of the velocity distributions of evaporated molecules from a cluster after high velocity collisions with an argon atom. The velocity distribution measured for mixed clusters protonated pyridine and water has two components: a low velocity part which corresponds to the evaporation of a water molecule after energy redistribution in the cluster, and a high velocity part in which the molecule is evaporated before total energy redistribution. Comparison with the distribution calculated by statistic molecular dynamic simulation shows that the low velocity part can be interpreted as the contribution of two possible excitations induced by collision: excitation on protonated pyridine and excitation on a water molecule.

Table of Contents

Introduction

In January 2005, the sun ended its 23rd solar activity circle and became very active. Intense variation in the ground-level cosmic ray was observed and the neutron monitor in the Antarctic recorded up to several thousand percent more counts [1] [2]. Changes in the radiation environment in the earth's atmosphere due to the increase of high energetic particles is common and results in a continuous shower of secondary particles on the earth surface which interact with us and our environment. The initial action of radiation in microscopic scale is an electronic excitation in a molecule and the observation of the energy distribution in its environment is a key point for understanding the effect of radiation.

After energy absorption, the molecule can transfer the energy among all its degree of freedom and slowly go back to its initial low excited state by radiation or by energy exchange with its environment and remain stable. In the other competing process, the energy absorbed is close to or higher than the dissociation threshold, the molecule is unstable and dissociate to create fragments with lower internal energy.

Isolated molecular clusters in gas phase are a very good model system to study the molecule interaction under radiation. Isolated clusters cannot indeed interact with other molecules and the intrinsic properties of the molecules can be measured. Through the addition of solvent molecules one by one and thus creating clusters, the molecule properties between gas phase and liquid phase can be better understood. The study of nanoscale systems has been recently an important part of radiation science [3] as it is not out of the range for theory and can already be discussed as condensed phase. The interactions between the molecules and their environment characterize the redistributions of excess energy within the whole cluster.

However, the addition of solvent molecules adds a lot of complexity into the problem, increasing the number of reaction channels or difficulties to calculate molecular dynamics of large molecules, for example. Lowering the internal energy of the system into ro-vibrational ground states improves existing studies and the selection of a single reaction channel.

This work investigates the properties of some cold ionic molecular clusters and their gas phase reactions. This is done with two experimental setups: the Riken cryogenic electrostatic (RICE) storage ring in Japan and the Dispositif d'irradiation de nanosystèmes biomoléculaires (DIAM) at IPNL in Lyon. The experiments provide complementary information about the energy distribution after excitation of molecular cluster.

The first project, the RICE ring, is dedicated to the study of collision dynamics of the stored molecular ions by merging experiments between the molecule of interest and a laser or a beam of neutral atoms [4]. The ring has an ultra-high vacuum of the 10^{-13} mbar order and at a cryogenic temperature of around 4 K. To provide a cold cluster beam to the RICE ring, a specific beamline was build which includes a cryogenic RF octupole trap. Aside from the trap, the beamline consists in an electrospray ion source (ESI), a quadrupole mass filter, RF octupole ion guides and a 20 keV pulsed acceleration tube. After acceleration, the cluster ions can be probed by a laser or injected in the ring. The ESI-source produces in gas phase large molecular ions and especially molecular ions surrounded by water cluster.

These clusters are mass-selected in a quadrupole mass filter and guided through octupole to an ion trap. The RF ion trap can be cool down to 5K and produces bunch of cold ions, the trap extraction is improved with extraction electrodes which reduce the size of the bunch. The bunch is then accelerated to up to 20 keV. The bunch can be probed by a laser to measure a photo-absorption spectrum, or the bunch can be injected in the RICE-ring.

The second project, the dispositif d'irradiation d'agrégats moléculaires (DIAM-IPNL), investigates processes induced by irradiation at the nanoscale. A molecular ion beam selected in mass and energy can be produced [5] [6]. In this work, we studied protonated pyridine water cluster: $PyH^+(H_2O)_{n=1\text{-}4}$ accelerated at 8keV and its collision with a target of helium atoms. A cluster collides with a single atom, at high velocity, and energy is deposited as an electron excitation in the cluster. The resulting excited cluster is unstable and can evaporate one or several water molecules. The products of this collision induced dissociation are detected by the Correlated Ion and Neutral Time of Flight (COINTOF) mass spectrometer used in combination with a Velocity-Map Imaging (VMI) method. The arrival time and position of each fragment (neutral and charged) are measured and recorded on an event by event basis. From the position distribution of fragments on the detector which is fully symmetric, the radial distribution of the neutral detected fragment can be extracted and an unfolding method calculates the velocity distribution of the evaporated water molecule [7]. Recently, the evaporated water velocity distribution from protonated water cluster was successfully measured [8] [9]. The next step was to put a pyridine molecule in the cluster and to study how it changes the energy distribution in the cluster after excitation. The measurement of the velocity distribution of the evaporated water molecule from 8 keV-$PyrH^+(H_2O)_{n=1\text{-}4}$ are directly compared with the velocity distribution calculated from statistic molecular dynamics simulation (SMD) [10] [11].

The thesis is divided in 3 chapters:

- Chapter 1 presents the motivation to study the energy distribution in gas phase. Both experimental setups, DIAM and RICE, will be described as well as the theoretical requirement to understand both experiments.

- Chapter 2 is a detailed explanation of the commissioning of the ion trap beam line at RIKEN with the ESI source, the Q-mass filter, the ion trap and the acceleration tube. Result of the first photo dissociation of methylene blue will then be presented.

- Chapter 3 is dedicated to the measurement of the velocity distribution of the water molecules evaporated from 8 keV-$PyrH^+(H_2O)_{n=1\text{-}4}$ after a single collision with a neutral argon atom. The measured velocity distributions of the evaporated water molecules are presented and compared to the velocity distribution measured for protonated water clusters. The experimental results are supported by statistical molecular dynamics calculations.

References

[1] D. Matthia, B. Heber, G. Reitz, M. Meier, L. Sihver, T. Berger and K. Herbst, "Temporal and spatial evolution of the solar energetic particle event on 20 January 2005 and resulting radiation doses in aviation," *JOURNAL OF GEOPHYSICAL RESEARCH,* vol. 114, p. A08104, 2009.

[2] R. Butikofer, E. Fluckiger, L. Desorgher and M. Moser, "The extreme solar cosmic ray particle event on 20 January 2005 and its influence on the radiation dose rate at aircraft altitude," *Science of The Total Environment,* vol. 391, no. 2-3, pp. 177-183, 2007.

[3] A. Castelman and P. Jena, "Clusters: A bridge across the disciplines of environement, material science, and biology," *Proc. Natl. Acad. Sci. USA,* vol. 103, no. 28, pp. 10554-10559, 2006.

[4] Y. Nakano, Y. Enomoto, T. Masunaga, S. Menk, P. Bertier and T. Azuma, "Design and commissioning of the RIKEN cryogenic electrostatic ring (RICE)," *Review of Scientific Instruments,* vol. 88, p. 033110, 2017.

[5] G. Bruny , S. Eden, R. Fillol, K. El Farkh, M. Harb, C. Teyssier, S. Ouaskit, H. Abdoul-Carime, B. Farizon, M. Farizon and T. D. Mark, "A new experimental setup designed for the investigation of irradiation of nanosystems in the gas phase: a high intensity mass-and-energy selected cluster beam.," *Rev Sci Instrum.,* vol. 83, no. 1, p. 013305, 2012.

[6] C. Teyssier, R. Fillol, H. Abdoul-Carime, B. Farizon, M. Farizon and T. D. Mark, "A novel “correlated ion and neutral time of flight” method: Event-by-event detection of neutral and charged fragments in collision induced dissociation of mass selected ions," *Review of Scientific Instruments,* vol. 85, p. 015118, 2014.

[7] F. Berthias, L. Feketeová, R. Della Negra, T. Dupasquier, R. Fillol, H. Abdoul-Carime, B. Farizon, M. Farizon and T. Mark, "Measurement of the velocity of neutral fragments by the “correlated ion and neutral," *REVIEW OF SCIENTIFIC INSTRUMENTS,* p. 083101, 2017.

[8] F. Berthias, "Thermalisation dans une nanogoutte d eau," Université de Lyon, Lyon, 2016.

[9] H. Abdoul-Carime, F. Berthias, L. Feketeová, M. Marciante, F. Calvo, V. Forquet, H. Chermette, B. Farizon, M. Farizon and T. D. Mark, "Velocity of a Molecule Evaporated from a Water Nanodroplet: Maxwell–Boltzmann Statistics versus Non-Ergodic Events," *Angewandte,* vol. 54, no. 49, p. 14685–14689 , 2015.

[10] F. Calvo, F. Berthias, L. Feketeová, H. Abdoul-Carime, B. Farizon and M. Farizon, "Collision-induced evaporation of water clusters and contribution of momentum transfer," *Eur. Phys. J. D,* vol. 71, no. 110, 2017.

[11] M. Marciante and F. Calvo, "Modelling infrared action spectra of protonated water clusters," *Molecular Simulation,* vol. 40, no. 1-3, pp. 176-184, 2013.

I. Molecular ions in gas phase

1. Molecular ions in gas phase

A. Isolated molecule in gas phase

The introduction of soft ionization technic in the late 1980s brings a massive progress in the study of molecule in gas phase. Electrospray ionization (ESI) [1] and matrix-assisted laser desorption/ionization (MALDI) [2] method allows to transfer large molecular species into the vacuum without breaking covalent and even hydrogen bond. These methods became a very powerful tool for mass spectrometry and for the characterization of molecular cluster.

The measurements of completely isolated molecules in gas phase allow the determination of the molecule intrinsic properties like ionization energies, electron affinities, dipole moments, bond strengths, photo abortion, intramolecular interaction and many more [3] [4]. These measurements can be directly compared with theoretical calculations and can be used to test models.

The measurements of molecules in gas phase complement liquid phase measurements. By adding solvent particles (atoms or molecules) to the cluster one at the time we can bridge the gap between isolated molecules and condensed matter. Indeed, structural, spectroscopic and dynamical properties evolve with cluster size: the environment of the molecule dissipate the absorbed energy and change the energy distribution in the system. A clear example was measured by Chatterley et al. [5] who measured the action spectrum of indigo in gas phase, in blue in Figure 1, and compared it with the spectrum made in methanol solution (red dashed line). The red-shift introduced by solvation in the $S_0 \rightarrow S_1$ absorption of 40 nm was interpreted as a larger HOMO (Highest Occupied Molecular Orbital)-LUMO (Lowest Unoccupied Molecular Orbital) gap in the gas phase in the absence of the polar stabilization of the LUMO by the methanol.

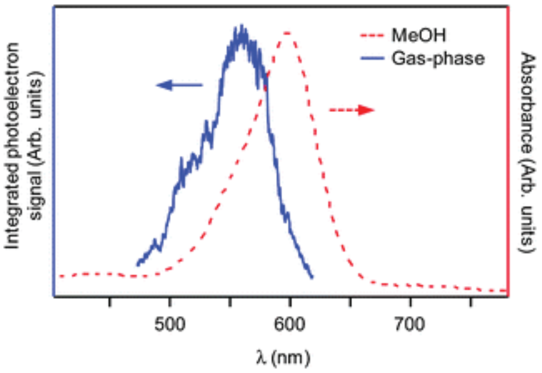

Figure 1: On the intrinsic photophysics of indigo: a time-resolved photoelectron spectroscopy study of the indigo carmine dianion. Reproduced directly from Adam S. Chatterley ab, Daniel A. Horke a and Jan R. R. Verlet, PCCP, 2012 [5]

Comparisons with studies made in solution allow us to understand the interactions between the molecules and their environment and to identify possible perturbations. The surrounding molecules allow for redistribution of the excess energy and of the charge within the cluster.

The study of solvated cluster reveals some irregularity of the cluster property depending of the size of the cluster: some cluster size can be produced with a higher abundance than others and are called magic number. The best and well know cluster example with magic number is protonated water cluster which is specifically stable for $(H_3O)^+(H_2O)_{20}$ and $(H_3O)^+(H_2O)_{30}$. Miyazaki et al. [6], found the existence of three different forms in protonated water cluster: chain structure for $n<10$, 2D sheet or net structures for $10<n<21$ and cages structures for $n>21$ [7].

The last motivation to study molecular cluster in gas phase is to understand our atmosphere which is a vast and dynamic system. Molecular clusters act as precursor for the formation of atmospheric particles which have large effect on the global climate. For example with water molecules, the third most abundant molecule and the principal radiation absorber in the atmosphere [8]: the model of atmospheric transitions which are using the well-known rotation and vibration excited states does not correspond with the atmosphere absorption spectrum [9]. Learning about the cluster formation, growth, physical and chemistry properties is useful to improve the models.

B. Charged molecular ions

The motivation to studying ions are both fundamental as practical. The charged particle, electron or proton, can move within the cluster and the physical and chemical cluster properties will change with the position of the charge and the number of solvent molecules. Mercier et al. studied the lifetime of the protonated tryptophan electronic excited state and its evolution under microsolvation [10]. The 3D structure of tryptophan is shown in the top part of Figure 2 (a). The charged transfer from the indole ring (shown in the bottom part) of tryptophan to a nearby electrophile is highly sensitive to the local electrostatic environment [11] [12] [13] [14]. The electronic photofragment action spectra of protonated tryptophan were measured with 0, 1 and 2 water molecules attached. Their results are shown in Figure 2 (b). The protonated tryptophan has a wide absorption peak which was explained as a mix between the $\pi\sigma^*$ and the $\pi\pi^*$ states and fast dissociative channel [15] [16]. Hydration of the NH_3^+ group shift the anti-bonding σ^* to higher energy and so decouple the $\pi\sigma^*$ and the $\pi\pi^*$ states and create long-lived excited states.

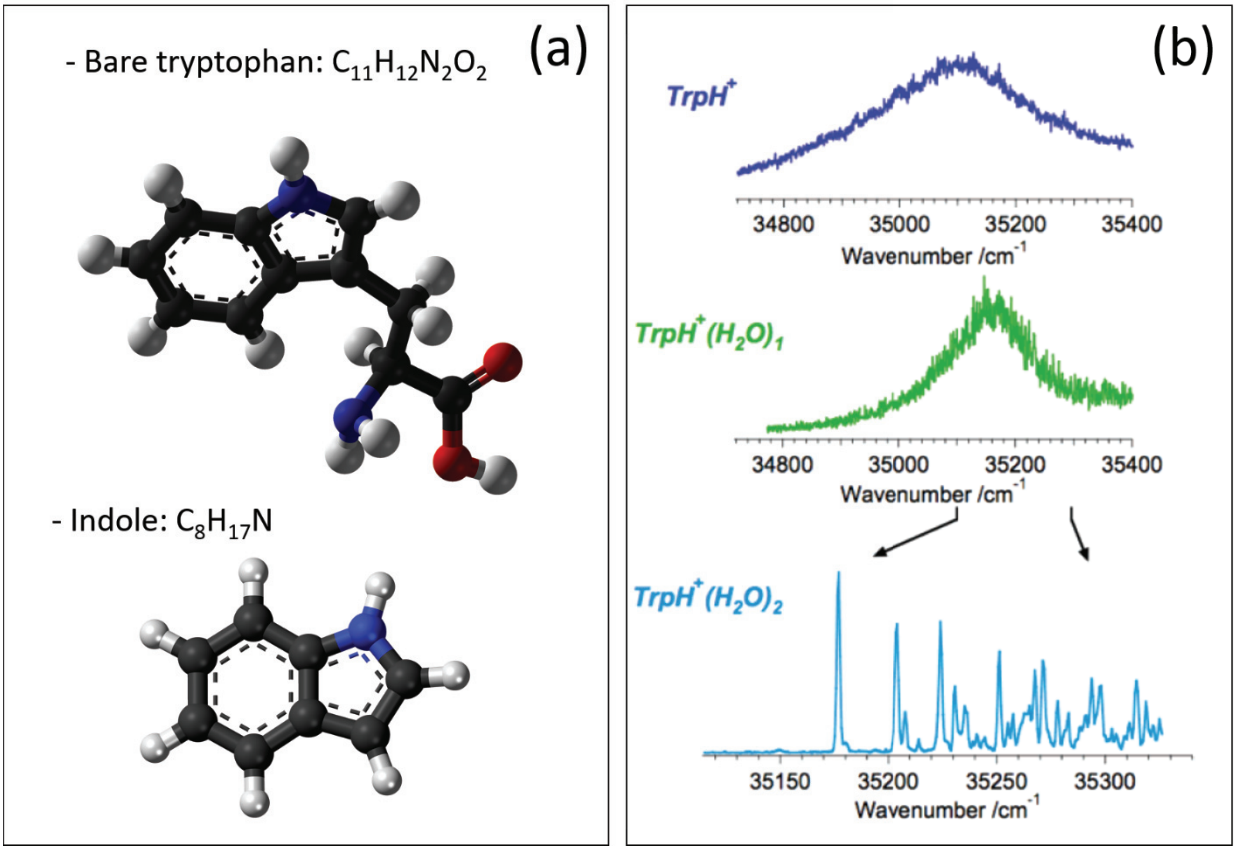

Figure 2: Electronic photofragment action spectrum of protonated tryptophan with 0, 1 and 2 water molecules (copy from [10]).

Practically, in nature, clusters are often founded ionized. For example, molecules in vivo are often globally or locally charged: amino acid at pH 7, neutral, have a deprotonated carboxylate group (COO^-) and a protonated ammonium group (NH_3^+). The charge movement imply a change in the configuration of the molecule which is especially important for bio-molecule as their shape determine their function.

In this work, we studied two molecular clusters: protonated pyridine water cluster and methylene blue water cluster.

Methylene blue is a blue dye with a strong absorption spectrum in visible light and a medication. Methylene blue is a heterocyclic aromatic chemical compound with the chemical formula $C_{16}H_{18}N_3SCl$ and its 2D-structure is shown in Figure 3. Once in solution, the chloride ion Cl^- will set apart, and always methylthioninium cation: $C_{16}H_{18}N_3S^+$ is studied. In this work, methylene blue cation will refer to methylthioninium cation.

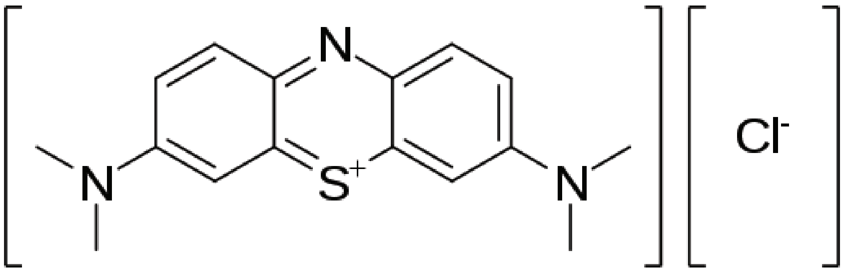

Figure 3: 2D-structure of methylene blue with the methylthioninium cation on the left and the chloride anion on the right [17].

Methylene blue is used as medication. It is mentioned in the world health organization's list of essential medicines as a protector against neurodegeneration and an antidote to carbon monoxide and cyanide poisoning. In our case, methylene blue was mainly studied because it is easy to produce in gas phase with an electrospray source and the absorption spectrum is well known in visible light in liquid phase [18] [19] [20] [21], so we can use it as a test for our beam line.

Protonated pyridine (PyrdineH$^+$, pyridinium or $C_5H_6N^+$) is a basic heterocyclic organic compound. Heterocyclic molecules as pyridine or pyrimidine are prebiotics materials and are building block of most of biomolecules. Pyridine derivatives have been detected in meteorites [22] [23], and may exist in extraterrestrial atmospheres [24] [25]. Meteorites might have brought these composites on earth which could have been the origin of life on earth [26] [27]. As well, heterocyclic molecules might have been found on Titan, the largest moon of Saturn. This is very important as Titan has many similarities with Earth: it has an atmosphere, sees, lakes and mountains. Titan could be a good candidate to host life.

The formation and photo stability of N-heterocycles in space was studied by Zeeters et al. [27]. They measured the UV destruction rate of nitrogen containing heterocyclic molecules and their results are shown in Figure 4. They found that molecules were rapidly destroyed by UV radiation and that their stability decrease with the increase of nitrogen atom in the molecules.

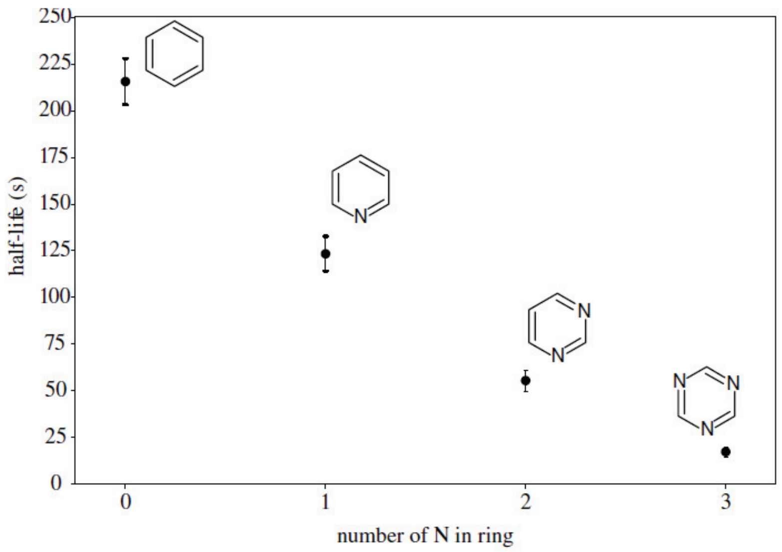

Figure 4: Half-lives of the three N-heterocycles plotted as a function of the number of nitrogen atoms in the ring. The benzene half-life was measured by Ruiterkamp et al. [28]

By comparison with the UV fluxes of astronomically relevant environment, they conclude that N-heterocycles molecules will not survive long in space. Pyridine was as well found in the Earth atmosphere, essentially in the troposphere, the lowest layer of Earth's atmosphere. In the troposphere, water vapor plays a key role as it absorbs solar energy and thermal radiation from the planet's surface. As pyridine and water cohabit together, they might associate each other and create pyridine water cluster. In a solvated cluster, pyridine might be more stable against UV radiation. The 3D-structure of protonated pyridine water cluster is shown in Figure 5.

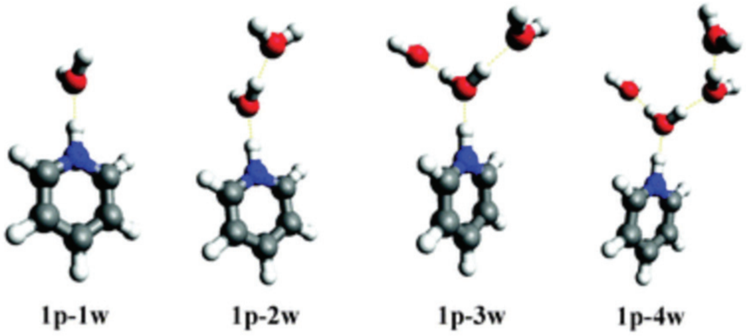

Figure 5: Structure of the protonated pyridine water cluster calculated by Ryding et al. [29].

The protonated pyridine is hydrophobic and the water molecules in the cluster will be all together on the same side [30] [31] [32]. The redistribution of the energy in protonated pyridine water cluster will be studied in this work and so the stability of solvated pyridine under UV radiation.

2. The experimental set-up

A. Experiment

Probing molecular cluster in gas phase is challenging as the ion density is small and the common methods used to study molecular structure and dynamics is usually not applicable. Several methods have been developed to probe the structures of molecular ions in gas phase such as mobility spectroscopy, ion-molecule reactions including proton transfer and hydrogen/deuterium exchange, collision induced dissociation or captured electron [33].

To study these molecular ions in gas phase, two specific experimental set-up were build: the RICE storage ring in RIKEN and DIAM project in the IPNL. Both set-up have common goals: study ions in gas phase and study the interactions between ions and energy. However, the two set-up are complementary and allow us to measure different parameters.

The storage ring let us explore the molecular and atomic ions over extended periods of time: an ion bunch can be stored for more than 10 min in the ring. The temperature of the ring can be controlled and vary from 4 K to room temperature. The beam can be probed by interaction with a laser or a neutral bunch. After excitation, the molecular ions can dissociate and the neutral fragment will be detected. We can directly measure the excited states, their level and their lifetime.

On the other side, DIAM investigates fast processes as the observation window is in the order of a few hundred nanoseconds. DIAM let us study the energy dissipation in the system after collision: the fragmentation process and velocity distribution measurement of evaporated particle. The detection system allows us to measure all the fragments, neutral and charged event-by-event.

B. *The RICE: Riken Cryogenic Electrostatic storage Ring.*

The RICE: Riken Cryogenic Electrostatic storage Ring was developed very recently in RIKEN [34]. Molecular ions can be stored in the ring for a long range of time, several minutes, with kinetic energies of up to 20 keV. The primary mission is to explore low-energy collisions and reactions of cold molecular ions in a specific vibrational and rotational states prepared in this ring. The group hopes to take advantage of an electrostatic ring without limitation of the mass of stored ions to learn more about the excitation and de-excitation dynamics of large bio-molecular ions or cluster ions and the energy-differential cross-sections of relevant collisions. The ring is under ultra-high vacuum of the 10^{-13} mbar order and kept at a very cold temperature around 4 K. An overview of the RICE facility is shown in Figure 6. The storage ring RICE is in the middle, the ions sources are on the right: an electron cyclotron resonance (ECR) ion source and an electrospray ion source (ESI) coupled with a cryogenic ion trap. On the left, the cesium sputter source and the photo-detachment chamber produce a neutral beam. The neutral beam is used to probe the ions bunches.

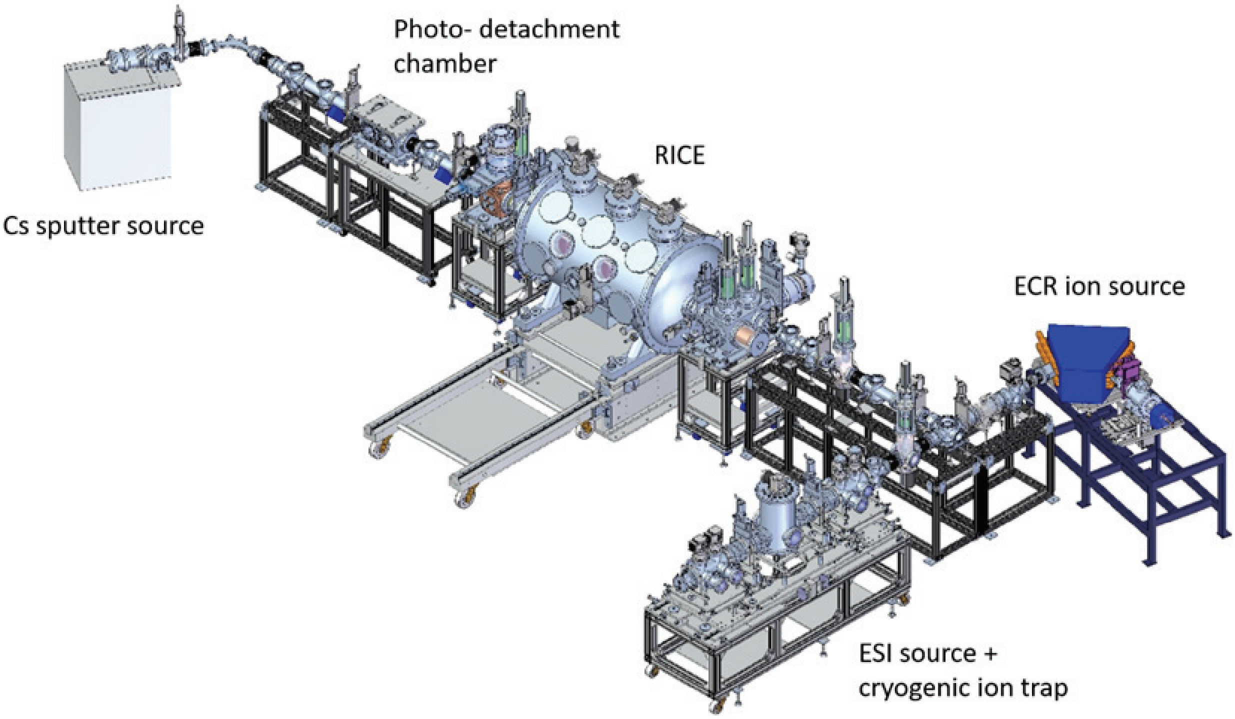

Figure 6: overall view of RICE: Riken Cryogenic Electrostatic ring

Once these ions are stored, different techniques can be used to probe them. Conventional spectroscopy cannot be achieved in such an experimental set-up because the density of ions is too small: the absorbance of light by a sample monitoring the intensity of the incident and transmitted light is insufficient.

Action spectroscopy is used to study ions in the ring. An observable ''action'' i.e., dissociation is required to determine an absorption spectrum. After the ions get excited to a higher energy level through photon absorption, several different de-excitation channels are possible: internal conversion, electron detachment or fluorescence for example. The daughter product ions or neutrals formed after dissociation are monitored for each laser wavelength and an action spectrum is obtained because the magnitude of the photoproducts is correlated to the number of ions undergoing an absorption process [35].

After dissociation, ionic fragments will be deflected and will not be stored in the ring due to the different kinetic energy, while neutral products will be unaffected by electrostatic deflector and can be detected at the end of a straight line with detectors. We can get information on lifetime of excited states and stability of ions.

The ions temperature can be controlled in the ring: longer storage time means lower temperature. Indeed, the hottest ions auto-dissociate, creating different fragments with different velocities which cannot be stored in the beam anymore. Furthermore, ions will cool down by radiation and the energy distribution within the ion bunch will shrink. However, to cool the ion internal energy down to the rotational level required that the ions have a strong dipole moment and that their modes are IR actives and the cooling process will anyway take long time. To produce cold ions, an ion trap beam line was built. The ion trap is cool down to 4 K and cold helium is injected in the trap as buffer gas. By collision with the cold helium gas, ions will lose internal energy until they reach a thermal equilibrium with the gas.

The Atomic, Molecular and Optical laboratory gather many other projects around RICE. For the trap beam line, a laser ablation source is now under commissioning to produce different ions than ESI as carbon metal clusters for example. A neutral beam line is under construction to be later injected in the ring, this study aims to investigate the dynamics of low-energy ion-molecule reactions and its dependence on the collision energy and molecular temperature. A superconducting tunnel junction (STJ) detector operating at 1.6 K is under development and will be able to detect the energy of the detected particle with high resolution. The last project is the study of molecular ions in superfluid helium droplets at 0.4 K.

C. The Dispositif d’irradiation de nanosystèmes biomoléculaires, DIAM

The Dispositif d’irradiation de nanosystèmes biomoléculaires, DIAM, was developed in IPNL [36] [37] and is dedicated to the study of collision induced dissociation of nanosystem. It gathers technics and knowledge from high-energy physics, molecular and cluster physics and mass spectrometry. DIAM has two beamlines: a high intensity proton beam accelerated between 20 keV and 150 keV and a cluster beam selected in mass and energy accelerated between 1 keV and 20 keV. The detection system has two different detectors: a commercial mass spectrometer and the COINTOF-VMI detectors [36]. A schematic view of the DIAM set-up is given in Figure 7.

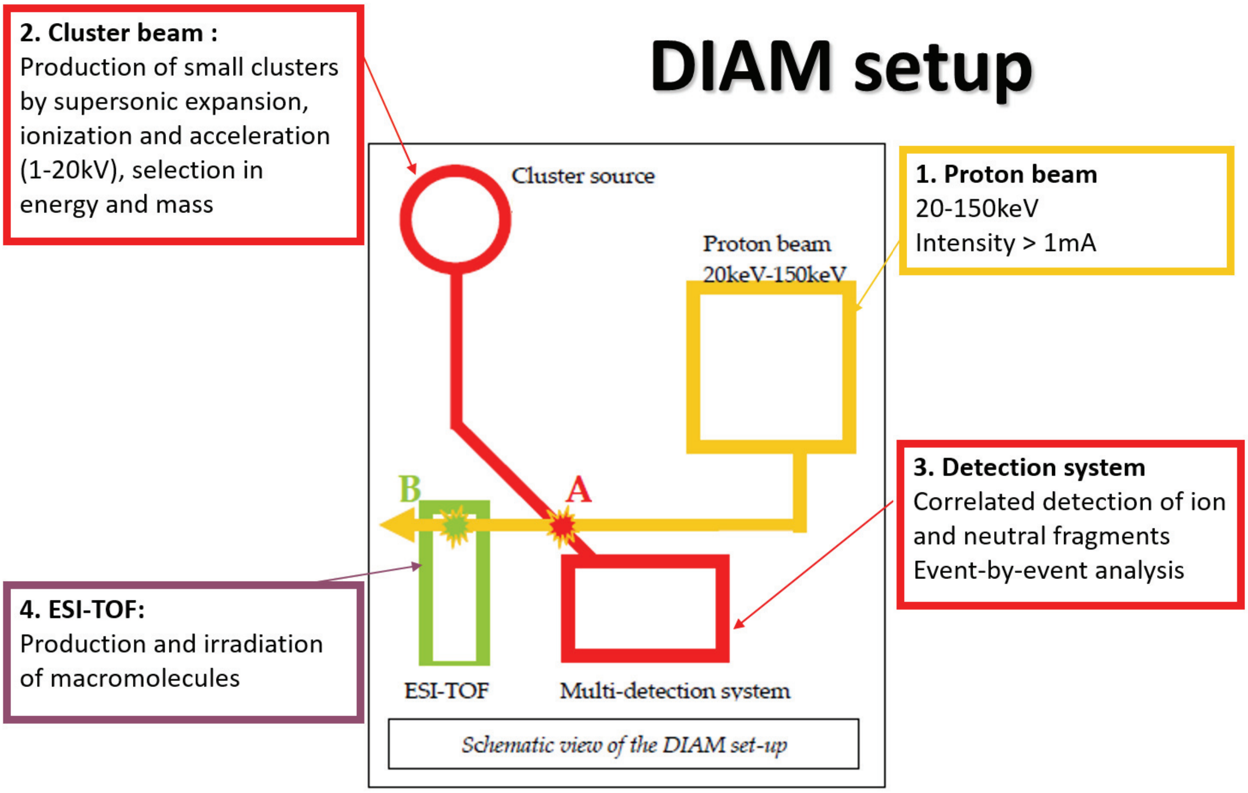

Figure 7: Schematic view of DIAM: the Dispositif d'irradiation de nanosystèmes biomoléculaires. DIAM has two beam lines and two detection systems. It produces a beam of mass and energy selected ion clusters.

There are two cross points where the proton beam (in yellow) can be used to irradiate the molecular system: either from the cluster beam line (A, in red) or in the industrial mass spectrometer (B, in green). Experiment without the proton beam are carried out in A where the beam collides with a target of neutral atoms and the fragments can be detected with the COINTOF VMI detector (Correlated Ion and Neutral Time-of-Flight Velocity Map Imaging). The COINTOF VMI detector allows correlated detection of ion and neutral fragments, and event-by-event analysis. The VMI method allows the measurement of the velocity distribution of the detected fragments. The observation window defined between the interaction region and the detector allows the measurement of short time events, in the order of a few hundred nanoseconds.

3. The physics underlying the experiments

A. Theoretical description of the system

The experimental set-up was built to study the interaction between energy and cluster. In this frame, energy is deposited in the system and its evolution is studied. Two different ways are used for energy deposition: interaction with a laser or collision with a neutral gas. With a laser interaction, the exact amount of energy absorbed by the system is known while in neutral collision, only an energy range deposition can be determined.

Large amounts of energy need to be handled internally by the molecular ions. Part of this energy will contribute to translational or rotational energy but most of it will be stored in the internal modes of the molecules. The internal modes have three excitation levels: rotation, vibration and electronic. The rotation can store a little amount of energy compared to vibration and electronic excitations which can store several electronvolts each [38].

The Jablonski diagram shown in Figure 8 presents the main photo-physical processes after a photon absorption: the transitions between the different electronic states and their vibrational levels. All these processes are dependent of the time scale of each transition: a fast transition will occur more likely than a slow transition.

After a photo absorption (A), an electron can be excited to a higher excited state. Once excited to the excited state S_N, the extra energy will be distributed among different modes of the molecule. It will preferentially promote the molecules to a singlet excited state S_N as the spin is a conserved quantum number.

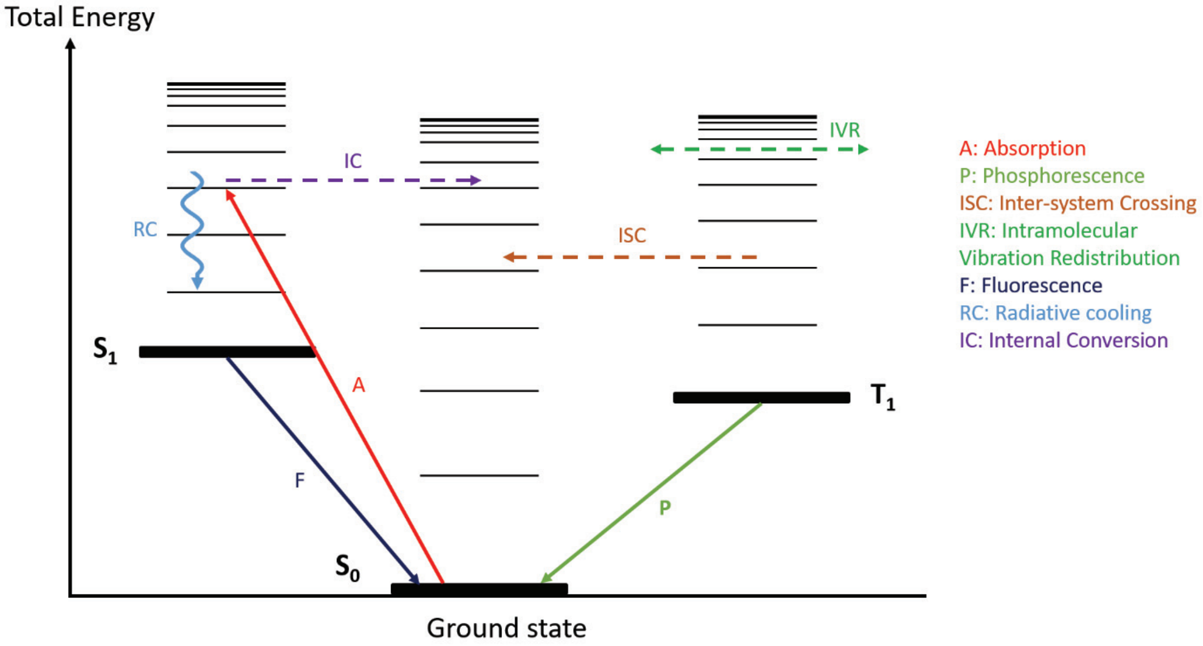

Figure 8: Jablonski diagram of the various physical processes after excitation [39].

Several processes compete in the deactivation of this excited state.

By fluorescence (F), the molecule will emit a photon and relax to a lower excited state without changing its spin while by phosphorescence (P) the spin will change. Fluorescence and phosphorescence are slow processes on the order of 10^{-5}-10^{-9} seconds and 10^{-}-10^{-4} seconds, respectively [40] [41] [42].

Inter-system crossing (ISC) is a radiation less transition in which the spin will change. This transition is allowed thanks to the spin-orbit coupling and its rate varies over a wide range. Inter-system crossing is the slowest process and ranges from 10^{-6} to 10^{-9} seconds for $S_1 \rightarrow T_1$ transitions for molecules that do not contain heavy atoms, and on the order of 10^{-}-10^{-3} seconds for $T_1 \rightarrow S_0$ [40].

Intramolecular vibration redistribution (IVR): the energy initially localized in one mode is redistributed among all 3N-6 modes, N being the number of atoms in the molecules. Radiative cooling (RC): the molecule emits a photon and relaxes to a lower excited state.

Internal conversion (IC) is a radiation less de-excitation process: $S_n \rightarrow S_m$ with n > m with no change in the spin of the molecule. As the separation of the levels decrease with increasing n (the nuclear wavefunctions overlap better), $S_n \rightarrow S_{n-1}$ will be faster than $S_{n-1} \rightarrow S_{n-2}$. S_1 will be fast occupied and because $S_1 \rightarrow S_0$ is slow (on the order of 10^{-5}- 10^{-8} s), lots of molecule will stay in the S_1 states. The IC can be faster if there are a crossing point between the potential energy surfaces (conical intersection), on the order of 10^{-13} second [40].

The absorbed energy might be above the dissociation threshold and the molecular ions become unstable. Unstable ion undergoes a dissociative channel in which the cluster will fragment to create parts with lower internal energy. There are three possible ways of relaxing the energy when it is above the dissociation energy. In a first case, the excited state S_1 is weakly bound and dissociative, the cluster ion can directly fragment in the S_1 states. In the case when S_1 state is not dissociative, but crosses a S_2 or T_1 dissociative states, the ion cluster can by internal conversion or inter-system crossing dissociate in the S_2 or T_1 states. Or if the ground state is dissociative, the ion cluster can go down to the dissociative ground states S_0 by internal conversion and then undergoes a fragmentation.

After energy deposition in a molecular ion, the energy can be redistributed among all degrees of freedom of the molecule via the processes shown in the Jablonski diagram and if the energy is higher than the dissociation energy, the molecular ions will probably fragment and produce fragments with lower internal energy. Thus, in order to understand the energy redistribution in a molecular ion, it is important to study its excited states.

B. Relation between observation and theory

Each energy level and excited state can be approximated with different calculations as the density function theory (DFT) or ab initio calculation. The DFT is a computational quantum mechanical modelling which is using functional, i.e. functions of another function, calculating the properties of a many-electron system. Ab initio calculation is as well a computational quantum mechanical method, and its goal is to solve the Schrödinger equation with simplification using the Hartree-Fock method for example.

These theories can predict numbers as excited state level energy and binding energy for example which can be compared with our experimental results. Spectroscopy is a good tool for validating calculated structures of large molecular ions in the gas phase. However large molecule with many atoms have a very dense spectrum and the distinction of each excited states might be impossible. Theory requires high resolution spectra to distinguish unambiguously the corresponding excited state. Cooling molecular ions to sufficiently low temperature may collapse all of the thermal congestion which is indispensable to measure the rotation and vibration levels.

As an example, the spectroscopy of cold, protonated tyrosine has been measured by Boyarkin et al. [43] and compared to the spectrum measured with uncooled ions. Their results are shown in Figure 9. The spectrum in Figure 9 (a), made with uncooled protonated tyrosine shows two broad bands at 35 100 cm^{-1} and at 35 850 cm^{-1} corresponding to the excitation of a ππ* electronic transition. In Figure 9 (b) the spectrum made with protonated tyrosine cooled in ion trap shows sharp and well resolved peaks associated to rotational band. The thermal congestion is reduced down to the rotation energy and their results compared with calculated energy level.

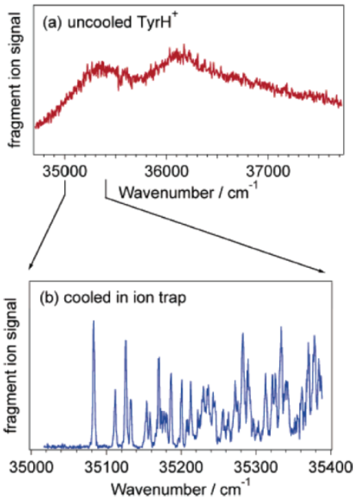

Figure 9: Electronic spectroscopy of cold, protonated tyrosine measured by Boyarkin et al. (copy from [43])

The cryogenic ion storage ring coupled with the ion trap aim to measure the ion properties at cold temperature. Cold absorption spectrum will be measured with well resolved bands which could be directly compared by theory.

C. Energy redistribution in the cluster

The energy redistribution in a molecular cluster ion can be explained with the Maxwell-Boltzmann theory. The Maxwell-Boltzmann theory is applied to a particle ensemble which does not interact with each other and which is in a thermal equilibrium at a temperature T. In our studies, we consider molecular ions in gas phase and so isolated with each other. The thermal equilibrium means a total redistribution of the energy among all degrees of freedom of the molecule. After energy absorption, the ions cluster can evaporate a molecule to create two fragments with lower internal energy. The measurements of the velocity distribution of the fragment give us information about the energy dissipation among the degrees of freedom of the ion cluster. The measurements of the velocity distribution probe a specific degree of freedom which is the translational energy. Measuring a velocity distribution with a shape of a Maxwell-Boltzmann distribution will tell that the energy was totally redistributed among the translational degree of freedom of the ion cluster.

However, two components have been evidenced in the velocity distribution of the evaporated molecules [45] [46] : a low velocity part and a high velocity part. The experimental results are supported by statistical molecular dynamics calculations performed by Florent Calvo [47] [48].The low velocity part of the distribution was fitted with a Maxwell-Boltzmann distribution and corresponds to the cluster in which the absorbed energy was totally redistributed among the degree of freedom of the molecule. The high velocity part was associated with non-ergodic event which comes from ion cluster in which the absorbed energy was not totally redistributed.

The study of out of equilibrium water nanodroplets is an open field of research which is of interest especially for the development of nanotechnology, for atmospheric study and in astrophysics to study the formation of prebiotic matter in the interstellar space under radiation.

In this work, we use two experimental set-ups to study the energy absorption process of ion cluster. In the storage ring RICE, the long-time range event can be studied with precise energy deposition. In

DIAM, the short range events are studied and the velocity distribution of the evaporated molecule is determined.

References:

[1] J. Fenn, M. Mann, C. Meng, S. Wong and C. Whitehouse, "Electrospray ionization for mass-spectrometry of large biomolecules.," *Science,* vol. 246, no. 4926, pp. 64-71, 1989.

[2] F. Hillenkamp, M. Karas, R. Beavis and B. Chait, "Matrix-assisted laser desorption ionization mass-spectrometry of biopolymers," *Anal. Chem.,* vol. 63, no. 24, pp. A1193-A1202, 1991.

[3] M. Jarrold, "Peptides and proteins in the vapor phase," *Annu. Rev. Phys.Chem.,* vol. 51, pp. 179-207, 2000.

[4] R. Weinkauf, J. Schermann, M. de Vries and K. Kleinermanns, "Molecular physics of building blocks of life under isolated or defined conditions," *Eur.Phys.J.D,* vol. 20, p. 309, 2002.

[5] A. S. Chatterley, D. A. Horke and J. R. R. Verlet, "On the intrinsic photophysics of indigo: a time-resolved photoelectron," *Phys. Chem. Chem. Phys.,* vol. 14, p. 16155–16161, 2012.

[6] M. Miyazaki, A. Fujii, T. Ebata and N. Mikami, "Infrared Spectroscopic Evidence for Protonated Water Clusters Forming Nanoscale Cages," *Science,* vol. 304, no. 5674, pp. 1134-1137, 2004.

[7] "The properties of ion-water clusters. I. The protonated 21-water cluster".

[8] R. Saykally, "Viewpoint: Simplest Water Cluster Leaves Behind its Spectral Fingerprint," *Physics,* vol. 6, no. 22, 2013.

[9] N. Goldman, C. Leforestier and R. Saykally, "Water Dimers in the Atmosphere II: Results from the VRT(ASP-W)III Potential Surface," *The journal of physical chemistry A,* vol. 108, no. 5, pp. 787-794, 2004.

[10] S. Mercier, O. Boyarkin, A. Kamariotis, M. Guglielmi, I. Tavernelli, U. Cascella, U. Rothlisberger and T. Rizzo, "Microsolvation Effects on the Excited-State Dynamics of Protonated Tryptophan," *Journal American Chemical Society,* vol. 128, pp. 16938-16943, 2006.

[11] N. Greenfield, A. Kostyukova and S. Hitchcock-DeGregori, "Structure and Tropomyosin Binding Properties of the N-Terminal Capping Domain of Tropomodulin 1," *Biophysical Journal,* vol. 88, no. 1, pp. 372-383, 2005.

[12] P. Callis and J. Vivian, "Understanding the variable fluorescence quantum yield of tryptophan in proteins using QM-MM simulations. Quenching by charge transfer to the peptide backbone," *Chemical Physics Letters,* vol. 369, no. 3-4, pp. 409-414, 2003.

[13] C. Marquezin, I. Hirata, L. Juliano and A. Ito, "Tryptophan as a probe for acid–base equilibria in peptides," *peptide science,* vol. 71, no. 5, p. 569–576 , 2003.

[14] C. Dedonder-Lardeux, C. Jouvet, S. Peruni and A. Sobolewski, "External electric field effect on the lowest excited states of indole: ab initio and molecular dynamics study," *Physical Chemistry Chemical Physics,* vol. 5, no. 22, pp. 5118-5126 , 2203.

[15] H. Kang, C. Jouvet, C. Debonder-Lardeux, S. Martrenchard, G. Gregoire, C. Desfrancois, J. Schermann, M. Barat and J. Fayeton, "Ultrafast deactivation mechanisms of protonated

aromatic amino acids following UV excitation," *Physics Chemistry Chemical Physics,* vol. 7, no. 2, pp. 394-398 , 2004.

[16] G. Gregoire, C. Jouvet, C. Dedonber and A. Sobolewski, "On the role of dissociative πσ* states in the photochemistry of protonated tryptamine and tryptophan: An ab initio study," *chemical physics,* vol. 324, no. 2-3, pp. 398-404, 2006.

[17] Harbinary, "Methylene blue," Wikipedia, [Online]. Available: https://commons.wikimedia.org/w/index.php?curid=8525246. [Accessed 06 07 2017].

[18] S. Prahl, "Methylene Blue Spectra," Oregon Medical Laser Center, 8 march 1998. [Online]. Available: http://omlc.org/spectra/mb/mb-water.html. [Accessed 07 04 2017].

[19] T.-J. Whang, H.-Y. Huang, M.-T. Hsieh and J.-J. Chen, "Laser-Induced Silver Nanoparticles on Titanium Oxide for Photocatalytic Degradation of Methylene Blue," *International journal of molecular sciences,* vol. 10, pp. 4707-4718, 2009.

[20] D. Melgoza, A. Hernandez-Ramirez and J. Peralta-Hernandez, "Comparative efficiencies of the decolourisation of Methylene Blue using Fenton’s and photo-Fenton's reactions," *Royal Society of Chemistry,* vol. 8, pp. 596-599, 2009.

[21] E. Morgounova, Q. Shao, B. Hackel, D. Thomas and S. Ashkenazi, "Photoacoustic lifetime contrast between methylene blue monomers and self-quenched dimers as a model for dual-labeled activatable probes," *Journal of Biomedical Optics,* vol. 18, no. 5, p. 056004, 2013.

[22] P. G. Stocks and A. W. Schwartz, "Basic nitrogen-heterocyclic compounds in the Murchison meteorite," *Geochimica et Cosmochimica Acta,* no. 46, pp. 309-315, 1982.

[23] P. G. Stocks and A. W. Schwatrz, "Nitrogen-heterocyclic compounds in meteorites significance and mechanisms of formation," *Geochimica et Cosmochimica Acta,* no. 44, pp. 563-569, 1981.

[24] A. Somogy, C. H. Oh, M. Smith and J. Lunine, "Organic Environments on Saturn’s Moon, Titan: Simulating Chemical Reactions and Analyzing Products by FT-ICR and Ion-Trap Mass Spectrometry," *Cover image Journal of the American Society for Mass Spectrometry,* no. 16, pp. 850-859, 2005.

[25] S. Soorkia, C. Taatjes, D. Osborn, T. Selby, A. Trevitt and K. Wilson, "Direct detection of pyridine formation by the reaction of CH (CD) with pyrrole: a ring expansion reaction," *Physical Chemistry Chemical Physics,* no. 12, pp. 8750-8758, 2010.

[26] V. Dryza, J. Sanelli, E. Roberston and E. Bieske, "Electronic Spectra of Gas-Phase Polycyclic Aromatic Nitrogen Heterocycle Cations: Isoquinoline+ and Quinoline+," *The Journal of Physical Chemistry A,* no. 116, pp. 4323-4329, 2012.

[27] Z. Peeters, O. Otta, S. Charnley, Z. Kisiek, Y. J. Kuan and P. Ehrenfreund, "Formation and photostability of N-heterocycles in space - I. The effect of nitrogen on the photostability of small aromatic molecules," *Astronomy and Astrophysics,* vol. 433, no. 583-590, 2005.

[28] R. Ruiterkamp, Z. Peeters, M. Moore, R. Hudson and P. Ehrenfreund, "A quantitative study of proton irradiation and UV photolysis of benzene in interstellar environments," *Astronomy and Astophysics,* vol. 440, no. 1, pp. 391-402, 2005.

[29] M. Ryding, A. Zatula, P. Andersson and E. Uggerud, "Isotope exchange in reactions between D2O and size-selected ionic water clusters containing pyridine, H+(pyridine)m(H2O)n," *Royal Society of Chemistry,* vol. 13, pp. 1356-1367, 2011.

[30] M. C. Sicilia, C. Munoz-Caro and A. Nino, "Theoretical Analysis of Pyridine Protonation in Water Clusters of Increasing Size," *ChemPhysChem,* vol. 6, p. 139 – 147, 2005.

[31] M. C. Sicilia, A. Nino and C. Munoz-Caro, "Mechanism of Pyridine Protonation in Water Clusters of Increasing Size," *J. Phys. Chem. A,* vol. 109, pp. 8341-8347, 2005.

[32] Y. Ibrahim, R. Mabrouki, M. Meot-Ner and M. S. Ei-Shall, "Hydrogen Bonding Interactions of Pyridine•+ with Water: Stepwise Solvation of Distonic Cations," *J. Phys. Chem. A ,* vol. 111, pp. 1006-1014, 2007.

[33] A. Iavarone, D. Duft and J. H. Parks, "Shedding Light on Biomolecule Conformational Dynamics Using Fluorescence Measurements of Trapped Ions," *The journal of physical chemistry A,* vol. 110, no. 47, p. 12714–12727, 2006.

[34] Y. Nakano, Y. Enomoto, T. Masunaga, S. Menk, P. Bertier and T. Azuma, "Design and commissioning of the RIKEN cryogenic electrostatic ring (RICE)," *REVIEW OF SCIENTIFIC INSTRUMENTS,* vol. 88, p. 033110, 2017.

[35] S. Nielsen and J. Wyer, Photophysics of Ionic Biochromophores, Spinger, 2014.

[36] C. Teyssier, R. Fillol, H. Abdoul-Carime, B. Farizon, M. Farizon and T. Mark, "A novel “correlated ion and neutral time of flight” method: Event-by-event detection of neutral and charged fragments in collision induced dissociation of mass selected ions," *REVIEW OF SCIENTIFIC INSTRUMENTS,* vol. 85, p. 015118, 2014.

[37] G. Bruny, S. Eden, S. Feil, R. Fillol, K. Ei Farkh, M. Harb, C. Teyssier, S. Ouaskit, H. Abdoul-Carime, B. Farizon, M. Farizon and T. Mark, "A new experimental setup designed for the investigation of irradiation of nanosystems in the gas phase: a high intensity mass-and-energy selected cluster beam.," *Review of Scientific Instruments,* vol. 83, p. 013305, 2012.

[38] T. Mark, "Fundamental aspects of electron impact ionization," *International Journal of Mass Spectrometry and Ion Physics,* vol. 45, pp. 125-145, 1982.

[39] M. Guidi, "Spectroscopy and Dissociation Dynamics of Cold, Biomolecular Ions," ÉCOLE POLYTECHNIQUE FÉDÉRALE DE LAUSANNE, Lausanne, 2010.

[40] N. Turro, Modern Molecular Photochemistry, Menlo Park: Benjamin/Cummings, 1978.

[41] J. Lakowicz, Principles of Fluorescence Spectroscopy., New York: Kluwer Academic / Plenum Publisher., 1999.

[42] E. Priestley and A. Haug, "Phosphorescence Spectrum of Pure Crystalline Naphthalene," *J. Chem. Phys.,* vol. 49, no. 2, p. 622, 1986.

[43] O. V. Boyarkin, S. R. Mercier, A. Kamariotis and T. R. Rizzo, "Electronic spectroscopy of cold, protonated tryptophan and tyrosine.," *J Am Chem Soc.,* vol. 128, no. 9, p. 2816–2817, 2006.

[44] A. Pereverzev, X. Cheng, N. Nagornova, D. Reese, R. Steele and O. Boyarkin, "Vibrational Signatures of Conformer-Specific Intramolecular Interactions in Protonated Tryptophan," *The journal of physical chemistry A,* vol. 120, no. 28, pp. 5598-5608, 2016.

[45] F. Berthias, "Thermalisation dans une nanogoutte d eau," Universite de Lyon IPNL, Lyon, 2016.

[46] H. Abdoul-Carime, F. Berthias, L. Feketeova, M. Marciante, F. Calvo, V. Forquet, H. Charmette, B. Farizon, M. Farizon and T. Mark, "Velocity of a Molecule Evaporated from a Water Nanodroplet: Maxwell–Boltzmann Statistics versus Non-Ergodic Events," *Angewandte Chemie,* vol. 54, no. 49, p. 14685–14689 , 2015.

[47] Z. Peeters, O. Botta, S. Charnley, Z. Kisiel, Y. Kuan and P. Ehrenfreund, "Formation and photostability of N-heterocycles in space".

[48] grhowes, "Pyridinium," Wkipedia, 10 06 2010. [Online]. Available: https://en.wikipedia.org/wiki/Pyridinium. [Accessed 06 07 2017].

II. Development of a beam line for the production of cold molecular ion bunches

This chapter is dedicated to the detailed description of the experimental setup developed in RIKEN: an ion beamline producing bunches of cold ions. An overview of the beamline is given in Figure 10 and the basic concepts of its components are presented. The molecular ions are produced by an electrospray ionization (ESI) source. The species of interest are mass selected in a quadrupole mass filter and then trapped and cooled down in an octupole radio-frequency ion trap. The extracted ion bunch is then accelerated to a kinetic energy of up to 20 keV. Finally, the bunch is probed by a pulsed laser or injected in the ring for further experiments. Preliminary experiments on photo-dissociation of methylene blue cations will be described.

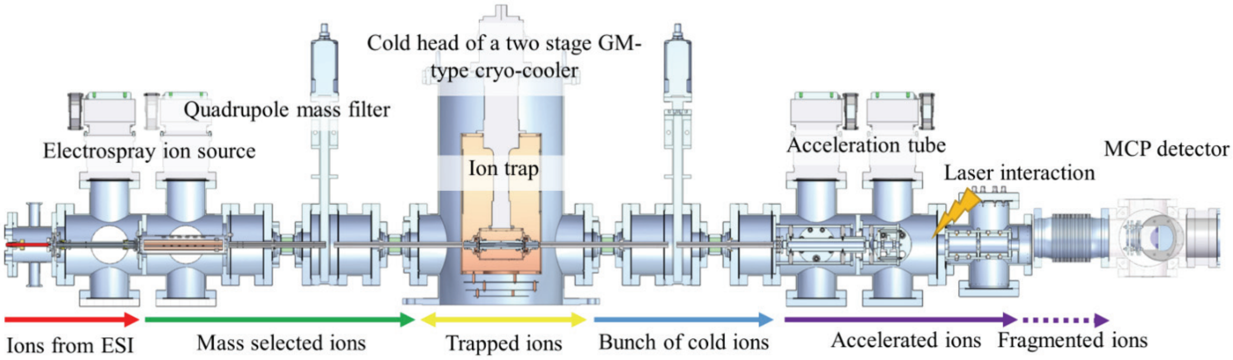

Figure 10: Beamline overview with the ion source, the quadrupole mass filter, the ion trap and the acceleration tube. The ions produced in the ESI are cooled, bunched and accelerated up to 20 keV to be probed by a laser or injected in the ring.

1. The electrospray ionization source

a. The ion source

Electrospray ionization is a technique used to produce positive or negative ions in gas-phase. It was first introduced by Fenn in 1989 to analyze intact chemical species, such as proteins [1]. One of the advantages over former ion sources is that ESI is a soft ionization technique. It produces large molecular systems such as biomolecules and clusters of molecules with a small fragmentation rate. Indeed, a small residual energy is stored in the molecular ions and even weak noncovalent interactions are preserved in gas-phase [2]. It became very popular for the study of large element and thus rapidly developed by chemists or biologists. “A few years ago the idea of making proteins or polymers “fly” by electrospray ionization (ESI) seemed as improbable as a flying elephant, but today it is a standard part of modern mass spectrometers" as stated by the Professor Fenn in his Nobel lecture [3]. The ESI mechanism is described in detail in a review article written by Shibdas Banerjee and Shyamalava Mazumdar [4].

A schematic view of the ESI source used in this work is given in Figure 11. The molecule of interest is mixed with a solvent and injected with a needle (Hamilton ID 0.47 mm, flat tip) at a constant flow rate of ~ 40 µl/min using a syringe pump (YMC YSP-101 Syringe Pump). A high voltage (3-5 kV) is applied to the gap of ~ 5-20 mm between the needle and the capillary (Scientific instrument services, ID 0.8 cm, 11 cm long) leading into the vacuum chamber. At a critical field, the surface of the liquid will be deformed and form a Taylor cone [5]. The competition between the Coulomb electric field force and the surface tension leads to the formation of a zone of high turbulence where charged droplets are formed. The produced small droplets are accelerated from the cone to the capillary. Collisions with the atmospheric gas induce solvent evaporation and the ions of interest are released from the droplets.

The capillary (0.2 mm inner diameter, 60 mm length) is heated in order to insure a complete desolvation of the droplets. The ions are then focused by a lens (+180 V) through a skimmer (0-80 V, 2 mm diameter) and are guided through an octupole until the quadrupole mass filter. A skimmer is used to separate the first pumping stage (0.5 mbar) at the exit of the capillary and the second pumping stage (10^{-5} mbar) with the octupole ion guide.

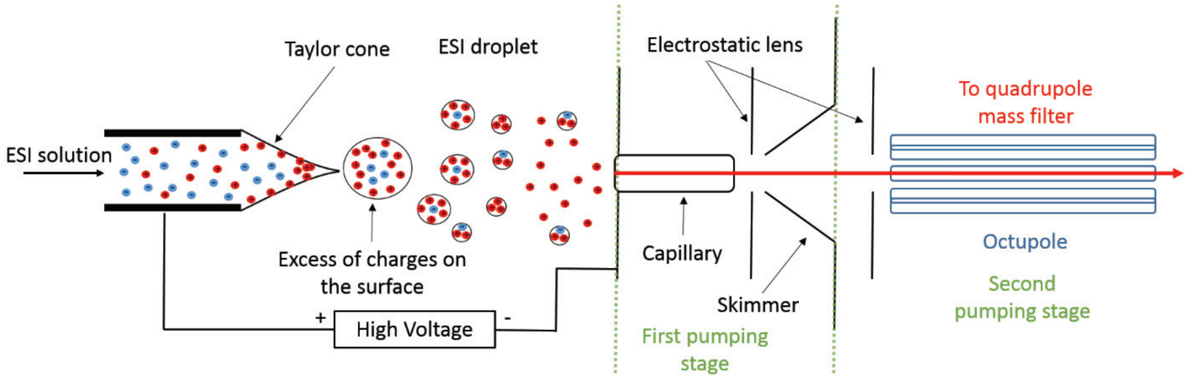

Figure 11: Scheme of the ESI source mechanism. Positive ions are represented in red, negative ions in blue. The ions are traveling from the left to the right. Two differential pumping stages are shown in green separated from the atmosphere by a capillary and between each other by a skimmer.

Many other kind of ESI sources are used as pneumatically assisted electrospray [6] [7] [8], ultrasonic nebulizer electrospray [9] [10], electrosonic spray [11] and nanoelectrospray [12] [13]. Our homemade ESI source is adapted to the production of cluster, e.g. water molecules are easily attached to the molecular ions of interest.

b. The beam line vacuum and detection system

1) The vacuum system

Since the ESI source is connected to atmospheric pressure, many differential pumping stages are needed to obtain high vacuum in the following ion beamline. The beamline is thus separated into 4 pumping areas which are shown in red in Figure 12: the source, the Q-mass, the trap and the acceleration tube. In total 9 vacuum pumps are used for the beamline: 3 scroll pumps, 5 turbo molecular pumps (TMP) and a dry pump (see Table 1 and Figure 12 for details).

Number	Name	Pumps	Pressure (mbar)
①	Source	Edwards iGX dry pump 172 L/sec (IGX600N): ①	①: $5x10^{-1}$
②	Q mass	TMP Osaka TG220F (200L/s nitrogen, 100L/s helium) ⑤⑥ Edwards RV8A654-01-904 scroll pump (3.6x 10^7 L/sec) ②	②: $8x10^{-4}$ ③: $2x10^{-6}$
③	trap	TMP 1100 L/sec (nitrogen), 820 L/sec (helium) (Osaka, model TG1100F):⑦ Edwards RV8A654-01-904 scroll pump (3.6x 10^7 L/sec) ③	④: $1x10^{-8}$
④	acceleration tube	TMP Osaka TG220F (200L/s nitrogen, 100L/s helium) ⑧⑨ Edwards RV8A654-01-904 scroll pump (3.6x 10^7 L/sec) ④	⑤: $1x10^{-8}$

Table 1: The vacuum system of the beamline with the position, name and pressure of the four different pumping areas. The different pumps are listed with their characteristics.

The source and the Q-mass filter are separated with a skimmer (2mm diameter). The Q-mass filter and the trap as well as the trap and the acceleration tube are separated by two octupole guides fixed in a narrow chamber to improve the differential pumping. Five Pfeiffer compact full range vacuum gauges (PKR 251) (green in Figure 12) are used to measure the vacuum pressure: one in the source (just a Pirani gauge), one in the first octupole guide, one in the Q mass filter, one in the bottom of the vacuum chamber of the trap and one in the acceleration tube. We note that in this thesis, the trap pressure refers to the pressure at the vacuum gauge number 4, and not the actual pressure inside the trap. None of the above vacuum pressures are helium corrected.

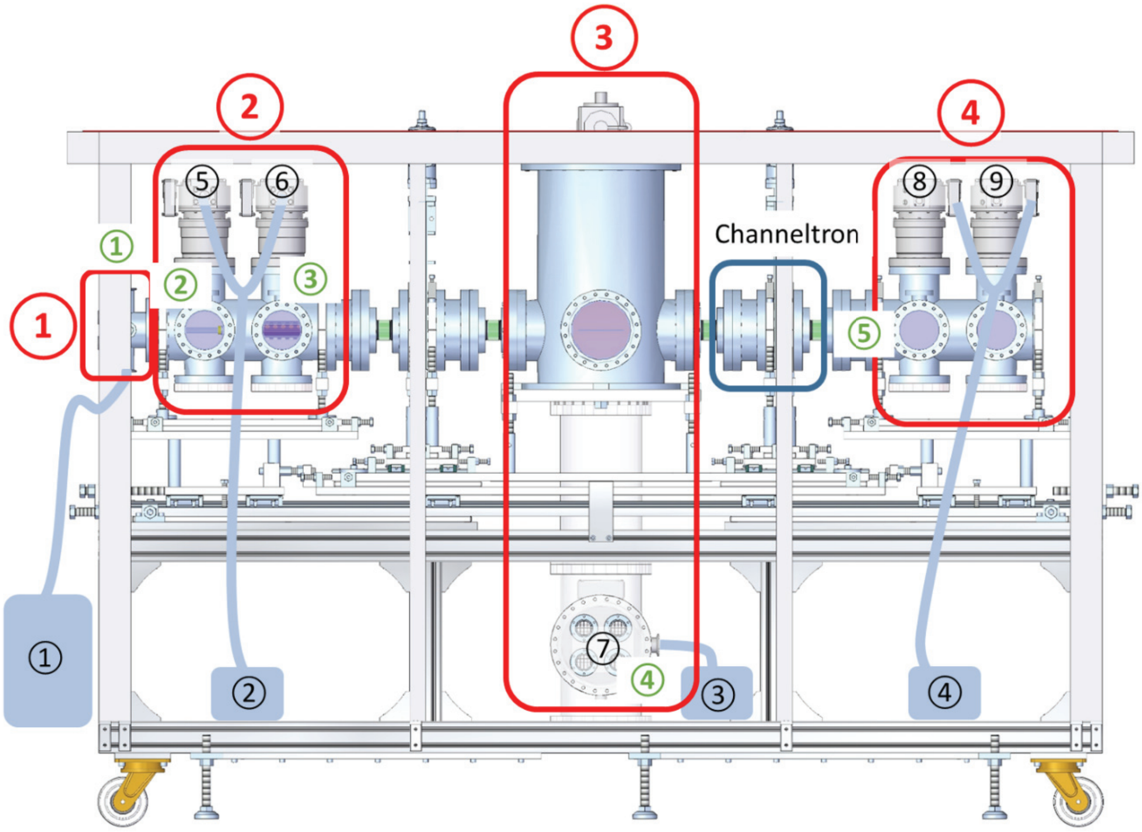

Figure 12: The vacuum pumping system with in red the different pumping areas, in black the pumps and in green the position of the 5 vacuum gauges. All number are referenced in Table 1.

2) *The detection system*

Two particle detectors are installed in the beamline: a channeltron electron multiplier (CEM) detector (DeTech 402AH Electron Multiplier) and two multichannel plate (MCP) detectors from Hamamatsu.

A CEM is used to multiply incident charges of the ions and thus convert them into a measureable signal. The CEM is usually made of glass with an emissive material. Secondary electrons from the ion impact will create a couple of new electrons which again can produce more electrons in a cascade. In this CEM configuration, the incoming positive ion at first hits a converter plate at high-voltage set at -4 kV, secondary electrons are emitted from the plate and enter the channeltron where they create a cascade of electrons which are detected at the back end of the detector. For the detection of negative ions, the situation is different and another method is used. In addition to electrons, positives ions are also produced at the surface of the converter plate after the ion impact [14]. The converter plate potential is set at +4 kV, and the channeltron at -2 kV so positive ions will enter the channeltron and create the electron cascade.

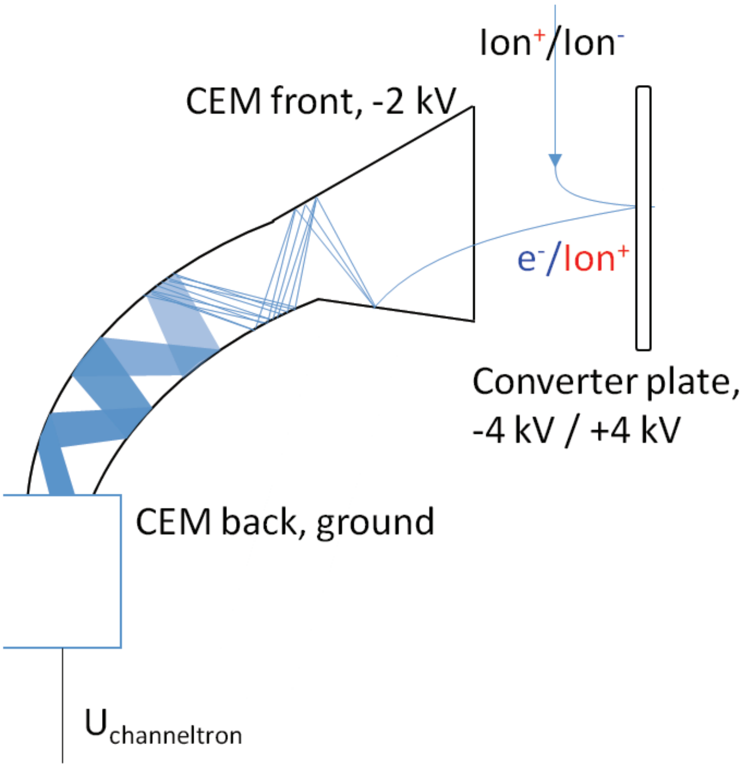

Figure 13: Scheme of channeltron electron multiplier mechanism. The channeltron is composed with a converter plate and a cone made with an emissive material.

The channeltron is installed in the beam line after the trap (Figure 12 and Figure 14). The whole beam line is mounted on rails and each pumping area is set on different platforms which are connected to each other with bellows. Bellows can be compressed or stretches to displace one pumping area away or closer to another. In the channeltron operating mode, case 1 in Figure 14, the octupoles are pulled away by stretching a bellow and the ions can be detected in the gap. In guiding mode (case 2), the octupoles are close together and the channeltron is grounded to avoid perturbation in the ion transportation.

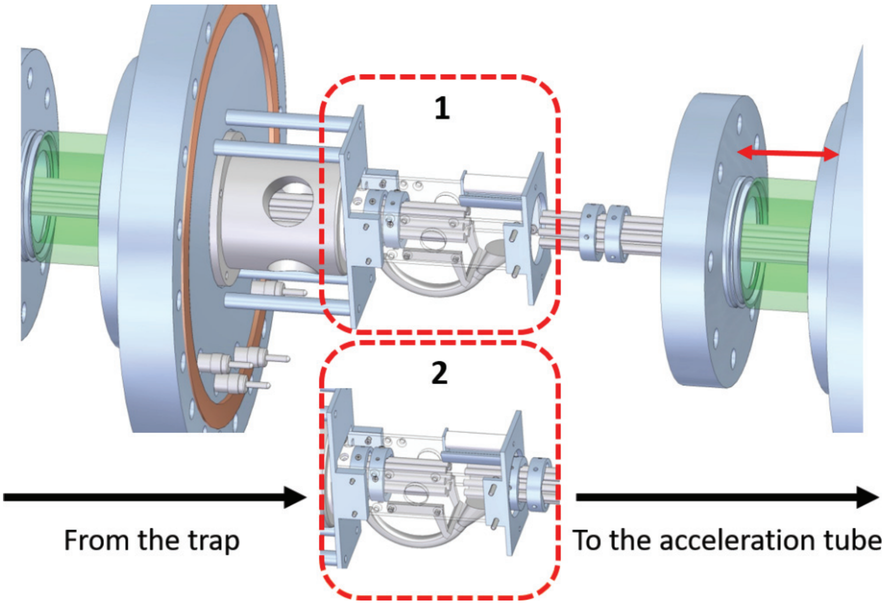

Figure 14: The channeltron detector in the beam line with two different positions: in 1, the channeltron is in operated mode. In 2, the below is pressed and the channeltron is covered by the octupole: this is the guiding mode.

The MCP is used for particles detections using an electron multiplier. A MCP is a planar component with a regular array of microchannel evenly distributed on the surface. Each microchannel is an electron multiplier: a particle hits one side of the channel and an electron cascade is created in the channel. A single metal anode gathers the signal from all channels and measures the total current. A picture of the beam can be observed by adding a phosphor screen after the MC plate: electrons from the plate will hit the screen and the phosphor will emit light where the particle hit the detector.

A movable MCP detector is installed at the end of the beamline after the acceleration tube. The detector is mounted on a movable support and can thus be positioned in the center of the beam line. To detect positive ions, the front is usually set at negative high voltage (~ - 2 kV) and measures the pulsed signals at the grounded back side. To inject ions into the ring, the MCP detector is moved to its high position to clear the beam line. The acquisition system and the MCP detector will be discussed in more detail in 3).

The four pumping areas which composed the beam line are connected with ion guides. Ion guide, Q mass and octupole ion trap use the same principle: radio frequency multipole.

c. Radio frequency multipole

1) Radio frequency multipole principle

The beam line has 8 octupoles: 7 ion guides and one ion trap, and they are all represented in the beam line order in Figure 15 (a); the length of each is given in the legend. A multipole consists of 2n stainless steel rod-shaped electrodes arranged in a circular array, where n is called the order of the multipole. In Figure 15 (b), an example of a multipole trap with n=4, an octupole, is displayed as a 3D model created with Solid Edge ST3. Alternating rods are connected together to form two sets of n rods. A transversal cut through an octupole is shown in Figure 15 (c.1); where connected electrodes are in the same color (four orange and four magenta rods). The two electrode sets are connected to opposite phases of a radio frequency sources so that radio frequency voltages of equal magnitude but opposite phase are applied. The RF field represented in Figure 15 (c.2) is applied to the octupole with the orange phase connected to the orange electrodes and the magenta phase to the magenta electrode. The x-axis shows time and the y-axis the amplitude of the signal. The radio frequency voltage creates a large field-free region in a cylindrical shape along the axis where ions are trapped. This octupole configuration can be used to guide ions along the z-axis. However, by applying a DC voltage to both end cap ring electrodes, ions can be trapped in all three dimensions [15]. As showed in Figure 15 (b), two connectors are used to electrically combine the two electrodes and supply them with their radio frequency signal. The insulators at both sides of the multipole support the rods and insulate the end cap and the rod electrodes.

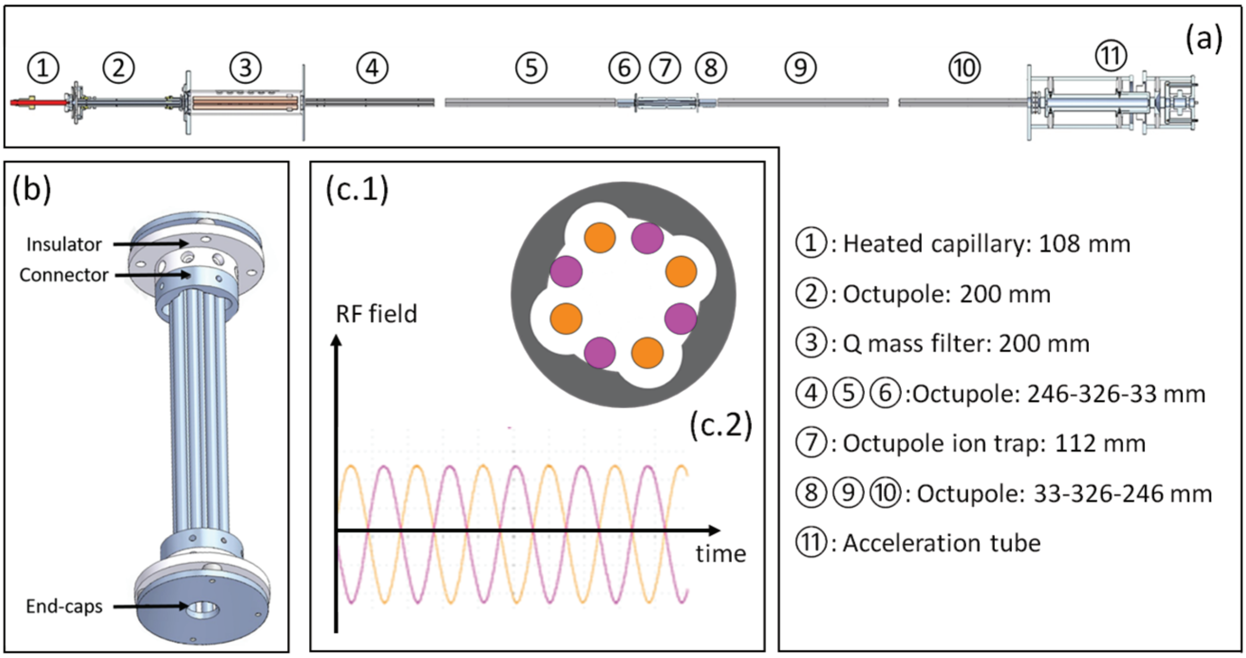

Figure 15: Explanation of the multipole system: (a) electrodes and multipoles in the beam line with name and length of each device, (b) design of an octupole trap with the voltage connector, the mounting system and electrodes as 3D model using Solid Edges, (c.1) perpendicular cut of the trap and (c.2) radio-frequency signal which is distributed in the two electrodes (with a frequency of 1 MHz and an amplitude of 200 V).

The octupoles are all driven by four homemade RF power supplies following the design of [16]. The first RF power supply has one output and is connected with the first octupole (number ② in Figure 15), the second and the fourth have two outputs for the guiding octupole (number ④, ⑤, ⑨ and ⑩) and the third has three outputs for the trap octupole (number ⑥,⑦ and ⑧). For the mass range of interest (1-2000 atomic mass unit (amu)), the frequency of the RF generator was set to 1 MHz. Usually a RF amplitude of 200 V is used, while the DC voltage of each octupole can be adjusted independently (±300 V).

2) *Potential and ion trajectory in a multipole*

The effective potential that ions are subjected to in a multipole is shown in Figure 16(a). The x-axis represents the normalized radial distance from the center of the multipole, and the y-axis is the potential at distance r normalized by the potential at r_0, the potential at the electrode. The potential is given by the equation:

$$U_{eff}(r,\varphi) = U_{eff}(r_0) r^n cos\,(n\varphi) \tag{1}$$

With:

- r, φ: polar coordinates
- r_0: radial position of the rods (maximum radius)
- n: order of the multipole

The choice of the multipole order *n* depends on the specific experiment as it directly affects the shape of the potential. As the number of poles increases, the repulsive wall becomes steeper and the field free region enlarges. On the other hand, for lower *n*, the potential increases smoothly from the center of the trap to the electrode. In a quadrupole, the ions will be well localized in the center of the trap. Such ion localization is critical for experiments with direct probing of the bunch, like with a laser for example. In a 22-pole, the trap volume is optimized and many ions can be trapped.

The ions trajectory in the orthogonal directions, (x,y) axis, is shown in Figure 16(b) [17].

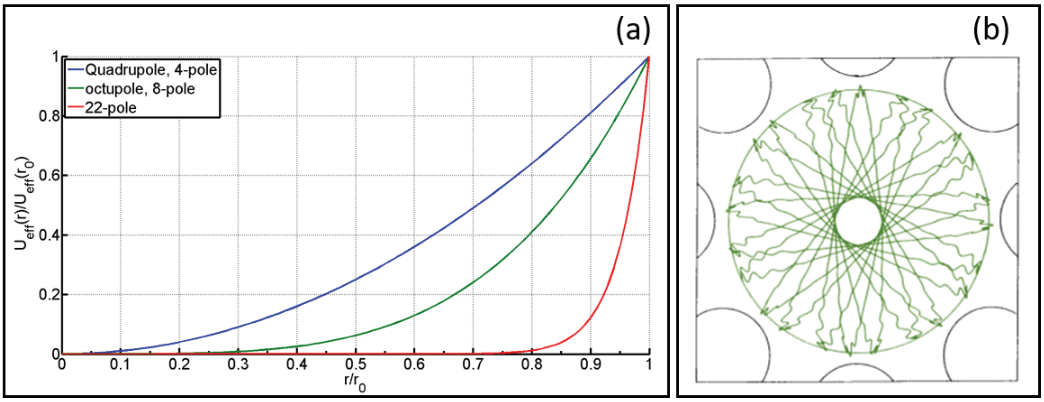

Figure 16: Study of the ion behavior in the multipole. (a) is the effective potential of multi-poles. (b) is the calculated trajectory of an ion in an octopole [17].

The motion of the ions can be approximated as a combination of a rapid oscillation with the trap frequency ω, the so-called micromotion, and a slower macromotion (or secular motion) at frequency Ω_i in the effective harmonic trap potential with:

$$\Omega \approx \frac{\omega}{2}(a_i + \frac{q_i}{2}) \tag{2}$$

d. The quadrupole mass filter

1) Theory of a quadrupole mass filter

In a quadrupole mass filter (Q-mass), ions with different mass to charge ratio m/q are separated. We use a commercial quadrupole mass filter (Extrel core Mass Spectrometers). A quadrupole is a multipole with n=2 and 4 rods.

In the Q-mass, the equations of motion are given by the Mathieu equations [18]

$$\frac{d^2u_i}{d\tau^2} + (a_i + 2q_i\cos(2\tau))u_i = 0 \tag{3}$$

with

- $u_i = x,y$. (x,y) is the position of the ion in the quadrupole.
- $\tau = \frac{1}{2\omega}$
- $a_x = a_y = -\frac{a_z}{2} = \frac{4qU_{dc}}{mr_o^2\Omega^2}$
- $q_x = q_y = -\frac{q_z}{2} = \frac{2qV_{dc}}{mr_o^2\Omega^2}$
- ω: trap frequency

This equation gives the stability of the motion: the ions have a stable motion and stay in the guide for a small range of parameters a_i and q_i.

The Q-mass has a fixed radio frequency of 440 kHz, and r_0= 9mm and q=1 are fixed (for singly charged ions). The Q-mass is designed to filter ions with masses between 20 to 16000 amu by changing the U_{AC} and V_{DC} voltages simultaneously. Each mass has its own stability region where the ion trajectory is stable. In Figure 17, 3 stability regions: m/q 50, 70, 100 respectively and two mass lines are represented. The blue area is the stability region of the ion. Typical ion trajectories (Figure 17 (b)) are plotted for three U_{DC} and V_{DC} conditions of the graph, all around the stability of ions with m/z 100 ratio: A, before the stability region, B in the stability region and C after the stability region. Z-axis is the beam line axis. Only in the point B, the ion has a stable trajectory and will go through the Q-mass [19]. In A, the trajectory of the ions is not stable in the x direction: the ratio ${}^{V_{DC}}/_{U_{AC}}$ is too small. In C, the trajectory of the ions is not stable in the y direction: the ratio ${}^{V_{DC}}/_{U_{AC}}$ is too high.

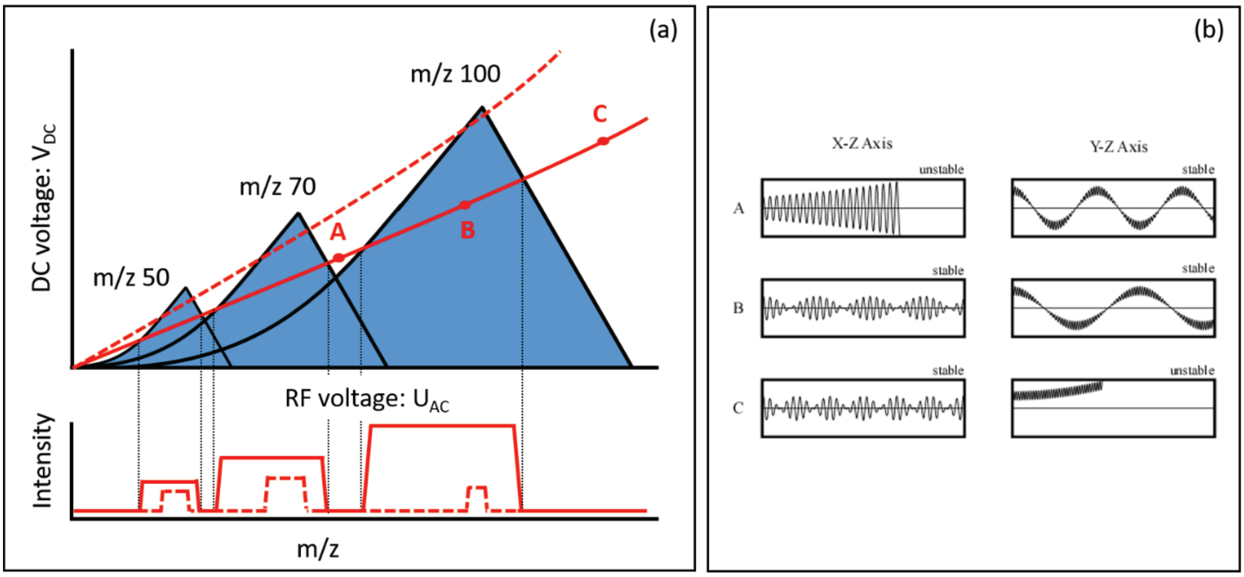

Figure 17: Ion stability region in the Q-mass. In upper (a), stability diagram for different ion masses and two different mass scan lines. In the bottom is the intensity of ions going throw the Q-mass for the two mass scan lines: in full line is for high ion intensity, dotted line for high resolution. In (b) is the typical trajectory of the ions in different conditions (the ion trajectory is imported from [19]).

2) *The Q-mass calibration*

A mass spectrum is obtained by scanning the AC and DC voltages through the different stability region: the line defined by the function f(AC,DC) is named the mass scan line. As example, the bottom part of Figure 17 (a) shows the ions intensity for each mass and each mass scan line. The dash line corresponds to high resolution spectrum and the line is close to the summit of the stability region. The full line is lower in the f(AC,DC) map, the mass selection has low resolution while the ions intensity is higher.

Two parameters control the mass scan line: ΔRes (to change the slope of the mass scan line) and ΔM (to change the Y offset, the Y axis interception). These parameters are ranging from -5 to +5. By increasing the value of any of this parameter, the resolution improves. In the mass range of interest, 280 amu – 500 amu, the mass spectrum is not very sensitive to change with ΔRes and we fixed ΔRes = 5. However, a variation in ΔM changes the mass spectrum feature: Figure 18 displays a mass spectrum around methylene blue mass for three different Q mass resolutions detected with the channeltron: ΔM:-0.7 (black), ΔM:-0.5 (red), ΔM:-0.3 (blue). Data for each mass is accumulated for two seconds and the mass changed one amu per one amu. The x-axis is the mass of the selected ions in atomic mass units (amu) and the y-axis is the intensity of the ions beam measured with the channeltron after the trap.

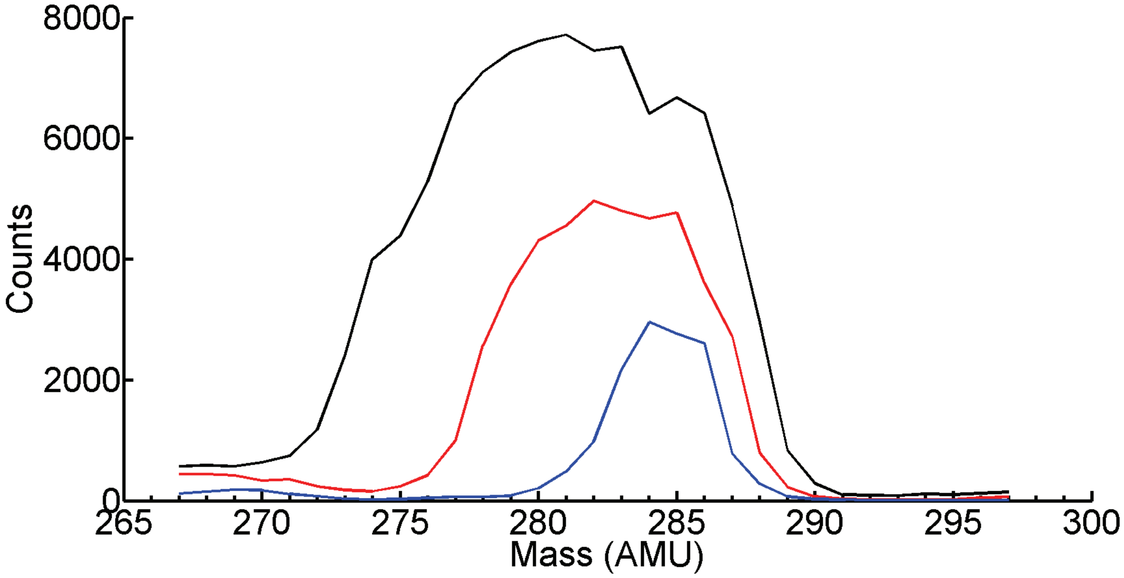

Figure 18: Mass spectrum of methylene blue (mass 284 amu) for three different Q-mass resolution: ΔM:-0.7 (black), ΔM:-0.5 (red), ΔM:-0.3 (blue). The capillary is at room temperature and the signal is measured with the channeltron after the trap used as an ion guide. Data for each mass were accumulated for two seconds and the mass changed one amu per one amu.

By increasing the value of ΔM:-0.7 (black), ΔM:-0.5 (red), ΔM:-0.3 (blue), the mean value of the peak is shifted to higher mass. The high resolution reproduces well the methylene blue mass: 284. But, for ΔM:-0.5, the average mass is 283 and for ΔM:-0.7, the average mass reduces to 281.5. By increasing ΔM, the ion count rate decreases: the total number of ions is 10^5 for ΔM:-0.7, 4.6 10^4 for ΔM:-0.5 and 1.4 10^4 for ΔM:-0.3. ΔRes and ΔM are fixed for each experiment and adapted to control the ion beam characteristics as the number and the mass range of the ions.

Thus even for the same mass, with different mass scan lines, the mean mass value shifts. Thereby a precise calibration of the spectrum is required. A solution of trifluoroacetate published in [20] for which the exact mass value of each peak is given can be used to calibrate the spectrum. In Figure 19, the mass spectrum of the solution of trifluoroacetate made with our set-up is shown in blue (X-axis: mass of the ion in atomic mass unit and y-axis, intensity of the selected ion beam measured with the channeltron after the trap). The exact mass value is given by the red dashed line. The experimental data vs the theoretical expected value is plotted and a correction equation is extracted (calibration equation). Our measured spectrum is transformed with the calibration equation and is adjusted to the red line. This calibration equation is used to calibrate any spectrum measured with the same Q-mass parameters.

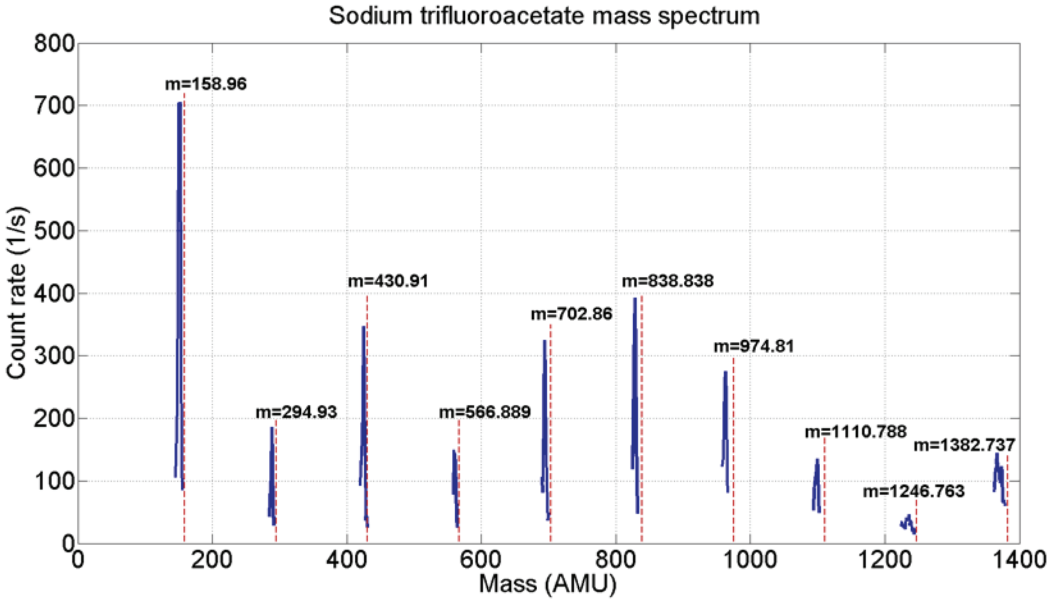

Figure 19: Mass spectrum of sodium trifluoracetate (in full blue line) and mass of the different molecules produced (in dotted red line and explicitly written above each peak). The capillary is at 66°C and the signal is measured with the channeltron after the trap used as ion guide. ΔM=-0.25. Data for each mass were accumulated for five seconds and the mass changed every 0.5 amu.

A specific calibration equation is needed for each Q-mass configuration. Parameters often change depending of the ions mass or energy and a new calibration spectrum needs to be produced every time the Q-mass parameters are changed.

Some solutions will give a spectrum with 2 series of cluster: a series with the cluster of interest and one with the solvent cluster only. As an example, Figure 20 shows the mass spectra of a solution containing pyrimidine and water and a solution of pure water. The solutions are obtained as following:

- pure water spectrum (blue): 0.18 mmol/L of H_2SO_4 in H_2O, capillary at 72°C

- pyrimidine-water spectrum (green): Pyrimidine: 4g/L in 0.18 mmol/L of CH_3COOH in H_2O, capillary at 66°C.

Some specific mass ranges are exhibited below the full investigated mass range spectra. As it can be seen, the blue peaks coincide with the green peaks which are indicative of the signature of protonated water clusters. The green peaks that do not coincide with the protonated water clusters are attributed to the heterogeneous protonated pyrimidine-water clusters, according to the m/q position.

The protonated water spectrum from pyrimidine solution fits well the protonated water cluster in the green spectrum. In between each protonated water cluster is a protonated pyrimidine water cluster: the mass of water clusters is 1+18*n= 19, 37, 55, 73, 91, 109, 127 (n=1-7) and the mass of protonated pyrimidine water clusters: 81+18*n= 99, 117, 135 (n=1-3).

Both spectrum have the same behaviour and are divided in two parts. The first part between 0 and 500 amu in which the count intensity goes up until m= 380 amu with a maximum count intensity for both spectra around 1500 counts and then go fast down to 700 counts at 500 amu. The other part is from 500 amu to 1400 amu: the count intensity increases to around 700 amu with a maximal count intensity of 1300 counts. The spectrum finally slowly goes down to zero. The peak around 1200 amu in the green spectrum is a noise from the source.

In the following examples of mass spectra, the Q-mass accumulates data for each point during one second and the spectrum is plotted as a step of one amu.

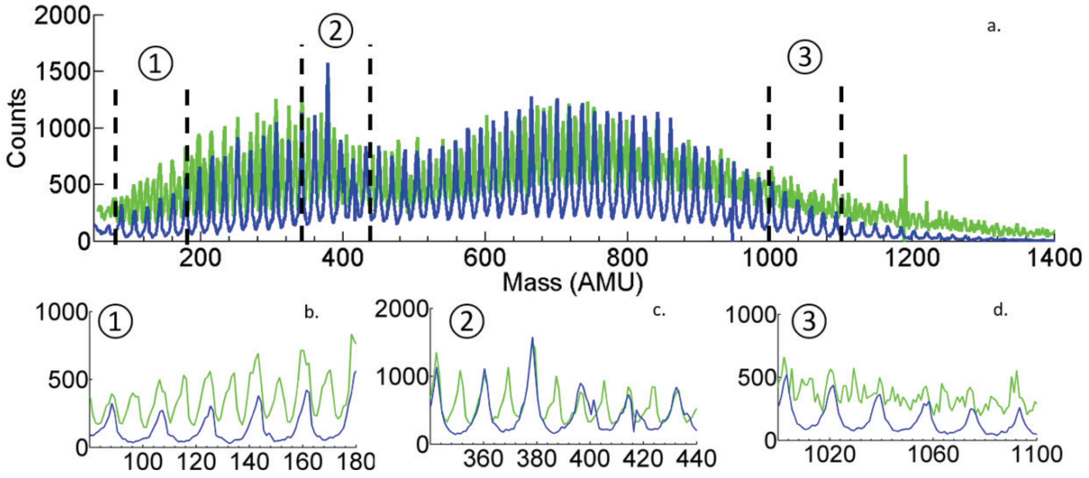

Figure 20: Calibration of protonated pyrimidine water cluster spectrum (in green), with a pure water spectrum (in blue). The signal is measured with the channeltron after the trap used as ion guide.

e. The ion production

1) Comparison of production of negative and positive water pyrimidine clusters.

A wide range of ions are produced, both positive and negative. In Figure 21, different mass spectra are displayed: in green, the same spectrum of positive protonated pyrimidine as in Figure 20 (X-axis: mass of the ion in atomic mass unit and y-axis: intensity of the selected ion beam measured with the channeltron after the trap). In red, a negative spectrum of pyrimidine water clusters (3 times enlarged). Cluster of $Py(H_2O)_n^-$ with n<10 and $PyH^+(H_2O)_m$, with m< 70 can be produced. The protonated positive mass spectrum was described above. The negative mass spectrum reaches its maximum intensity between 200 and 250 amu around 300 counts, then the ion intensity decreases. After 300 amu, the structure of the mass spectrum is unclear and each cluster mass cannot be observed. The intensity of the negative cluster is 3 times smaller than in the positive mode.

A solution usually contains water as a solvent, an acid as a proton-donor and a volatile molecule to help the evaporation like ethanol or methanol. Hao et al. reported the influence of several experimental conditions such as concentration, solution pH and instrument operating conditions such as desolvation temperature, solution flow rate, and capillary voltage on the formation of cluster ions [21] [22]. The choice of the solution influences the spectrum characteristics and two parameters are changed as example in the following paragraph for the solution made for the production of protonated pyrimidine water cluster.

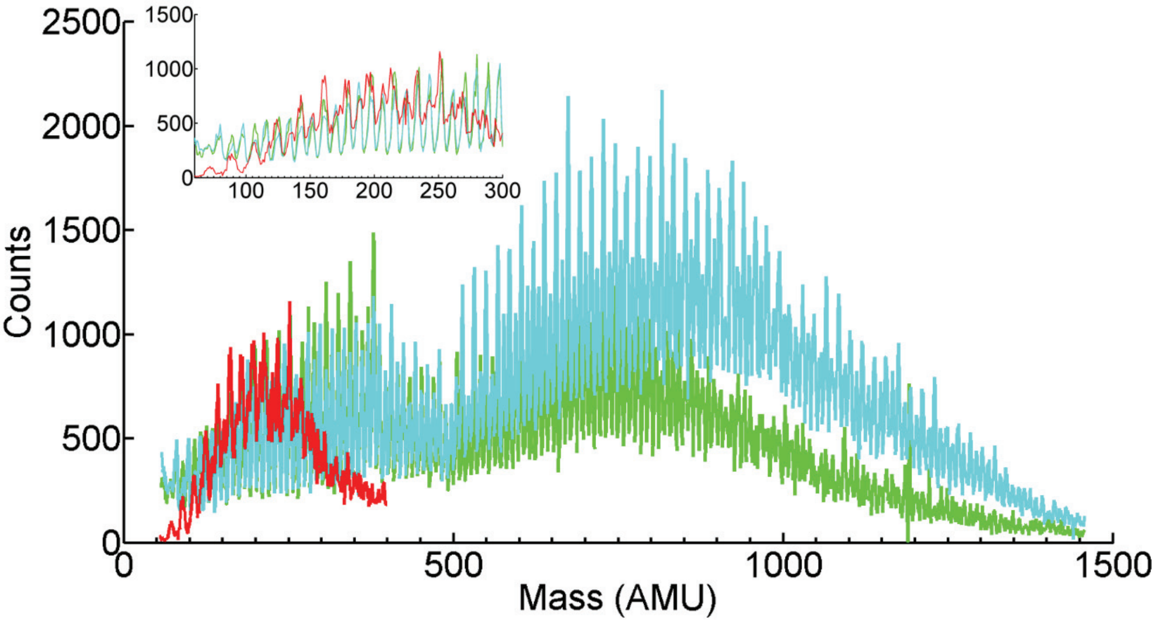

Figure 21: Mass spectrum of protonated pyrimidine water cluster. In cyan and green, positive cluster made from a solution with sulfuric and acetic acid respectively. In red the spectrum of negative pyrimidine water cluster(X3). The signal is measured with the channeltron after the trap used as ion guide.

2) *Ion production with different acids*

The first parameter is the choice of the acid. Acid is added in the solution to provide a substantial quantity of protons. In Figure 21, two spectra made with two different acids are compared: in cyan sulfuric acid and in green acetic acid. Both spectra were measured under the same conditions: temperature of the capillary, Q-mass parameter, solution concentration in acid and pyrimidine and octupole guide voltage. The green spectrum was already detailed before. The cyan spectrum has a double shape structure as well. The first part ranges from 0 to 500 amu with a maximum ion intensity around 350 amu at 1000 counts. The second part ranges from 500 to 1500 amu with a maximum plateau from 700 to 900 amu with an ion intensity of around 2000 counts. The two spectra show a very similar shape, however, the ratio between the lower and larger masses has changed. With acetic acid the low masses have higher intensity than the higher masses, while with sulfuric acid, the low masses have lower intensity.

3) *Ions production with different pyrimidine and acid concentrations*

The other key parameter is the concentration of the solution. Figure 22 shows two spectra of positive protonated pyrimidine water clusters at different concentrations (X-axis: mass of the ion in atomic mass unit and y-axis, intensity of the selected ion beam measured with the channeltron after the trap).

The first spectrum, in cyan, is the same spectrum as the cyan one in Figure 21: the concentration in pyrimidine is 4 g/L and 0.18 mmol/L in acid. The other spectrum (brown) was made by diluting the previous solution with water leading to a lower concentration of pyrimidine and acid, the concentration of pyrimidine being 0.15 g/L and 0.106 mmol/L in acid. Both spectra were normalized per area to emphases the result (the brown spectrum produce totally 1.3 times more ions). As all other protonated pyridine water cluster spectra, the brown spectrum has two parts. The first part range from 0 to 500 amu: the ion intensity increases until m= 397 amu. The second part range from 500 amu to 1500 amu: the ion intensity increases until 680 amu, is stabilized until 850 amu and slowly decrease to 1200 amu. The shapes of both spectra are similar but the intensity ratio between water cluster and protonated pyrimidine water cluster has changed. In cyan the water cluster has higher intensity while in dark green, the pyrimidine cluster has higher intensity.

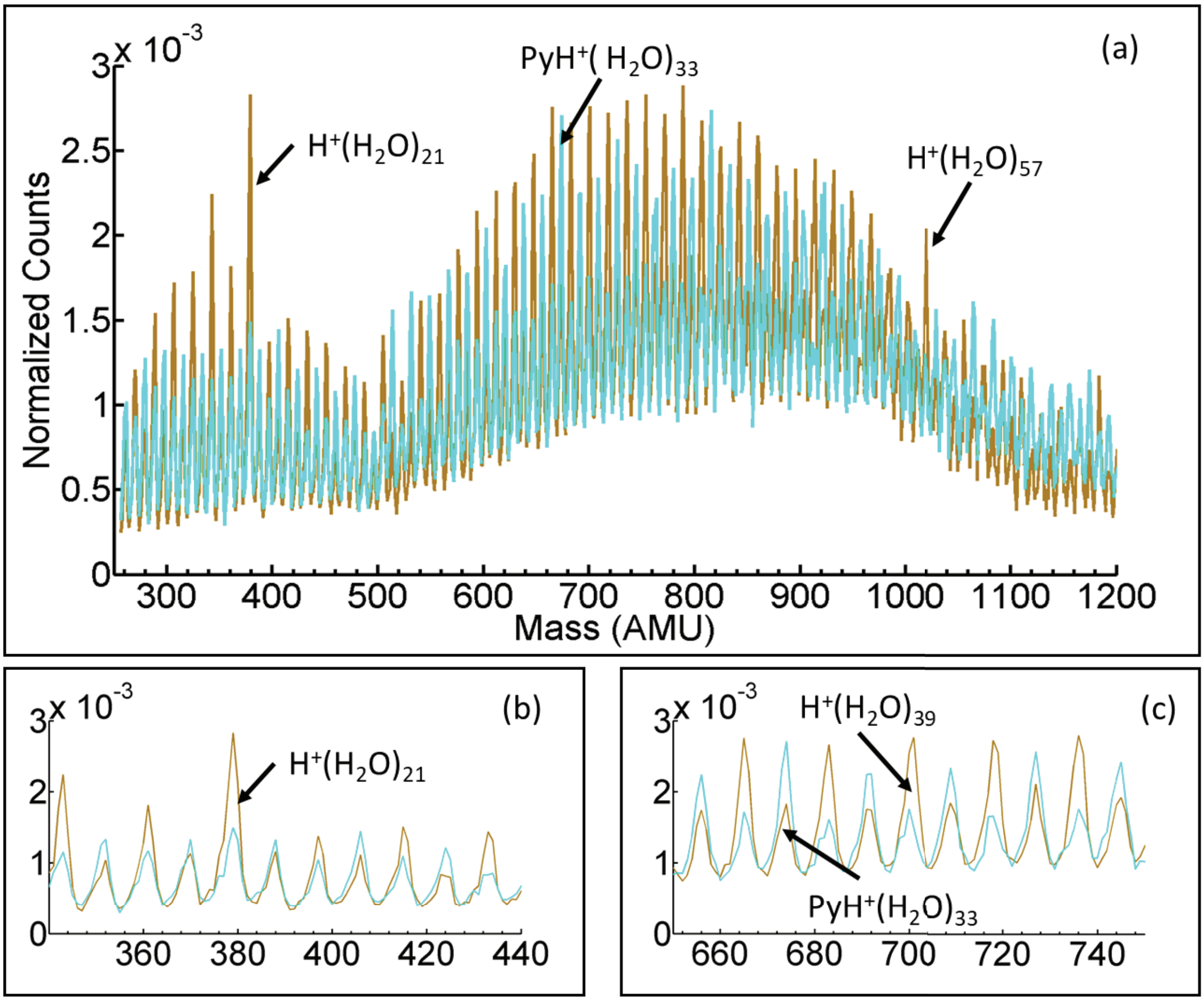

Figure 22: Protonated pyrimidine water cluster mass spectrum with two different pyrimidine concentrations: 0.18 mmol/L in cyan and 0.106 mmol/L in brown. The capillary is at 66°C and the signal is measured with the channeltron after the trap used as ion guide.

4) Capillary's temperature dependence

The capillary can be heated to help the desolvation process of the cluster. Figure 23 compares a spectrum of cesium clusters at two different capillary temperatures made from a solution for both spectrum of: 5.10^{-3} mol/L of CsI in CH_3CN (X-axis: mass of the ion in atomic mass unit and y-axis: intensity of the selected ion beam measured with the channeltron after the trap). In blue, the capillary is at room temperature. In red, the spectrum is obtained with the capillary heated at 100°C. The blue spectrum is made of cesium water cluster: $Cs^+(H_2O)_n$, n< 80. The intensity is high for the cesium ion: around 1200 counts. From 133 amu (cesium mass) to 200 amu, the ion intensity decreases. From m= 200 amu to 500 amu, the spectrum has low intensity: around 300 counts. Then the cluster intensity increases from 500 amu to 943 amu which correspond to $Cs^+(H_2O)_5$, then it decreases until 1500 amu. When the capillary is heated, the spectrum looks totally different: the cesium water cluster disappeared and the iodine cesium cluster is clearly observed. The red spectrum is almost always negligible except for the cesium iodine cluster in which the cluster intensity is up to 250 counts for $Cs^+(CsI)_3$. $Cs^+(CsI)_n$ are visible until n=7.

By heating the capillary, the water cluster intensity is reduced and other lower intensity clusters are highlighted. The temperature of the capillary can be adjusted depending on the cluster family to be studied. The pollution of methylene blue is due to previous experiment.

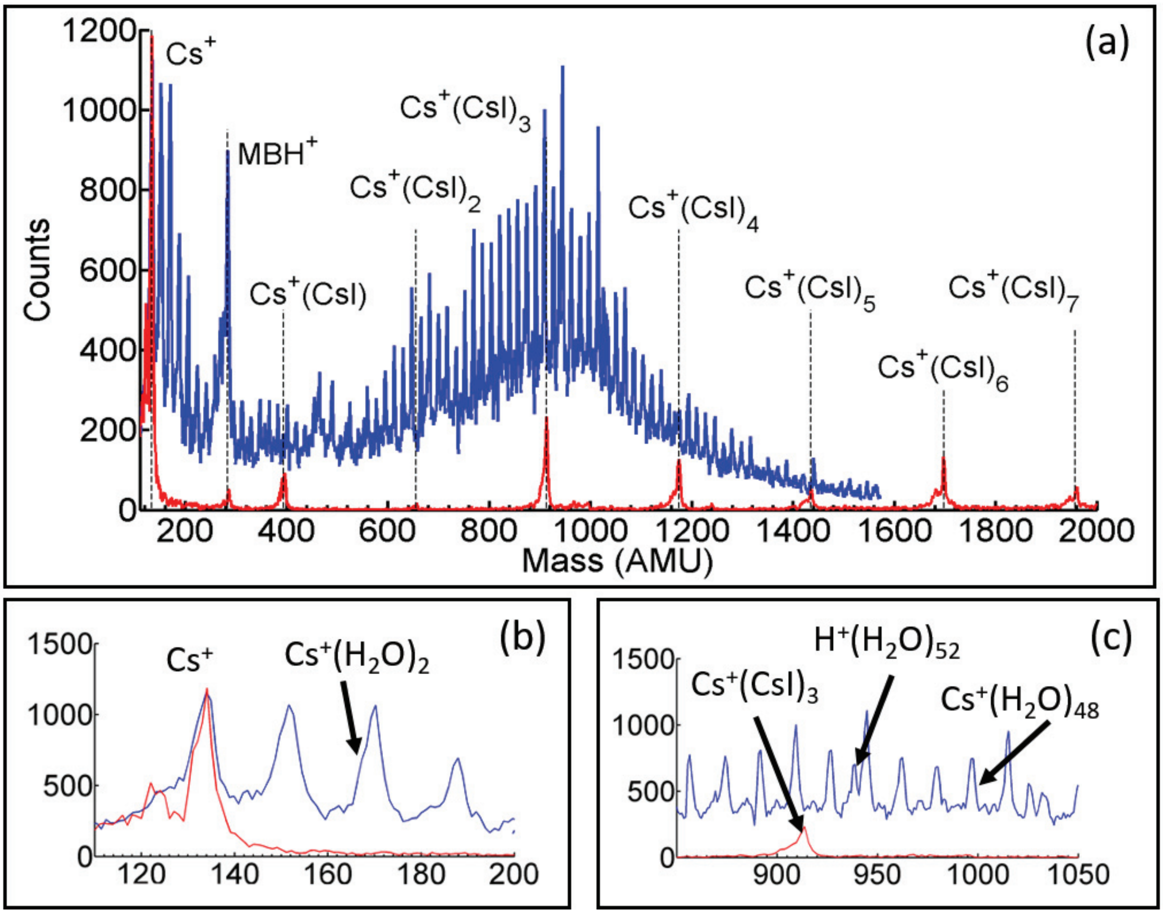

Figure 23: Production of cesium iodine water clusters for two different capillary temperatures: in blue the capillary is at room temperature while in red, the capillary is at 100°C. The signal is measured with the channeltron after the trap used as ion guide.

Another example of the capillary temperature influence is given in Figure 24. Methylene blue water cluster spectra at three different capillary temperatures are shown made from a solution of: 5.10^{-4} mmol/L of Methylene Blue in 7/3, CH_3CN/H_2O (x-axis: mass of the ion in atomic mass unit and y-axis: intensity of the selected ion beam measured with the channeltron after the trap). In blue, the capillary is at room temperature, in green the capillary is heated to 36°C and in red to 55°C. The blue spectrum at room temperature has a peak for methylene blue at 284 amu with 900 counts, the methylene blue water cluster slowly appears at 500 amu for n= 10, reaches its maximum for n= 24 at 500 counts and decreases until 1200 amu. Methylene blue water cluster can be distinguished until n= 50. At 36°C, the methylene blue peaks at 284 amu is higher: 2500 counts. The methylene blue water clusters appear after 350 amu: from $MB^+(H_2O)_4$ directly at 200 counts, their intensity slowly increases until 600 amu and reach 600 counts, their intensity finally decreases until 1100 amu. Methylene blue water cluster can be identified until n= 45. At 55°C, the methylene blue peak is the highest and almost reaches 4000 counts. A few methylene blue water clusters can be seen from n=4 to n=15, but the ion counts always stay low: below 150 counts. The different peaks below mass 284 are due to the dissociation of methylene blue and the dissociation of CH_2. The cluster family is named Thionine: $Th^+(CH_2)_n$. Methylene blue is $Th^+(CH_2)_4$. For all capillary temperature, there are almost no cluster for n=1-3 and the minimum cluster size produced is $MB^+(H_2O)_{n=4.}$

The average size of the water cluster decreases between room temperature and 36°C. As well, the methylene blue: MB^+ peak increases. By increasing the capillary temperature to 55°C, all the water clusters are almost removed and the main peak of MB^+ has high intensity. The temperature of the capillary can be adjusted depending of the cluster size one would like to study.

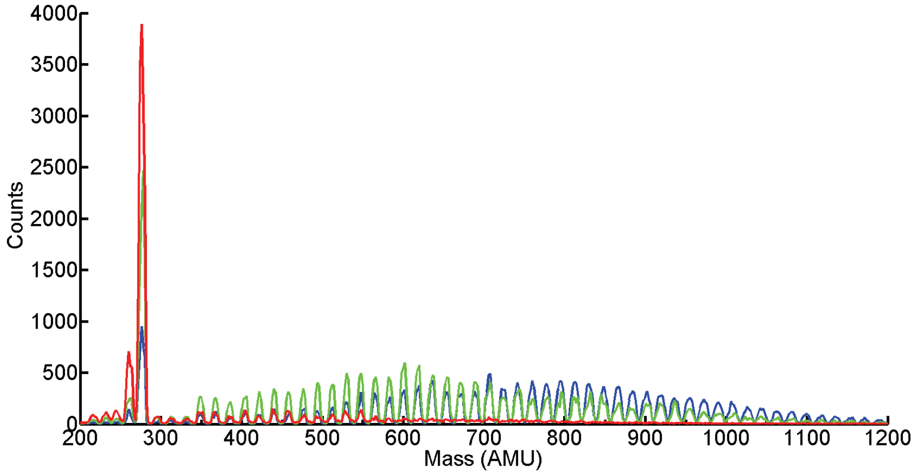

Figure 24: Evolution of MB^+ water cluster by heating the capillary at 26°C in blue, 36°C in green and 55°C in red. The signal is measured with the channeltron after the trap used as ion guide.

The hydration of methylene blue cation was studied by Sato et al. [23]. With the same set-up, they measured the mass spectrum of methylene blue at different temperatures. The evolution of the spectrum with the temperature is very similar with the one we measured in this work. They calculated the binding energy and the optimized structures using DFT calculation for $MB^+(H_2O)_{n=1-5}$. Under n=4, the molecular clusters have very small bonding energy: 0.22 eV for n=1, 0.52 eV for n=2 and 0.86 eV for n= 3. They found a very stable structure for n=4, with a binding energy of 0.22 eV for n= 1.3 eV. $MB^+(H_2O)_{n=1-3}$ is not a stable cluster and it is almost not visible in the mass spectrum.

The ESI source is an excellent way to produce cluster molecular ions: several mass spectra of positive cluster were measured as methylene blue water cluster, with n up to 40, cesium water cluster, with n up to 70, cesium iodine cluster, with n up to 7, protonated pyridine water cluster, with n up to 70 and protonated water cluster with n up to 65. A mass spectrum of negative pyrimidine water cluster was measured with n up to 10. Several parameters are adjusted to change the shape of the mass spectrum as the solution or the temperature of the capillary. However, the ESI source produces ions in a continuous mode and the ion storage ring often requires a bunch of cold ions. To accumulate ions in a bunch and to cool them down, an ion trap was built.

2. The 4K ion trap

Ion traps were first developed by Wolfgang Paul and a summary of his activities is given in his Nobel lecture [24]. Among all different kinds of traps, the one used here is a linear radiofrequency multipole trap. Mostly used to trap molecular systems with many degrees of freedom, these traps are used to study spectroscopy and reactivity to reveal their dynamics. The concepts of ion guiding and trapping with multipole have been well reviewed by Gerlich in 1992 [17].

a. *Principles and advantages*

1) *Design of the ion trap*

The trap shown in Figure 25 is an octupole guide and a pair of end cap electrodes provides the confinement in the direction along the rods (z) via a static trapping potential. The rods are 112 mm long, with a diameter of 3 mm and make a free cylindrical space of 9 mm diameter. An enclosure made from copper (named the inner shield) houses the ion trap, in which helium is pulsed as a buffer gas for collisional cooling of the trapped ions. In contrast to other cooling approaches like sympathetic ion-ion cooling or laser cooling, the translational motions as well as the internal degrees of freedom are cooled at the same time. The inner shield temperature, which sets the buffer gas temperature, is changed by mounting the whole assembly on a 4K cryo-cooler.

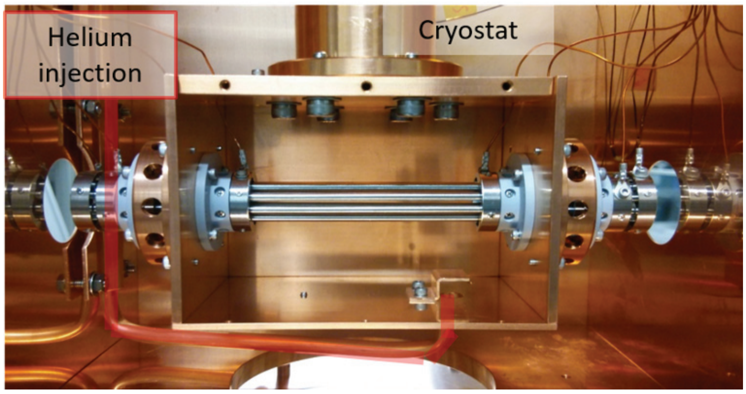

Figure 25: Picture of the trap with the connection to the beam line, the cryo-cooler and the helium injection line (in red).

2) *The trapping procedures*

The trapping schemes, shown in Figure 26, can be divided in 3 parts: the injection, trapping and extraction phases. The x-axis is the position in the beam line axis (z) and the y-axis is the potential in the trap with the ion kinetic energy in red. $Z_{entrance}$ and Z_{exit} are the position of the entrance and exit of the trap. V_{trap}, $V_{entrance}$ and V_{exit} are the potential of the octupole, entrance end-cap and exit end-cap.

- Injection (a): ions and helium buffer gas are injected in the trap. The ions have sufficient kinetic energy to overcome the potential of the entrance electrode and are then decelerated rapidly by buffer gas collisions. Due to this energy loss inside the trap, the ions cannot overcome the entrance potential anymore. The entrance potential must be optimized with respect to the ion's kinetic energy distribution. The exit end cap's potential is usually set high enough to repel all ions in the trap. The ions are injected in the trap continuously for an extended period of time (usually ms to s) which is advantageous when the ion source produce only a few ions of interest per second.

- The trapping (b): to perform isolated ion trapping the entrance end cap electrode is set to a high potential and the ions from the source are prevented from entering. In the trap, the ions collide with helium and are expected to reach a thermal equilibrium with the cold helium gas. The interaction of the molecular ions with the helium, depending on their inelastic collision cross sections, determine the time scale for the buffer gas cooling and is usually less than 1 ms [25].

- The extraction (c): in order to avoid collisions between ions and helium during the extraction, sufficient waiting time should be accounted for pumping the helium out of the trap. This is usually in the order of up to 100 ms after the last pulsed helium injection. The exit end cap voltage is then lowered down and the ions move out from the trap. The bunch of ions is then guided through two sets of ion guides to the acceleration tube.

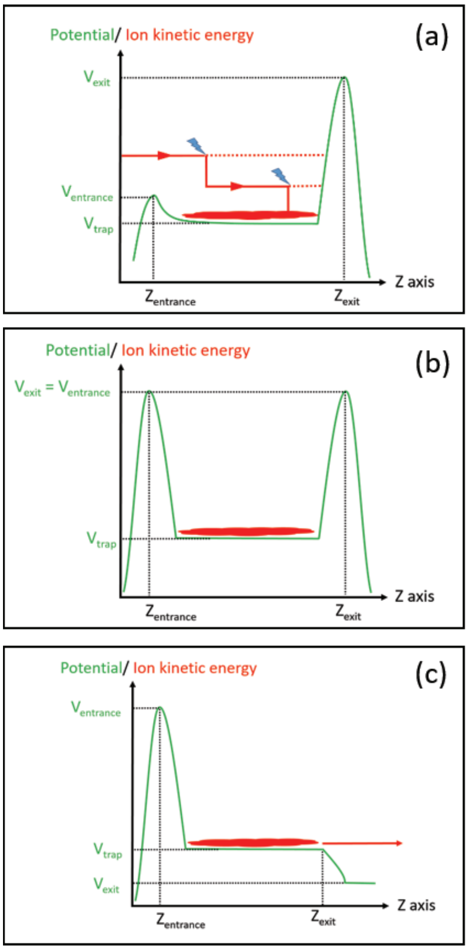

Figure 26: Schematic view of 3 steps of the ions trapping process: injection and cooling (a), trapping (b) and extraction (c). The x-axis is the position in the beam line axis (z) and the y-axis is the potential in the trap in green and the ion kinetic energy in red. $Z_{entrance}$ *and* Z_{exit} *are the position of the entrance and exit of the trap.* V_{trap}, V_{exit} *and* $V_{entrance}$ *are the potential of the octupole, entrance end-cup and exit end-cup.*

3) *The cryogenic system*

In order to cool down the trap, two shields made of copper are employed as shown in Figure 27 (a). The inner shield, ⑦ in Figure 27, surrounds the trap and the outer shield, ⑧, encloses the inner shield. The inner shield is used to cool down the trap and the injected helium. The outer shield minimizes the blackbody radiative heating from the room temperature environment. To cool down the shields, a GM cryo-cooler (Sumitomo RDK-408D2) is used. It is composed of two cooling stages which are cooled down to different temperatures: the first stage is cool down to 43 K with a power of 40 W, ④ in Figure 27, and the second stage to 4.2 K with a power of 1 W, ⑥. The resulting temperature is measured with 3 silicon diode temperature sensors (Lakeshore DT-670-CU: ①, ② and ③) fixed to the bottom and the top of the inner shield, and to the outer shield (see Figure 27 (a)).

Figure 27 (b) shows the temperature of the trap during the cool down process. The x-axis is the time, the left y-axis is the temperature in K. The shields initially at room temperature slowly cool down to 60 K in 1h 45 minutes and then drastically reach it final temperature at 5 K in less than 10 min. This change in the cooling speed is due to the heat capacity and to the thermal conductivity of copper. The heat capacity for copper is slowly decreasing when the temperature decreases until around 50 K, then the heat capacity drops down very quickly. The heat capacity of copper is 16 J. K^{-1}. mol^{-1} at 100 K, 6.15

J. K^{-1}. mol^{-1} at 50 K and is below 0.1 J. K^{-1}. mol^{-1} below 12 K [26]. As well, the copper thermal conductivity is slowly increasing when the temperature is decreasing until 60-50 K, then below 50 K the copper thermal conductivity is very high. The thermal conductivity of copper is 400 W/mK at 300 K, 413 W/mK at 200 K, 482 W/mK at 100 K, 1250 W/mK at 50 K and reaches its maximum at 9 K with 25 000 W/mK from [27].

Within two hours, the top inner shield reaches 5.4 K, the bottom inner shield, 6.1 K and the shield 27 K, respectively. After the cool down of the trap, the vacuum pressure decreased from 1.8×10^{-7} mbar to 5×10^{-8} mbar.

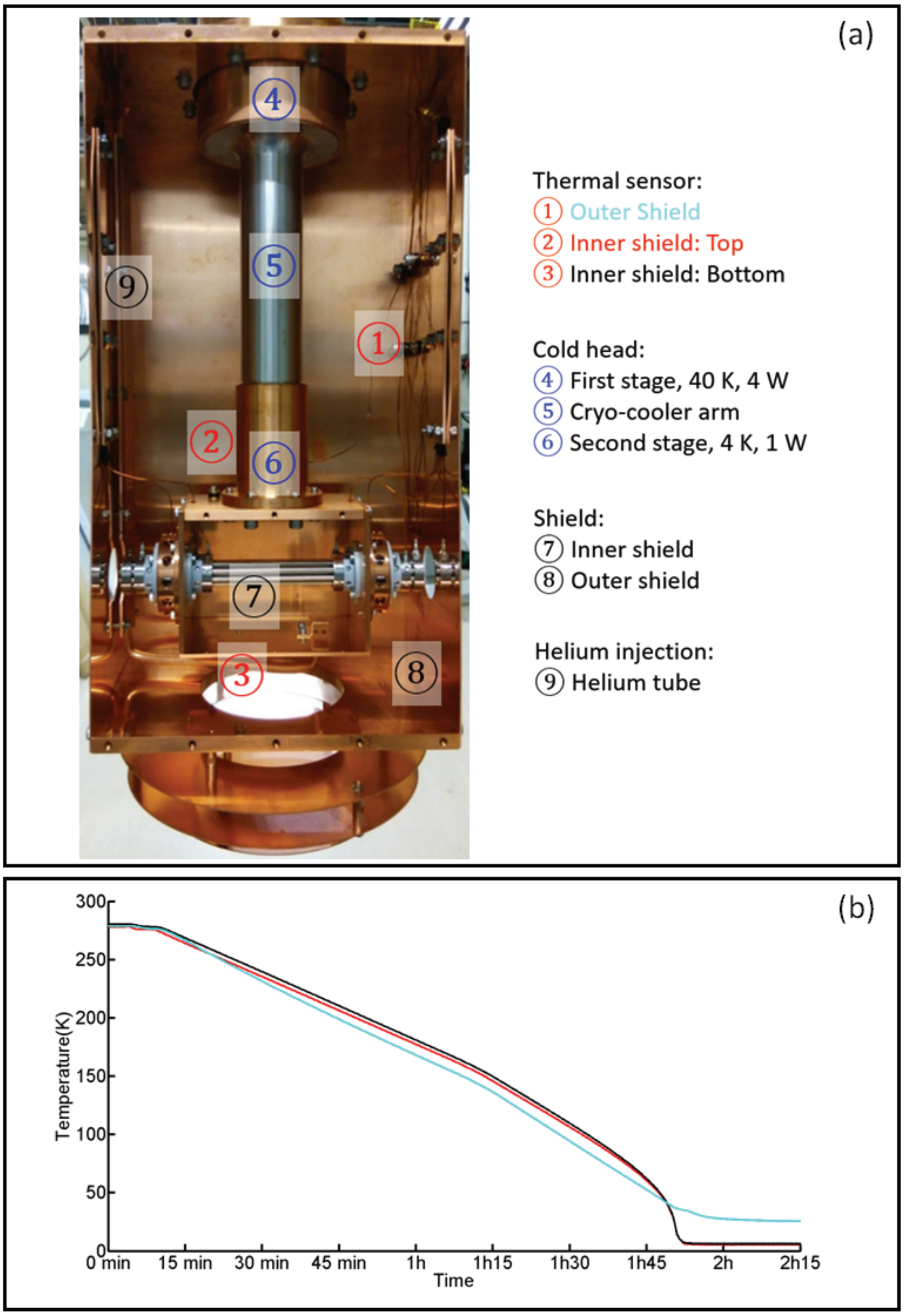

Figure 27: (a) is a picture of the trap with in red the position of the three thermal sensors (①②③), in blue the cold head part (④⑤⑥), and in black the shields (⑦⑧) and the helium injection line (⑨). (b) is the evolution of the trap temperature during the cool down. The x-axis is the time in minute and the left y-axis is the temperature in K. The temperature of the inner top trap (magenta), the inner bottom trap (red) and the outer shield (cyan) are shown

Two ceramic heaters were added in series to the top of the trap to control the temperature (Figure 28 (b)). Each heater produces 3-25 W to heat up the shields. Figure 28 (a) shows the temperature evolution of the trap for different voltages applied to the heaters. The x-axis is the time in minutes and the left y-axis is the temperature in K. The heaters were switched on at t=6 min and off at t=18 min. The temperature of the inner shield changes according to the voltage applied to the heaters. The outer shield temperature only slightly increased. The heater test was performed up to a trap temperature of 18K.

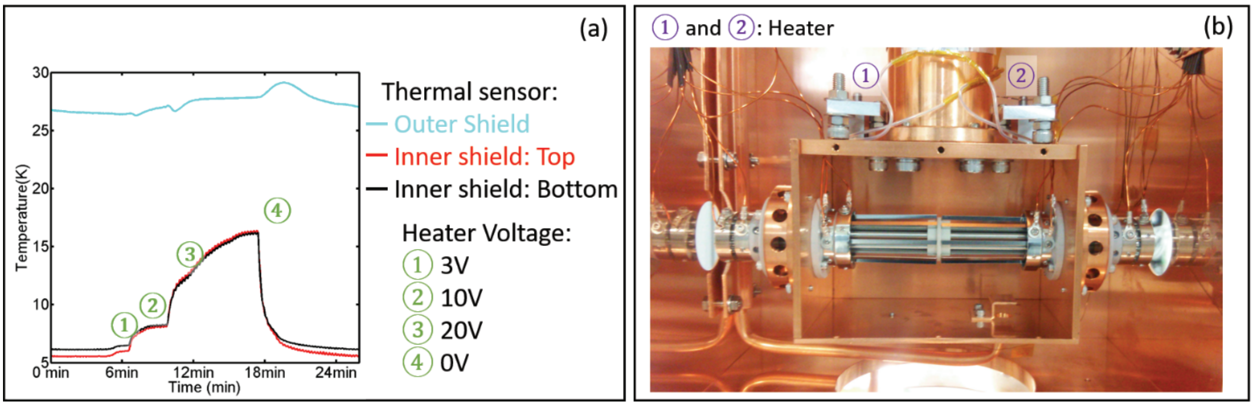

Figure 28: (a) shows the temperature evolution of the shields for different voltages of the heater. The x-axis is the time in minute, the y-axis is the temperature in K. In red is the top inner shield, in black the bottom inner shield and in cyan the outer shield. (b) is a photo of the trap with the two heaters: ① and ②.

4) Helium as buffer gas

The trapped ions are cooled by collisions with an inert buffer gas at a well-controlled temperature. Helium is chosen because of its high vapor pressure at low temperature and its easiness in manipulation. The helium gas is pre-cooled in the tube which is connected to the outer shield and then is injected in the inner shield where the helium gas equilibrates by collisions with the inner shield.

The ions collide with the buffer-gas atoms and transfer a part of their energy to them. The motion of the ions is damped until the ions reach thermal equilibrium with the cold helium gas. Calculation and simulation made in [28] show that only 3-10 collisions already lead to a distribution of the ion velocity close to a Maxwell-Boltzmann distribution. The simulated velocity distribution calculated in [28] of Cl^- in a 22-pole ion trap filled with 100 K helium gas can be fitted with a Maxwell Boltzmann distribution with a translational temperature of 106 K which corresponds to velocity ranging from 100 $m.s^{-1}$ to 500 $m.s^{-1}$. The buffer gas is pulsed into the trap for 100 µs with a solenoid valve (from Parker part number 009-1421-900) driven by a homemade pulsed valve driver (300 V).

Figure 29 shows the effect of helium injection on the ion intensity and vacuum. The trap was used only as an ion guide and one helium pulse is injected in the trap while the ion count rate is measured on the channeltron after the trap. The x-axis is the time in minutes, the y-axis of Figure 29 (a) is the ion intensity in count per second and the y-axis of the Figure 29 (b) is the pressure in mbar. The helium pressure was 0.5 bar at the entrance of the pulse valve. The helium is injected with a 100 µs delay as a 100 µs long pulse (green) and a 200 µs long pulse (red). The duty circle is one second and the experiment was repeated 20 times. The ion count rate dropped down immediately after the helium injection. After a few ms, the ion beam intensity slowly increases on the detector: the helium is pumped out and the ions can freely reach the detector again. During the helium injection, helium and ions collide and exchange energy. The collision induces the diffusion of the ions which are ejected out of the trap, thus no signal is detected. This shows that the helium pressure is sufficient to stop the ions in the trap. For continuous ion injection, the helium is pulsed with 10 Hz repetition rate to keep the pressure high enough.

In Figure 29 (b) is the pressure evolution: from 0 to 20 s is the injection of helium with a pulse length of 200 µs. From 45 s to the end is the injection of helium with a pulse width of 100 µs. In both experiment, the vacuum pressure increases from $p_i = 10^{-7}$ to $p_f = 10^{-5}$ mbar at the first injection and recovers back to normal in a few second.

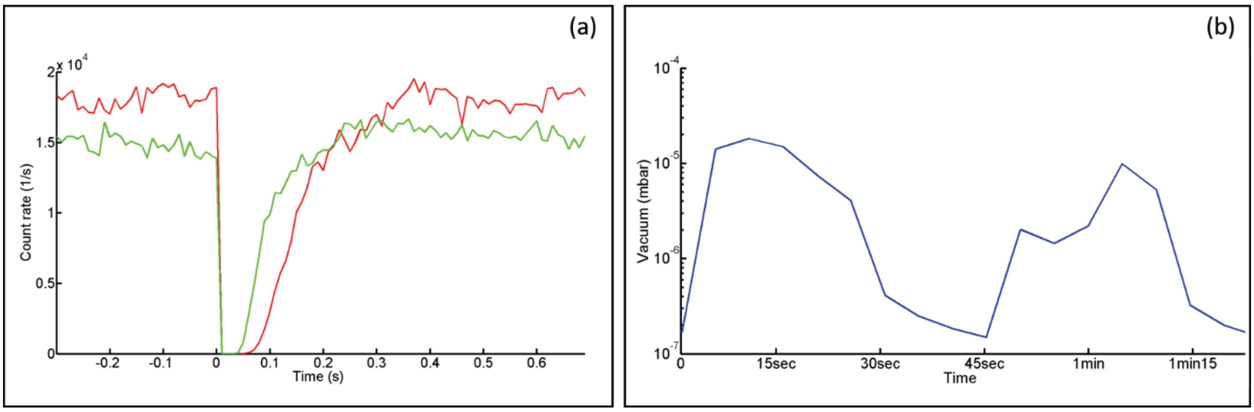

Figure 29: Effect of helium injection on the ion intensity and vacuum for 20 injections of helium. (a) is the ion count rate vs the time of the experiment (1s). The pulse length is changed from 200 µs in red to 100 µs in green. Helium is injected at time 0 + 100 µs. (b) is the pressure evolution: from 0 to 20 s is the injection of helium with a pulse length of 200 µs. From 45 s is the injection of helium with a pulse width of 100 µs.

The pressure and the density of helium atoms in the trap can be calculated with the ideal gas low:

$$pV = nRT \tag{4}$$

With:

- p: the pressure of the gas

- V: the volume of the gas, $V_{chamber} = 0.7\ m^3$ in the vacuum chamber, $V_{trap} = 0.0045\ m^3$ in the trap

- n: the amount of the gas (in moles)

- R: the gas constant, $R = 8.314\,4598\ kg.m^2.s^{-2}.K^{-1}.mol^{-1}$.

- T: the temperature of the gas, T= 300 K

From equation 4, the amount of gas injected in the chamber, n_{inj} can be calculated:

$$n_{inj} = \frac{V_{chamber}}{RT}\,(p_f - p_i) \tag{5}$$

$n_{inj} = 2.6560328\ 10^{-8}$ mole = $160\ 10^{14}$ atoms of helium.

The pressure in the trap during helium injection is: p_{trap} (the initial number of helium atom in the trap was neglected).

$$p_{trap} = \frac{n_{inj}RT}{v_{trap}} \tag{6}$$

The helium pressure in the trap during injection is: $1.5\ 10^{-4}$ mbar

And the helium density in the trap: ρ_{trap}:

$$\rho_{trap} = \frac{n_{inj}}{v_{trap}} \tag{7}$$

gives ρ_{trap}= 3.5 10^{18} m^{-3}

From the helium density, the mean free path, λ is calculated:

$$\lambda \approx \frac{1}{\rho_{trap}\sigma} \tag{8}$$

With σ, the cross section of the helium-molecule collisions. σ_{max}= $\pi(r_{helium}+r_{molecule})^2$ ~ $\pi r_{molecule}^{\ 2}$ ~ 3.10^{-16} m^2 for a molecule of 10 nm radius. σ_{min} ~ 3.10^{-18} m^2 for a molecule of 1 nm radius.

And finally, λ_{max}= $9.3.10^{-4}$ m= 0.93 mm for a molecule of 10 nm radius, λ_{min}= $9.3.10^{-2}$ m= 93 mm for a molecule of 1 nm radius. The number of collision with helium gas should be in both cases at least 2 or 3 and so enough to cool down the molecule.

Then, Figure 30 displays the effect of helium injection on the trap pressure and temperature. The x-axis is the time in minutes, the y-axis in the left side is the temperature in K and the y-axis in the right side is the pressure in mbar. At t=0, helium starts to be injected in pulsed mode at 10 Hz, 3000 times with a width of 100 µs. The evolution of the temperature of the inner shield of the trap is plotted with in red, the bottom of the inner shield, in black the top of the inner shield and in blue the pressure with the time. The temperatures of these three different parts of the trap slowly increase and reache 6.5 K and 7.5 K after 3 min. Then the temperature is stabilized. After the last helium shot, the temperature quickly recovers back to its lowest value. At the same time, the pressure quickly increases to 10^{-4} mbar, and stays constant until the last shot. Then the pressure drops down back to 10^{-8} mbar. The helium is cold when injected in the trap and reaches a thermal equilibrium with the trap set-up at 6.5K.

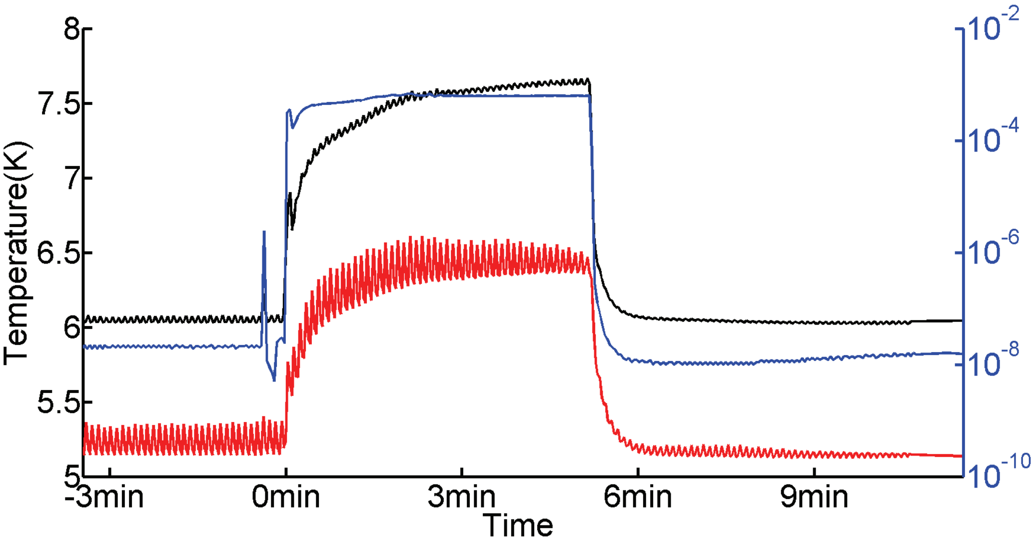

Figure 30: Effect of helium injection on the trap pressure and temperature. The x-axis is the time in minute, the left y-axis is the temperature in K and the right y-axis is the pressure in mbar. In red is the temperature of the inner bottom shield, in black the temperature of the inner shield top and in blue the pressure. Helium is injected for 3000 shots at 10 Hz with a pulse width of 100 µs.

5) *Radiofrequency heating and ion energy*

The fast oscillatory micro-motion perturbs the velocity distribution of trapped ions. This effect of radiofrequency heating during the wiggling motions of the ions leads to higher translational temperatures of the trapped ions than the buffer gas temperature. The collision temperature of the relative motion is given by [29]:

$$T = \frac{(m_i T_n + m_n T_i)}{m_n + m_i} \tag{9}$$

With:

- T mass weighted collision temperature
- T_n translational temperature of the neutral
- T_i translational temperature of the ion
- m_n mass of the neutral
- m_i mass of the ion

Heavy molecule or cluster (m_i>>1) may reach internal temperatures near the helium temperature, and experimentally both rotational [30] [31] and vibrational cooling [32] have been observed.

The kinetic energy of the micro-motion is determined by the shape of the confining effective potential. In steeper potential, the ions will spend more time in the field free region where buffer gas collision may not transfer micro-motion energy to the ion. The larger the multipole order, the smaller is the effective heating rate.

Three factors can lead to hot ions: insufficient number of cooling collisions, reheating in collisions with residual gas and RF heating. The final kinetic energy will be determined by a competition between collisional cooling of ions, which tends to produce a thermal distribution at the gas temperature, and these three factors.

b. The extraction electrode

The end cap potential does not affect the ions in the trap center, thus ions with different position or velocity will be ejected at different times [33]. To solve this problem an additional axial electric potential gradient is added to improve ion extraction. The process is well known with for example segmented multipole rods [34] [35] [36] [37] [38] [39] [40], conical rods [41], offset in one end of the multipole from the central z- axis [37], covering the multipole with segmented rings [38] [17] and insertion of electrodes between parallel rods [42]. The goal is to achieve a smooth electric field gradient in a mechanically simple way.

We chose to insert electrodes between the parallel rods with specific tapered shape (called fins) shown in the upper part of Figure 31. The axial potential has a minimum field distortion and it is free from constraint of construction: only 2 DC potentials are needed for the fins. The potential induced by the fins is shown at the bottom part of Figure 31. The x-axis is the position in the beam line axis (z) in mm and the y-axis is the potential in the trap in Volt. The black potential is the potential of the trap during trapping. Just before extraction (~10 µs), the fins potentials are switch on. The fins 1 pushes the ions toward the end of the trap while the fins 2 pull them out. Figure 31 shows in blue and red respectively two different voltage combinations for the fins to control the ion extraction: in red: fins1: +20 V/ fins 2: 10 V, in blue: fins 1: +30 V/ fins2: 0 V.

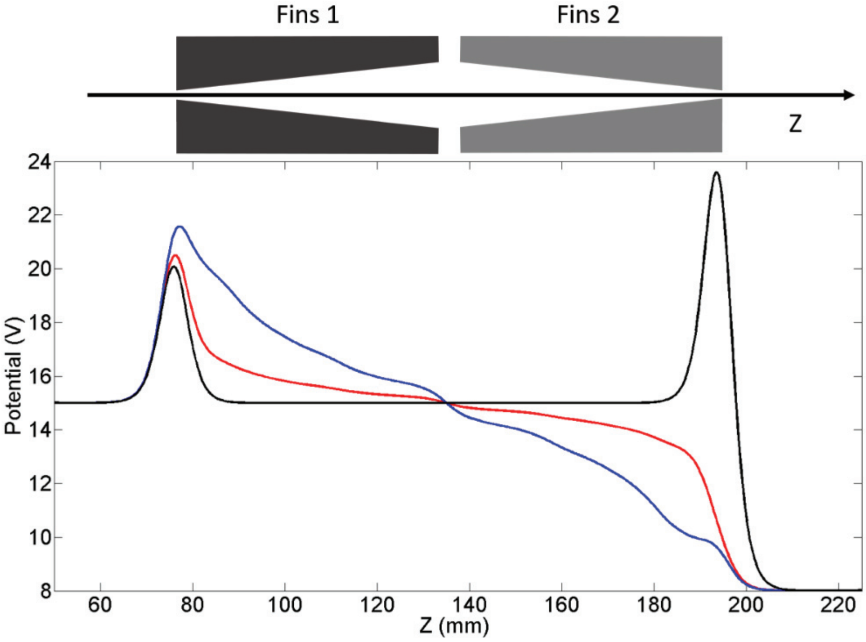

Figure 31: Potential in the trap with the extraction electrode on. The x-axis is the position in the beam line axis (z) in mm and the y-axis is the potential in the trap in Volt. In black is the potential during trapping (fins1=fins2=-10 V). In red and blue is the potential during extraction. In red fins1: +20 V/ fins 2: +10 V. In blue: fins 1: +30 V/ fins2: 0 V. The trap is at 15 V, the entrance end cap at 25 V and the exit end cap at 35 V.

In Figure 32, the ion bunch detected by the channeltron after trapping is compared with and without using the fins. The x-axis is the time in second and the y-axis is the ion count rate per second on the detector. In red, the bunch is made without using the fins: the fins potential stays at the trap potential: 15 V. In blue is a bunch extracted with the fins: the fins 1 is switched from +15 V to +80 V and the fins 2 from 15 V to 0 V. The total number of ions in the red bunch is 260 and is 270 in the blue bunch.

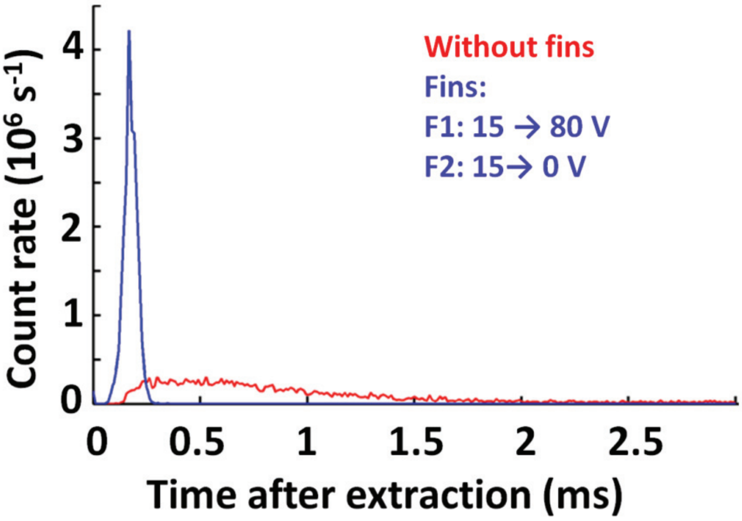

Figure 32: Ion bunch after trap extraction with and without extraction electrode. The bunch is normalized by the total number of injections. A bunch was made without extraction electrode (red), the other bunch with the extraction electrode on (blue).

The width of the bunch decreases from 1 ms to 0.1 ms and the height of the distribution increase from 0.3×10^6 to 4.2×10^6 counts per second. The total number of ions is conserved: the bunch is shortened in width but conserves the total number of ions.

3. The acceleration tube

a. Acceleration principles of operation

The ions are guided from the trap to the acceleration tube via two octupole guides. The DC potential of these octupoles can be adjusted to give a pre-acceleration kinetic energy to the ions. The acceleration tube is switched between two voltages and the lower voltage value is always set at -300 V to accelerate the ions into the tube. Once the bunch is in the tube, its voltage is quickly switched to a few kV. After passing through the tube, the ions will gain in kinetic energy: $E_{kin_{final}} = q(V_a^+ - V_a^-) + E_{kin_{initial}}$ with V_a^- , the low value of the acceleration tube and V_a^+, the high value potential of the acceleration tube. The principle of the operation of the acceleration tube is explained in Figure 33. Figure 33 (a) is the configuration of the beam line, Figure 33 (b) is a view with all electrodes in the beam line and Figure 33 (c) is a schematic drawing illustrating the electrode potentials in the beam line. The z-axis is the direction of the beam line and the y-axis is the potential.

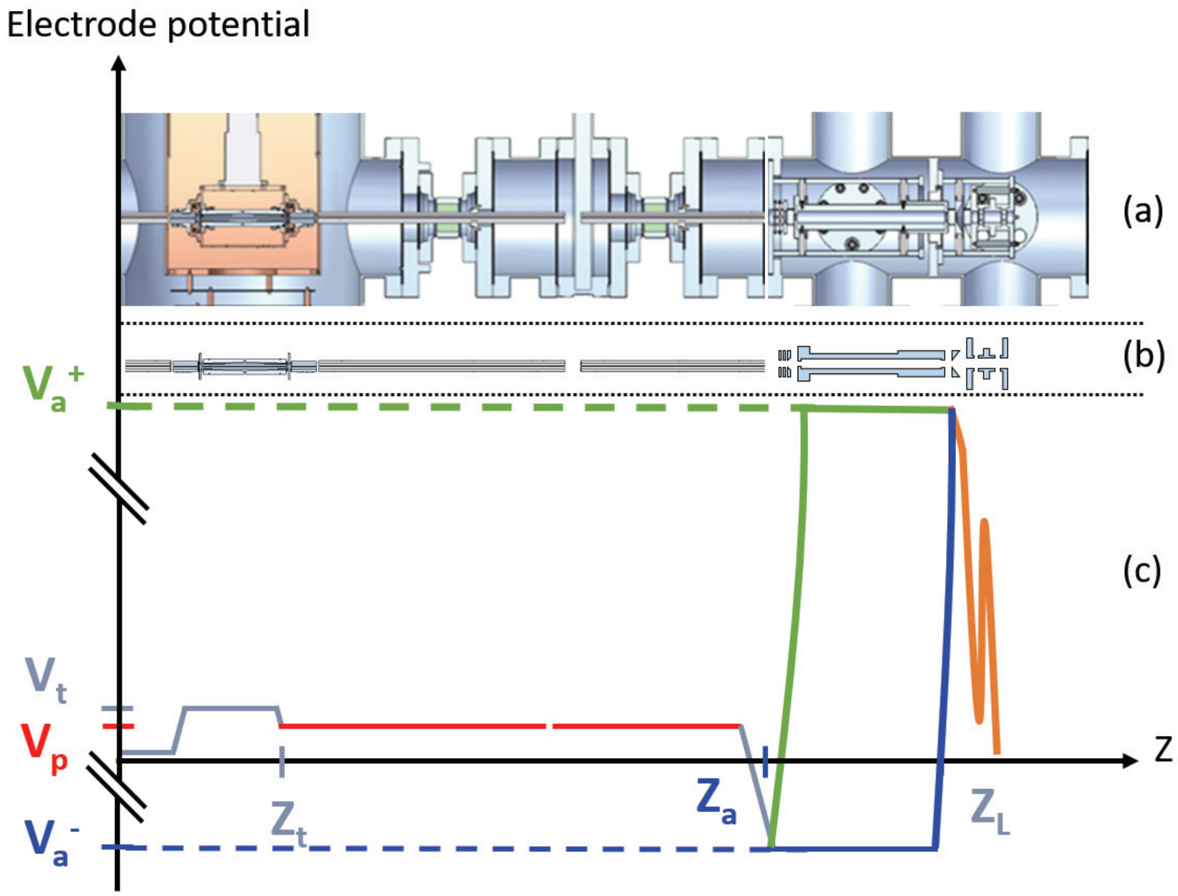

Figure 33: At the top part is a cut of the 3D model view of the beam line. In the middle is the beam line with only electrodes. At the bottom part is a schematic drawing illustrating the principles of operation of the acceleration tube. V_a+is the high value potential of the acceleration tube; V_t is the potential of the trap; V_p is the pre acceleration potential; V_a- is the low value of the acceleration tube.

V_t is the potential of the trap and is usually set between -10 V and +10 V. The red line shows the pre-acceleration potential applied to the two octupoles which are between the trap and the acceleration tube. It is adjustable to control the kinetic energy of the ions (V_p usually ranges from 0 to 30 V). In blue is the low potential of the tube (V_a^-=-300 V) and in green the high potential of the tube (V_a^+=few kV). Behind the tube, an Einzel lens is used to focus the ion beam by creating the orange potential.

b. The acceleration tube setup

The pulsed high voltage power supply is from BEHLKE together with the fast high-voltage push-pull switch (HTS 241-20-GSM). This device can switch within a range of 24 kV DC and with a maximum current of 200 A. The schematic switch potential shape is shown in Figure 34 and has four characteristic values: the low and high voltage whose difference defines the ion energy, as well as the rise and fall time. In this figure, x-axis is the time, y-axis is the potential of the switching signal after the switch. V_a^+ and V_a^- are the low and high value of the acceleration tube voltage.

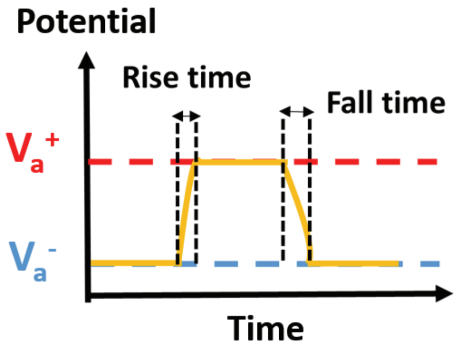

Figure 34: Potential of the acceleration tube vs time with V_a^+ and V_a^- the high and low values of the acceleration tube. X-axis is the time; Y-axis is the potential of the signal after the switch.

The rising time should be as short as possible to avoid uncertainty in the acceleration timing and to limit energy dispersion in the ion bunch. The falling time can be as long as the voltage is back to its low value before the next switching.

To obtain a short rising time and a stable voltage, a dedicated electronic circuit was added. The circuit is shown in Figure 35.

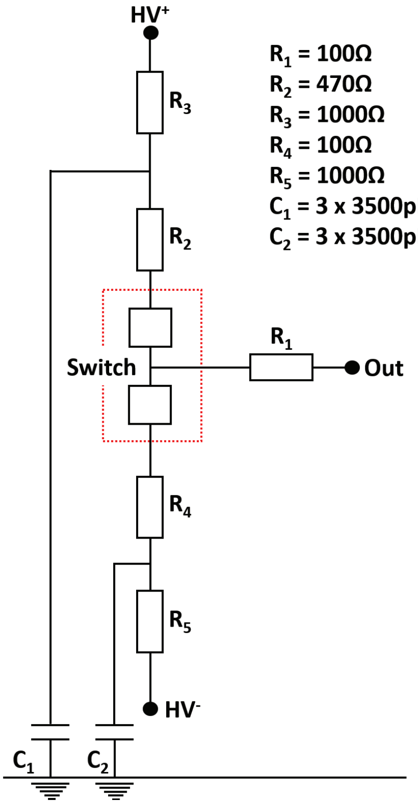

Figure 35: High Voltage circuit for the switch and value of each of the component.

Two buffer capacitors C_1 (three 3500 pF capacitors in parallel) and C_2 (three 3500 pF capacitors in parallel) store charges to provide during the switching time the charges needed to have a sharp and short rising time. Resistance R_2 and R_4 (470 Ω) limit the inrush and fault current when R_3 and R_5 (1000 Ω) charge the capacitors. The resistance R_1 (100 Ω) provides damping to reduce output pulse oscillations.

Figure 36 shows the output of the switch measured with a fast voltage probe (1:100 ratio, maximum voltage 4 kV) and an oscilloscope. x-axis is the time in µs (a) or ns (b), the y-axis is the voltage in kV (left) or V (right). In cyan is the voltage output of the switch (left y-axis) and magenta is the signal on the MCP which is the noise from the switch (right y-axis). Figure 36 (a) displays a full 100 µs pulse while Figure 36 (b) is a zoom of the rising time: from t=0 s to t= 800 ns.

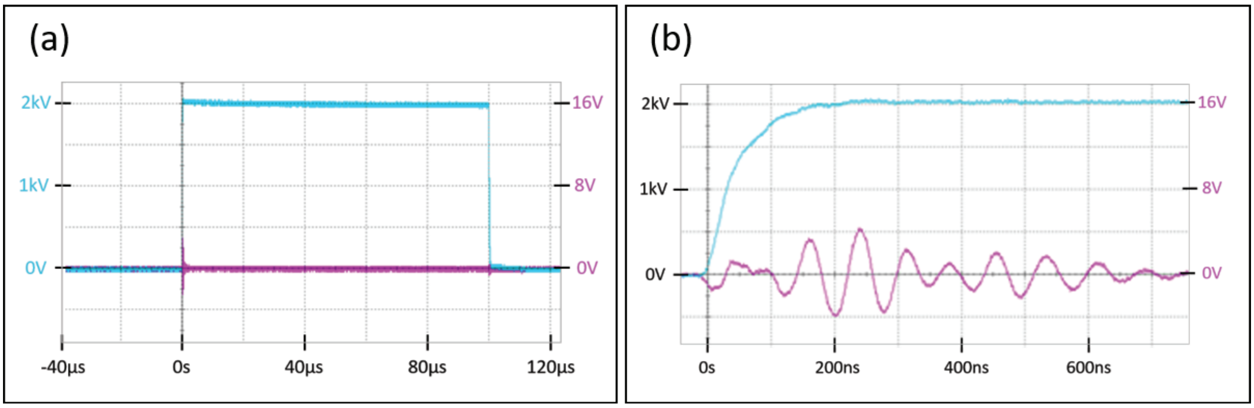

Figure 36: Signal after the switch measured with a probe limited at 2 kV and an oscilloscope. X-axis is the time in µs (a) or ns (b), the Y-axis is the voltage in kV (left) or V (right). In cyan is the voltage output of the switch (left axis) and in magenta is the signal on MCP back: the noise from the switch (right axis).

At t=0 s, the signal rises from 0 V to 2000 V in 200 ns. There is no noise during the switch and the voltage remains stable at 2000 V during the all measurements (100 µs). The rise time at 67% is around 50 ns and at 99%, 200 ns. $H^+(H_2O)_{21}$, with a mass of 379 amu and a kinetic energy of 300 V, needs around 16 µs to go through the whole tube. These values are suitable for our experiment as 200 ns is negligible in front of the bunch size (16 µs) and only a few ions will be in the tube entrance during the switching.

The noise on the MCP is a damped oscillation with a maximum amplitude of 4 V. After 800 ns, the noise is reduced to a negligible small amplitude. As the noise disappears in less than 1 µs, it does not interfere with our experiment nor the ion detection.

c. The pre-acceleration voltage

The pre-acceleration voltage on the octupoles can be adjusted between the trap and the acceleration to set the kinetic energy of the ions and the resulting arrival time of the bunch in the tube. Figure 37 shows the ion bunch on the MCP, after acceleration with different pre-acceleration voltages while the trap is kept at 15 V: V_p=0 V in red, V_p=5 V in yellow, V_p=10 V in green, V_p=12 V in blue, V_p=14 V in purple. The ions are $H^+(H_2O)_n$. x- axis is the time in second and y-axis is the count rate per second. After trapping the ions kinetic energy is negligible. The trap voltage V_T is set at 15 V with a pre-acceleration voltage at V_p, thus ions will have a kinetic energy of $q(V_T - V_p)$. V_p ranges from 0 to 14 V, the ion kinetic energy from 1 to 15 eV. At t=0, the exit of the trap is opened and the ion extraction starts. The ion bunch arrives at different time at the position of the MCP detector and is shifted depending on the ion kinetic energy. For V_p= 0 V, the maximum of the bunch arrives 140 µs after the trap opening. The time of flight of $H^+(H_2O)_{21}$ with 15 eV between the trap and the detector is 134 µs, which is in good accordance with the experimental value of 140 µs. The results are summarized in Table 2.

Pre acceleration voltage (V)	**Experimental delay (µs)**	**Kinetic energy (eV)**	**Calculated TOF (µs)**	**color**
0	140	15	134	Red
5	165	10	164	Yellow
10	205	5	232	Green
12	245	3	299	Blue
14	290	1	519	purple

Table 2: Change of the ion time of flight with the pre acceleration voltage: value of the pre-acceleration voltage, measured experimental delay, ion kinetic energy and calculated time of flight of $H^+(H_2O)_{21}$ *between the trap and the detector.*

For ion kinetic energy between 15 and 5 eV, the shift value corresponds to the time of flight (TOF) with specific ion kinetic energy. At low kinetic energy, slow ions make a wider bunch and the calculated TOF does not well reproduce the data. At low kinetic energy, the initial ion energy is not negligible, the real ion kinetic energy is higher and the TOF is overestimated. The kinetic energy of trapped ions cooled by buffer was measured for $^{40}Ca^+$ by Liang et al. and they found 0.2 eV to 0.5 eV depending of the gas pressure [43].

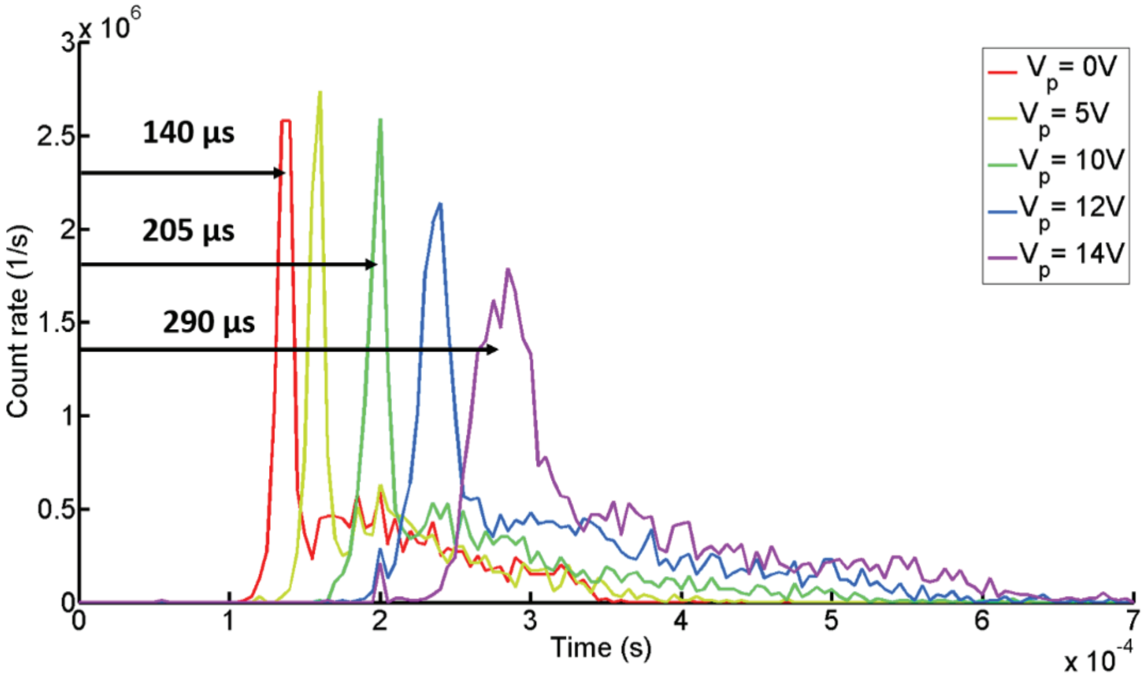

Figure 37: Time of flight of the ion bunch for different pre acceleration voltage V_p: V_p*=0 V in red,* V_p*=5 V in yellow,* V_p*=10 V in green,* V_p*=12 V in blue and* V_p*=14 V in purple. X-axis is the time after the ion extraction from the trap, in second, y-axis is the count rate per second on the detector. (Bin size = 5 µs).*

d. The acceleration tube delay

The delay of the switching of the acceleration tube can be adjusted to select a specific part of the bunch. In Figure 38, the acceleration tube is switched with different delays of 80 µs (red), 90 µs (green), 100 µs (cyan) and 110 µs (purple) after the trap extraction. The delay is the time between the trap extraction and the acceleration tube switching. For each delay, the signal is composed of two bunches, with the first one being the switching noise from the acceleration tube (already discussed in Figure 36). The actual ion bunch arrives at the MCP after the flight time of around 20 µs and can thus be easily distinguished from the noise.

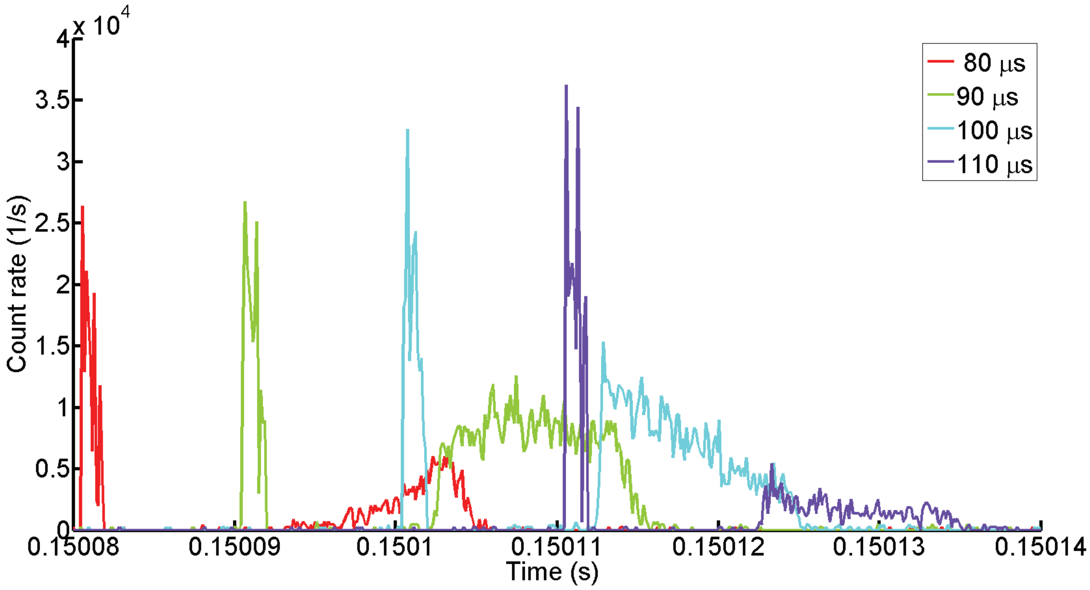

Figure 38: Ion bunch distribution for different acceleration tube delays: 80 µs in red, 90 µs in green, 100 µs in cyan and 110 µs in purple. The signal has two components: peak noise due to high voltage switch and the ions bunch. X-axis is the time in second, y-axis is the count rate per second on the detector. (Bin size = 120 ns).

With a delay of 80 µs, in red, the detected ion bunch is only 5 µs long with a maximum height of 0.6 10^4 counts per second and exhibits a rising signal shape. Only the front part of the ion bunch reached the tube and was accelerated. Between 90 µs (green) and 100 µs (cyan) is the best timing to switch the tube as the main part of the ion bunch will be accelerated. The bunch is then 13 µs long and reaches 10^4 counts/s. After 110 µs (purple), the accelerated bunch has very low intensity (below 0.5 10^4 count/s) and the acceleration tube was switched too late. Here, most of the bunch already passed through the tube and only the last part of the bunch is accelerated. By changing the switching delay of the tube, the actual bunch length and shape can be completely reconstructed.

e. *The acceleration tube width*

The last parameter to adjust is the acceleration tube pulse width, which means how long time the acceleration tube is kept at high-voltage. In the Figure 39, the acceleration tube pulse width is changed to 5 µs (red), 10 µs (black) and 100 µs (blue).

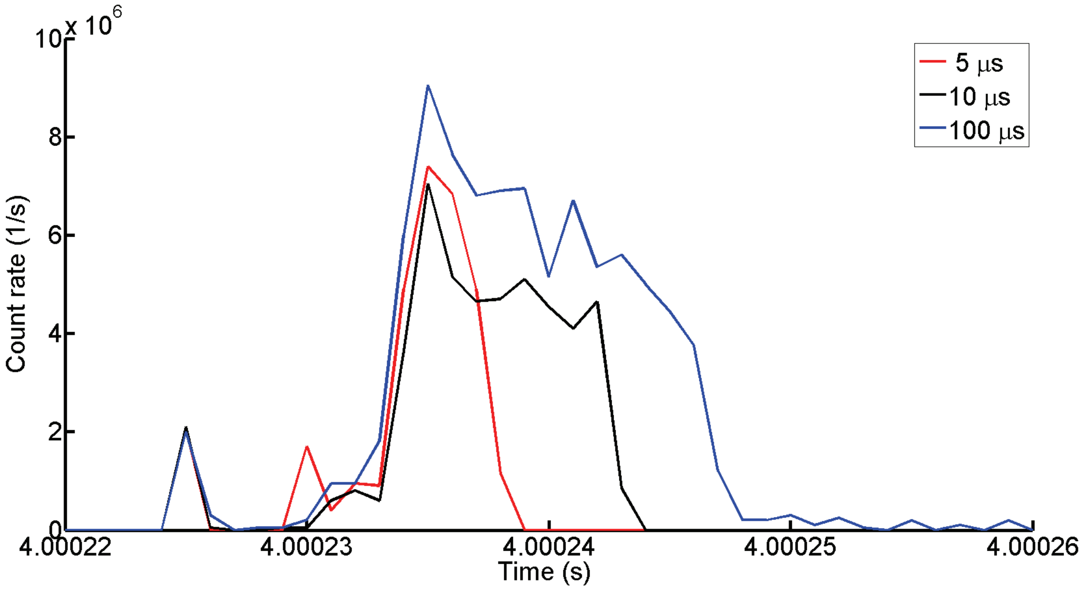

Figure 39: Evolution of the bunch for different lengths of the acceleration tube pulse: 5 µs in red, 10 µs in black and 100 µs in blue. X-axis is the time in second, y-axis is the count rate per second on the detector. (Bin size = 1 µs).

As a result, the width of the bunch increases. For the pulse width of 5 µs in red and 10 µs in black the obtained ion bunches exhibit the same duration. For 100 µs pulse width only a bunch length of 15 µs is observed as this is the maximum bunch length that fits in the acceleration tube for these settings. Indeed, for $H^+(H_2O)_{21}$, with mass 379 amu with a kinetic energy of 300 eV, the time of flight in the tube is 16 µs. To have a longer bunch, the ion kinetic energy can be decreased by increasing the low acceleration tube voltage for example (from -300 V to -200 V will give a bunch of 20µs). The maximum bunch width which can be achieved with this setting is 15 µs long.

A beam of mass selected cluster can be produced, bunched and accelerated to a few keV. Photo dissociation experiments will be explained in the following section.

f. The beam preparation

After the ions were accelerated, different settings of electrostatic lenses can be used to modify the size and the direction of the beam. The beam can be prepared for laser experiments or for injection in the ring. In the following experiment, we study and measure a bunch of methylene blue cations, accelerated at 10 kV.

1) Electrostatic components: the Einzel lens

The Einzel lens is mounted right after the acceleration tube, the scheme of the beam line is shown in Figure 40. It is a uni-potential lens that focuses the ion beam without changing its energy and is composed of three electrodes. The first and last electrodes are grounded, the middle electrode is set at high voltage, usually in the same order but lower than the beam energy.

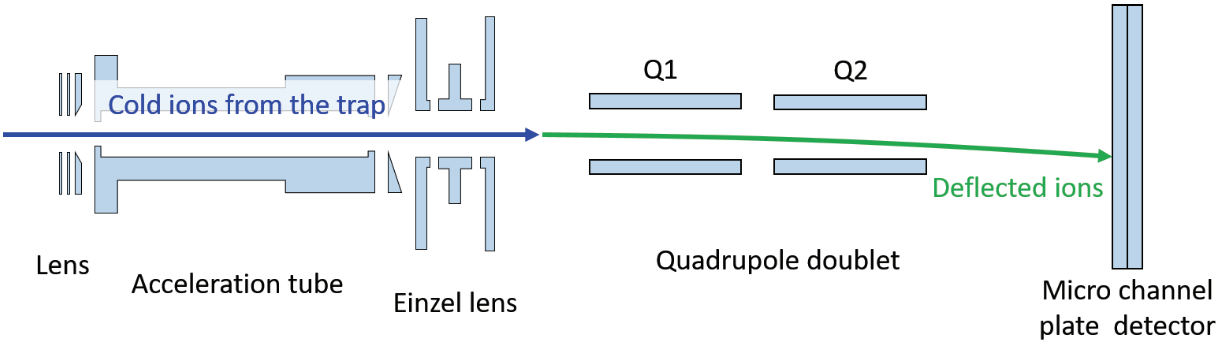

Figure 40: Electrostatic lenses used to control the beam. An Einzel lens focuses the beam and a pair of quadrupole doublet modifies the beam shape and size.

We monitored the shape of the beam with the combination of the MCP followed by a phosphor screen and a CDD camera (Basler acA2500- 14gm). Figure 41 shows pictures of the phosphor screen under the conditions of different Einzel lens voltages: in (a): 6800 V, in (b): 7200 V, in (c): 7400 V, in (d): 7600 V, in (e): 7800 V, in (f): 8000 V and in (g): 8100 V.

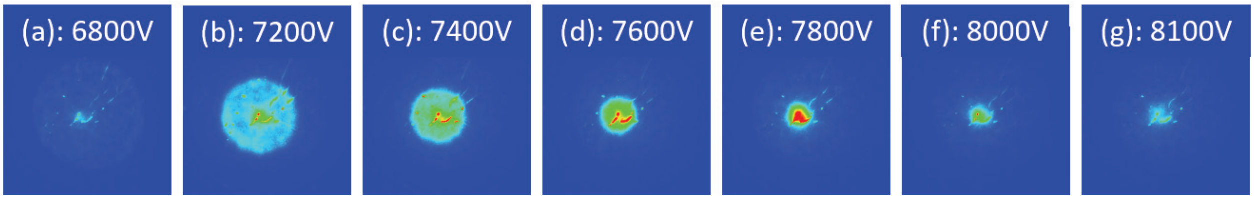

Figure 41: Shape of the scattered beam monitored by the phosphor screen for different einzel voltage: 6800 V (a), 7200 V (b), 7400 V (c), 7600 V (d), 7800 V (e), 8000 V (f) and 8100 V (g). The best focuses occur at 7800 V.

From 6800 V to 7800 V, it is clearly observed that the beam is more and more focused on the detector. At 7800 V, the beam is the best focused. From 7800 V to 8100 V, the beam is rather defocused.

2) *Electrostatic components: the quadrupole doublet lens*

The quadrupole doublet lens is composed of two sets of four electrodes mounted behind each other and is used to modify the beam shape and size. A set consists of 4 opposing electrodes with a round contour, which are used to approximate the hyperbolical quadrupole field. Hereafter, they are addressed as left, right, up and down relatively to the beam direction. The high-voltage on each electrode can be applied independently, however, as the acceleration tube and the MCP detector are well aligned, only symmetric voltages are usually applied: $V_{left}= V_{right}= - V_{up}= -V_{down}$. Proper focusing on the detector was found by simulations and confirmed by the experiment for values of $V_1= \pm390$ V and $V_2=\pm480$ V. With these values, the Einzel voltage has to be slightly changed to have a better focus on the detector as shown on Figure 42, in which 7500 V is applied on the Einzel lens to have a good focus. The finally obtained beam is not round, but elliptical in the vertical direction: after being accelerated, ions will be injected in the ring through a quadrupole deflector. The entrance and the exit of the deflector have vertical slits which would cut the side of a circular beam: the beam shape was chosen to optimize the beam transmission in the different lenses of the beam line.

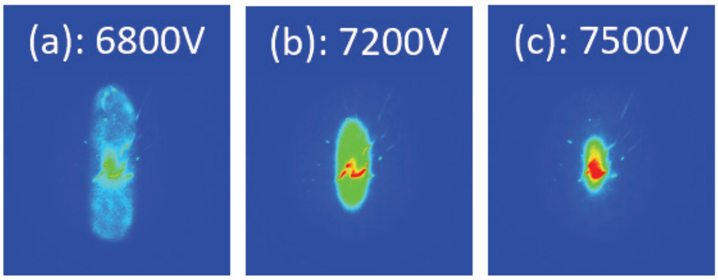

Figure 42: Picture of the phosphor screen for different Einzel voltage: 6800 V (a), 7200 V (b) and 7500 V (c). The best focus occurs at 7500 V.

To see how the quadrupole doublet can change the position of the beam, a round shape beam was used with $V_{Q1}=V_{Q2}= \pm480$ V and the beam can be seen on Figure 43 (a). An offset is applied on the second quadrupole electrodes to adjust the beam position while the first quadrupole voltage was constant, $V_{Q1}= \pm480$ V. First the beam was moved on the left and on the right, by changing V_{left} and V_{rigth}, V_{up} and V_{down} being kept at ±480 V. In Figure 43 (b), the beam was bent on the rigth by using 200V offset: V_{left}= 680 V and V_{rigth}= 280 V. In Figure 43 (c), the beam was bent on the left with: V_{left}= 280 V and V_{rigth}= 680 V. Then the beam moved up and down, by changing V_{up} and V_{down}, V_{left} and V_{rigth} are kept at ±480 V. In Figure 43 (d), the beam was bent toward the bottom by using 200 V offset: V_{up}= -280 V and V_{down}= -680 V. In Figure 43 (e), the beam was bent toward the top with: V_{up}= -680 V and V_{down}= -280 V.

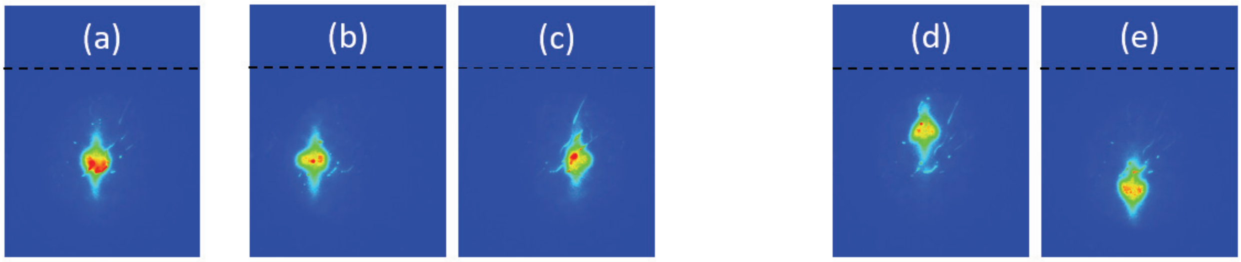

Q1 Offset	(b)	(c)	Q2 Offset	(d)	(e)
Left	-200 V	+200 V	Up	-200 V	+200 V
Right	+200 V	-200 V	Down	+200 V	-200 V

Figure 43: Picture on the phosphor screen of a round shape beam with different quadrupole voltages: both quadrupole are at ±480 V (a), then an offset of 200 V is applied at the second quadrupole to move the beam to the right (b), to the left (c), to the bottom (d) and to the top (e).

Thus, an electrospray ion source produces positive and negative clusters in gas-phase. We studied different parameters which influence the beam production such as the solution or the temperature of the capillary. The quadrupole mass filter is used to measure the mass spectrum, and different calibration methods were explained. One is a published calibrated solution, the other is a well-known spectrum of protonated water cluster. Then a radio frequency octupole ion trap is used to store, cool and bunch the ions. The trap is cool down to 5.2 K and helium is used as a buffer gas to allow continuous injection in the trap and to cool the ions. The extraction electrodes are used to shorten the ion bunch width down to 15 µs without losing any ions. The bunch is guided through octupole guides to the acceleration tube where they gain up to 20 keV in kinetic energy.

Different lenses allow us to control the position and the focusing of the beam. It is very important to control the combinations of applied voltages and the beam shape precisely to inject ions in the ring. The ion injection in the ring is detailed in Appendix 1. For photo-dissociation experiments, the laser interaction region is prepared between the Einzel lens and the quadrupole doublet. In this case, the Einzel lens voltage was optimized to maximize the signal on the MCP. The quadrupole doublet will be exclusively used at a high-voltage to remove the charged fragments and ions from the neutral fragments.

4. The photo-dissociation experiment

The photo-dissociation experiment of methylene blue in gas phase was performed to test the beam line. The data obtained with this setup can then be compared to those published in the literature [44] [45] [46] [47] in order to validate our instrument.

a. The photo-dissociation setup

1) Description of the photo-dissociation experiment

The molecular ions are probed with a tunable laser and the photo-dissociation signal will be measured for different wavelengths. The action spectrum is compared with a measured absorption spectrum in liquid phase. The goal is to dissociate the methylene blue molecule by interaction with a laser. The most probable reaction is $MB^+ + \gamma - > (MB\text{-}CH_3)^+ + CH_3$ in which the CH_3 might split from the $-N(CH_3)_2$ group. The dissociation energy of this reaction is around 3.1 eV [48]. The photon will electronically excite methylene blue and the $S_0 \rightarrow S_1$ transition which correspond to the promotion of an electron from a n to a π^* orbital. An Optical Parametric Oscillator (OPO) tunable laser is used with wavelength ranges from 700 nm (1.77 eV) to 500 nm (2.48 eV). To reach the dissociation level of CH_3, the internal energy of the methylene blue has to be between 1.33 ev and 0.62 eV.

By probing the ion beam with a tunable laser, the action spectrum of the ions is measured. However, the ion density is low, less than one ion in 10^{-8} m^3, and the reduction of the laser beam intensity due to photo-absorption is too low to be observed. Instead, action spectroscopy is used and products resulting from the photon absorption are measured. The ion bunch is irradiated with a tunable OPO laser in the visible light range after acceleration. If the photon energy corresponds to the energy of an excited state of the molecule, the photon will be absorbed, and the molecule might dissociate into charged and/or neutral fragments. After the interaction zone, a quadrupole deflector is set at high voltage (±2 kV), the charged fragment will be deflected and lost. The photo-dissociated neutrals are not be deflected and will hit the detector. A signal on the detector will be a trace of photo-dissociation. Then the wavelength of the laser is changed and the signal on the detector is recorded, larger neutral yield corresponding to higher absorption at this energy. The experimental scheme is shown in detail in Figure 44.

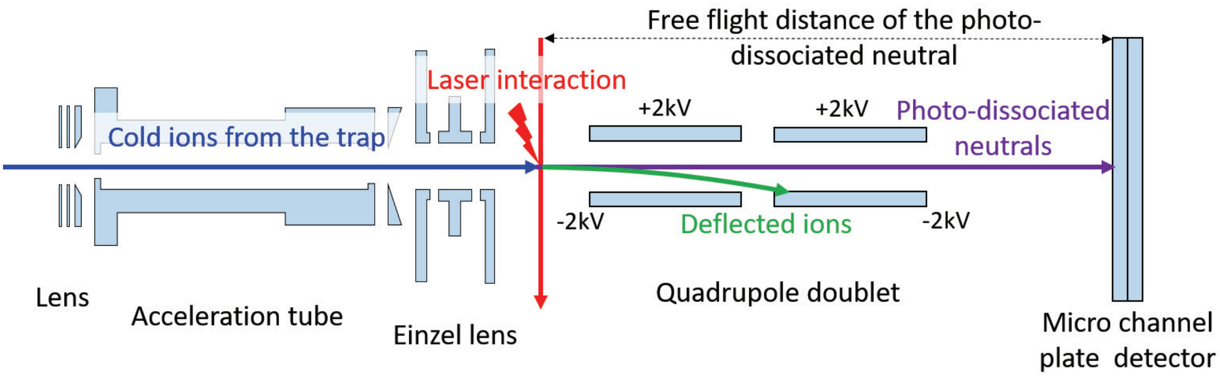

Figure 44: Experimental scheme: ions from the trap are accelerated to up to 20 kV and are probed by a laser. If the energy of the laser corresponds to an excited state of the molecule, this molecule might dissociate and create a neutral and a charge fragments. The charge fragment is deflected by a quadrupole using a high deflection voltage of ± 2 *kV and the neutral is detected on the MCP.*

2) *Description of the laser*

An optical parametric oscillator (OPO) laser is used as photon source (schematically shown in Figure 45(a)). Optical parametric processes are three photon interactions, in which one photon (the pump photon, frequency ω_p) splits into two photons called signal and idler (ω_s, ω_i) by a nonlinear BBO (beta-barium borate) crystal. The ratio between signal and idler wavelengths can be changed by rotating the crystal under conservation of $\omega_p = \omega_s + \omega_i$ (Figure 45 (b)). The OPO consists essentially of a resonator where the pump beam is split in two lower energy beams and an amplifier in which the intensity of the beam is increased.

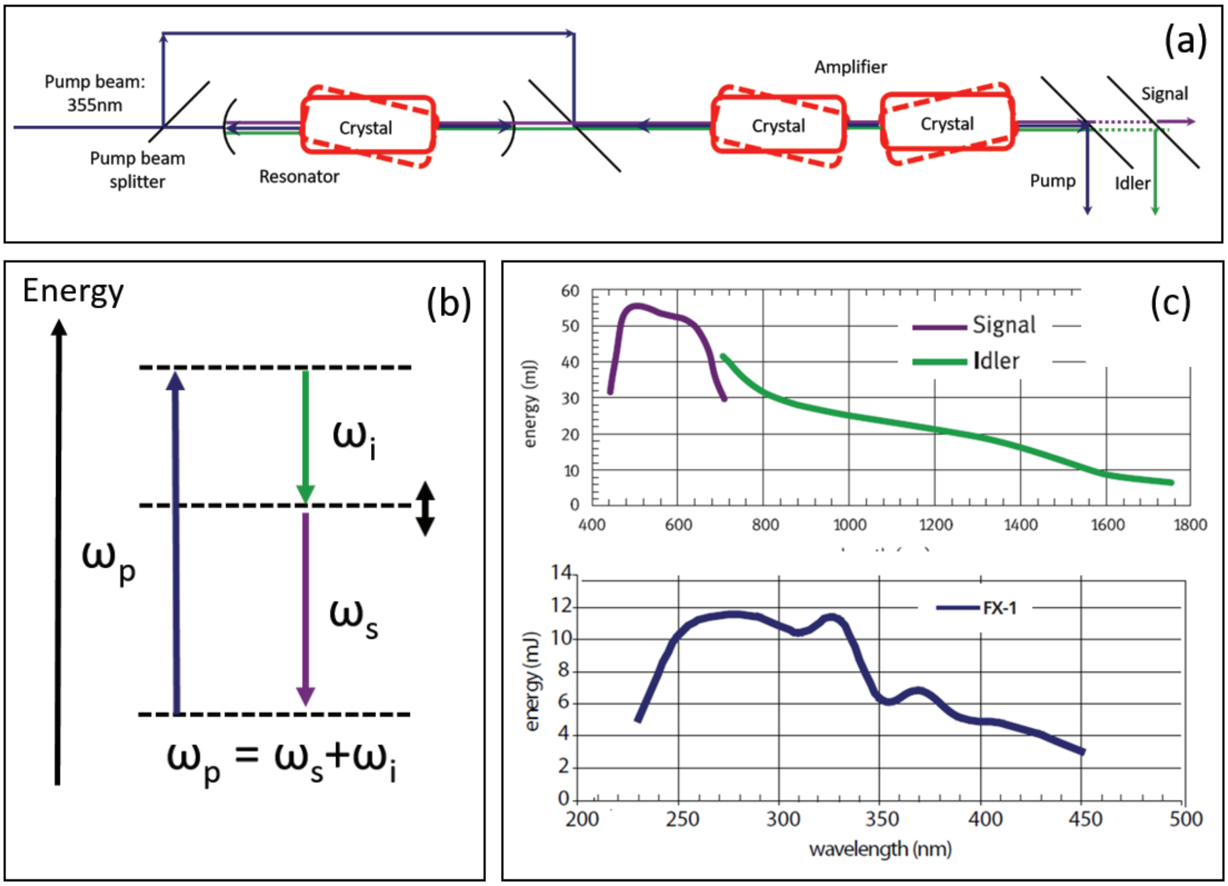

Figure 45: Description of the OPO laser. (a) is a scheme of the laser with its different components: a resonator and an amplifier. The pump beam in blue is divided in the crystal in a signal and idler beams in green and purple respectively. (b) shows the energy diagram with the energy of the pump photon and of the signal and idler photons. (C) shows the laser performance: with in x-axis, the output wavelength and in the y-axis, the power of the output beam (from the company manual [49]).

An OPO laser from Continuum (Sunlite EX OPO PL 8000) is used. The OPO output photon energy can be changed from 445 nm (2.78 eV) to 1750 nm (0.7 eV). The repetition rate is 10 Hz, the spot diameter is 4-6 mm, the beam width 3-6 ns long and the linewidth is below 0.075 cm^{-1}. Figure 45 (c), shows the energy per laser pulse of the laser output versus the wavelength. The laser internal clock is triggered and synchronized with an external wave function generator (Stanford Research Systems DG645). The Q-switch of the laser is triggered by the same wave function generator and enables the laser pulse generation.

In this experiment the signal beam of the OPO in the visible region is used. At a photon energy of 2 eV corresponding to 600 nm, the specified maximum pulse energy at the output of the laser is around 50 mJ. Experimentally a maximum of 40 mJ could be obtained. After the 10 meter beam transportation to the trap, the beam energy decreased to 15 mJ behind the collision zone, however it is sufficient for the present experiment.

3) The detector and the acquisition system

The same acquisition system is used for the channetron and for the MCP detector. The whole acquisition system is shown in Figure 46. The signal is read out from the anode of the channeltron or the anode of the MCP. The scheme diagram of the acquisition system is shown in Figure 46. The signal from the back of the detector is connected to a RC box (R= 50 Ω and C= 150 pF) to couple the signal out and to protect the fast pre-amplifier against high voltage discharges in the MCP. The signal is amplified (Fast pre-amplifier: Ortec VT120 with a gain of 20) and transferred to a constant fraction discriminator (TC CFD454, pulse width 40ns) and a level adaptor for NIM to TTL conversion. A BNC terminal block (BNC 2121, National Instruments) is used to connect the TTL-signal to the acquisition card (PXIe-6612, National Instruments). A minimum pulse width of 40 ns from the discriminator is needed to record the signal as the card operates at a clock frequency of 25 MHz. The dead time of the acquisition is 80 ns corresponding to a maximum sampling rate of 12.5 MHz.

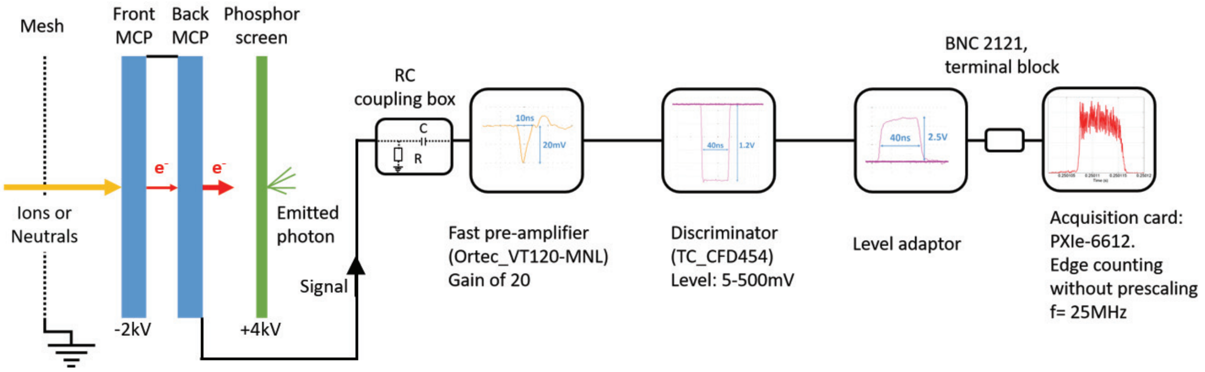

Figure 46: Scheme of the acquisition system chain with the MCP detector, the pre-amplifier, the discriminator, the level adaptor, the terminal block and the acquisition card.

A specific data-editing program was developed using National Instruments LabVIEW 2012, it controls the acquisition card as shown in Figure 47. An external pulse generator (Stanford Research Systems DG645) triggers the experiment for each experimental cycle using four outputs: three for the laser (Q-switch, seeder and flash lamp triggers) and one for the acquisition system (called injection trigger). One cycle consists on the ion trap injection, extraction of the ion bunch, acceleration of the bunch, interaction with the laser, detections of the fragments and saving of the data.

For the acquisition system, the LabVIEW program creates four tasks: each line of Figure 47 is a task. Each task can be in four different states: configured, ready, active and stopped. The black box represents a looped operation and is one cycle of the experiment; the program progresses from left to right in this diagram. At the end of each cycle, the task starts again at the left side of the loop.

The first task (master) will be active after receiving the external trigger from the wave generator (injection trigger) and will then send three triggers to start the three other tasks (counter, clock and timer). The 25 MHz clock is then started (and resets every loop) and when the counter receives a signal from the BNC block, it will read the current clock tick and save the corresponding time. The counter is configured as re-triggerable and thus can detect several signals in one cycle. The timer consists of several output channels and sends the triggers for the switches of the ion trap and acceleration tube.

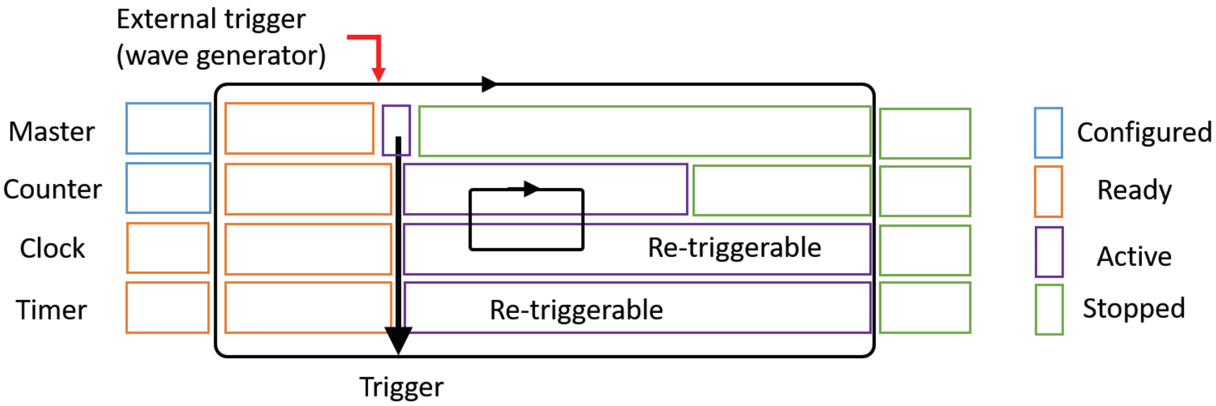

Figure 47: Schematic diagram of the LabVIEW program

4) *The timing*

Figure 48 shows the timing diagram of the experiment more in detail. The Q-switch timing and the injection trigger are provided from the wave function generator and have a time difference of delay 1. The trap master trigger is a delayed trigger of the injection trigger (delay 2). The Q-switch trigger is the reference time as it determines the laser pulse generation time. The cycle begins with delay 1: the time dedicated to save the data from the previous injection. Delay 2 is a buffer time which is used to adjust the characteristic times of the experiment (injections time, trapping time, ...) with respect to the laser pulse. Then, the timer outputs for the injection, trap, TOF and acceleration are executed. The next Q-switch signal defines the time of the laser irradiation and the data are saved. As this Q-switch trigger still falls in the acquisition time, it cannot be used to trigger the next injection. However, due to the delayed injection trigger (with delay 1) no time needs to be wasted to wait for the following Q-switch trigger.

Due to the ion interaction with the laser, photo-dissociation occurs, resulting fragments are detected and their arrival times are saved. To increase for example, the injection or trapping time, the whole timing has to be shifted with respect to the Q-switch timing by decreasing the buffer time (delay 2). If the buffer time is too short for one Q-switch cycle, one laser pulse will be skipped and one cycle will be added to the delay 2 to increase the buffer time length. The acquisition is on from the beginning of the injection to the end (determined by the user) and any signals are recorded in an active mode during this time.

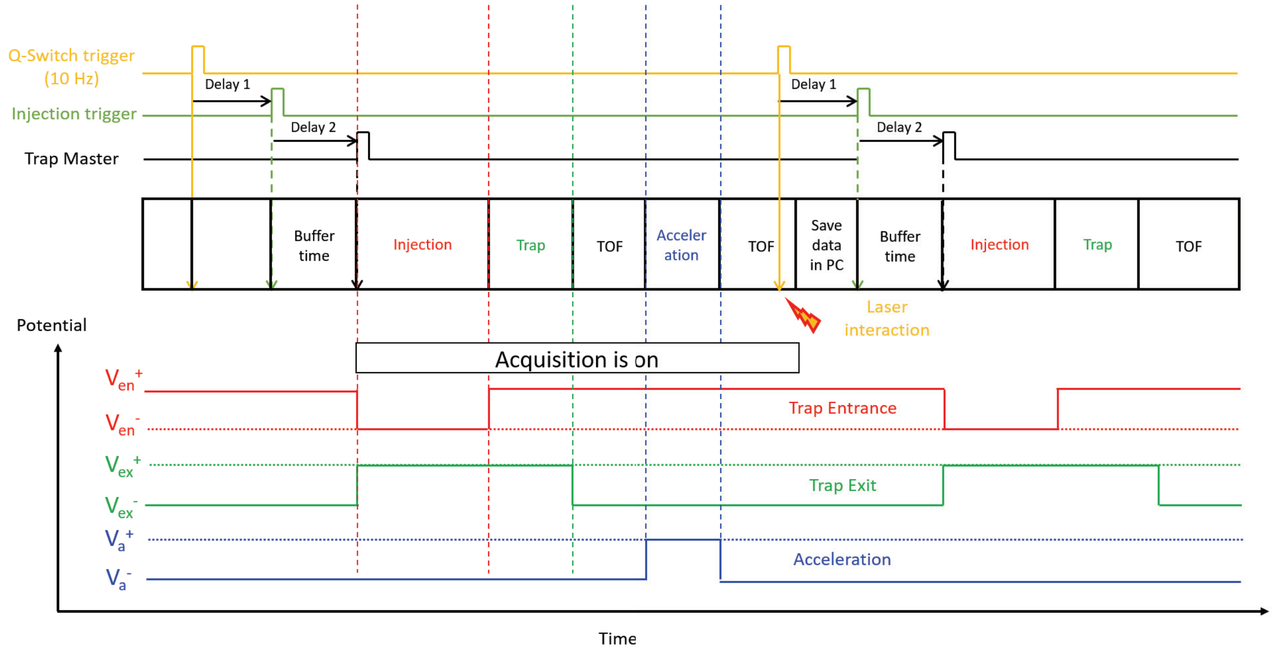

Figure 48: Timing diagram of the experiment

At the bottom of Figure 48 is the time of each experimental device during a cycle as a function of its potential. The x-axis is time and y-axis is the potential applied to the experimental devices where V_{en}^+ and V_{en}^- are the high and low potentials of the trap entrance end cap, V_{ex}^+ and V_{ex}^- that of the trap exit end cap and V_a^- and V_a^+ that of the acceleration tube, respectively.

5) *Data analyses*

The capillary temperature was set at 55°C to mainly have pure methylene blue cations (see the methylene blue spectrum at 55°C in Figure 24). The Q-mass is used as an ion guide to transfer as much ions as possible without selective mass. The wavelength of the laser was set at 600 nm and the beam energy at 12 mJ. The ions were injected in the trap for 0.249 seconds, trapped for 0.001 seconds, extracted and accelerated to 10 keV until the laser interaction region. The trap was at room temperature.

Figure 49 shows our result with in x-axis, the time and in y-axis, the number of counts detected per bunch. The red signal is the ion bunch without the laser and without using ion deflector. The histogram was made with a bin size of 240 ns. The maximum time resolution of our experiment is 80 ns and thus the maximum number of counts would be 3 per bin. It is noted that the plateau at 2.5 counts of the bunch signal is not the real number of ions in the bunch as the acquisition system is saturated.

The black line shows the neutral background which is obtained when the laser is off but the deflector is on (± 2 kV). This signal originates from collisional neutralization of ions with residual gas between the acceleration tube and the deflector, and with minor contribution from detector dark counts. Due to the much lower detector count rate of maximum 0.2 counts per bin, this signal is very close to the real bunch shape. However, the flat structure shown in red line was observed because of saturation of the detector. The background is used to estimate the number of the ions in the initial bunch assuming that the background intensity is proportional to this number of ions. Indeed, the full bunch cannot be totally measured as the acquisition system is totally saturated. This assumption is valid if the pressure in the beam line remains constant during the experiment.

The blue line shows the obtained signal of neutrals with the ion deflector and a photon wavelength of 600 nm (2.07 eV) with a pulse energy of ~12 mJ. It shows a similar shape to the background signal except for a peak around 0.250112 s of less than 1 µs in width, which is due to the radiation by the laser and is the trace of photo-dissociation. The overlap between the ion beam and the laser is about 1 cm long. By assuming the neutral fragment is CH_3 with a mass of 15 amu, it will have a kinetic energy of 1893 eV. The time of flight difference between both edges of the beam gives the signal length: 6.4 10^{-8} s. The width of the signal comes from the energy distribution of the bunch and the lifetime of the excited states: the molecules might dissociate at different time after excitation.

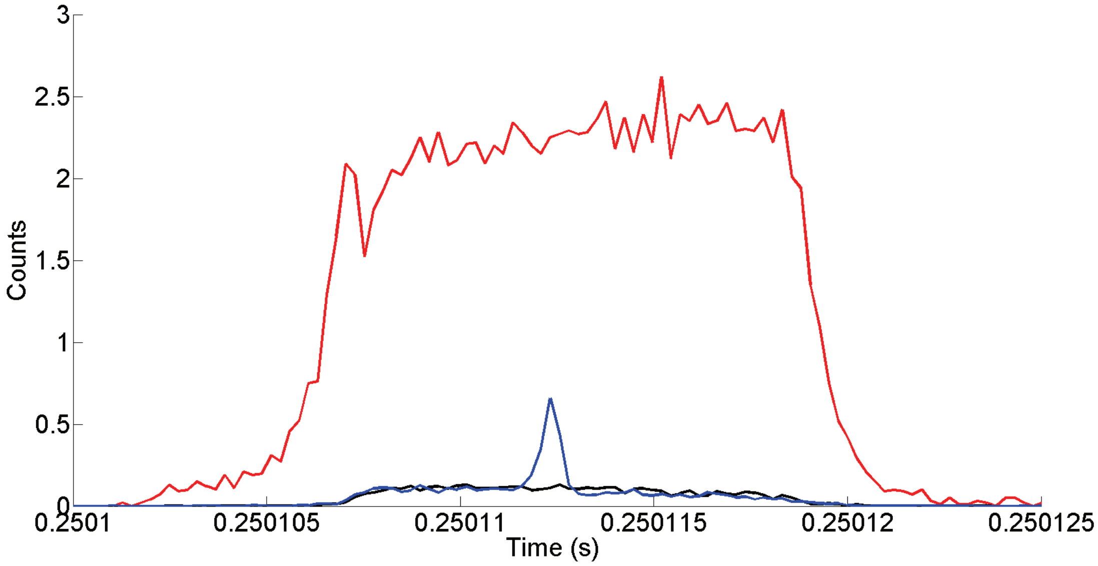

Figure 49: Photo-dissociation experiment for 1000 injections (normalized by the number of injections) with in red: the full ion bunch, in black the background (no laser) and in blue the signal due to the laser interaction, λ= 600 nm with 12 mJ (bin size = 0.24 µs)

The Time of flight spectra induced by the laser interaction is measured for different laser wavelengths. Then, the intensity of the signal is plotted as a function of the wavelength, this plot is called an action spectrum. Figure 50 explains how the intensity of the signal is extracted from the experimental data. In each graph, the x- axis is time after the trap extraction in µs and the y-axis is the count rate in s^{-1}.

Figure 50 (a) is the raw experimental data: the background ranges from 105 µs to 120 µs. The peak around 112 µs is the neutral counts from the background and from the interaction with the laser. In Figure 50 (b), the signal is extracted as the sum of the number of counts in the red zone divided by its width. In Figure 50 (c), the background is evaluated as the sum of the counts in the green area divided by its width. And in the Figure 50 (d), the noise is extracted as the sum of the counts in the purple area divided by its length.

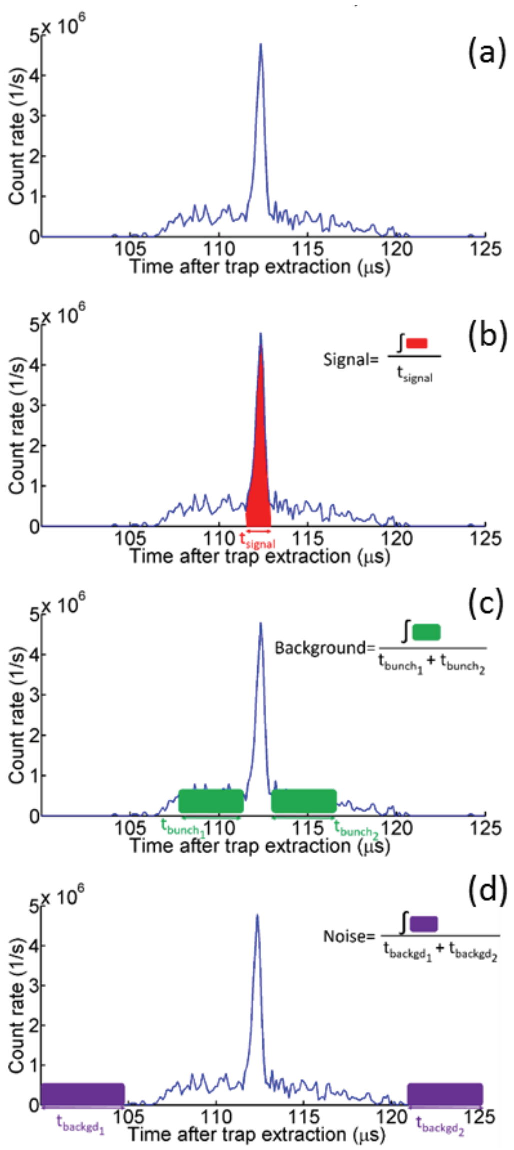

Figure 50: Step of the data analyses with in (a) a typical photo absorption distribution. In (b), the signal is extracted from the distribution (in red), in (c), the background and in (d), the noise.

The first step is the subtraction of the background from the signal: we remove in the peak area the background to select only the neutral which are coming from the laser interaction. Then to ensure that the result is independent of the initial number of the ions in the bunch, the signal is normalized by the background as it is proportional to the number of the ions in the bunch. The noise is finally removed from the background. The noise comes from the detector: dark counts or any electronic noise which come from the acquisition system.

The last step is to normalize the spectra by the laser pulse energy as the signal intensity is proportional to the laser power (in the range of the present power range). The signal dependence with the laser power was measured in Figure 51. The laser power was decreased from 1 mJ to 12 mJ by changing the delay between the pump and the seeder light. The signal was calculated with the above method and normalized by the laser power.

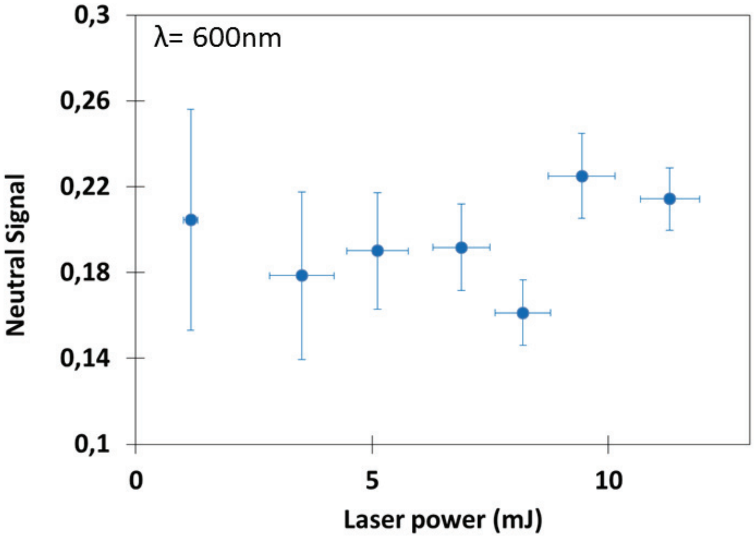

Figure 51: Normalized signal measured with different laser powers.

In this laser energy range, we observe that the signal is constant around 0.2, the signal is independent of the laser power. The energy of each laser pulse is measured, divided by the single photon energy and averaged over the whole experiment. The absorption coefficient is then divided by this value: I_{laser}.

The final absorption coefficient is given by the equation:

$$Abs = \frac{Signal - Background}{Background - Noise} \times \frac{1}{I_{laser}} \qquad 10$$

To control that the signal in independent of the number of ions produced by the source, we measure the absorption spectrum for bunches with different number of ions. Since the width of the laser is much narrower than the width of the bunch, the photo-dissociation signals were measured with different parts of the bunch by changing the time difference between the bunch and the laser as shown in Figure 52. The end side part of the whole ion bunch was selected by switching the acceleration later than usual and is shown in red line. This bunch was made with a low intensity beam to ensure there is no saturation on the detector and that the real structure of the bunch is known. The bin size is 320 ns and saturation should occur at 4 counts, however, the maximum signal is reduced to 2. The timing delay of the laser is changed to be injected into different parts of the bunch: the delay is the time between the ion extraction and the laser interaction. The delays used were: t_d= 105 µs in yellow, t_d= 106 µs in green, t_d= 108 µs in blue and t_d= 110 µs in purple.

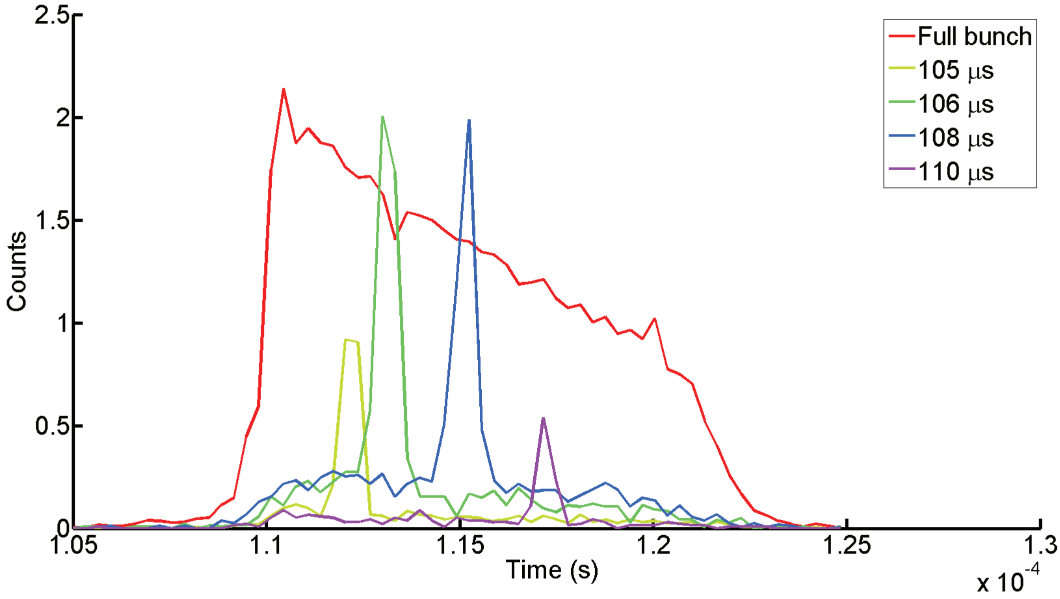

Figure 52: Photo dissociation experiment with different number of ions in the interaction region. The laser delay, t_d was changed in an ion intensity decreasing bunch (red curve): $t_d = 105\,\mu s$ in yellow, $t_d = 106\,\mu s$ in green, $t_d = 108\,\mu s$ in blue, $t_d = 110\,\mu s$ in purple. (binsize 320ns)

Using the analysis scheme described above, the absorption signals calculated are: 7±2.6 for t_d= 105 µs, 6.1±2.5 for t_d= 106 µs, 5.2±2.3 for t_d= 108 µs and 5±2.2 for t_d= 110 µs. As expected the four absorption coefficients are very similar within the error bar independently of the number of ions in the bunch.

The absorption coefficient does not depend on the number of the ions produced by the source, the laser intensity or the noise on the detector. To measure an action spectrum, we measure the absorption coefficient with a laser at different wavelengths.

b. Results and discussion

The obtained time of flight spectra after the procedure explained at the previous section is shown in Figure 53: the distribution is plotted for different wavelengths of the laser: in red, λ= 580 nm, in green, λ= 600 nm, in cyan, λ= 620 nm and in purple, λ= 640 nm. The background has always the same shape and height: from 106 µs to 120 µs with a height of about 0.1 counts. The results are averaged for 50 bunch-laser interactions and normalized. The laser is always injected at the same timing: between 112 µs and 113 µs. The obtained signal has a constant width of 1 µs but different heights. The purple curve at 640 nm is the highest with a maximum at 0.77 counts and the red curve at 580 nm is the lowest with a maximum at 0.42 counts. The spectra are not normalized by the laser intensity. The bin size is 120 ns.

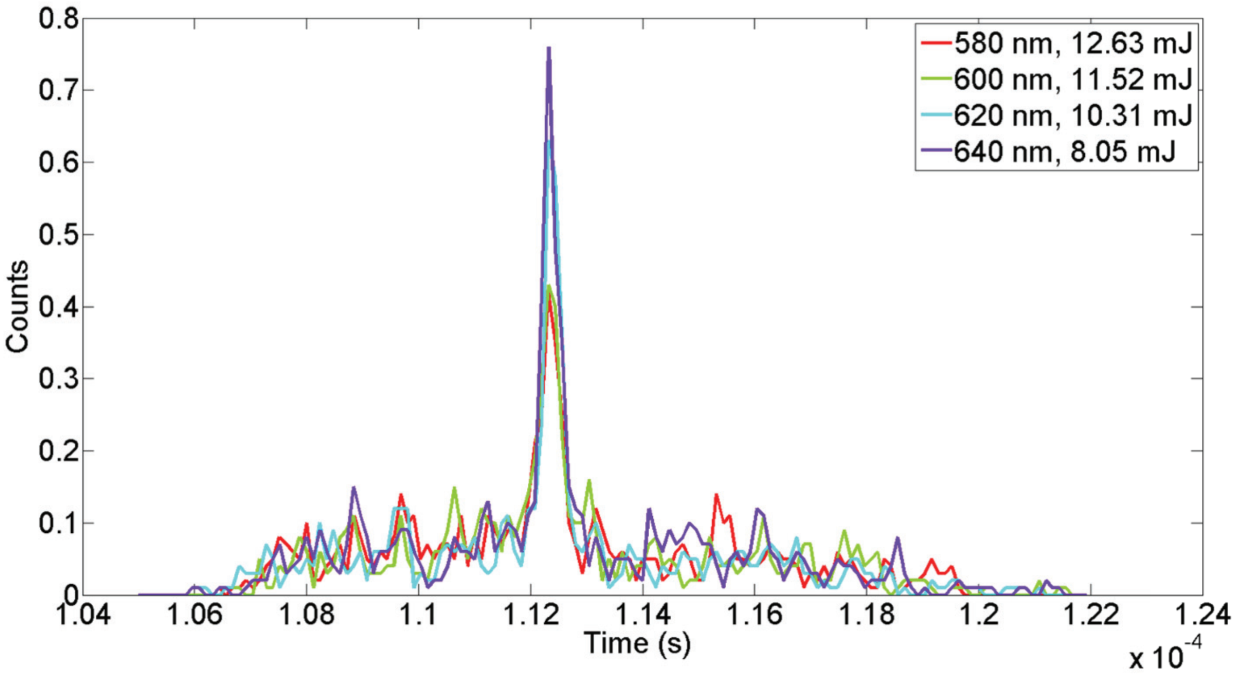

Figure 53: Photo-dissociation experiment with different laser wavelengths: λ=580 nm in red, λ=600 nm in green, λ=620 nm in cyan and λ=640 nm in purple. The results are averaged for 50 bunch-laser interactions and normalized.

From these distributions, we can extract the absorption coefficient as described above and plot an action spectrum.

For the action spectrum shown in Figure 54, we use an oscilloscope for the data acquisition (RHODE and SCHWARZ RTO 1014) working with a sample rate of 1 GHz. Compared with the acquisition card, the oscilloscope has a better time resolution, 1 ns but the accumulate data file size is huge. The results are averaged for 10 000 bunch-laser interactions and normalized. The code used to detect peaks in the signal was adapted from findpeaks, a Matlab function developed by Thomas C. O Haver in 2014 [50].

Figure 54 shows the action spectrum of methylene blue in red dots: the laser wavelengths were scanned from 530 nm to 680 nm. The blue dots are the absorption spectrum of methylene blue in liquid phase [44]. The results are averaged for 1000 bunch-laser interaction and normalized.

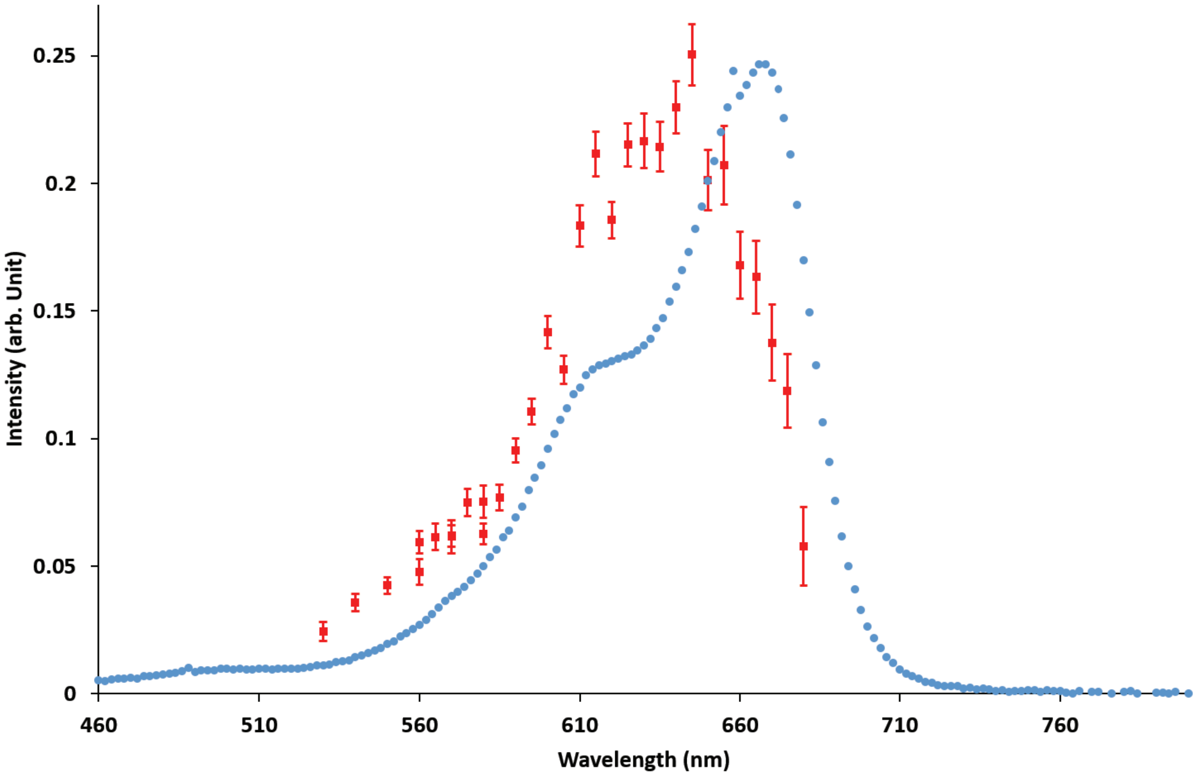

Figure 54: Photo-dissociation spectrum of methylene blue in gas phase (red spectrum) and in liquid phase (blue spectrum). The gas phase spectrum range from 530 nm to 680 nm and was made by average 1000 bunch-laser interactions.

The error bars come from the statistical error taking in account the laser power fluctuation:

$$dAbs(S,B,D,I) = \sqrt{\left(\frac{dAbs}{dS}\Delta S\right)^2 + \left(\frac{dAbs}{dB}\Delta B\right)^2 + \left(\frac{dAbs}{dD}\Delta D\right)^2 + \left(\frac{dAbs}{dI}\Delta I\right)^2} \qquad 11$$

Then: $\Delta X = \sqrt{total\ count}$ with X= S, B and D. ΔI is the standard deviation of the laser beam energy. Abs(S,B,D,I) is given in equation 10. Thus the error is:

$$dAbs(S,B,D,I) = \sqrt{\frac{S}{((B-D)I)^2} + B\left(\frac{D-S}{(B-D)^2 I}\right)^2 + D\left(\frac{S-B}{I(B-D)^2}\right)^2 + \Delta I^2\left(\frac{S-B}{(B-D)I^2}\right)^2} \qquad 12$$

The methylene blue spectrum has a main peak around 650 nm and a plateau between 610 nm and 650 nm. The spectrum made in liquid phase has its maximum at 670 nm and has a shoulder between 610 nm and 630 nm. Between 530 nm and 610 nm and between 655 nm and 680 nm, the measured spectrum resembles the liquid phase spectrum and is shifted by 15 nm.

As explained in the first chapter, the shift between gas and liquid phases was often observed for other molecules. In liquid phase, the methylene blue interacts with its environment which changes its properties. The hydrogen bonds in solution are breaking apart and reformed continuously while electrostatic interaction as dipole - dipole or charge - dipole remains. In gas phase, all kind of interactions are stable and the molecule bonds remain. After energy absorption, the energy is easily redistributed in the molecule environment.

The absorption spectrum of methylene blue in liquid phase is characterized by an absorption band at high energy (π-π* of benzen ring) around 300 nm which is not in our energy range and a band at low energy around 650-670 nm (moving according to the pH of the solution [51]) and corresponding to n-π* transitions (n is the free doublet on the nitrogen atom of C=N bond and the free doublet of S atom on S=C bond) [52][53]. The shoulder at 615 nm corresponds to a vibronic transition 0-1 (level 0 of ground state to level 1 of the excited state) [54] [55] [56].

The action spectrum measured in gas phase can be interpreted at a peak around its maximum at 650 nm with a shoulder between 610 nm and 630nm which corresponds to the n-π* transitions and to the vibronic transition 0-1. The peak corresponding to the n-π* transitions has a very narrower width while the shoulder width is in the same order than on of the spectrum made in liquid phase.

The overall profile of the gas phase action spectrum is very similar to the absorption spectrum in water, but is blue shifted by a few tens of nm. It suggests that the latter was disturbed by water, and the former is intrinsic.

Conclusion:

In this chapter, we detailed the design of the ion trap beam line injection for the RICE ring. An electrospray ion source produces positive and negative clusters in gas-phase. We studied different parameters which influence the beam production such as the solution or the temperature of the capillary. The quadrupole mass filter is used to measure the mass spectrum, and different calibration methods were explained. One is a published calibrated solution, the other is a well-known spectrum of protonated water cluster. Then a radio frequency octupole ion trap is used to store, cool and bunch the ions. The trap is cool down to 5.2 K and helium is used as a buffer gas to allow continuous injection in the trap and to cool the ions. The extraction electrodes are used to shorten the ion bunch width down to 15 µs without losing any ions. The bunch is guided through octupole guides to the acceleration tube where they gain up to 20 keV in kinetic energy. Different lenses, an einzel lens and a quadrupole doublet allow us to control the position and the focusing of the beam.

Then the beam is probed by a laser to measure an action spectrum. The lasers' photons collide the ion bunch after the acceleration tube. When a photon is absorbed, the cluster ion might dissociate the charged fragments and the non-dissociated cluster ions are removed from the beam with a pair of quadrupole deflectors. The neutral fragments are detected on a MCP detector placed after the quadrupole toward the beam line. Then we can extract the signal induced by laser fragmentation. We controlled that the signal induced by laser fragmentation is independent of the laser and the ion beam intensity. By changing the laser wavelength, we measured an action spectrum for methylene blue cation and compared it to a spectrum measured in liquid phase. The measured action spectrum has a main peak around 650 nm corresponding to n-π* transitions and a shoulder at lower wavelength: 610 nm – 630 nm corresponding to vibronic transition 0-1. The liquid phase spectrum is shifted by 15 nm in the red.

References:

[1] J. Fenn, M. Mann, C. Meng, S. Wong and C. Whitehouse, "Electrospray ionization for mass spectrometry of large biomolecules," *Science,* vol. 246, pp. 64-71, 1989.

[2] M. Przybylski and M. O. Glocker, "Electrospray mass spectrometry of biomacromolecular complexes with noncovalent interactions—New analytical perspectives for supramolecular chemistry and molecular recognition processes," *Angewandte Chemie,* vol. 35, no. 8, pp. 807-826, 1996.

[3] J. B. Fenn, "Electrospray wings for molecular elephants (Nobel lecture)," *Angewandte Chemie,* vol. 301, no. 5638, pp. 3871-3894, 2003.

[4] S. Banerjee and S. Mazumdar, "Electrospray Ionization Mass Spectrometry: A Technique to Access the Information beyond the Molecular Weight of the Analyte," *International Journal of Analytical Chemistry,* vol. 2012, pp. 1-40, 2012.

[5] G. Taylor, "Disintegration of Water Drops in an Electric Field," *Prodeeding of the royal society A,* vol. 280, no. 1382, pp. 383-397, 1964.

[6] A. Bruins, T. Covey and J. Henion, "Ion spray interface for combined liquid chromatography/atmospheric pressure ionization mass spectrometry,," *Analytical Chemistry,* vol. 59, no. 22, pp. 2642-2646, 1987.

[7] T. Covey, A. Bruins and J. Henion, "Comparison of thermospray and ion spray mass spectrometry in an atmospheric pressure ion source," *Organic Mass Spectrometry,* vol. 23, pp. 178-186, 1988.

[8] M. Ikinomou, A. Blades and P. Kebarle, "Electrospray-ion spray: a comparison of mechanisms and performance," *Analytical Chemistry,* vol. 63, no. 18, pp. 1989-1998, 1991.

[9] J. Banks, J. Quinn and C. Whilehouse, "LC/ESI-MS determination of proteins using conventional liquid chromatography and ultrasonically assisted electrospray," *Analytical Chemistry,* vol. 66, no. 21, pp. 3688-3695, 1994.

[10] J. Banks, S. Shen, C. Whitehouse and J. Fenn, "Ultrasonically assisted electrospray ionization for LC/MS determination of nucleosides from a transfer RNA digest," *Analytical Chemistry,* vol. 66, no. 3, pp. 406-414, 1994.

[11] Z. Takats, J. Wiseman, B. Gologan and R. Cooks, "Electrosonic spray ionization. A gentle technique for generating folded proteins and protein complexes in the gas phase and for studying ion-molecule reactions at atmospheric pressure," *Analytical Chemistry,* vol. 76, no. 14, pp. 4050-4058, 2004.

[12] M. Karas, U. Bahr and T. Dulcks, "Nano-electrospray ionization mass spectrometry: addressing analytical problems beyond routine," *Journal of Analytical Chemistry,* vol. 336, no. 6-7, pp. 669-676, 2000.

[13] M. Wilm and M. Mann, "Analytical properties of the nanoelectrospray ion source," *Analytical Chemistry,* vol. 68, no. 1, pp. 1-8, 1996.

[14] G. Staffoed, "Apparatus for Detecting Negative Ions". U.S. Patent 4,423,324, 27 12 1983.

[15] J. Koelemeji, B. Roth and S. Schriller, "Blackbody thermometry with cold molecular ions and application to ion-based frequency standards," *Physical Review A,* p. 23413, 2007.

[16] R. M. Jones, D. Gerlich and S. L. Andersona, "Simple radio-frequency power source for ion guides and ion traps," *Rev. Sci. Instrum.,* vol. 68, pp. 3357-3362, 1997.

[17] D. Gerlich, "Inhomogeneous RF Fields: A Versatile Tool for the study of Processes with Slow Ions.," *Advances in Chemical Physics Series,* vol. Vol. LXXXII, no. State-Selected and State-to-State Ion-Molecule Reaction Dynamics. Part 1: experiment, pp. 1-176, 1992.

[18] M. E, "Memoire sur le mouvement vibratoire d une membrane de forme elliptique," *Journal de Mathematiques pures et appliquees,* pp. 137-203, 1990.

[19] M. Henchman and C. Steel, "Understanding the Quadrupole Mass Filter," *The journal of chemical education,* vol. 75, no. 8, pp. 1049-1054, 1998.

[20] M. Moini, B. L. Jones, R. M. Rogers and L. Jiang, "Sodium Trifluoroacetate as a Tune/Calibration Compound for Positive- and Negative-Ion Electrospray Ionization Mass Spectrometry in the Mass Range of 100–4000 Da," *J Am Soc Mass Spectrom,* vol. 9, pp. 977-980, 1998.

[21] C. Hao, R. March, T. Croley, J. Smith and S. Rafferty, "Electrospray ionization tandem mass spectrometric study of salt cluster ions. Part 1— Investigations of alkali metal chloride and sodium salt cluster ions," *Journal of Mass Spectrometry,* vol. 36, no. 1, pp. 79-96, 2001.

[22] C. Hao and R. March, "Electrospray ionization tandem mass spectrometric study of salt cluster ions: Part 2 — Salts of polyatomic acid groups and of multivalent metals," *Journal of Mass Spectrometry,* vol. 36, no. 5, pp. 509-521, 2001.

[23] T. Sato, T. Majima, K. Hashimoto, K. Hashimoto, Y. Zama, J. Matsumoto, H. Shiromaru, K. Okuno, H. Tanuma and T. Azuma, "Microhydration of the methylene blue cation in an electrospray ion source," *The european physical journal D,* vol. 63, pp. 189-194, 2011.

[24] W. Paul, "ELECTROMAGNETIC TRAPS FOR CHARGED AND NEUTRAL PARTICLES," in *Nobel Lecture*, 1989.

[25] S. Chakrabarty, M. Holz, E. Campbell, A. Banerjee, D. Gerlich and J. Maier, "A Novel Method to Measure Electronic Spectra of Cold Molecular," *J. Phys. Chem. Lett,* vol. 4, pp. 4051-4054, 2013.

[26] J. White and S. Collocott, "Heat Capacity of reference materials: Cu and W.," *J. Phys. Chem. Ref. Data.,* vol. 13, no. 4, pp. 1251-1257, 1984.

[27] Efunda, "Thermal Conductivitu: copper," Efunda, 2017. [Online]. Available: http://www.efunda.com/materials/elements/TC_Table.cfm?Element_ID=Cu.

[28] R. Wester, "Radiofrequency multipole traps: Tools for spectroscopy and dynamics of cold molecular ions," *Journal of Physics B: Atomic, Molecular and Optical Physics,* vol. 42, 2009.

[29] D. Gerlich, Low Temperatures and Cold Molecules, London: I. W. M. Smith, 2008.

[30] S. Schlemmer, T. Kuhn, E. Lescop and D. Gerlich, "Laser excited N2+ in a 22-pole ion trap: experimental studies of rotational relaxation processes," *International Journal of Mass Spectrometry,* vol. 589, pp. 185-187, 1999.

[31] A. Dzhonsona, D. Gerlich, E. Bieskec and J. Maier, "Apparatus for the study of electronic spectra of collisionally cooled cations: para-dichlorobenzene," *Journal of Molecular Structure,* vol. 795, no. 1-3, pp. 93-97, 2006.

[32] O. Boyarkin, S. Mercier, A. Kamariotis and T. Rizzo, "Electronic spectroscopy of cold, protonated tryptophan and tyrosine.," *J Am Chem Soc,* vol. 128, p. 2816, 2006.

[33] B. Wilcox, C. Hendrickson and A. Marshall, "Improved Ion Extraction from a Linear Octopole Ion Trap: SIMION Analysis and Experimental Demonstration," *American Society for Mass Spectrometry,* vol. 13, pp. 1304-1312, 2002.

[34] M. E. Belov, E. N. Nikolaev, G. A. Anderson, H. R. T. P. Udseth, T. D. Veenstra, C. D. Masselon, G. M. V. and R. D. Smith, "Design and Performance of an ESI Interface for Selective External Ion Accumulation Coupled to a Fourier Transform Ion Cyclotron Mass Spectrometer," *Anal. Chem.,* vol. 73, pp. 253-261, 2001.

[35] G. Javahery and B. A. A. Thompson, "Segmented Radiofrequency-Only Quadrupole Collision Cell for Measurements of Ion Collision Cross Section on a Triple Quadrupole Mass Spectrometer.," *J. Am. Soc. Mass Spectrom ,* vol. 8, pp. 697-702, 1997.

[36] B. A. Thomson and C. L. Joliffe, "Spectrometer with Axial Field.". USA Patent 5,847,386, 1998.

[37] B. A. Thomson, C. Joliffe and R. Javahery, "RF-Only Quadrupoles with Axial Fields," in *Proceedings of the 44th ASMS Conference on Mass Spectrometry and Allied Topics*, Portland, OR, 1996.

[38] B. A. Thomson and C. L. Jolliffe, "Quadrupole with Axial DC". USA Patent 6,111,250, 2000.

[39] A. V. Tolmachev, H. R. Udseth and R. D. Smith, "Charge Capacity Limitations of Radio Frequency Ion Guides in their Use for Improved Ion Accumulation and Trapping in Mass Spectrometry," *Anal. Chem ,* vol. 72, pp. 970-978, 2000.

[40] A. Dodonov, V. Kozlovsky, A. Loboda, V. Raznikov, I. Sulimendov, A. Tolmachev, A. Kraft and H. Wollnik, "A New Technique for Decomposition of Selected Ions in Molecule Ion Reactor Coupled with Ortho-Time-of-Flight Mass Spectrometry," *Rapid Commun. Mass Spectrom ,* vol. 11, pp. 1649-1656, 1997.

[41] B. A. Mansoori, E. W. Dyer, C. M. Lock, K. Bateman, R. K. Boyd and B. A. Thompson, "Analytical Performance of a High-Pressure Radio Frequency-Only Quadrupole Collision Cell with an Axial Field Applied by Using Conical Rods.," *J. Am. Soc. Mass Spectrom ,* vol. 9, pp. 775-788, 1998.

[42] A. Loboda, A. Drutchnsky, O. Loboda, J. McNabb, S. V., W. Ens and K. Standing, "Novel LINAC II Electrode Geometry to Create an Axial Field in a Multipole Ion Guide," in *Proceedings of the 48th ASMS Conference on Mass Spectrometry and Allied Topics;*, Long Beach, CA, 2000 .

[43] C. Liang, S. Lei and G. Ke-Lin, "Kinetic Energy of Trapped Ions Cooled by Buffer Gas," *Chinese Physics Letters,* vol. 27, no. 6, p. 063201 , 2010.

[44] S. Prahl, "Methylene Blue Spectra," Oregon Medical Laser Center, 8 march 1998. [Online]. Available: http://omlc.org/spectra/mb/mb-water.html. [Accessed 07 04 2017].

[45] T.-J. Whang, H.-Y. Huang, M.-T. Hsieh and J.-J. Chen, "Laser-Induced Silver Nanoparticles on Titanium Oxide for Photocatalytic Degradation of Methylene Blue," *International journal of molecular sciences,* vol. 10, pp. 4707-4718, 2009.

[46] D. Melgoza, A. Hernandez-Ramirez and J. Peralta-Hernandez, "Comparative efficiencies of the decolourisation of Methylene Blue using Fenton's and photo-Fenton's reactions," *Royal Society of Chemistry,* vol. 8, pp. 596-599, 2009.

[47] E. Morgounova, Q. Shao, B. Hackel, D. Thomas and S. Ashkenazi, "Photoacoustic lifetime contrast between methylene blue monomers and self-quenched dimers as a model for dual-labeled activatable probes," *Journal of Biomedical Optics,* vol. 18, no. 5, p. 056004, 2013.

[48] F. Huang, L. Chen, H. Wang and Z. Yan, "Analysis of the degradation mechanism of methylene blue by atmospheric pressure dielectric barrier discharge plasma," *Chemical Engineering Journal,* vol. 162, pp. 250-256, 2010.

[49] Continuum, "Sunlite EX OPO," Continuum, Santa Clara.

[50] T. O haver, "A Pragmatic Introduction to Signal Processing," University of Maryland at College Park, 02 07 2017. [Online]. Available: https://terpconnect.umd.edu/%7Etoh/spectrum/. [Accessed 02 05 2015].

[51] G. Singhal and E. Rabinowitch, "Changes in the absorption spectrum of methylene blue with Ph," *The journal of physical chemistry,* vol. 71, no. 10, pp. 3347-3349, 1967.

[52] C. Parkanyi, C. Boniface, J. Aaron and M. Maafi, "A quantitative study of the effect of solvent on the electronic absorption and fluorescence spectra of substituted phenothiazines: evaluation of their ground and excited singlet-state dipole moments," *Spectrochimica Acta Part A: Molecular Spectroscopy,* vol. 49, no. 12, pp. 1715-1725, 1993.

[53] D. Heger, J. Jirkovsky and P. Klan, "Aggregation of Methylene Blue in Frozen Aqueous Solutions Studied by Absorption Spectroscopy," *J. Phys. Chem. A,* vol. 109, pp. 6702-6709, 2005 .

[54] G. Lewis, O. Goldschmid, T. Magel and J. Bigeleisen, "Dimeric and Other Forms of Methylene Blue: Absorption and Fluorescence of the Pure Monomer," *Journal of the american chemical society,* vol. 65, no. 6, pp. 1150-1154, 1943.

[55] K. Bergmann and C. O Konski, "A SPECTROSCOPIC STUDY OF METHYLENE BLUE MONOMER, DIMER, AND COMPLEXES WITH MONTMORILLONITE," *The journal of physical chemistry,* vol. 67, no. 10, p. 2169–2177, 1963.

[56] J. Cenens and R. Schoonheydt, "Visible spectroscopy of methylene blue on hectorite, laponite B, and Barasym in aqueous suspension," *Clays and Clay Mineral,* vol. 36, no. 3, pp. 214-224, 1988.

[57] P. Wolfgang, "Electromagnetic traps for charged and neutral particules," *Reviews of Modern Physics, 62,* pp. 531-540, 1990.

[58] T. M. a. G. Santambrogio., "Spatial distribution of ions in a linear octopole radio-frequency ion trap in the space-charge limit," *Physical review A,* p. 85:053414, 2012.

[59] P. Kebarle and L. Tang, "From ions in solution to ions in the gas phase - the mechanism of electrospray mass spectrometry," *Anal. Chem,* vol. 65, no. 22, pp. 972A-986A, 1993.

[60] S. Chakrabarty, M. Holz, E. K. Cambell, A. Banerjee, D. Gerlich and J. P. Maier, "A Novel Method to Measure Electronic Spectra of Cold Molecular," *J. Phys. Chem. Lett,* vol. 4, pp. 4051-4054, 2013.

[61] A. Dzhonsona, D. Gerlich, E. J. Bieskec and J. P. Maier, "Apparatus for the study of electronic spectra of collisionally cooled cations: para-dichlorobenzene," *Journal of Molecular Structure,* vol. 795, no. 1-3, pp. 93-97, 2006.

[62] O. Boyarkin, S. Mercier, A. Kamariotis and T. Rizzo, "Electronic spectroscopy of cold, protonated tryptophan and tyrosine.," *J Am Chem Soc,* vol. 128, p. 2816, 2006.

[63] B. E. Wilcox, C. L. Hendrickson and A. G. Marshall, "Improved Ion Extraction from a Linear Octopole Ion Trap: SIMION Analysis and Experimental Demonstration," *American Society for Mass Spectrometry,* vol. 13, pp. 1304-1312, 2002.

[64] M. E. Belov, E. N. Nikolaev, G. A. Anderson, H. R. T. P. Udseth, T. D. Veenstra, C. D. Masselon, G. M. V. and R. D. Smith, "Design and Performance of an ESI Interface for Selective External Ion Accumulation Coupled to a Fourier Transform Ion Cyclotron Mass Spectrometer," *Anal. Chem.,* vol. 73, pp. 253-261, 2001.

[65] G. Javahery and B. A. A. Thompson, "Segmented Radiofrequency-Only Quadrupole Collision Cell for Measurements of Ion Collision Cross Section on a Triple Quadrupole Mass Spectrometer.," *J. Am. Soc. Mass Spectrom,* vol. 8, pp. 697-702, 1997.

[66] B. A. Thomson and C. L. Joliffe, "Spectrometer with Axial Field.". USA Patent 5,847,386, 1998.

[67] A. V. Tolmachev, H. R. Udseth and R. D. Smith, "Charge Capacity Limitations of Radio Frequency Ion Guides in their Use for Improved Ion Accumulation and Trapping in Mass Spectrometry," *Anal. Chem,* vol. 72, pp. 970-978, 2000.

[68] A. Dodonov, V. Kozlovsky, A. Loboda, V. Raznikov, I. Sulimendov, A. Tolmachev, A. Kraft and H. Wollnik, "A New Technique for Decomposition of Selected Ions in Molecule Ion Reactor Coupled with Ortho-Time-of-Flight Mass Spectrometry," *Rapid Commun. Mass Spectrom,* vol. 11, pp. 1649-1656, 1997.

[69] B. A. Mansoori, E. W. Dyer, C. M. Lock, K. Bateman, R. K. Boyd and B. A. Thompson, "Analytical Performance of a High-Pressure Radio Frequency-Only Quadrupole Collision Cell with an Axial Field Applied by Using Conical Rods.," *J. Am. Soc. Mass Spectrom,* vol. 9, pp. 775-788, 1998.

[70] B. A. Thomson, C. Joliffe and R. Javahery, "RF-Only Quadrupoles with Axial Fields," in *Proceedings of the 44th ASMS Conference on Mass Spectrometry and Allied Topics*, Portland, OR, 1996.

[71] B. A. Thomson and C. L. Jolliffe, "Quadrupole with Axial DC". USA Patent 6,111,250, 2000.

[72] A. Loboda, A. Drutchnsky, O. Loboda, J. McNabb, S. V., W. Ens and K. Standing, "Novel LINAC II Electrode Geometry to Create an Axial Field in a Multipole Ion Guide," in *Proceedings of the 48th ASMS Conference on Mass Spectrometry and Allied Topics;*, Long Beach, CA, 2000.

[73] S. Schlemmer, T. Kuhn, E. Lescop and D. Gerlich, "Laser excited N2+ in a 22-pole ion trap: experimental studies of rotational relaxation processes," *International Journal of Mass Spectrometry,* vol. 589, pp. 185-187, 1999.

[74] Y. Nakano, Y. Enomoto, T. Masunaga, S. Menk, P. Bertier and T. Azuma, "Design and commissioning of the RIKEN cryogenic electrostatic ring (RICE)," *Review of Scientific Instruments,* vol. 88, no. 3, p. 033110, 2017.

[75] S. Jinno, "Storage of atomic/molecular ions in an electrostatic ring," Tokyo metropolitan University, PhD thesis, Tokyo, 2007.

III. Measurement of the velocity distribution of the water molecules evaporated from 8 keV-$PyrH^+(H_2O)_{n=1-4}$ cluster ions after a single collision with an argon atom.

Introduction

Collision induced dissociation of mass selected $PyrH^+(H_2O)_{n=1-4}$ cluster ion experiments have been performed on the DIAM apparatus developed at the nuclear physic institute of Lyon (IPNL). The evaporation of water molecules from 8 keV-$PyrH^+(H_2O)_{n=1-4}$ cluster ions is induced by a single collision with an argon atom. Combining the recently developed COINTOF technique and velocity map imaging measurements, the velocity distribution of the evaporated water molecules is measured. The experimental results are compared to statistical molecular dynamics calculations performed by F. Calvo (LIPHY, Grenoble). This chapter is divided in two parts. The first part is devoted to the description of the experimental set-up. In the second part, the velocity distribution of the evaporation of water molecule from $PyrH^+(H_2O)_{n=1-4}$ will be presented and discussed.

1. Measurement of the velocity distribution of evaporated molecules

DIAM facility produces a cluster beam from a supersonic expansion from a mixture of pyridine and water vapors. The neutral clusters are ionized by a 80 eV electron impact leading to various negatively and positively charged species. The latter are then extracted before being accelerated to 8 keV. The particular $PyrH^+(H_2O)_{n=1-4}$ cluster beam is selected in energy by an electrostatic deflector and in mass through an electro-magnet.

The cluster beam crosses a gas target of argon atoms with a controlled density to ensure single collision conditions. The COrrelated Ion and Neutral Time of Flight (COINTOF) device is aligned with the incident beam direction. Therefore, after collision, both charged and neutral fragments can reach the detector. For each dissociated cluster ion, arrival time and position of both charged and neutral fragments are recorded on an event-by-event basis. After the collision, an acceleration zone reduces the time of flight for the charged fragment according to their mass to charge ratio. The arrival time difference between charged and neutral fragments allows the selection of a given dissociation channel. The impact position of the neutral fragments and their radial distribution are recorded for a given dissociation channel. Then, the unfolding method developed recently in the IPM group allows us to calculate the velocity distribution from the radial distribution.

a. The COINTOF-VMI method

The set-up used to measure the velocity distribution is a combination of DIAM (Dispositif d'Irradiation d'Agrégats Moléculaire) which produces a cluster beam of ions selected in mass and energy, the COrrelated Ion and Neutral Time of Flight (COINTOF) mass spectrometer and the Velocity-Map Imaging (VMI) method.

1) Dispositif d'Irradiation d'Agrégats Moléculaire (DIAM)

The production of the cluster beam has been described in detail in the thesis of G. Bruny and in the associated papers [1] [2] and is schematically shown in Figure 55. The cluster beam is produced in a continuous supersonic expansion of vapor of the molecular systems that are studied. Liquid pyridine (99% purity) and water (spectroscopic grade) provided by Aldrich Sigma Ltd are mixed in a reservoir heated at 120°C. The vapor produced is expanded into a chamber through a 20 µm diaphragm increasing the background pressure to approximately 2.10^{-4} mbar. The neutral cluster jet is ionized by 80 eV electrons to produce a wide variety of positively (e.g., protonated pyridine water clusters) and negatively charged species. As we are interested in the cationic clusters, they are extracted by the 30 V bias maintained at the extraction plate and accelerated at 8 keV. The mass and energy selection is made with an electrostatic and magnetic mass spectrometer mounted in a double focusing configuration. Using the present settings and arrangement, the energy resolution is 0.26% and the mass resolution is 1.06/181 which was found to be adapted to the present experiment.

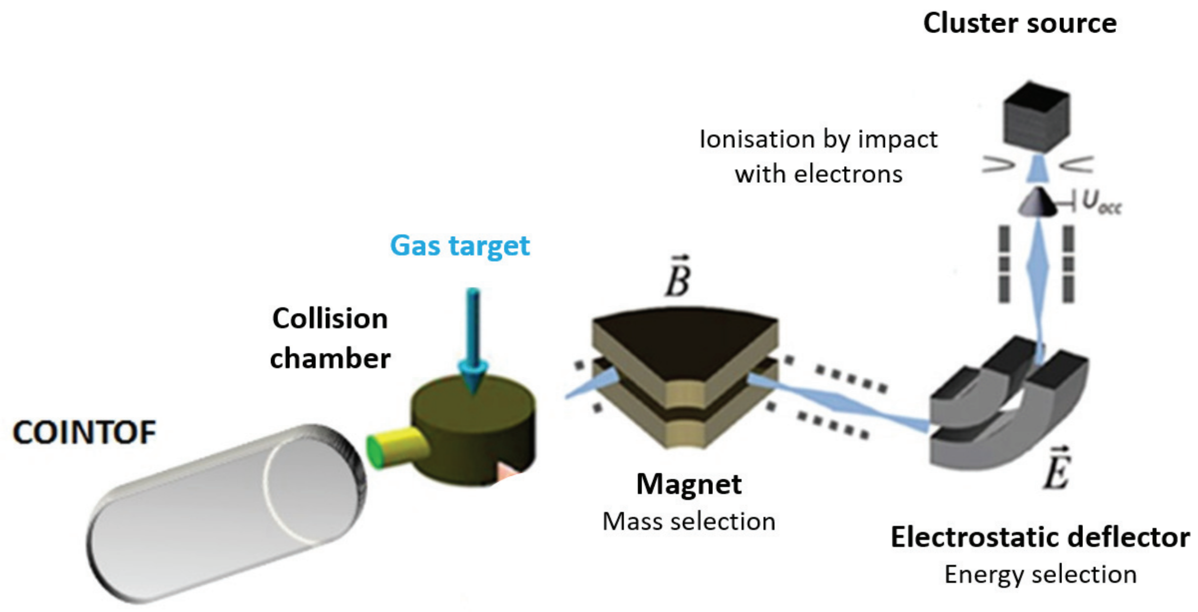

Figure 55: Schematic representation of DIAM connected to the COINTOF detector

The time between the ionization by electron impact and the mass selection is in the order of a millisecond, which give enough time (few µs) for excited ions to relax to form stable species. The clusters in the mass selected beam are expected at a typical temperature in the order of 150 K [2] (from [3], [1], [4] and references therein).

2) *The COINTOF method*

The group IPM has developed a new Mass Spectrometer (MS) which is able to detect and also to correlate on the same detector the neutral and charged fragments coming from the same dissociation event. Furthermore, this MS method, named COINTOF (Correlated Ion and Neutral Time Of Flight) [5] [6], has recently been coupled to a Velocity Map Imaging (VMI) method. The mass and energy selected parent ion colliding with an argon atom, in a single collision conditions, can undergo into dissociation in a charged fragment in addition to one or more neutral species. Both the charged particle and any neutral fragment can be detected *a priori* by the detector. The neutral fragments keep mostly the initial velocity of their parent ions. The charged particles are accelerated proportionally to their mass to charge ratio (m/q). The measurement of the arrival time of each fragment, i.e., the ion and at least one of the neutral counterparts, permits the identification of the charged species. For each dissociated cluster ion, every different arrival time is saved and labelled, event by event. The flying time between the collision chamber and the acceleration zone defines the observation window and ranges from 200 ns for $PyrH^+(H_2O)$ to 250 ns for $PyrH^+(H_2O)_4$. The typical evaporation time is expected to be in the magnitude of picosecond [7] so an excited molecule after collision has time to evaporate one or several molecules before reaching the acceleration zone.

The COINTOF apparatus is shown in Figure 56 and is divided in two parts. The first part is the acceleration zone, where an electric field is applied: the charged fragment will be accelerated and the neutrals will keep almost their initial speed. The second part is the free flight zone where the electric field is zero. As a consequence, the charged accelerated particle arrives on the detector before the neutral fragments.

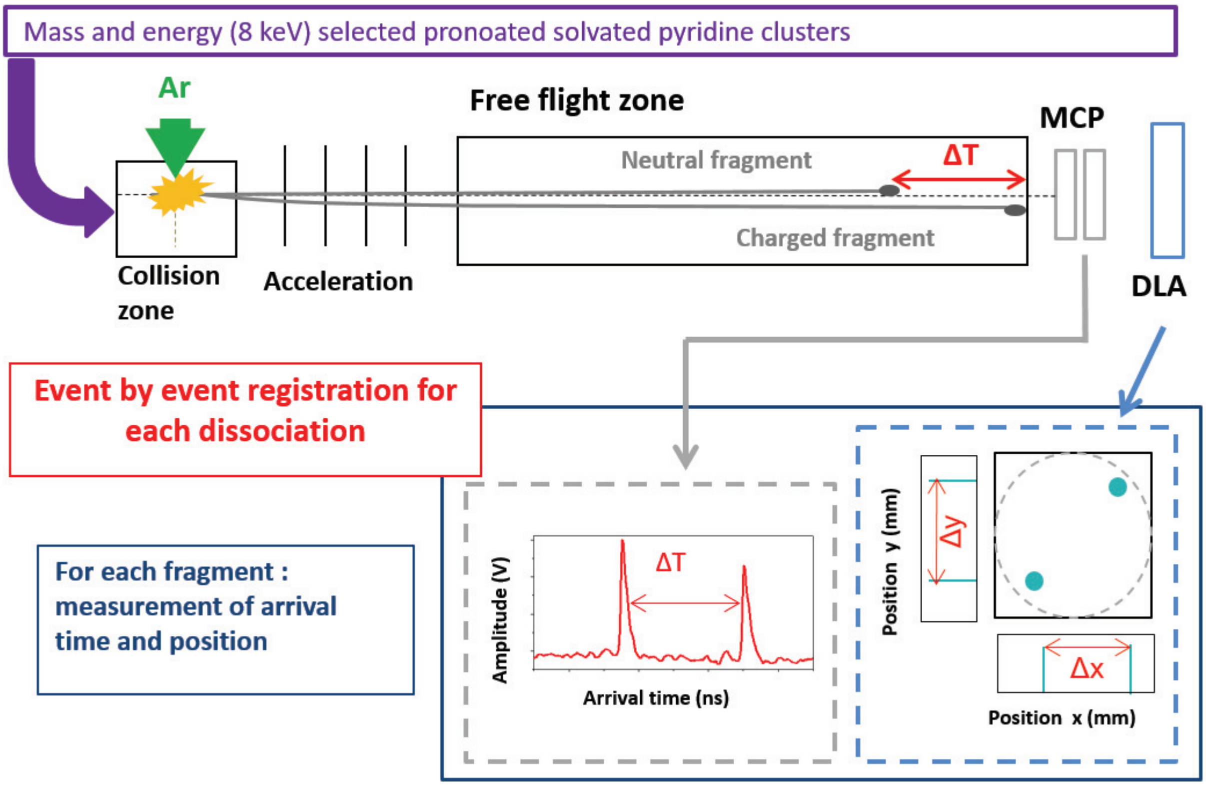

Figure 56: Schematic representation of the COINTOF method (from [3]).

The event-by-event measurement of the arrival time difference between the charged and the neutral fragments allow us to identify the mass of the ion fragment. The acceleration voltage is -1.7kV.

3) The correlated detection

All different fragments are detected with the same detector composed with a pair of Micro Channel Plates detectors (MCP F2225-21SX, Hamamatsu) of 40 mm diameter with channels rotated 90° from each other (chevron mode). A Delay Line Anode (DLA DLD40, Roentdek) is mounted behind this pair of MCP providing the position of the fragments hitting the detector. The measurement of the arrival time of any fragment is provided by the detection of a signal produced by the MCPs. The MCPs detection system was detailed in the previous chapter. The MCP front is set at -1400 V and the signal is measured on the back, grounded.

During the dissociation, any neutral fragment keeps almost the same velocity as their parent ions. Their arrival time on the detector is known, and served as time reference for the arrival time of the ion fragments. The difference between the arrival time of the neutral and the charged fragment, Δt, is characteristic of the ion mass over charge ratio of the fragment. From this correlated detection, we can build the time difference, Δt, histogram which represents the mass spectrum of the charged fragments. An example is shown in Figure 57 for an experiment of collision induced dissociation of 8keV-$PyrH^+(H_2O)_4$ on argon target.

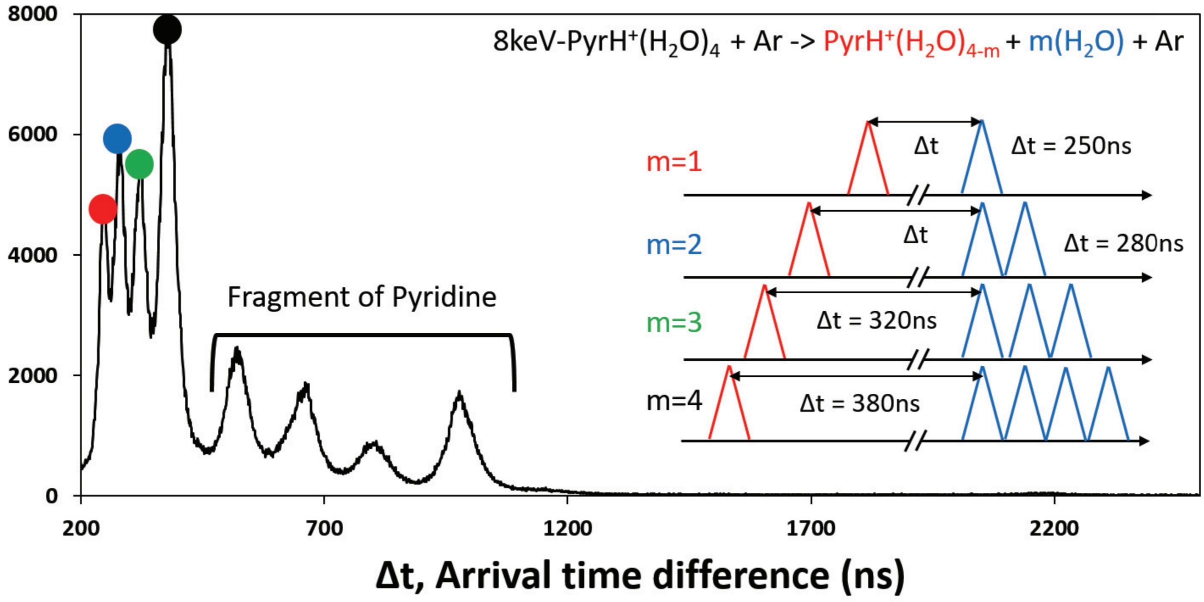

Figure 57: Example of a mass spectrum COINTOF of charged fragments from dissociation of 8keV-$PyrH^+(H_2O)_4$ induced by collision with argon atom.

We observe different peaks corresponding to different channels of dissociation associated to the evaporation of a single or several water molecules (200 ns< Δt<400 ns), and to fragmentation of the protonated pyridine molecule (400 ns<Δt<2400 ns). In the following, we will restrict our discussion on the first type of species that are labelled with coloured points (black, green, blue and red) corresponding to the loss of water units from the parent cluster. The light ions will be more accelerated, they will have larger Δt value. The difference of time between the different fragments is characteristic of a specific channel of dissociation. In this example of the dissociation of $PyrH^+(H_2O)_4$, the first peak, between 240 ns and 260 ns with a maximum around 250 ns (red) is correlated with the evaporation of a single molecule (m=1) and is associated with $PyrH^+(H_2O)_3$. The second peak, between 265 ns and 295 ns with a maximum around 280 ns (blue) is correlated with the evaporation of two molecules (m=2) and is associated with $PyrH^+(H_2O)_2$. The third peak, between 305 ns and 340 ns with a maximum around 320 ns (green) is correlated with the evaporation of three molecules (m=3) and is associated with $PyrH^+(H_2O)$. And the fourth peak, between 355 ns and 410 ns with a maximum around 380 ns (black) is correlated with the evaporation of four molecules (m=4) and is associated with $PyrH^+$. The CID mass spectra of protonated hydrated pyridine clusters were published and discussed elsewhere by F. Berthias et al [8]. This study of the dissociation of protonated pyridine water cluster shows proton transfer from protonated pyridine to water molecule. Indeed, in addition to the fragmentation channel associated with the evaporation of water molecule a competition between the production of the PyH^+ fragment and the production of $H^+(H_2O)$ or $H^+(H_2O)_2$ were observed. Here we focus on the velocity distribution of the evaporated water molecules.

4) The MCP-DLA detector

The velocity distribution is resulting from the measurement of the impact position of the evaporated molecules. The position of each fragment is given by the Delay Line Anode (DLA) detector (DLA DLD40, Roentdek). The DLA detector consists of two perpendicular layers of wires (in blue and red in Figure 58) which detect the electrons produced by the MCPs for each fragment impact. The position of the fragment is measured by the required time for the charge to reach the two ends of each wire. Each wire is associated to a coordinate (x and y) of the impact position on the detector.

The impact position coordinates: x and y can be calculated with a resolution lower than 0.1 mm from the equation:

$$x = v_s(t_{DLA_2} - t_{DLA_1}) \tag{13}$$

$$y = v_s(t_{DLA_4} - t_{DLA_3}) \tag{14}$$

With vs, the signal speed in the wire: v_s is equal to 0.68 mm.ns^{-1} [9] and experimentally measured in the order of 0.69 ±0.01 mm.ns^{-1} [3]. t_{DLA_1}, t_{DLA_2}, t_{DLA_3} and t_{DLA_4} represent the time needed for the signal to go from the impact position to the ends of the wires horizontally (1 and 2) and vertically (3 and 4) respectively. The Figure 58 is an illustration of the DLA detector: for each particle, 5 signals are produced: one from the MCP and four from the DLA.

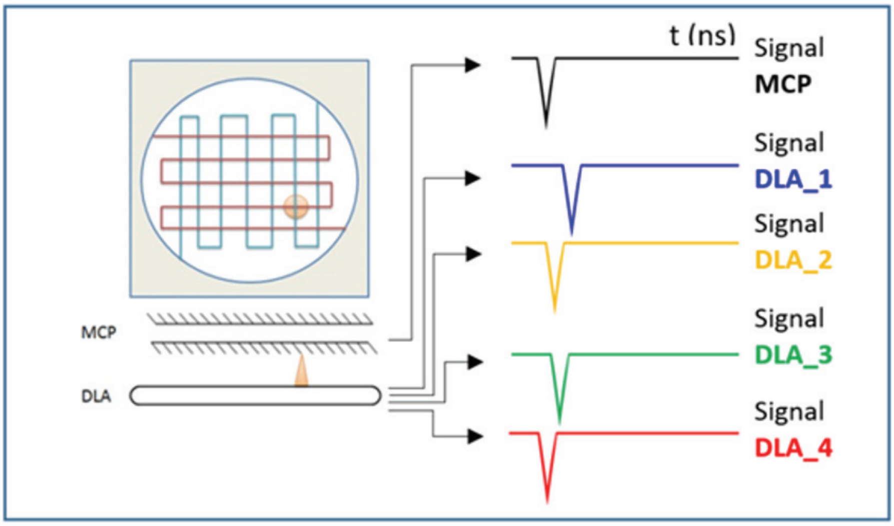

Figure 58: Measurement of the impact position on the detector from the signal measured at the back of the MCP-DLA detector. (from [3] and [10])

5) Acquisition system

The fives signals produced by the detector are shaped in a fast discriminator with a dead time of 10 ns. The arrival instant of each of the five hits in an acquisition window is measured with a multichannel Time to Digital Converter card (TDC), each of the five channels can save up to 16 hits per events (16 fragments) [1]. We call event, each trigger of the acquisition window which is 4 µs long. This window is triggered by an incoming signal on the MCP. The intensity of the incoming beam is always below 500 counts per second in order to minimize the probability to have two precursor ions in the same acquisition window.

A recorded event can be the detection of a single non-dissociated cluster. In the case of the detection of fragments from a dissociated cluster, an event includes at least two detected fragments. These hits are labelled and saved by order of arrival on each channel. The overall information, event by event, is saved to keep the correlation of the time and position information of all the fragments produced in a single cluster ion dissociation.

The data, representing typically 10 Go for a set of measurements, is transferred in the IN2P3 Computing Center (CCIN2P3) and exported in the ROOT frame [11] to be analyzed. ROOT was created by the CERN for multi-parameter data analyses of particle physics and is particularly useful for our data analyses.

6) *Validation of the reconstructed positions*

The accurate reconstruction of the particle impact position can be checked by using two quantities called S_x and S_y as:

$$S_x = t_{DLA_1} + t_{DLA_2} - 2t_{MCP} \tag{15}$$

$$S_y = t_{DLA_3} + t_{DLA_4} - 2t_{MCP} \tag{16}$$

S_x and S_y are expected to be constant [3]. Figure 59 (b) shows a plot of S_x as a function of S_y and their projection on each axes. We observe a main zone, with more than 99% of the events situated between 11 ns and 12.5 ns for S_x and 9 ns and 11 ns for S_y. This area corresponds to event with a well reconstructed impact position on the detector. A few events are out of this zone, they are events with a bad reconstructed impact position on the detector. The amplitude of one of the two signals may have been lower than the threshold of the discriminator and so this signal is missing. Figure 59 (a) an example when a signal on DLA 1 was not saved. The program will then use the second hit time and the position will be wrongly reconstructed. We will cut all these events and select only the 99% of events in the dense area which are inside the black circle drawn in Figure 59 in all analyses of this work.

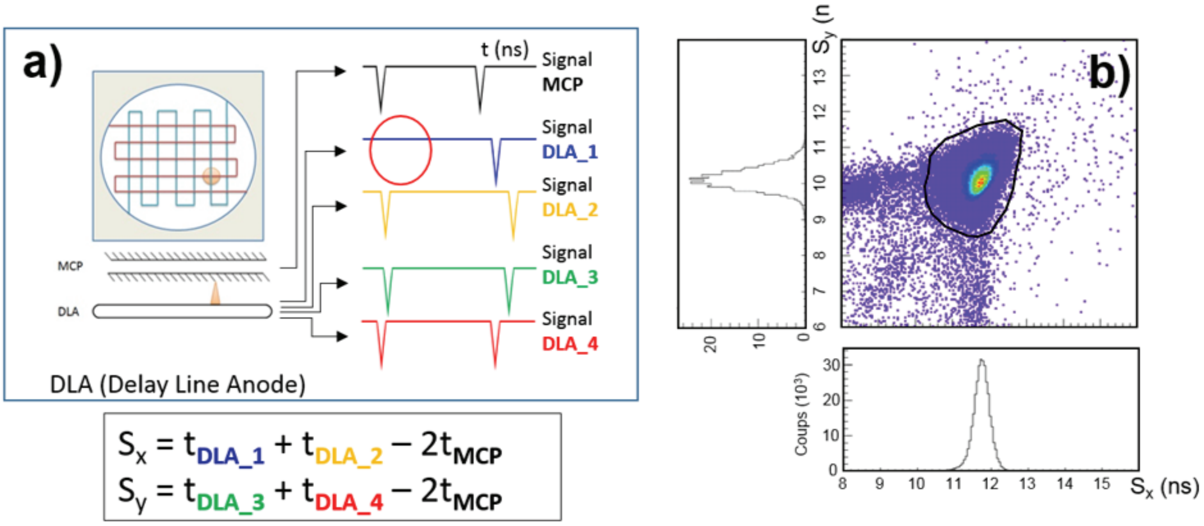

Figure 59: Validation of the impact position reconstruction on the detector with in (a), a scheme of the DLA detector and in (b) a plot of S_x as a function of S_y. (from [3])

7) *The radial distribution*

Figure 60 (a) shows a 2D pictures of the impact distribution of the 8 keV-$PyrH^+(H_2O)_4$ incident beam in the x-y space. Figure 60 (b) plots the impact distribution of the evaporated water molecule after collision. Here, the four dissociation channels are included (selected events: 200 < Δt < 410 ns). It is clear that the evaporated molecule impact distribution is wider than the incident beam. After collision, the deposited energy is leading to the incident cluster ion dissociation. The total kinetic energy released (KER), i.e., taken by each fragment, is partitioned because of the momentum conservation. Thus the evaporated molecule acquires an additional velocity randomly oriented in the center-of-mass reference frame (CMF) of the parent droplet. For the evaporated molecule, the additional velocity in the CMF leads to a transverse velocity component in the laboratory reference frame and consequently to a change in the impact position in the detection plane. The lack of events in the bottom right of the impact distribution (Figure 60 (b)) is due to damage on the detector resulting from previous experiment. The full quarter can be removed without modifying the data analyses [3].

Furthermore, both impact distributions exhibit a clear radial symmetry. After determination of the center of the impact distribution, the radius of the impact distribution, R, is sufficient to characterize the entire distribution. Thus, the 2D distribution can be restricted to a 1D distribution. Figure 60 (c) displays the function of the distribution of the impact, f(R), as the function of R the distance between the impact point and the center of the distribution. The red line is the 1D impact distribution for the evaporation of water molecules from $\mathrm{PyrH^+(H_2O)_4}$ (4 channels included) $_{\text{and}}$ the black line is the distribution of the $\mathrm{PyrH^+(H_2O)_4}$ beam. The incident beam width distribution is much narrower, by about a factor of 7.

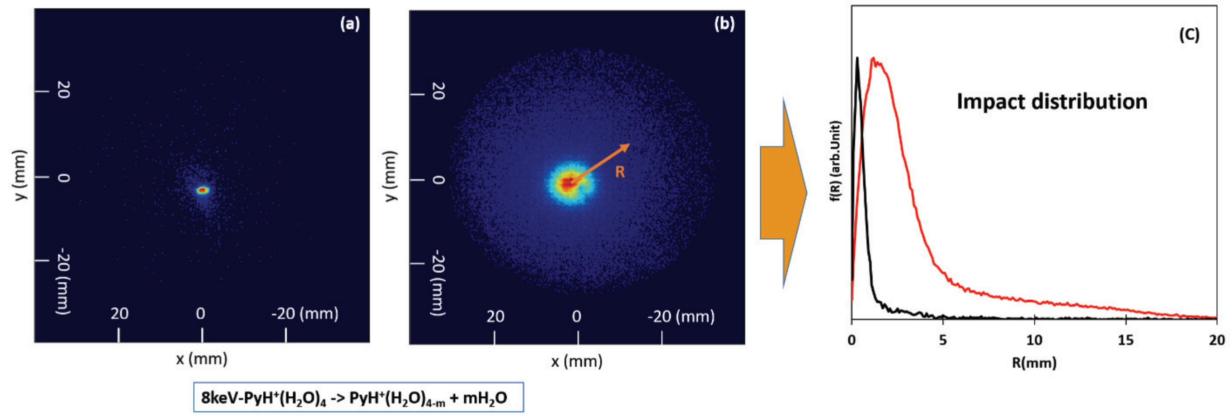

Figure 60: 2D impact distribution of (a) the incident protonated water cluster ion beam, i.e., 8keV-$\mathrm{PyrH^+(H_2O)_4}$, and (b) the evaporated water molecules, including all dissociation channels for the evaporation of water from $\mathrm{PyrH^+(H_2O)_4}$. (C) is the corresponding impact distribution: f(R), of the incident beam (black curve) and the evaporated water molecules (red curve) plotted as a function of the distance R between the impact point and the center of the distribution.

Determining the most accurately possible the center of the distributions is the prerequisite for the definition of R, and to plot the 1D impact distribution. To control the position of this center and the radial symmetry of the impact distribution, we plotted in Figure 61, the radial distribution for the evaporation of one molecule from $\mathrm{PyrH^+(H_2O)_4}$ from a quarter of the total 2D distribution. As it is shown any of the quarters of the total 2D distribution (black, red and blue) provides the same R distribution. All the distributions have the same shape with a low velocity peak from R= 0 to 4 mm with a maximum around 330 counts and a Full Width at Half Maximum (FWHM) of 1.6 mm, and a long tail from R= 4 mm to 20 mm (end of the detector) with the same height (maximum of around 25 counts at R=9 mm) for all distributions. Therefore, we can safely analyse our data by omitting the damaged quarter of the detector.

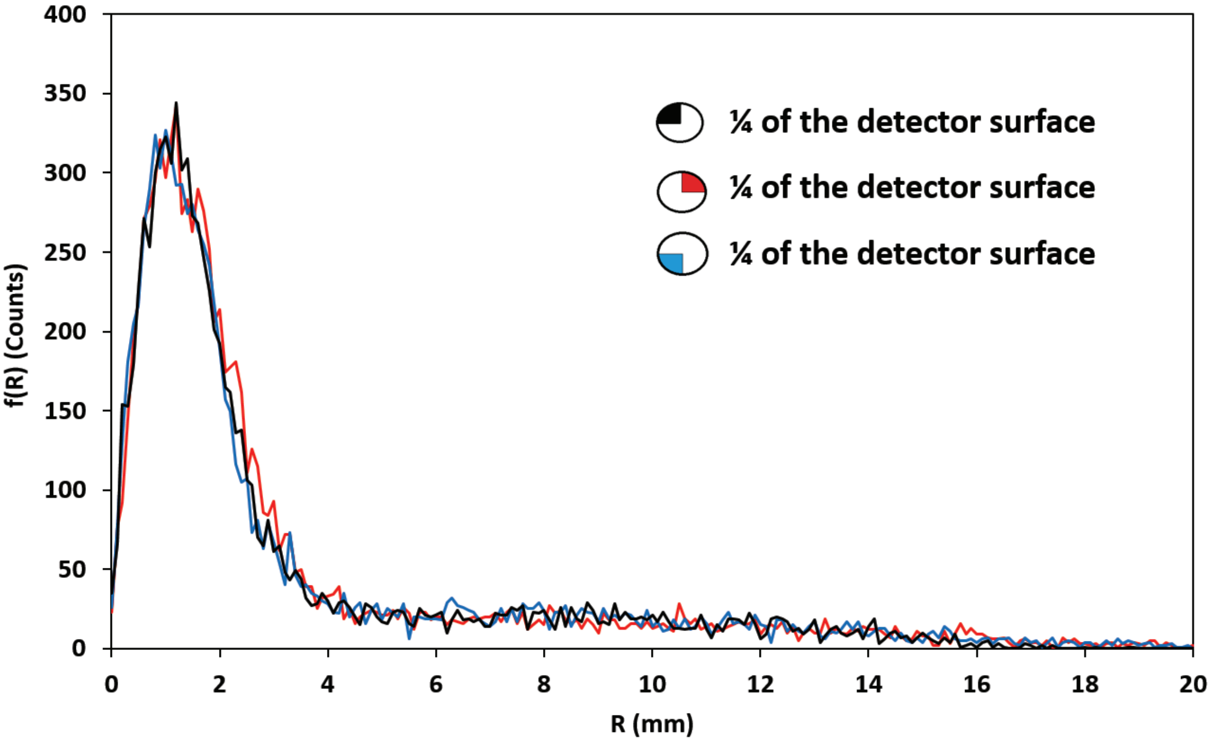

Figure 61: Impact distribution plotted by selecting different sectors of the detector for the evaporation of one molecule from $PyrH^+(H_2O)_4$.

b. From the radial distribution to the velocity distribution

Extracting the velocity distribution of the fragment from the radial distribution on the detector is an example of statistical inverse problem arising in data analysis. The unfolding technique, based on the Bayes theorem is detailed in [3] and [10]. The detailed schematic view of the computer code design is given in Figure 62. The dissociation of a cluster with a specific velocity can lead to different positions since the fragments are emitted with a random direction in the CMF of the parent cluster ion. A Monte Carlo simulation of the detection set-up gives the impact distribution calculated for a given velocity distribution. A learning matrix saves the physical constraint between the velocity distribution and the impact position.

The code works with an iterative procedure. For each iteration i, we calculate the velocity distribution $f(V_i)$ with M_i. We use the learning matrix to calculate the impact distribution $f(R_i)$ from $f(V_i)$. If $f(R_i)$ is similar to f(R), the measured radial distribution, $f(V_i)$ is a good estimation of the real distribution. If not, we change the matrix M_i accordingly to the Bayes theorem and start a new iterative step.

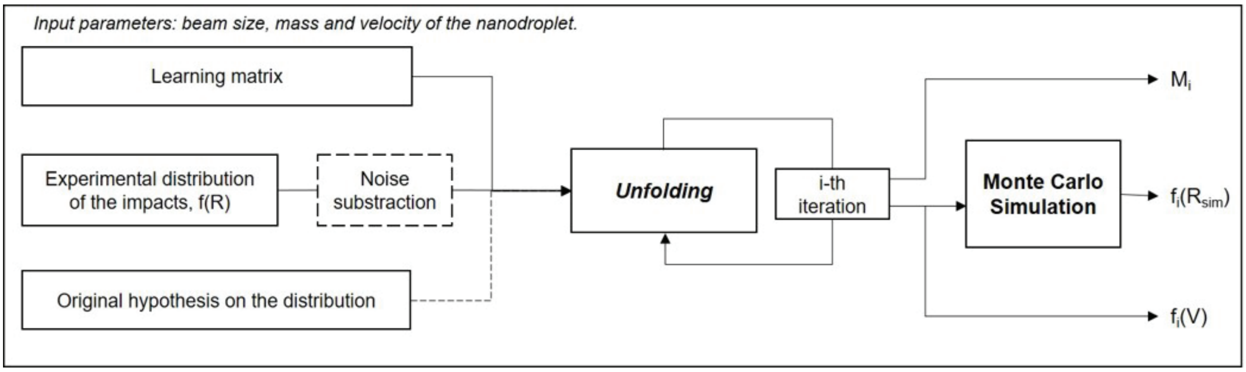

Figure 62: Schematic view of the unfolding technique allowing the determination of the velocity distributions f(V) from the impact position distributions: f_i(Rsim) corresponds to the simulated impact distribution from the velocity distribution at the ith iteration, f_i (V) corresponds to the velocity distribution at the ith iteration and M_i corresponds to the unfolding matrix at the ith iteration. (from [10])

A typical example is given in Figure 63 in the case of the evaporation of a single molecule by $PyH^+(H_2O)_4$ cluster ions. The left plot shows the measured radial impact distribution. The velocity distribution obtained after 7 iterations in the unfolding process is shown in the middle plot. The right plot shows the radial velocity distribution calculated with the Monte-Carlo simulation of the COINTOF spectrometer from the unfolded velocity distribution. The experimental radial impact distribution is superimposed for comparison. The excellent agreement observed in the right plot of Figure 63 demonstrates the efficiency of the unfolding technique.

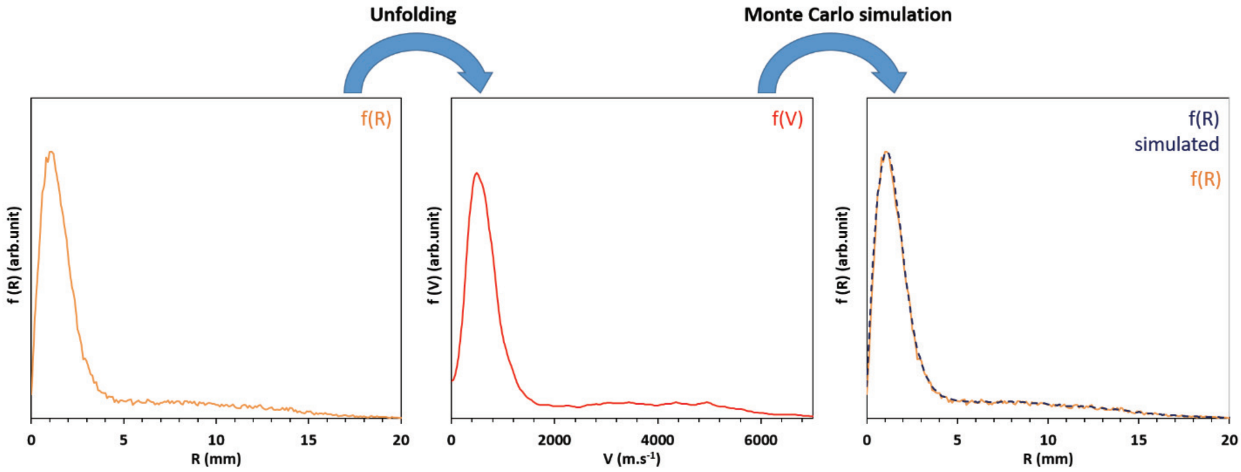

Figure 63: Validation with Monte-Carlo simulation of the velocity distribution calculated with the unfolding method.

The method described here has been used to water molecule evaporation from $PyrH^+(H_2O)_{n=1-4}$ cluster ions. For each cluster size, the entire set-up and the data acquisition system are tuned with the same settings except the magnetic field value, which is adapted to the selected cluster mass. The analyzing method has been carefully applied on each set of data: the selection of clusters evaporating a given number of water molecules, the production of the radial impact distribution of the water evaporated molecules and the unfolding step leading to the velocity distribution of the water molecules evaporated from an ensemble of clusters which have evaporated a selected number of molecule during the observation time window. For each cluster size several data sets have been produced and analyzed separately leading to similar velocity distributions.

2. Evaporation of water molecules induced by collision of 8 keV-$PyrH^+(H_2O)_{n=1-4}$ cluster ions with argon atoms

a. *Evaporation of a single water molecule*

A high velocity cluster (with V_i in the laboratory frame ranging from 1.10^5 $m.s^{-1}$ to $1.2.10^5$ $m.s^{-1}$) colliding with a single argon atom leads mainly to an ultrafast (fs) energy deposition in the cluster via electronic excitation of one of the molecules of the cluster [12] [13] [14]. This electronic excitation is rapidly relaxed into vibrational modes of the excited molecule [15].

High velocity collisions [16] [17] probe a broad range of energy deposition, in contrast to laser experiments in which the selection of a specific excited state only is possible [18] [19] [20]. The energy deposited into the system during the collision is typically in the range of 0-12 eV with around 80% below 4 eV [21]. This energy might be above the dissociation energy of the water or the pyridinium molecular ion in the cluster which ranges between 0.3 and 0.7 eV for the $PyrH^+(H_2O)_{n=1-4}$ cluster ions [22] [23]. After the fast collisional step, the out-of-equilibrium cluster is mainly observed to relax via the evaporation of one or several molecules. In this part, we will focus of the dissociation channel corresponding to the evaporation of one water molecule:

$$8keV\text{-}PyrH^+(H_2O)_n + Ar \rightarrow PyrH^+(H_2O)_{n-1} + (H_2O) + Ar$$

1) *Velocity distributions of the water molecule evaporated from $PyrH^+(H_2O)_{n=1-4}$ cluster ions*

The velocity distributions of the single evaporated molecule induced by collision of 8 keV-$PyrH^+(H_2O)_{n=1-4}$ cluster ions with argon atoms are shown in Figure 64. The measured distributions are drawn in red full line. Each part of the Figure 64 corresponds to a selected size of parent cluster ions. From the left, in Figure 64 (a), n=1: $PyrH^+(H_2O) \rightarrow PyrH^+ + (H_2O)$, in Figure 64 (b), n=2: $PyrH^+(H_2O)_2 \rightarrow PyrH^+(H_2O) + (H_2O)$, in Figure 64 (c), n=3: $PyrH^+(H_2O)_3 \rightarrow PyrH^+(H_2O)_2 + (H_2O)$ and in Figure 64 (d), n=4: $PyrH^+(H_2O)_4 \rightarrow PyrH^+(H_2O)_3 + (H_2O)$. For each n value, the velocity distribution covers a wide velocity range from 0 $m.s^{-1}$ to 8000 $m.s^{-1}$. The experimental distributions exhibit two distinct contributions: a low velocity component between 0 and 2000$m.s^{-1}$ and a high velocity component between 2000 $m.s^{-1}$ and 6000 $m.s^{-1}$. The maximum value of the peak observed in the low velocity part of the distribution is around 900 $m.s^{-1}$ for n=1 and 600 $m.s^{-1}$ for n=4. The width and the value of the maximum are decreasing with the increase of the number n of molecules in the cluster. The high velocity component ranging from 2000 and 6000 $m.s^{-1}$ has a wider distribution than the peak observed in the low velocity part of the distribution. The maximum height of the high velocity part of the distribution is about 16 times lower than the maximum height of peak at low velocity.

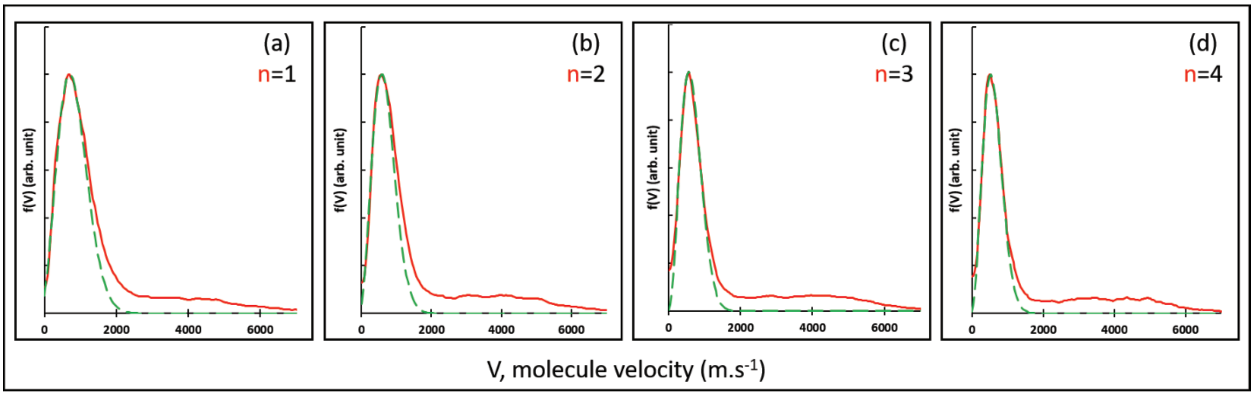

Figure 64: Evaporation of a single molecule induced by collision of 8 keV PyrH$^+$*(*H_2O*)*$_{n=1-4}$ *cluster ions with argon atoms: velocity distributions of the evaporate water molecules. Solid line: experimental data, dashed line: Maxwell-Boltzmann (MB) fit of the low velocity part of the distributions*

Such behavior is similar to the one observed in the CID experiments with protonated water cluster [24] [3]. These previous results on protonated water clusters show that the low velocity part can be fitted with a Maxwell-Boltzmann distribution. The corresponding fragmentation events are named Maxwell-Boltzmann events. For a thermalised macroscopic system, the evaporation of a water molecule follow the Maxwell-Boltzmann statistics associated with the thermal equilibrium. At the microscopic scale, the thermal equilibrium corresponds to the statistical distribution of the internal energy among all the modes of the system. In the CID experiments, the out-of-equilibrium protonated water nanodroplets are isolated into vacuum. However, the observation of a Maxwell-Boltzmann shape in the velocity distribution of the evaporated molecule evidences a pre-equilibrium step with a kind of thermalisation associated with the redistribution of the deposited energy in the vibrational modes of the entire droplet.

A high velocity contribution is also observed in the CID experiments on protonated water cluster. These events for which observed abundance do not fit with the Maxwell-Boltzmann proportion are associated with evaporation of a water molecule before energy redistribution in the droplet. These events are called non-ergodic events [24] [3].

In the present case, a Maxwell-Boltzmann function has been adjusted on the low velocity part of the distribution (green dashed lines in Figure 64). This fit can reproduce the most important part of the low velocity distribution but does not reproduce the shape of the measured low velocity peak. More precisely, in the 1500-2000 m.s^{-1} velocity region a significant contribution is observed to be out of the fit for all cluster sizes. This point will be discussed in paragraph A4). However, the Maxwell-Boltzmann fit can be used to extract a correct order of magnitude of the width and of the maximum value of the low velocity part of the distribution. Therefore, the Maxwell-Boltzmann fit will be used in the two following paragraphs in order to compare quantitatively the evaporation of a single molecule from PyH$^+$(H_2O) and H_3O^+(H_2O) cluster ions.

2) *Comparison of the experimental results for the evaporation of a single molecule from PyrH*$^+$*(*H_2O*)*$_n$ *cluster ions and* H_3O^+*(*H_2O*)*$_n$*. cluster ions*

We focus here on the low velocity part of the velocity distribution. To describe the behavior of the distribution with the size of the cluster n, we extract the average value and the width of the distribution via the Maxwell-Boltzmann fit. Figure 65 shows the evolution of the average velocity <V> (upper part) and the width of the distribution ΔV (lower part) of the low velocity part of the distribution for the evaporation of a single molecule as a function of the size of the parent cluster: n. The protonated pyridine water cluster experimental results are in red, the results for protonated water cluster are reproduced in black for comparison [3].

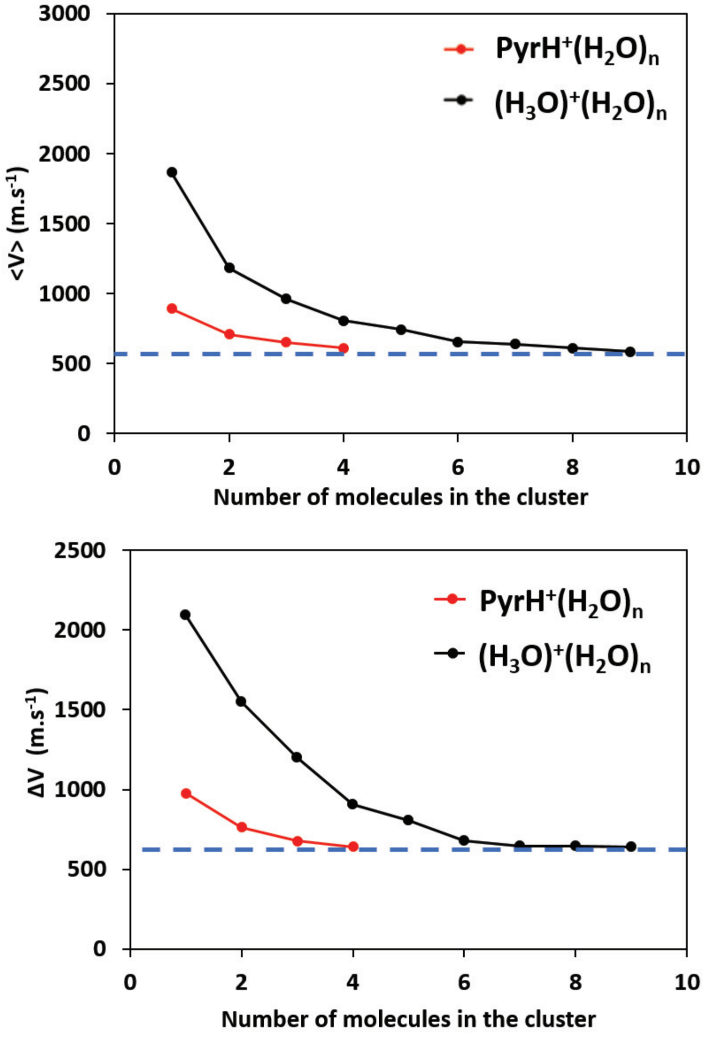

Figure 65: Low velocity part of the experimental velocity distribution of the evaporated water molecule from $PyrH^+(H_2O)_n$ cluster ions (red) and $H_3O^+(H_2O)_n$. cluster ions (black) [24] [3]. Upper part: average velocity: <V>, lower part: Full Width at Half Maximum: ΔV.

For both parent clusters, the average value and the width for the low part of the velocity distribution are decreasing with n and tend to 580 m.s^{-1} and 640 m.s^{-1} respectively at high n. The blue dashed line shows the common limit. For protonated pyridine water cluster, the average value of the distribution ranges from 893 m.s^{-1} for $PyrH^+(H_2O)$ to 612 m.s^{-1} for $PyrH^+(H_2O)_4$. For protonated water, the average value of the distribution ranges from 1865 m.s^{-1} for $H_3O^+(H_2O)$ to 585 m.s^{-1} for $H_3O^+(H_2O)_9$ with value between 655 m.s^{-1} and 611 m.s^{-1} for n=7-9. The average value for the protonated water cluster decreases more slowly than for protonated pyridine water cluster. Protonated pyridine water cluster average value seems to saturate from n=2, and from n=5 for protonated water cluster.

Regarding the width of the distribution, the tendency to decrease with n and to reach a limit is similar than for <V>. For protonated pyridine water cluster, ΔV ranges from 975 m.s-^{1} for $PyrH^+(H_2O)$ to 640 m.s^{-1} for $PyrH^+(H_2O)_4$. For protonated water, the width of the distribution ranges from 2095 m.s^{-1} for $H_3O^+(H_2O)$ to 640 m.s^{-1} for $H_3O^+(H_2O)_9$.

The average value and the width of the distribution for the protonated water cluster decrease more slowly than for protonated pyridine water cluster. Protonated pyridine water cluster seems to saturate from n=2, and protonated water cluster from n=5.

3) *Characteristic of the low velocity part of the distribution and binding energy of the water molecule*

The velocity of the evaporated molecule velocity is associated to a kinetic energy release (KER) resulting from the dissociation of the molecular cluster ion. According to conservation laws, both fragments take a part of the total KER. The KER distribution was previously measured for the charged fragment in MIKE (Mass-Analyzed Ion Kinetic Energy) experiments [25]. The KER distribution can also be deduced from the velocity distributions measured for the neutral fragment.

The KER determination can provide information about ion structures, reaction energetics and dynamics [26] [27]. The KER distributions measured with atomic and molecular clusters were often analyzed in the frame of a statistical model assuming the statistical equilibrium. Klots proposed the evaporative ensemble description in order to formulate the link between KER and binding energy of the cluster [28] [29]. The evaporative model from Klots is a convenient way to calculate the cluster binding energy and was used by Hansen to calculate the activation energies for evaporation from protonated and deprotonated clusters from mass spectroscopy data [30].

i. Kinetic energy release: KER

The velocity of the evaporated molecule is directly related to the Kinetic Energy Release (KER) during the dissociation. In our analyses, KER will refer to the total kinetic energy release associated with the evaporation of a single water molecule, i.e. the kinetic energy of the daughter ion plus the kinetic energy of the water molecule. Using the momentum and energy conservation laws it is possible to determine the average value of the total KER from the average velocity of the evaporated molecule:

$$< KER > \; = \frac{1}{2} m_{H_2O} < V^2 > \left(\frac{m_{H_2O}}{m_{ion}} + 1 \right) \tag{17}$$

with: $< V^2 > = \frac{3\pi}{8} < V >^2$ *for a Maxwell -Boltzmann distribution.*

The calculated values are presented in Figure 66 (red line) as a function of the cluster size: n.

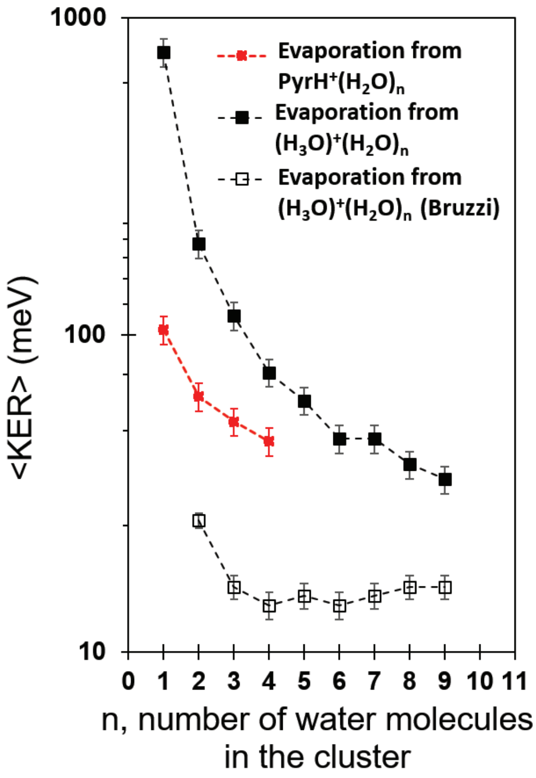

Figure 66: Mean value of the total Kinetic Energy Release (KER) deduced from the Maxwell-Boltzmann fit of the low velocity part of the velocity distributions measured for $PyrH^+(H_2O)_{n=1-4}$ *cluster ions (red). For comparison results for* $H_3O^+(H_2O)_n$ *cluster ions are shown in black : with the same set-up [3] and in gray by Bruzzie et al. [31].*

We observe that the KER is decreasing with n and ranges from 104 meV for $PyrH^+(H_2O)$ to 46 meV for $PyrH^+(H_2O)_4$. For comparison, the KER of protonated water cluster measured in the same condition is shown in black. The distribution follows the same behaviour and decrease with n, ranging from 780 meV for $H_3O^+(H_2O)$ to 35meV for $H_3O^+(H_2O)_9$.

The last serie of measurements reported in Figure 66 in open black square is the KER distribution measured by Bruzzie et al [31] for the evaporation of a molecule from metastable cluster $H_3O^+(H_2O)_{n=2-29}$. The KER shows a low dependence with n. The KER is constant around 16-18 meV except for n=3 for which the KER is 26 meV. Differently from our experiment, they focused on the decay of metastable cluster ions. In their experiment, the analysis of the charged fragment energy takes place at much longer time than in our experiment. The KER values measured for such metastable decays are much lower KER values.

The KER values measured in our experiment could be thought as the highest value that can be observed for the evaporation of a single molecule. In our experiment, the amount of energy deposited is broad and can be above the amount of energy necessary to evaporate more than one molecule. Therefore, the shape of the velocity distribution is not limited by the energy deposition but is resulting from the out-of-equilibrium dynamics: to stay in the measured distribution, the out-of-equilibrium droplets must have evaporated a molecule during the observation time window but not more than one. When increasing the amount of energy deposited there is a competition between evaporation of a molecule with a high velocity and evaporation of two molecules. This competition is resulting from the out of dynamics in the droplet, typically from the ability to exchange energy between the intramolecular and intermolecular modes.

ii. Correlation between the characteristics of the low velocity part of the distribution and the binding energy of the cluster

Assuming the fit of the low velocity part of the distribution with a Maxwell-Boltzmann distribution, the width of the distribution can be related to an equivalent temperature related to the translational degree of freedom.

$$k_b T = \frac{< V >^2 \, \pi m}{8} \qquad 18$$

With <V>: the average velocity of the Maxwell-Boltzmann distribution, k_b the Boltzmann constant and m, the reduced mass of the evaporated molecule.

A theoretical description using a Maxwell-Boltzmann thermalisation initially developed by Klots characterizes the evaporation process and is involving in particular the number of degrees of freedom and the internal energy. The theoretical model gives a relation between the width of the distribution of the velocity represented by k_bT and the binding energy of the evaporated molecule: Ed. This formula which relates the binding energy, Ed and k_bT includes different parameters such as the Gspann factor. According to literature, different values of the Gspann factor have been used in order to analyze KER measurements for atomic or molecular clusters.

Taking into account that binding energy can be obtained by quantum chemistry calculation with a sufficient accuracy for our purpose, we propose to draw a correlation plot between the available binding energy values (calculated or measured) and the K_bT values measured from the experimental velocity distributions according to equation 6.

The correlation plot is shown in Figure 67 for protonated pyridine water cluster and protonated water cluster. Each point corresponds to a certain number of molecules in the cluster. Red points correspond to protonated pyridine water cluster and blue corresponds to for protonated water cluster [3]. Figure 67 (a) shows the correlation between the measured k_bT values and the calculated binding energies (F. Calvo and [32] [33] [34] [35] [36] [37]). Figure 67 (b) shows the correlation between the measured k_bT values and the measured binding energy ([38] [39] [40] [41] [42] [43] [44] [45] [46] [47] [22] [48]). The y-axis is the value of the binding energy in electron volt. The x-axis gives at the bottom gives the k_bT value in electron volt and at the top the temperature in kelvin.

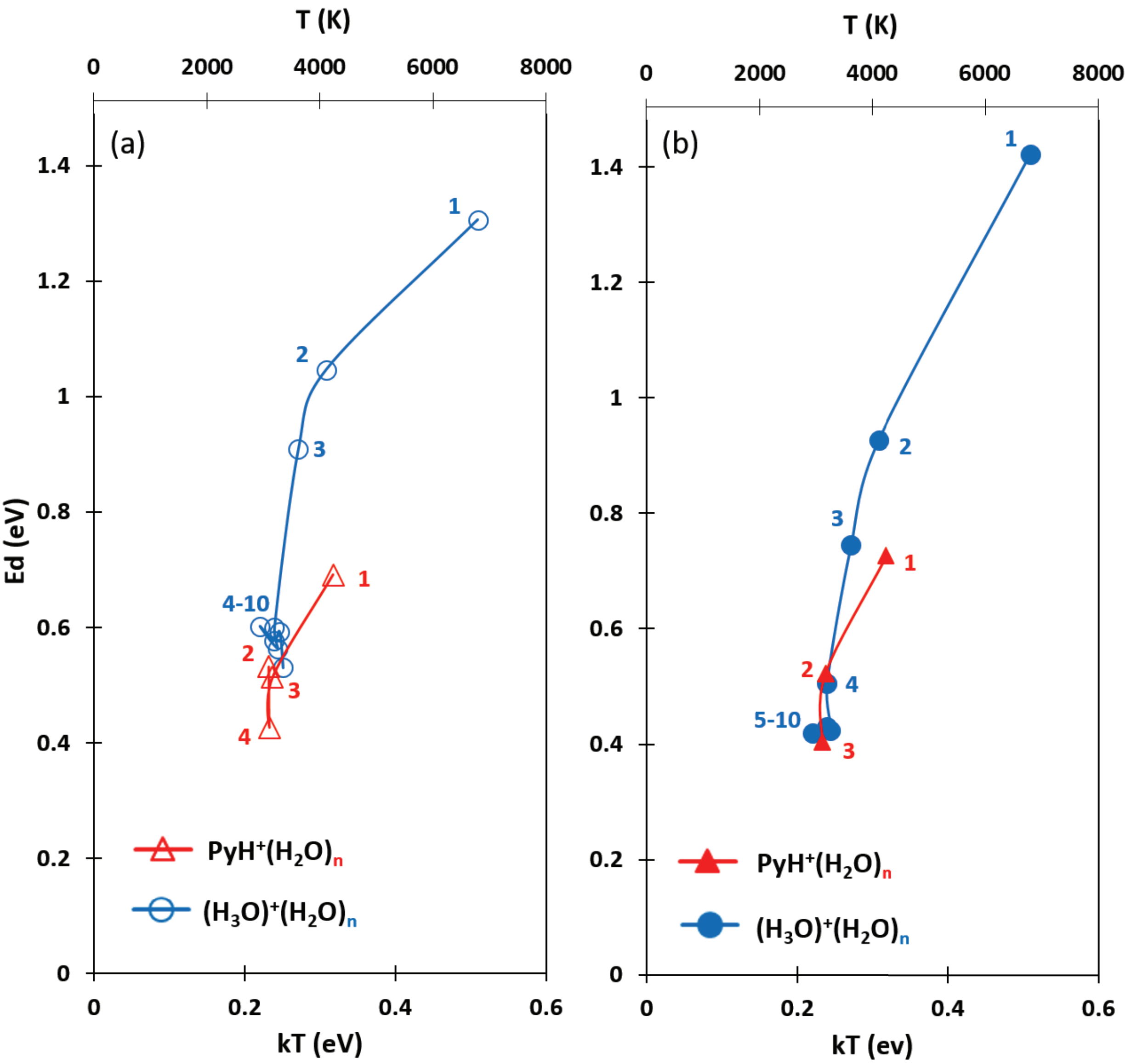

Figure 67: Correlation between k_bT values deduced from the average value of the Maxwell-Boltzmann fit of the distributions and the binding energy for protonated pyridine water cluster: $PyH^+(H_2O)_n$ in red and for protonated water cluster: $(H_3O)^+(H_2O)_n$ in blue. The binding energy come from the literature, calculated in (a) [32] [33] [34] [35] [23] [22]and measured in (b) [38] [39] [40] [41] [42] [43] [44] [45] [46] [47] [22] [48].

The K_bT values are decreasing with n as seen before for the width of the distribution. They are ranging from 0.232 eV for $PyH^+(H_2O)_4$ to 0.318 eV for $PyH^+(H_2O)$ and from 0.25 eV for $(H_3O)^+(H_2O)_9$ to 0.51 for $(H_3O)^+(H_2O)$. The order of magnitude of the corresponding temperature, typically 2000 K-6000 k reminds the out-of-equilibrium character of evaporative ensemble that we have selected.

The binding energy of protonated pyridine water cluster has been measured by Davidson et al. [47], Ibrahim et al. [37] and Meot-Ner et al. [48]. They are deduced from the measurement of equilibrium constants in a drift cell. In a drift region, the clusters collide with a buffer gas and clusters with different n reach at a given pressure and field intensity a statistical equilibrium, which determines the binding energy of the cluster. For protonated pyridine water cluster, the experimental dissociation energy is decreasing from 0.67 eV for $PyH^+(H_2O)$, 0.45 eV for $PyH^+(H_2O)_2$ to 0.33 eV for $PyH^+(H_2O)_3$.

The protonated pyridine water cluster binding energies are calculated with the density functional theory (DFT) by Florent Calvo from the Laboratoire Interdisciplinaire de Physique (LIPhy) de Grenoble (DFT/M06-2X/aug-cc-PVTZ.). The values are in good agreement with previous calculation done by Ryding et al. [36] and Ibrahim et al. [37]. The average theoretical values are decreasing from 0.7 eV for $PyH^+(H_2O)$, to 0.52 eV for n>1. We notice that the binding energy is almost constant from n≥2.

A number of studies on the binding energies of small protonated water clusters are available. Wroblewski et al. [38], Magnera et al [39] and Honma et al. [40] measured the binding energy of protonated water cluster using drift cell and the measurement of the equilibrium constants. Wang et al. [41] measured the protonated water dissociation energy in an ion trap by measuring the dissociation rates at various trap temperatures associated with DFT calculation to calculate their vibrational frequencies. Cunningham et al. [42], Kebarle et al. [43] , Meot-Ner et al [44], [45] and Lau et al. [46] measured the protonated water cluster binding energy in a pulsed electron beam high pressure mass spectrometer by measuring the gas temperature dependence of the equilibrium rate constants. For protonated water cluster, the average experimental dissociation energy is decreasing from 1.4 eV for $(H_3O)^+(H_2O)$ to 0.42 eV for n>4. The binding energy is stabilized from n=4.

The protonated water cluster binding energies were calculated with Density Functional Theory (DFT) and with ab initio calculation by Douberly et al. [32], Natarajan et al. [33] and Hodges et al. [35], [34]. The theoretical values are decreasing from 1.3 eV for $(H_3O)^+(H_2O)$ to 0.54 eV for n>7. The binding energy is stabilized from n=7.

For both protonated pyridine water cluster and protonated water cluster, the calculated dissociation energy is always higher than the experimental dissociation energy. It is probably because in experiments, the clusters are not totally cool down to the ground state and they have some internal energy: less energy is needed to dissociate them. We note as well than a single water molecule is enough to stabilize the protonated pyridine water cluster while n=4 in experiment and n=7 in theory are needed to stabilize the dissociation energy of protonated water cluster.

The fluctuation of the dissociation energy with the number of water molecule in the cluster comes from size or structure effects.

In the correlation plot, Figure 67, we observe that both the binding energy and the kT values are decreasing with the decrease of the number of molecules. The limit for high n values appears to be the same for protonated pyridine water cluster and protonated water cluster and this can be related to the fact that the role of the proton will decrease rapidly with the number of water molecules. With the decrease of n we observe first a decrease of the binding energy without significant change for the k_bT value. For the smallest values of n, both binding energy and k_bT values are increased. The points corresponding to n=1 (only one water molecule) appear to be shifted on the right. We notice that in the case n=1 we have only two molecules linked by a proton located in between.

4) *Comparison of the measured distributions with statistical molecular dynamic simulation*

This experimental results are supported by statistical molecular dynamic simulation (SMD) performed by Florent Calvo. The SMD calculations provide new insights in the dynamical properties of ensembles of molecules: interactions and dynamics at microscopic scale. The challenge is to able to model the interactions between molecules, their bonds, forces and all constraints over sufficient time in order to get results which can be compared with the experimental data. Similar calculations were previously achieved for protonated water cluster [49] [24].

The calculations were made in three steps cluster per cluster:

- Each $PyrH^+(H_2O)_{n=1-10}$ cluster is initially taken from a canonical ensemble of clusters set at 100 K.

- An excitation energy randomly selected from a flat distribution ranging from 2 eV to 8 eV is converted into atomic kinetic energy.

- After one nanosecond, the different possible fragments are selected with a distance criterium and their kinetic energy, so their velocity, are calculated.

Three types of excitations are separately made: global excitation, local excitation on pyridine molecule and local excitation on one water molecule. The global excitation means that the energy is distributed among all degrees of freedom of the molecules. In local excitation, the energy is precisely deposited either on a single water molecule or on the pyridine molecule.

In the simulation, time increases by step of 0.25 fs, the position and velocity of each atom are calculated by resolution of the Newton movement equation and the calculated interaction force come from a pseudo empirical potential.

The simulations are performed with a flexible and polarizable anharmonic potential [50] [51] which describes the inter and intra molecular interaction. The water or pyridine molecule dissociation is not taken into account in the simulation as it is a different process than evaporation. The intermolecular proton transfer is neglected, the proton is bound to the pyridine molecule. Simulations with other potential in which the proton is free of moving as the reactive OSS2 potential [52] were performed and gave similar velocity distribution [24] [3].

The excited cluster can evaporate through several consecutive evaporations. The daughter ion becomes the parent and has the possibility to evaporate another molecule. The molecule is considered as evaporated with a distance criterion. The event trajectory stopped when the daughter energy is lower than the dissociation energy, or if the simulation reached the time limit, i.e., one nanosecond after energy deposition. As in the experiment, events are sorted depending of the number of evaporated molecules at the detection time. A number of 10^5 independent trajectories were generated for each cluster size and the resulting velocity distribution calculated can be directly compared with the experimental result.

The result of the calculations is given as a table in Figure 68. The table summarizes all results on the evaporation of a single water molecule. Each line is a different cluster size: n. The first column is the experimental data (same as Figure 64) with in red: the data, in green dashed line: the Maxwell-Boltzmann fit of the low velocity part and in dashed orange line: a Gaussian fit of the non-ergodic event. The second column is the theory for global excitation. In dark blue full line is the result of the SMD calculation and in dashed green line is the Maxwell-Boltzmann fit of the distribution. The third column is the result of the theory for the local excitation on pyridine. In full blue line is the result of the SMD calculation and in dashed green line is the Maxwell-Boltzmann distribution. The fourth and last column is the result of the theory for local excitation on a water molecule. In full light blue is the result of the SMD calculation, in green the Maxwell-Boltzmann fit of the low velocity part of the distribution and in orange a Gaussian fit of the non-ergodic event. In each graph, the x-axis represents the velocity in $m.s^{-1}$ and the y axis is the velocity intensity in arbitrary unit.

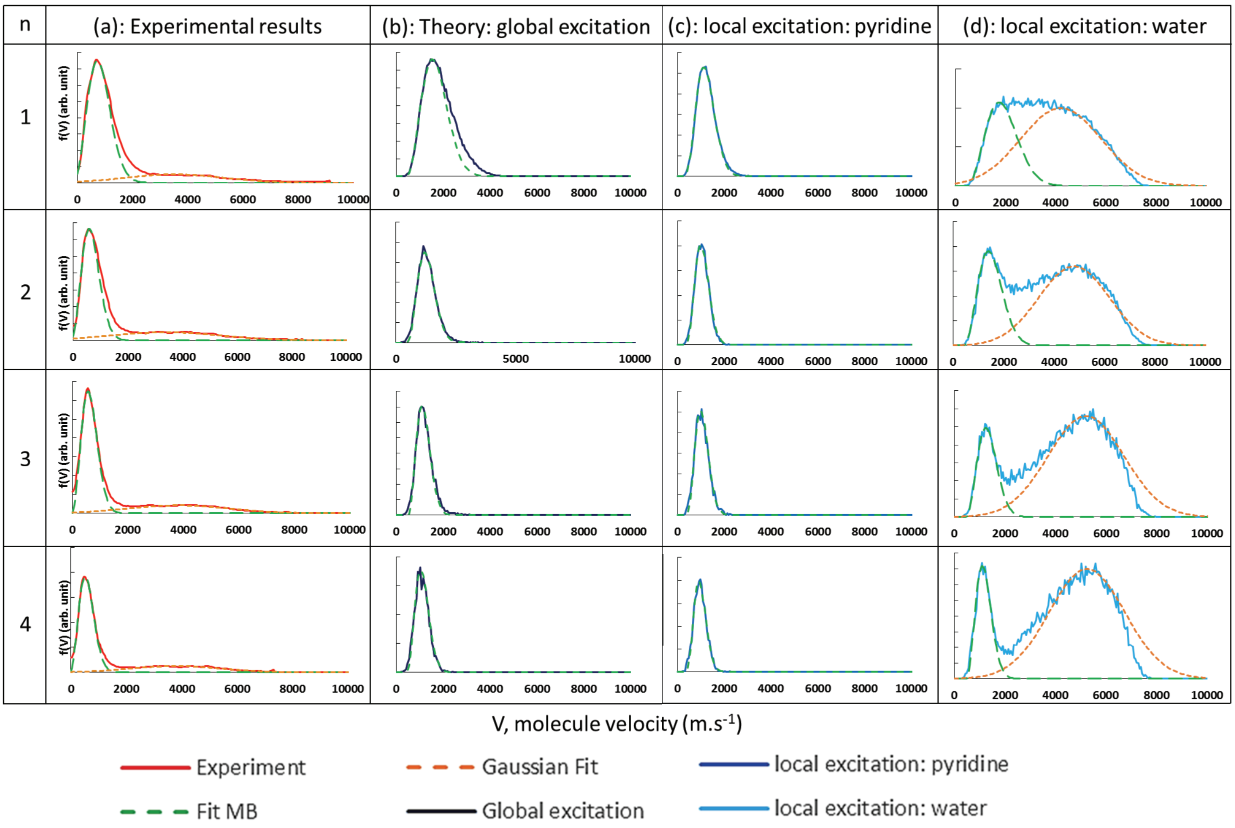

Figure 68: Evaporation of a single water molecule from $PyrH^{+}(H_2O)_{n=1\text{-}4}$ *cluster ions: the experimental velocity distributions (a) and the calculated ones : (b) : SMD – global excitation, (c) SMD – local excitation on a pyridine molecule, (d) SMD – local excitation on a water molecule. The dashed green curve corresponds to a Maxwell-Boltzmann fit of the low velocity part of the distributions, the dashed orange curve to a Gaussian fit of the non-ergodic events. X-axis is the molecule velocity in* $m.s^{-1}$ *for each plot.*

At very low velocities, i.e., below 1500 $m.s^{-1}$, each velocity distribution is accurately fitted by a Maxwell-Boltzmann distribution. In the global excitation and in the local excitation of a pyridine molecule, there is no non-ergodic event, that is, contribution at higher velocities. The behavior of the distribution for the maximum value and the width of the distribution with the size of the cluster are similar to the experimental distribution: for each type of excitation, the width and the average value of the distribution decrease with n. In the higher part of the low velocity part, between 1500 and 2000 $m.s^{-1}$, the experimental data and the simulation for global excitation with n=1 show some events out of the Maxwell-Boltzmann fit.

The local excitation on water exhibits an important component of non-ergodic events. The heights of the Maxwell-Boltzmann event distribution and of the non-ergodic Gaussian fit event are similar but the width of the non-ergodic distribution is larger. In the simulation only the local excitation on water has some non-ergodic event. For n=1, there are no significant distinction between Maxwell-Boltzmann event and non-ergodic event. The Maxwell-Boltzmann fit was adjusted on the low velocity part of the distribution.

5) *Low velocity part of the velocity distribution of the evaporated water molecule from PyrH$^+$(H$_2$O)$_n$ cluster ions. Comparison of the experimental data with the statistical molecular dynamics (SMD) calculations*

In the framework of the evaporation of a single molecule and to hold on the study of the low velocity part, we compare now the average value and the width of the velocity distribution resulting from the experiment and from the SMD calculation. Figure 69 shows the average value of the low velocity part of the velocity distribution: <V> (top part) and the width of the distribution: ΔV (bottom part) as a function of the cluster size: n. The experimental data (in full red line, with n=1-4) is compared with the result of the SMD calculation (n=1-10) with: in dark blue: the theory for global excitation, blue: the local excitation on pyridine molecule and cyan: local excitation on a water molecule.

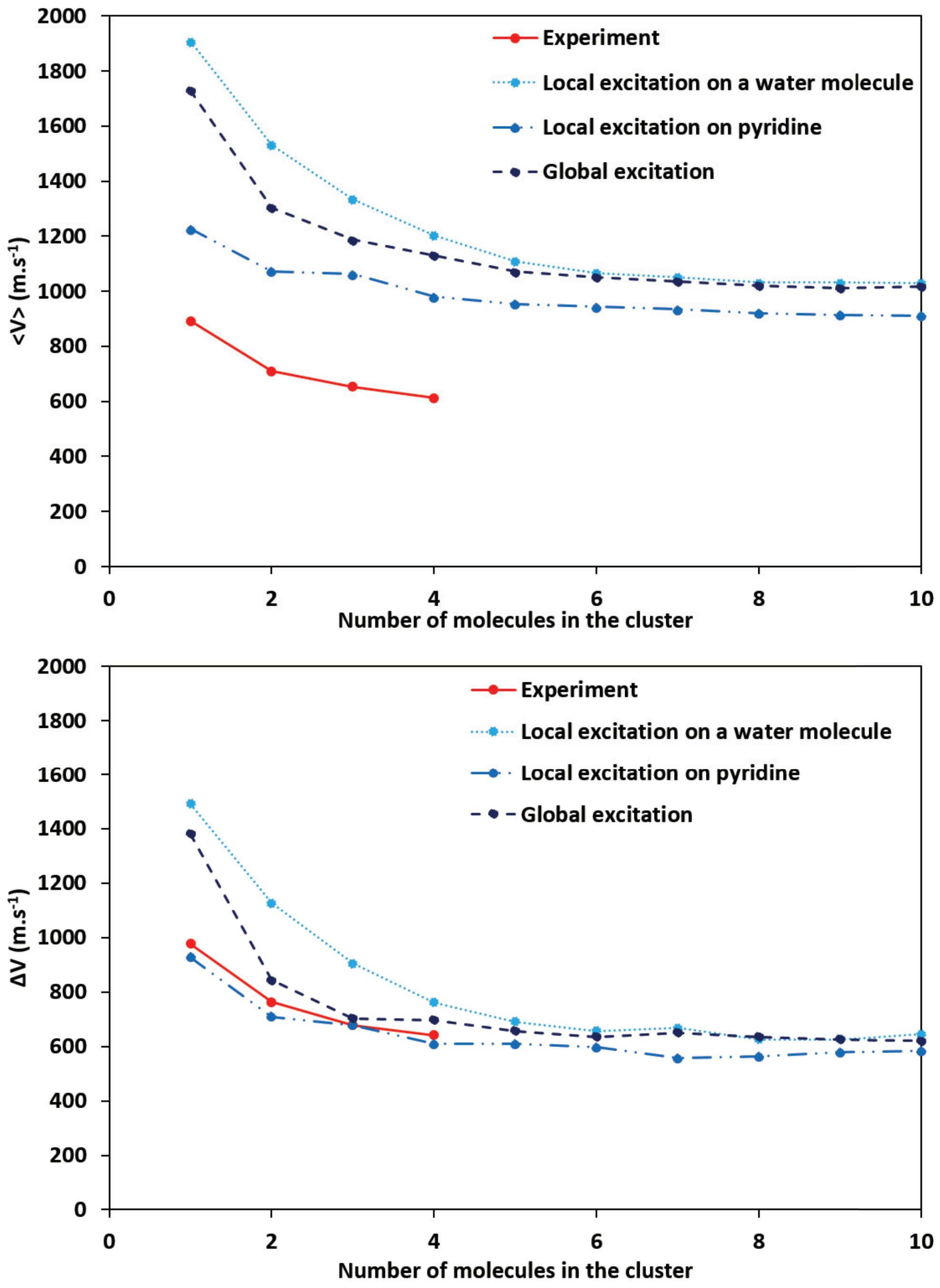

Figure 69: Low velocity part of the velocity distribution of the evaporated water molecule from PyrH$^+$(H$_2$O)$_{n=1-4}$ cluster ions. Comparison of the experimental data (red) with the values obtained from statistical molecular dynamics calculations with in dark blue: global excitation, in blue: local excitation on a pyridine molecule and in cyan: local excitation on a water molecule. Upper part: average velocity: <V>, lower part: Full Width at Half Maximum: ΔV.

The average value and the width of the distribution are both decreasing with the cluster size n for each type of excitation and are saturating. The molecule is evaporated with lower and lower velocities and with a velocity range more and more restrain.

The SMD calculations of the average value of the velocity distribution seem to behave similarly to the experimental data. Nevertheless, the SMD calculations are always shifted to higher velocity. The theory with local excitation on water is the highest with an average value ranging from 1907 m.s^{-1} for

$PyrH^+(H_2O)$ to 1031 m.s^{-1} for $PyrH^+(H_2O)_{n=8\text{-}10}$. For the global excitation, the average value range from 1729 m.s^{-1} for $PyrH^+(H_2O)$ to 1020 m.s^{-1} for $PyrH^+(H_2O)_{n=8\text{-}10}$. The local excitation on pyridine is the lowest with an average value ranging from 1230 m.s^{-1} for $PyrH^+(H_2O)$ to 915 m.s^{-1} for $PyrH^+(H_2O)_{n=8\text{-}10}$.

To compare the experimental result to the SMD calculation for the average value of the distribution, we can add a global shift to the calculation. Such global shift was already observed in the study of the protonated water cluster. It can be interpreted as a difference in the observation window between the calculation (1 ns) and the experiment: (~ 200 ns). To fit the local excitation on pyridine with the experimental result we have to add a shift of -350 m.s^{-1}, to fit the global excitation: -600 m.s^{-1} and for the local excitation on water: -680 m.s^{-1}. In the previous result for the study of protonated water cluster a shift of -740 m.s^{-1} was added to the SMD calculation to fit the experimental data [49] [24].

For the width of the distribution, the SMD calculated distributions are in good agreement with the experimental values. The experimental values sit above the local excitation on a pyridine molecule and below both the global and the local excitations on a water molecule. The theory with local excitation on water ranges from 1490 m.s^{-1} for $PyrH^+(H_2O)$ to around 640 m.s^{-1} for $PyrH^+(H_2O)_{n=6\text{-}10}$. For the global excitation, the average value range from 1380 m.s^{-1} for $PyrH^+(H_2O)$ to 640 m.s^{-1} for $PyrH^+(H_2O)_{n=5\text{-}10}$. The local excitation on pyridine is the lowest with an average value ranging from 930 m.s^{-1} for $PyrH^+(H_2O)$ to 570 m.s^{-1} for $PyrH^+(H_2O)_{n=7\text{-}10}$.

For the average value and the width of the distribution at high n, the theory on local excitation on a water molecule and the theory for global excitation reach the same limit at 1020-1030 m.s^{-1} for <V> and 640 m.s^{-1} for ΔV. The local excitation on pyridine saturate at lower value: 915 m.s^{-1} for <V> and 570 m.s^{-1} for ΔV.

The local excitation on pyridine gives a lower average value of the evaporated molecule. The pyridine cluster does not produce a good energy transfer to the water molecule: the energy is stored in the covalent bond of pyridine and only a small amount of energy is available for the water molecule to evaporate.

6) *Comparison of the calculated distribution (SMD) for the evaporation of a single molecule from $PyrH^+(H_2O)_n$ cluster ions and $H_3O^+(H_2O)_n$ cluster ions (low velocity part)*

As we discussed with Figure 65, the experimental average value and the width of the distributions for protonated pyridine water cluster and protonated water cluster are similar: both decrease with n and tend to a limit at high values of n. The protonated water cluster is above the protonated pyridine water cluster by around 800 $m.s^{-1}$ for n=1 and 500 $m.s^{-1}$ for n=2 for the average value, and by 1000 $m.s^{-1}$ for n=1 and 800 $m.s^{-1}$ for n=2 for the width of the distribution.

Figure 70 shows a comparison between protonated water cluster in green and protonated pyridine water cluster in blue. The average value: <V> (top part) and the width of the low velocity part of the SMD distributions: ΔV (bottom part) are plotted as a function of the cluster size: n. The SMD calculations are made in the same condition for protonated pyridine water cluster and for protonated water cluster. The dark green long dashed line corresponds to calculation with global excitation. The green small dotted lines correspond to local excitation i.e. excitation of a water molecule of the cluster. For protonated pyridine water cluster the dark blue line corresponds to the global excitation. For local excitations two cases have to be considered: the excitation of pyridinium molecular ion (in blue) and excitation of a water molecule (in cyan).

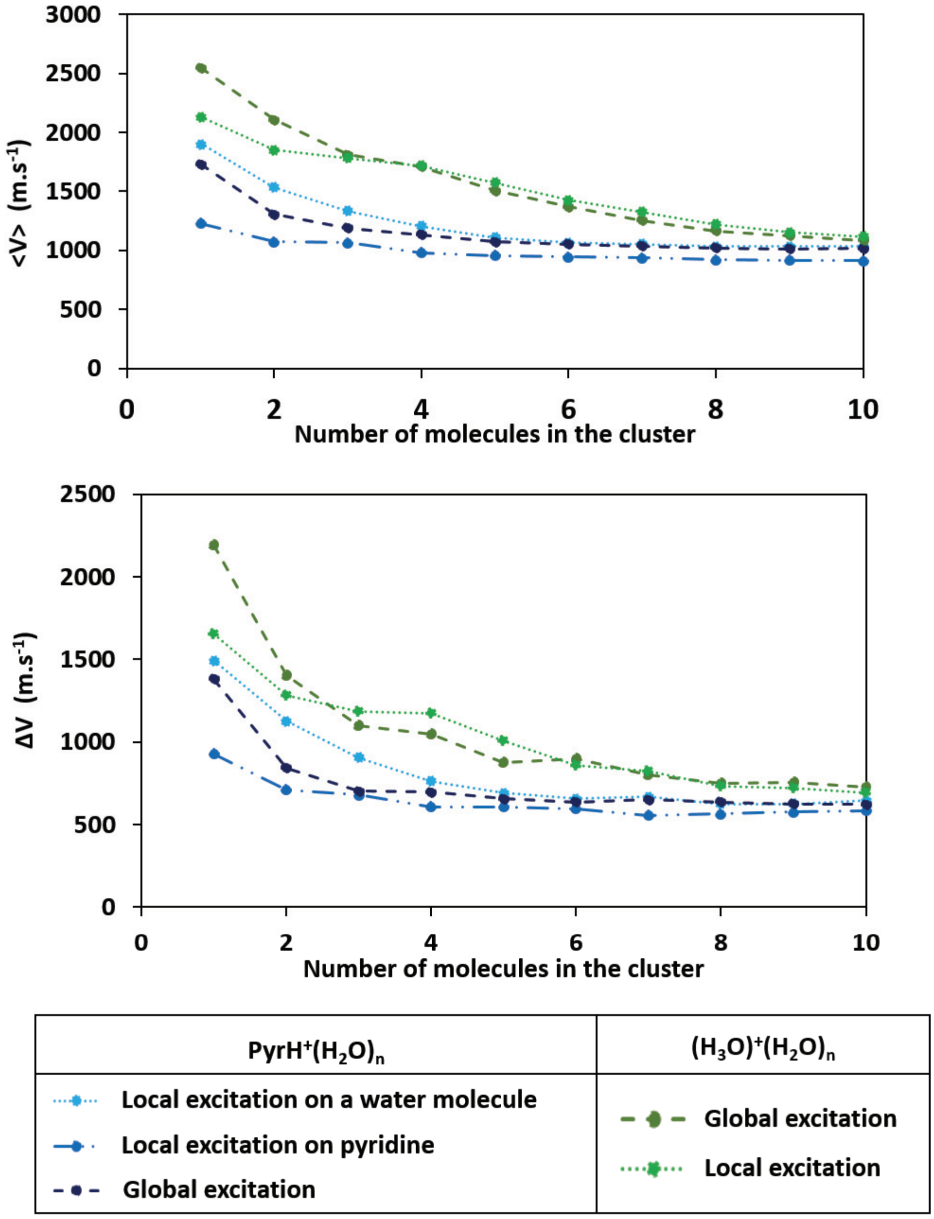

Figure 70: Low velocity part of the SMD calculated velocity distribution of the evaporated water molecule from $PyrH^+(H_2O)_{n=1\text{-}4}$ cluster ions for global excitation in dark blue, local excitation on pyridine in blue and local excitation on a water molecule in cyan and from $H_3O^+(H_2O)_{n=1\text{-}4}$: global excitation in dark green and local excitation in green. Upper part: average velocity: <V>, lower part: Full Width at Half Maximum: ΔV.

The results on protonated water clusters and on protonated pyridine water clusters follow the same trend: the average velocity and the width of the distribution decrease with n and saturate.

For the protonated water cluster, the mean velocity of the water molecule evaporated after global excitation ranges from 2500 $m.s^{-1}$ for $H_3O^+(H_2O)$ to 1000 $m.s^{-1}$ for $H_3O\ ^+(H_2O)_9$. The mean velocity of the water molecule evaporated after local excitation ranges from 2000 $m.s^{-1}$ for $H_3O^+(H_2O)$ to 1100 $m.s^{-1}$ for $H_3O\ ^+(H_2O)_9$. Until n= 4, the velocity distribution of the evaporated molecule after global excitation has higher <V>, then for higher n the velocity distribution of the evaporated molecule after local excitation has higher <V> value. The velocity distribution of the evaporated molecule after both kind of excitations tend to saturate around 1000 $m.s^{-1}$ which is very similar but slightly above the results for the protonated pyridine water cluster after global excitation and local excitation on water. The average value of the velocity distribution for the protonated water cluster decrease more slowly than for protonated pyridine water cluster which seems to saturate form n=5 against n= 10 for protonated water cluster. Only the local excitation of a pyridine molecule reaches a lower saturation value at 900 $m.s^{-1}$ while all others saturate at 1000 $m.s^{-1}$.

Regarding the width of the distribution, protonated water cluster ranges from 2200 $m.s^{-1}$ for $H_3O^+(H_2O)$ to 725 $m.s^{-1}$ for $H_3O^+(H_2O)_9$ for global excitation and from 1650 $m.s^{-1}$ for $H_3O^+(H_2O)$ to 690 $m.s^{-1}$ for $H_3O^+(H_2O)_9$ for local excitation. The local excitation is higher between n=3 and n=6. After n=6, both kind of excitations slowly decrease. ΔV saturation appears from n=4 for protonated pyridine water cluster against n=6 for protonated water cluster but it is still decreasing and all seems to saturate at the same value for high n at around 650 $m.s^{-1}$.

For the protonated water cluster, the saturation of <V> and ΔV is similar for both kinds of excitations while for protonated pyridine water cluster, the local excitation is always above the others.

In the case of proton water cluster, the low velocity part of the distribution is similar in the case of global excitation and in the case of the excitation of single molecule of the cluster. This leads to conclude that the low velocity part of the distribution corresponds to the redistribution of the energy from the excited molecule to the entire cluster. Differently, for pyridine water cluster, energy deposition in the pyridinium leads to a shift of the low velocity part of the distribution towards lower velocity. The energy deposition in a water molecule of the cluster leads to a distribution which for large n value is similar to the one calculated for protonated water cluster.

Such differences show that the low velocity part of the distribution still depends on the excitation mechanism and lead us to conclude that in the case of excitation of a water molecule, evaporation takes place after partial thermalisation in the water part of the cluster but before complete redistribution in the entire cluster.

b. Sequential evaporation of several molecules

The experimental set-up allows us, in the analyses of the same experiment, to select clusters depending of the number of molecules they have evaporated during the observation time window. In the previous part, we have selected clusters which have evaporated a single water molecule. In this section we present the analysis of the velocity distribution of the evaporated molecules for clusters which evaporate two and three water molecules.

1) Evaporation of several molecules: the case of n=4

We first study the specific case of $PyrH^+(H_2O)_4$ -> $PyrH^+(H_2O)_{4-m}$ + $m(H_2O)$. Collision inducing evaporation of several atoms or molecules from clusters has been demonstrated to be sequential evaporation of a single molecule: evaporation of a single molecule by the parent cluster ions, followed by the evaporation of a single molecule by the daughter cluster ions etc…

In the analysis of the data we select events with the detection of the residual cluster ion and the detection of a single water molecule. The number of evaporated molecules is deduced from the mass of the residual cluster ions. The detected molecule is one of the evaporated molecules. Consequently, the measured velocity distribution is the average distribution of different molecules sequentially evaporated.

The upper part of Figure 71 shows the impact distributions of the evaporation of several water from $PyrH^+(H_2O)_4$ with in Figure 71 (a) the evaporation on one water molecule, in Figure 71 (b): two water molecules, in Figure 71 (c): three water molecules and in Figure 71 (d): four molecules of water are evaporated. As explained at the beginning of the chapter, a 1D radial distribution can be extracted from the 2D impact distribution picture and is shown for each dissociation channel.

We observe two contributions in the impact distribution: a very intense zone localized in the middle of the detector and a halo at low intensity which surrounds the first contribution. In the histogram of the impact distribution, we can see both contributions with a peak between 0 and 5 mm and a long tail until 15 mm. The width and the maximum value of the first peak increase with the number of evaporated molecules.

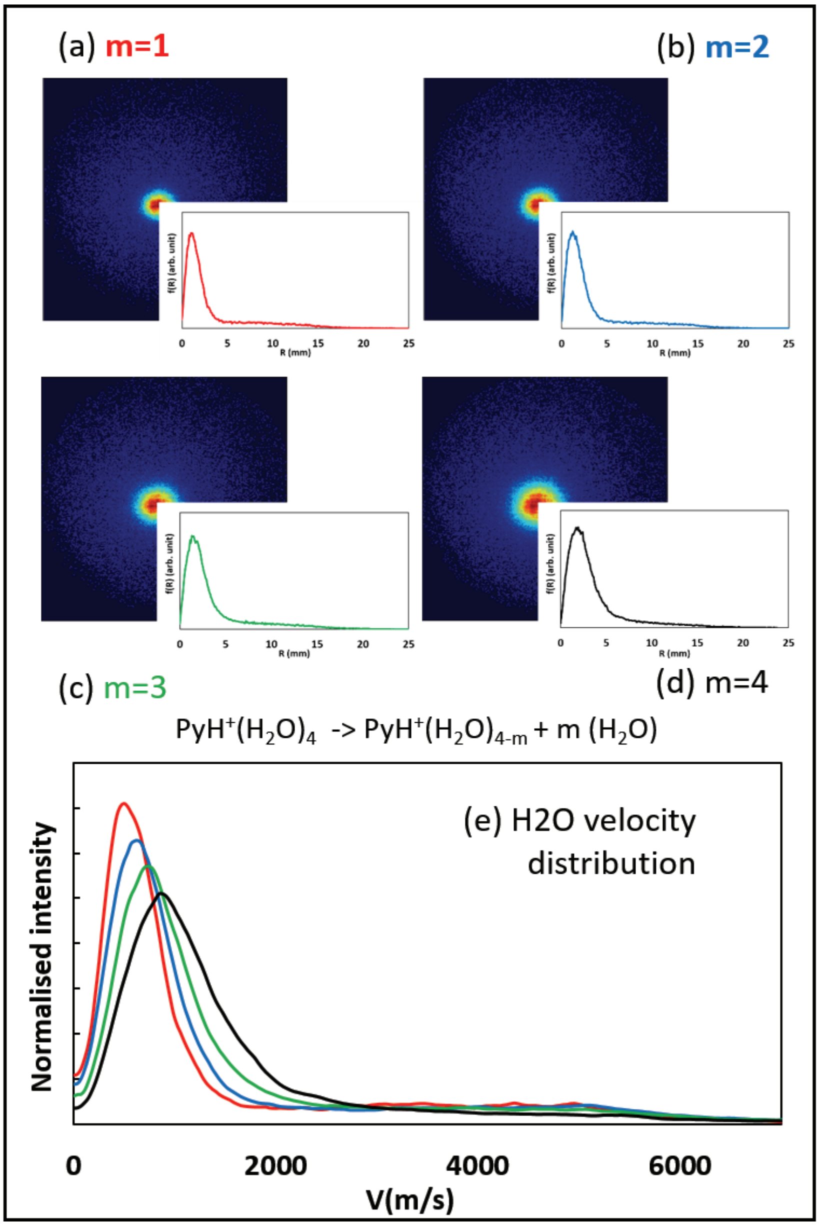

Figure 71: Impact and velocity distributions of molecules evaporated from $PyrH^+(H_2O)_4$ *clusters. (a-d): 2D impact distributions of the evaporated molecules with their corresponding 1D radial distribution. (e) is the velocity of the water molecule evaporated from* $PyrH^+(H_2O)_4$ *clusters with in red the evaporation of one water molecule, in blue: two, in green: three and in black: four.*

As described previously, the velocity distributions shown in Figure 71 (e) are extracted from the impact distributions. The velocity distributions of the 4 dissociation channels are represented: the evaporation of one, two, three and four molecules, in red, blue green and black, respectively. All of them have two components: a peak between 0 and 2000 $m.s^{-1}$ and a large tail until 6000$m.s^{-1}$. The average value and the width of the low part of the velocity distribution increase with the number of evaporated molecule m.

2) Velocity distribution for the evaporation of two molecules

As done previously for the evaporation of a single molecule, we summarize the results of the evaporation of two molecules: Figure 72 shows the experimental data and the results of the SMD calculations. Each line is a different cluster size: n. The first column is the experimental data, with in red: the data, in green dashed line: the Maxwell-Boltzmann fit of the low velocity part and in dashed orange line: a Gaussian fit of the non-ergodic events. The second column is the theory for global excitation. In dark blue full line is the result of the SMD calculation and in dashed green line is the Maxwell-Boltzmann fit of the distribution. The third column is the result of the theory for the local excitation on pyridine. In full blue line is the result of the SMD calculation and in dashed green line is the Maxwell-Boltzmann distribution. The fourth and last column is the result of the theory for local excitation on a water molecule. In full light blue is the result of the SMD calculation, in green the Maxwell-Boltzmann fit of the low velocity part of the distribution and in orange a Gaussian fit of the non-ergodic events. In each graph, the x-axis represents the velocity in m.s^{-1} and the y axis is the velocity intensity in arbitrary unit.

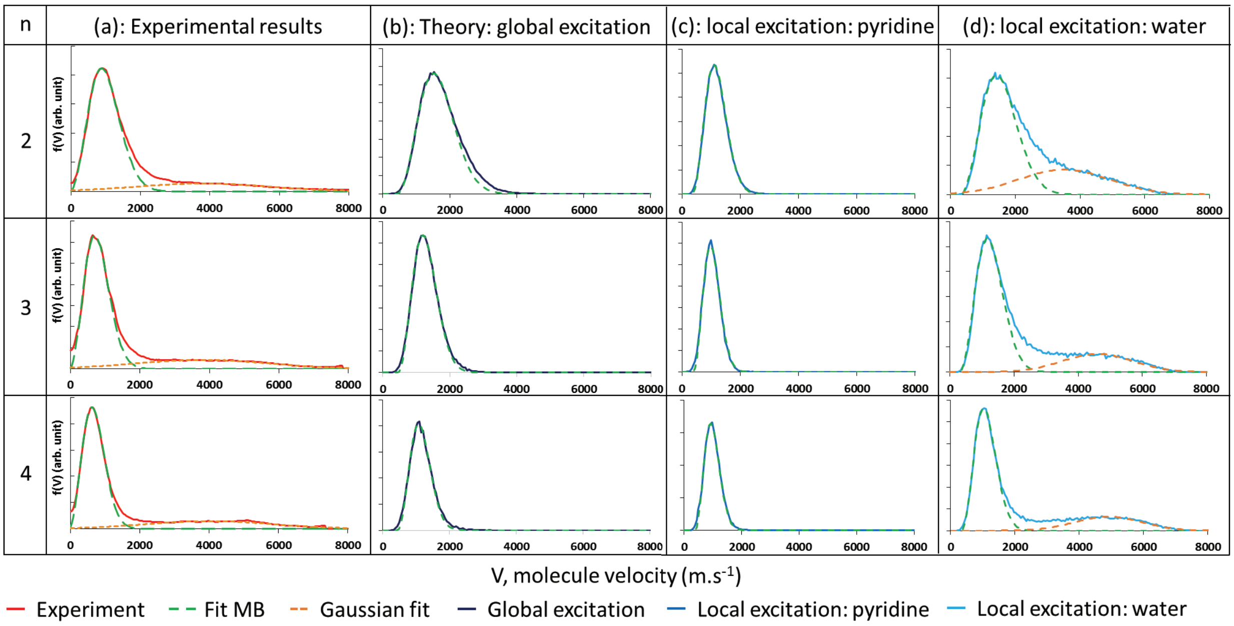

Figure 72: Evaporation of two water molecules from PyrH$^+$(H$_2$O)$_{n=1-4}$ cluster ions: the experimental velocity distributions (a) and the calculated ones : (b) : SMD – global excitation, (c) SMD – local excitation on a the Pyridine molecule, (d) SMD – local excitation on a water molecule. The dashed green curve corresponds to a Maxwell-Boltzmann fit of the low velocity part of the distributions, the dashed orange curve to a Gaussian fit of the non-ergodic events.

At very low velocities, i.e., below 1500 m.s^{-1}, each velocity distribution is accurately fitted by a Maxwell-Boltzmann distribution. In the global excitation and in the local excitation of a pyridine molecule, there are no non-ergodic events, that is, contribution at higher velocities. The behavior of the distribution for the maximum value and the width of the distribution with the size of the cluster is similar to the experimental distribution: for each type of excitation, the width and the average value of the distribution decrease with n. In the high part of the low velocity part: between 1500 and 2000 m.s^{-1}, the experimental data and the simulation for global excitation with n=1 manifest some event out of the Maxwell-Boltzmann fit.

We notice that only calculated distributions assuming excitation of a water molecule exhibit a high velocity component associated with the non-ergodic events. The non-ergodic events are less abundant than that is observed for the evaporation of a single molecule. The proportion of the non-ergodic events is decreasing with n: the number of water molecule in the parent cluster.

3) *Velocity distribution for the evaporation of three molecules*

As we did for the evaporation of one and two molecules, we summarize bellow the results obtained for the evaporation of three molecules: Figure 73 shows the results of the SMD calculation compared with the experimental data. Each line is a different cluster size: n. The first column is the experimental data, with in red: the data, in green dashed line: the Maxwell-Boltzmann fit of the low velocity part and in dashed orange line: a Gaussian fit of the non-ergodic events. The second column is the theory for global excitation. In dark blue full line is the result of the SMD calculation and in dashed green line is the Maxwell-Boltzmann fit of the distribution. The third column is the result of the theory for the local excitation on pyridine. In full blue line is the result of the SMD calculation and in dashed green line is the Maxwell-Boltzmann distribution. The fourth and last column is the result of the theory for local excitation on a water molecule. In full light blue is the result of the SMD calculation, in green the Maxwell-Boltzmann fit of the low velocity part of the distribution and in orange a Gaussian fit of the non-ergodic events. In each graph, the x-axis represents the velocity in m.s^{-1} and the y axis is the velocity intensity in arbitrary unit.

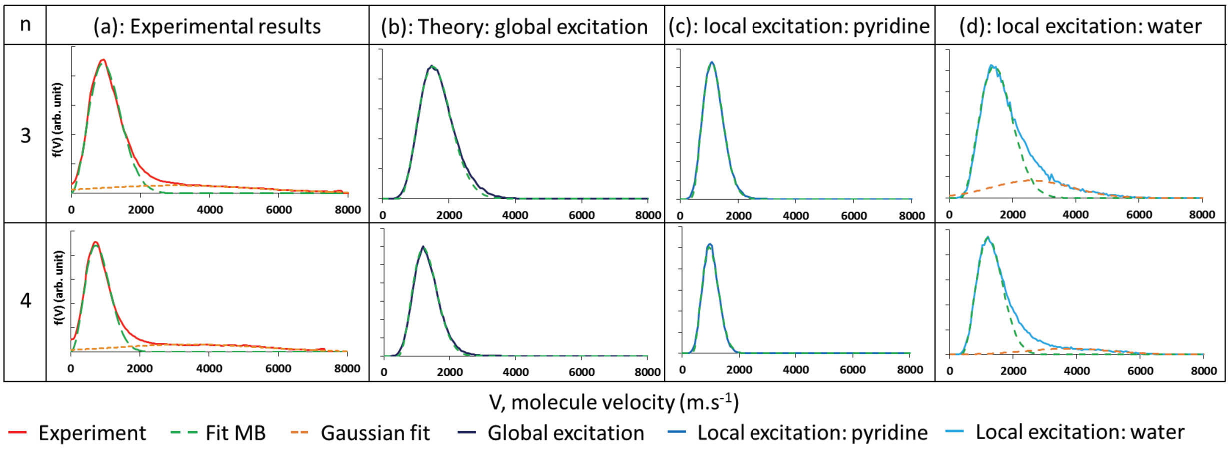

Figure 73: Evaporation of three water molecules from $PyrH^+(H_2O)_{n=1\text{-}4}$ cluster ions: the experimental velocity distributions (a) and the calculated ones : (b) : SMD – global excitation, (c) SMD – local excitation on a the Pyridine molecule, (d) SMD – local excitation on a water molecule. The dashed green curve corresponds to a Maxwell-Boltzmann fit of the low velocity part of the distributions, the dashed orange curve to a Gaussian fit of the non-ergodic events.

We can draw the same conclusion as for the evaporation of two molecules. At very low velocities, i.e., below 1500 m.s^{-1}, each velocity distribution is accurately fitted by a Maxwell-Boltzmann distribution. In the global excitation and in the local excitation of a pyridine molecule, there are no non-ergodic events, that is, contribution at higher velocities. The behavior of the distribution for the maximum value and the width of the distribution with the size of the cluster is similar to the experimental distribution: for each type of excitation, the width and the average value of the distribution decrease with n. In the high part of the low velocity part: between 1500 and 2000 m.s^{-1}, the experimental data and the simulation for global excitation with n=1 manifest some event out of the Maxwell-Boltzmann fit.

The local excitation on water exhibits a component of the non-ergodic events. But as for the evaporation of two water molecules, the non-ergodic events are less abundant than for the evaporation of a single molecule. The proportion of the non-ergodic events is decreasing with n: the number of water molecule in the parent cluster.

4) *Average velocity and width of the distribution for the low velocity part of the distributions*

Figure 74 shows a comparison of the Maxwell-Boltzmann fit adjusted on the low velocity part of the different velocity distribution presented in Figure 68, Figure 72 and Figure 73. The average value: <V> (on the left) and the width: ΔV (on the right) of the low velocity part of the velocity distribution is plotted as a function of the cluster size n, for the evaporation of one (red), two (blue) and three (green) water molecules for the experiment (full markers) and the theory (empty markers).

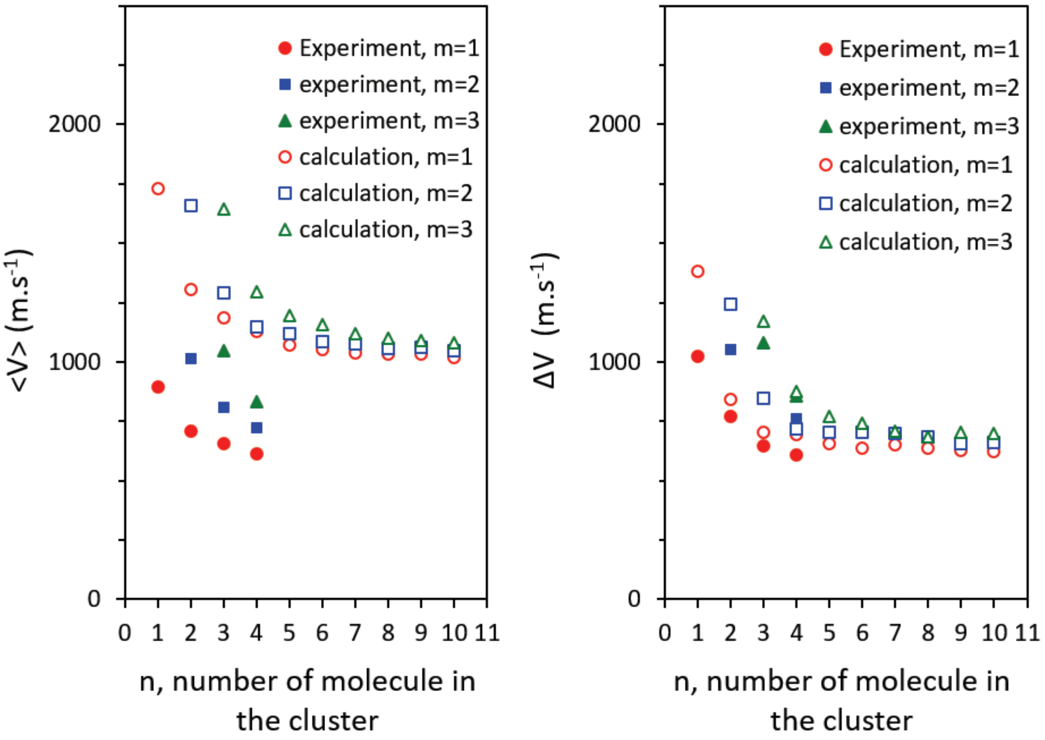

Figure 74: Average velocity and width of the distribution measured (full marker) and calculated (empty marker) for the low velocity part of the distribution, m is the number of evaporated molecules.

The behavior for the dissociation channel leading to the evaporation of 2 and 3 molecules is similar to the one observed for the evaporation of a single molecule: the average value and the width of the distribution decrease with n and saturate. For all clusters studied, the average value and the width of the distribution for the evaporation of 3 water molecules is always higher than the one for the evaporation of two molecules which is always higher than the one for the evaporation of a single molecule. However, the difference of <V> and ΔV between m=1 and m=3 is decreasing with n.

The calculated distribution with global excitation reproduced qualitatively the same behavior: the values obtained for the evaporation of 3 water molecules are always higher than the one obtained for the evaporation of two molecules which are always higher than the one for the evaporation of a single molecule. However, the difference of <V> and ΔV between m=1 and m=3 is decreasing with n.

The width of the calculated distribution is in quantitative agreement with the experimental results. The average velocity for the calculated distribution is always higher than the experimental one but the calculations reproduce the dependency with the cluster size. Such global shift has already been obtained for the protonated water cluster.

For the evaporation of two molecules, the average value of the experimental distribution ranges from 1000 $m.s^{-1}$ for n=2 to 720 $m.s^{-1}$ for n=4 whereas the SMD calculations range from 1650 $m.s^{-1}$ for n=2 to 1050 $m.s^{-1}$ for n=10. For the evaporation of three molecules, the average value is 1050 $m.s^{-1}$ for n=3 and 830 $m.s^{-1}$ for n=4 when for the SMD calculation, it ranges from 1650 $m.s^{-1}$ for n=3 to 1080 $m.s^{-1}$ for n=10.

The value of <V> and ΔV for the evaporation of one, two and three molecules shows that the low velocity part of the distribution is wider when n decreases. The evaporation of several molecules is the result of the successive evaporations of a single molecule. As the width of the distribution increases when n decreases: the width of the velocity distribution for the evaporation of the second molecule will be larger. And the measured velocity distribution is the average of all the real evaporated velocity distributions so more molecules are evaporated, wider will be the velocity distribution. The recoil velocity taken by the daughter ions also gives a contribution to the increase of the width of the velocity distribution. Lighter the daughter ion is, more its recoil velocity will be important and more the velocity distribution of the next evaporation will be wide. This can be quantitatively tested by using a Monte-Carlo simulation.

5) *Monte-Carlo simulation of the velocity distribution for the sequential evaporation of several molecules*

The simulation described in [49] calculate the velocity distribution of the evaporation of two and three molecules from the velocity distribution measured for the evaporation of one molecule and taking into account the contribution of the recoil velocity of the daughter ions.

All velocity distributions have a low velocity part which could be fit with a Maxwell-Boltzmann distribution. In this frame, the energy deposit during the collision is redistributed among all degrees of freedom of the molecule and the evaporation of several molecules has to be sequential.

Assuming the sequential evaporation, the evaporation process of m molecules from a cluster of n molecules can be seen as:

$PyrH^+(H_2O)_n$ -> $PyrH^+(H_2O)_{n-1}$ + (H_2O),

Then $PyrH^+(H_2O)_{n-1}$ -> $PyrH^+(H_2O)_{n-2}$ + (H_2O),

… and so on until $PyrH^+(H_2O)_{n-m}$ -> $PyrH^+(H_2O)_{n-(m+1)}$ + (H_2O).

The Monte-Carlo simulation is based on a random selection of the velocity of each evaporated molecule in the velocity distribution measured for the evaporation of a single water molecule. For each step of the evaporation process, the velocity magnitude of the evaporated molecule is determined from the probability given by the velocity distribution measured for the evaporation of a single molecule. Its direction in the cluster center of mass frame is randomly picked in 4π steradians. At each evaporation, the recoil velocity of the daughter ion is calculated with the conservation of the momentum and is added to the velocity of the center of mass frame parent ion. We repeat it for 10^5 events to get the velocity distribution for the evaporation of several molecules for a cluster with a given number of molecules. The trajectory of all the water molecules is calculated in a simulation and the average velocity can be extracted. In the calculation presented here we don’t introduce the exponential decay of the excited cluster ions. We suppose that the time to evaporate a molecule, in the order of picosecond, can be neglected in front of the observation window, around 200 ns: after evaporation, the daughter ion does not move until it dissociates all its water molecules. The method has been previously tested on protonated water clusters giving a very good agreement with the experimental distributions.

We have performed different calculations using this simulation. In a first step, the single molecule velocity distribution used is not the total measured distribution but only the low velocity part associated to the Maxwell-Boltzmann events. In Figure 75, the distributions calculated with this simulation (in dashed blue line) are compared with the measured distributions (in full red line) for the evaporation of two molecules from PyrH$^+$(H$_2$O)$_4$ (Figure 75(a)), PyrH$^+$(H$_2$O)$_3$ (Figure 75(b)) and PyrH$^+$(H$_2$O)$_2$ (Figure 75(c)).

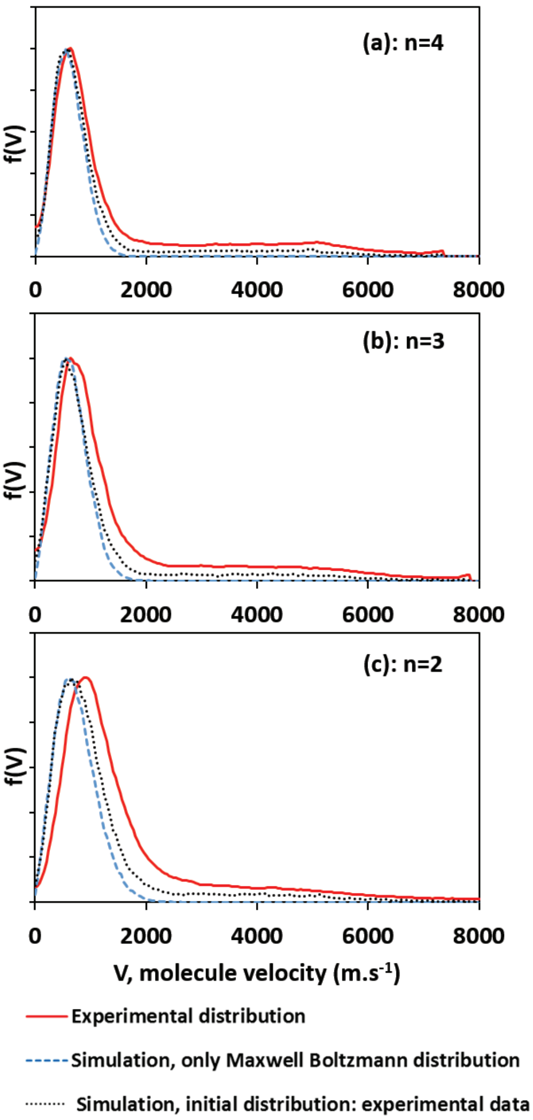

Figure 75: Velocity distribution calculated with Monte-Carlo simulation from the measured experimental distribution for the evaporation of a single molecule in the case of evaporation of two molecules for PyrH$^+$(H$_2$O)$_n$: n= 2 (c), n= 3 (b) and n= 4 (a). Full red line: experimental data, dashed blue line: simulation from the fit of the low velocity part of the distribution and in grey dotted line: simulation from the full experimental velocity distribution.

We observed that the simulated and the measured distributions are different: the measured distribution is wider and its average value is higher, this difference is decreasing while increasing the number of molecules in the cluster: n. The maximum values of the simulated distributions are shifted by around 60 m.s^{-1} for n=4, around 85 m.s^{-1} for n=3 and around 300 m.s^{-1} for n=2 with the experimental distribution.

In the previous calculation we did not take into account the non-ergodic events but they are a non-negligible portion of the observed distribution. We put now in our calculations the total measured velocity distribution for the first evaporated molecule. For the second evaporation, we use the low velocity part of the distribution as before. This way, we assume that only the first evaporated molecule can be evaporated with a high velocity (non-ergodic events). As before, the calculated distribution is the average of the first and the second evaporated distributions as the experimental distribution.

The results are shown in black dotted line in Figure 75 in comparison with the first calculation and the experimental distribution. The low velocity part of the black distribution is similar to the blue distribution until the maximum. Then the black distribution is wider and a few events at high velocity appear. These events are non-ergodic events.

Therefore, this behavior differs from what was obtained previously by F. Berthias [3] for protonated water cluster. The velocity distribution measured for the evaporation of two molecules cannot be reproduced from the distributions measured for the evaporation of a single molecule.

Moreover, this different behavior is also observed for the evaporation of three molecules. The results are shown in Figure 76 with in red the measured distribution, in blue dashed line, the calculated distribution with the low velocity part only and in black dotted line, the calculated distribution with the first evaporated molecule distribution as the experiment distribution and the following distribution, the low velocity part of the distribution only. In Figure 76 (a): the cluster size is n=4 and in Figure 76 (b), n= 3.

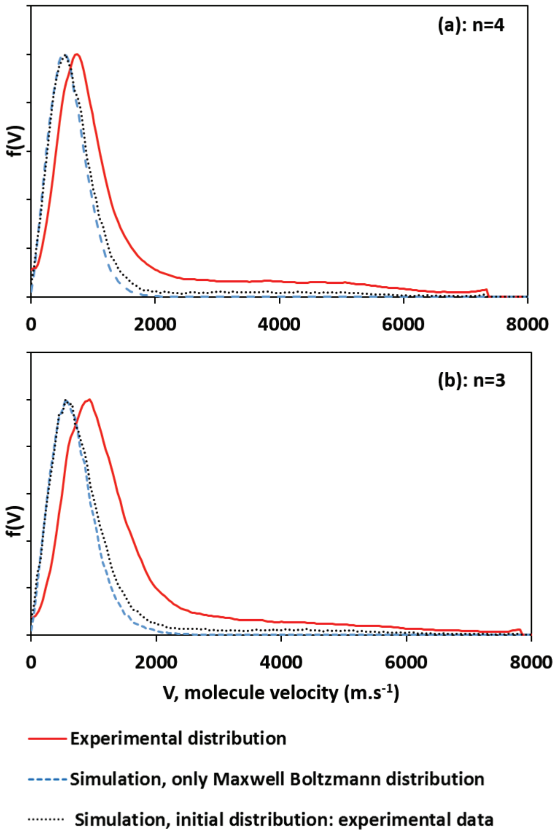

Figure 76: Velocity distribution calculated with Monte Carlo simulation from the measured experimental distribution for the evaporation of a single molecule in the case of evaporation of three molecules for $PyrH^+(H_2O)_n$*: n= 3 (b) and n= 4 (a). Full red line: experimental data, dashed blue line: simulation from the fit of the low velocity part of the distribution and in grey dotted line: simulation from the full experimental velocity distribution.*

The result of the evaporation of three molecules is similar to the evaporation of two molecules. The calculated distribution for the sequential evaporation of three molecules does not fit with the measured distribution for the evaporation of three molecules. The measured distribution is wider and shifted to higher velocity. The maximum values of the simulated distribution are shifted by around 212 $m.s^{-1}$ for n=4 and around 384 $m.s^{-1}$ for n=3 with the experimental distribution. We can conclude that the sequential evaporation model as we did for the evaporation of two and three molecules is really inappropriate for the interpretation of our measurements.

The same Monte-Carlo distribution was performed for protonated water cluster and the result of the simulation was really similar to the measured distribution of the evaporation of two molecules; it was clear that the model was well reproducing our experiments.

This is the second part of our analyses that clearly do not fit with sequential evaporation and leads us to question the association of the low velocity part of the distribution with complete energy redistribution in the entire cluster. Moreover, as mentioned previously the measured velocity distribution for the evaporation of a single molecule (Figure 68, Figure 72 and Figure 73) are not well fitted with a single Maxwell-Boltzmann distribution: some events remain out of the fit at intermediate velocity.

It is worth reminding that for protonated water cluster, the Maxwell-Boltzmann distribution was fitting well the measured distribution and the sequential evaporation model could be applied.

Additionally, the low velocity part of the experimental distribution fit with the SMD distribution for global excitation and with the low velocity part of the calculated distribution for local excitation.

Differently, in the case of pyridine protonated water clusters the SMD calculation evidences different behaviors associated with the two possible kinds of local excitation: excitation on a pyridine molecule or excitation on a water molecule. Each kind of excitations gives a distribution which can be well fitted with a Maxwell-Boltzmann function but with different width and different average value.

In the following we will use the SMD velocity distribution to analyze the experimental velocity distributions.

c. Local excitation of a water molecule versus local excitation of the pyridine

Using the results of the SMD calculation we show in this section that the measured velocity distribution for the evaporation of a single molecule and the evaporation of several molecules can be understood from two distinct contributions: the local excitation of the pyrimidium ion and the excitation of a water molecule of the cluster.

1) Low velocity part of the distribution: fit with the Maxwel- Boltzmann part of the SMD distributions calculated for local excitation of the pyridine molecule and of a water molecule

i. Evaporation of a single molecule

We consider first the evaporation of a single molecule. Using the corresponding SMD velocity distributions we fit the experimental distribution with two Maxwell-Boltzmann distributions: the width of the first one is given by the SMD distribution obtained with local excitation on the pyridinium molecular ion. The second is given by the low velocity part of the calculated distribution obtained with local excitation on a water molecule. As previously done for protonated water cluster a global shift of the average velocity will be introduced. But the difference of the average values calculated with the two excitations included in the fit will be the same between the two distributions of the SMD calculation and the two distributions used to fit our experimental distribution. We adjust both contribution proportions to fit our experimental distribution as:

$$Exp\ distribution = a \times contribution\ \ pyridine + b \times contribution\ water \qquad 19$$

Where “Exp distribution” is the experimental velocity distribution, “contribution pyridine” is the Maxwell-Boltzmann function corresponding to the local excitation on pyridine, “contribution water” is the Maxwell-Boltzmann function corresponding to the local excitation on a water molecule, and a+b=1.

The results are shown in Figure 77 with in red the experimental distribution, in dashed green line the distribution corresponding to a local excitation on pyridine and in dotted orange line a local excitation on a water molecule from $PyrH^+(H_2O)_4$ (Figure 77 (a)), $PyrH^+(H_2O)_3$ (Figure 77 (b)), $PyrH^+(H_2O)_2$ (Figure 77 (c)) and $PyrH^+(H_2O)$ (Figure 77 (d)). The blue line is the sum of the orange and green lines. The x-axis is the velocity and the y-axis, the velocity distribution: f(V).

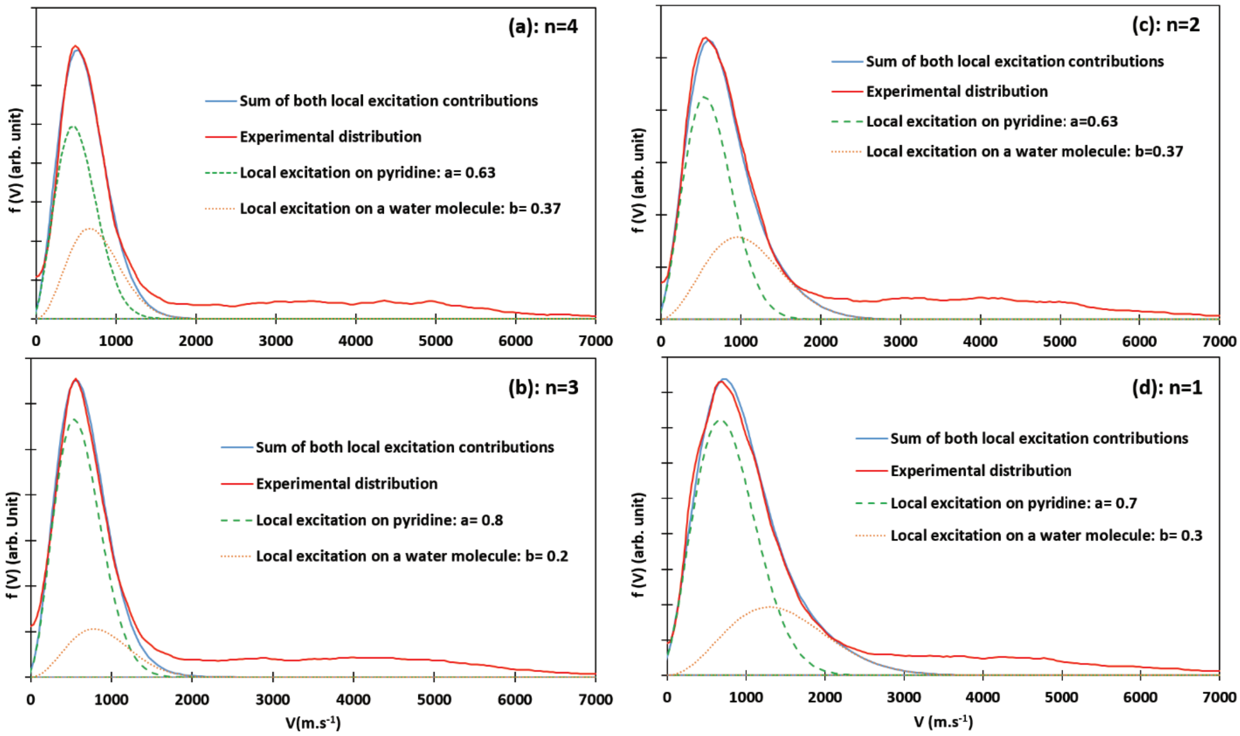

Figure 77: Fit of the experimental distribution with two Maxwell-Boltzmann functions, from the contribution of two local excitations: local excitation on a single water molecule (orange) and local excitation on pyridine (green) for the evaporation of a single molecule from n=4 (a), n=3 (b), n=2 (c) and n=1 (d). The blue line is the sum of both contributions and the red line is the experimental distribution.

The value for the width and the average value are extracted from the SMD calculation. The width of the green curve is fixed at 609 m.s^{-1} for n=4, 678 m.s^{-1} for n=3, 709 m.s^{-1} for n=2 and 928 m.s^{-1} for n=1. The width of the orange curve is fixed at 762 m.s^{-1} for n=4, 905 m.s^{-1} for n=3, 1127 m.s^{-1} for n=2 and 1491 m.s^{-1} for n=1. And the difference of the average value between them is fixed at 224 m.s^{-1} for n=4, 271 m.s^{-1} for n=3, 458 m.s^{-1} for n=2 and 681 m.s^{-1} for n=1. We applied a global shit of 450 m.s^{-1} for both distributions for n=1-4.

The low velocity parts of the experimental distribution are well fitted and most of the experiment events are in the sum of both contributions. The value of a and b corresponding to the fit of the experimental data will be discussed after the discussion of the results for sequential evaporation of several molecules.

iii. Evaporation of two molecules:

a) Calculated distributions

We use the Monte-Carlo simulation for the sequential evaporation as we used in the previous paragraph. We make two calculations with different inputs for the velocity distribution for the evaporation of a single molecule: the SMD calculated distribution for the evaporation of one molecule as a local excitation of pyridinium molecular ion and as a local excitation of a water molecule on another side. The output of the program is the distribution for the evaporation of two molecules for each kind of excitation. The results are shown in Figure 78 with in red the experimental distribution for the loss of two water molecules, in green dashed line, the simulation results for local excitation on pyridine and in orange dotted line the result for local excitation on a water molecule from PyrH$^+$(H$_2$O)$_4$ (Figure 78 (a)), PyrH$^+$(H$_2$O)$_3$ (Figure 78 (b)) and PyrH$^+$(H$_2$O)$_2$ (Figure 78 (c)).

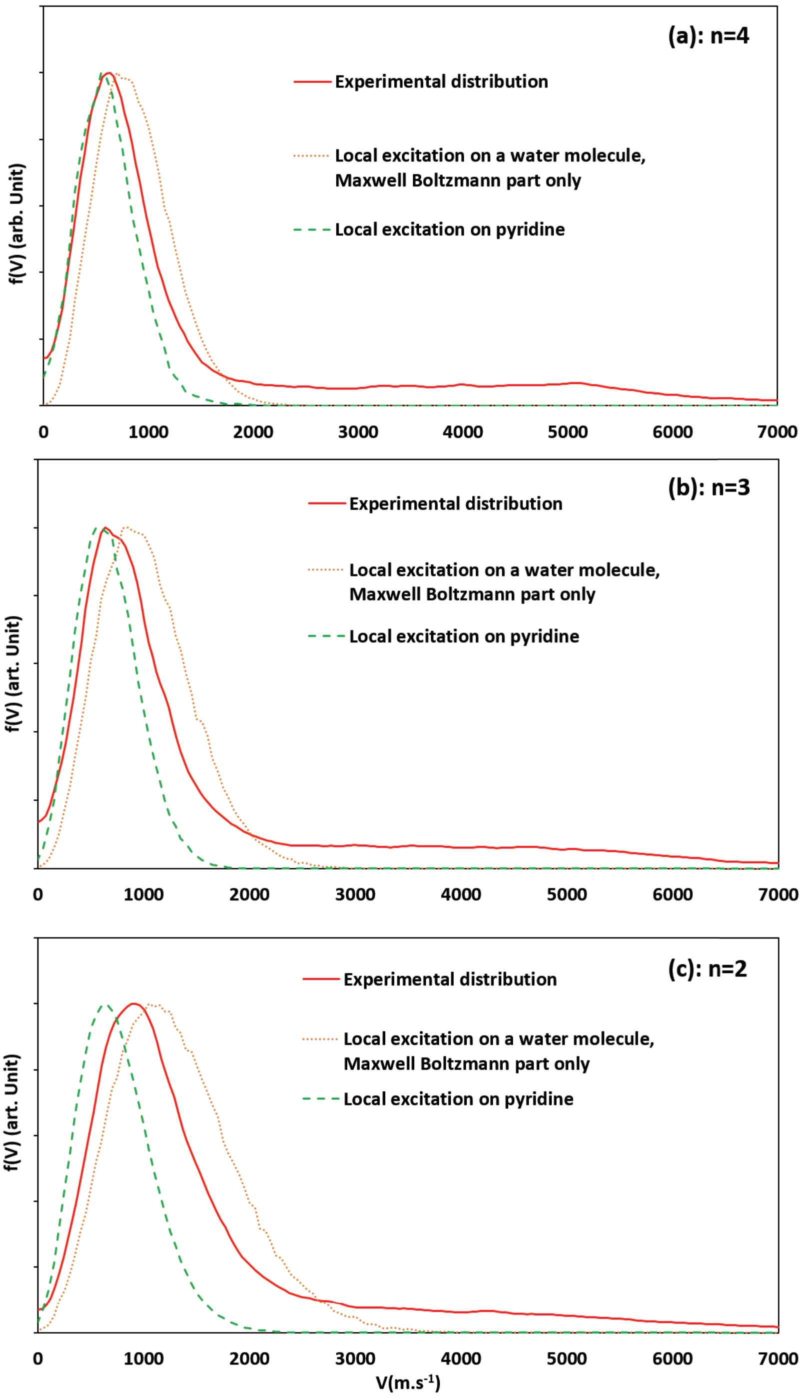

Figure 78: velocity distribution calculated with Monte-Carlo simulation from the SMD calculated distribution for the evaporation of a single molecule: evaporation of two molecules for n= 2 (c), n= 3 (b) and n= 4 (a). Full red line: experimental data, dashed green line: simulation from local excitation on pyridine, orange line: simulation from local excitation on a single water molecule.

All distributions are normalized at their maximum and plotted with a global shift of -400 m.s^{-1}. The local excitation on a water molecule has a wider distribution and the maximum is higher than that is observed for local excitation on pyridinium molecular ion. For n=4, the maximum of the distribution for local excitation on a water molecule is 70 m.s^{-1} higher and the maximum of the distribution for local excitation on pyridine is 80 m.s^{-1} lower than the experimental distribution (with the -400 m.s^{-1} shift). For n=3, the maximum of the distribution for local excitation on a water molecule is 215 m.s^{-1} higher and the maximum of the distribution for local excitation on pyridine is 85 m.s^{-1} lower than the experimental distribution (with the -400 m.s^{-1} shift). For n=2, the maximum of the distribution for local excitation on a water molecule is 125 m.s^{-1} higher and the maximum of the distribution for local excitation on pyridine is 275 m.s^{-1} lower than the experimental distribution (with the -400 m.s^{-1} shift).

It appears that the discrepancies between local excitation of a water molecule and the pyridinium ion are clearly increased in the velocity distribution calculated for the evaporation of two molecules. This is resulting from the fact that both in the experiment and in the calculation the evaporation is resulting from a single excitation and therefore evaporation of the first and second molecules are both due to the same initial excitation.

b) Fit of the low velocity part

We use the distributions calculated above to fit the experimental distribution. We proceed as for the evaporation of one molecule. The width of the Maxwell-Boltzmann function is the one of the distribution calculated in the previous paragraph. The difference of the average value of the two Maxwell-Boltzmann functions will be the calculated value. However, we use a global shift of the calculated distribution has done previously. We adjust both contribution proportions to fit our experimental distribution as:

$$Exp\ distribution = a \times contribution\ \ pyridine + b \times contribution\ water \qquad 20$$

Where “Exp distribution” is the experimental velocity distribution, “contribution pyridine” is the Maxwell-Boltzmann function corresponding to the local excitation on pyridine, “contribution water” is the Maxwell-Boltzmann function corresponding to the local excitation on a water molecule, and a+b=1.

The results are shown in Figure 79 with in red the experimental distribution, in dashed green line the distribution corresponding to a local excitation on pyridine and in dotted orange line a local excitation on a water molecule from $PyrH^+(H_2O)_4$ (Figure 79 (a)), $PyrH^+(H_2O)_3$ (Figure 79 (b)) and $PyrH^+(H_2O)_2$ (Figure 79 (c)). The blue line is the sum of the orange and green lines. The x-axis is the velocity and the y-axis, the velocity distribution: f(V).

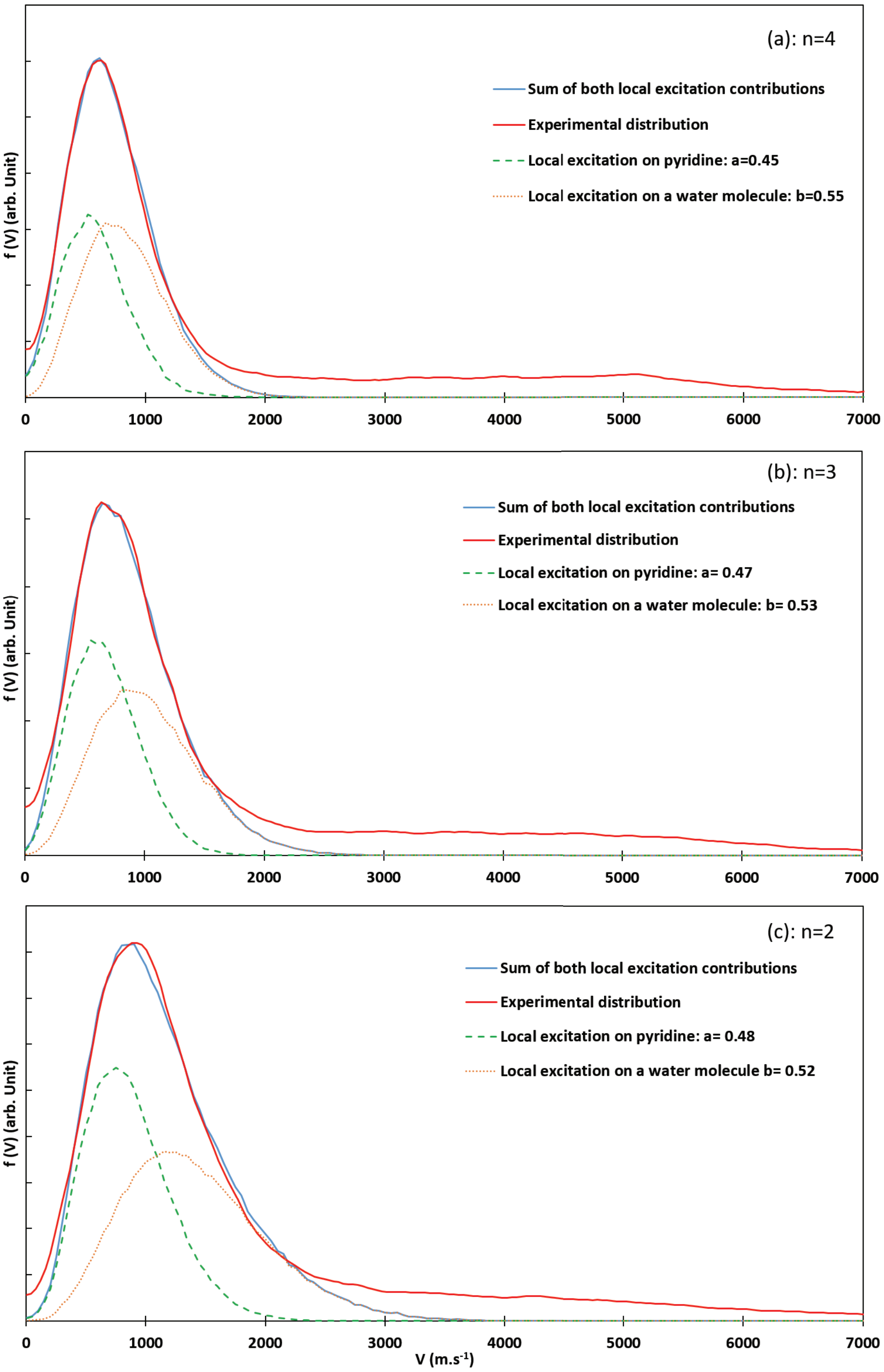

Figure 79: Fit of the experimental distribution with two Maxwell-Boltzmann functions, from the contribution of two local excitations: local excitation on a single water molecule (orange) and local excitation on pyridine (green) for the evaporation of two molecules from n=4 (a), n=3 (b) and n=2 (c). The blue line is the sum of both contributions and the red line is the experimental distribution.

From the SMD calculation, the width of the green curve is fixed at 638 $m.s^{-1}$ for n=4, 702 $m.s^{-1}$ for n=3 and 812 $m.s^{-1}$ for n=2. The width of the orange curve is fixed at 846 $m.s^{-1}$ for n=4, 1010 $m.s^{-1}$ for n=3 and 1330 $m.s^{-1}$ for n=2. And the difference of the average value between them is fixed at 259 $m.s^{-1}$ for n=4, 364 $m.s^{-1}$ for n=3 and 567 $m.s^{-1}$ for n=2. We apply a global shift for both contributions of -430 $m.s^{-1}$ for n=4, n= -400 $m.s^{-1}$ for n=3 and n= -300 $m.s^{-1}$ for n=2.

The low velocity parts of the experimental distributions are well fitted and most of the experiment events are in the sum of both contributions. Both contributions have almost the same importance even if the local excitation on a water molecule is slightly higher. We will discuss the value of a and b after the presentation of the results for the evaporation of three molecules.

iv. Evaporation of three molecules:

a) Calculated distributions

As for the evaporation of two molecules, we use the Monte-Carlo simulation to calculate the distribution of the evaporation of three molecules from velocity distributions obtained by the SMD calculations for the evaporation of a single molecule. As previously, the input of the simulation is the SMD distribution of the evaporation of a single molecule for each kind of local excitation. The output is the calculated distribution for the evaporation of three molecules considering a sequential evaporation. The results are shown in Figure 80 with in red the experimental distribution for the loss of two water molecules, in green dashed line, the simulation results for local excitation on pyridine and in orange dashed line the result for local excitation on a water molecule from $PyrH^+(H_2O)_4$ in Figure 80 (a) and from $PyrH^+(H_2O)_3$ in Figure 80 (b).

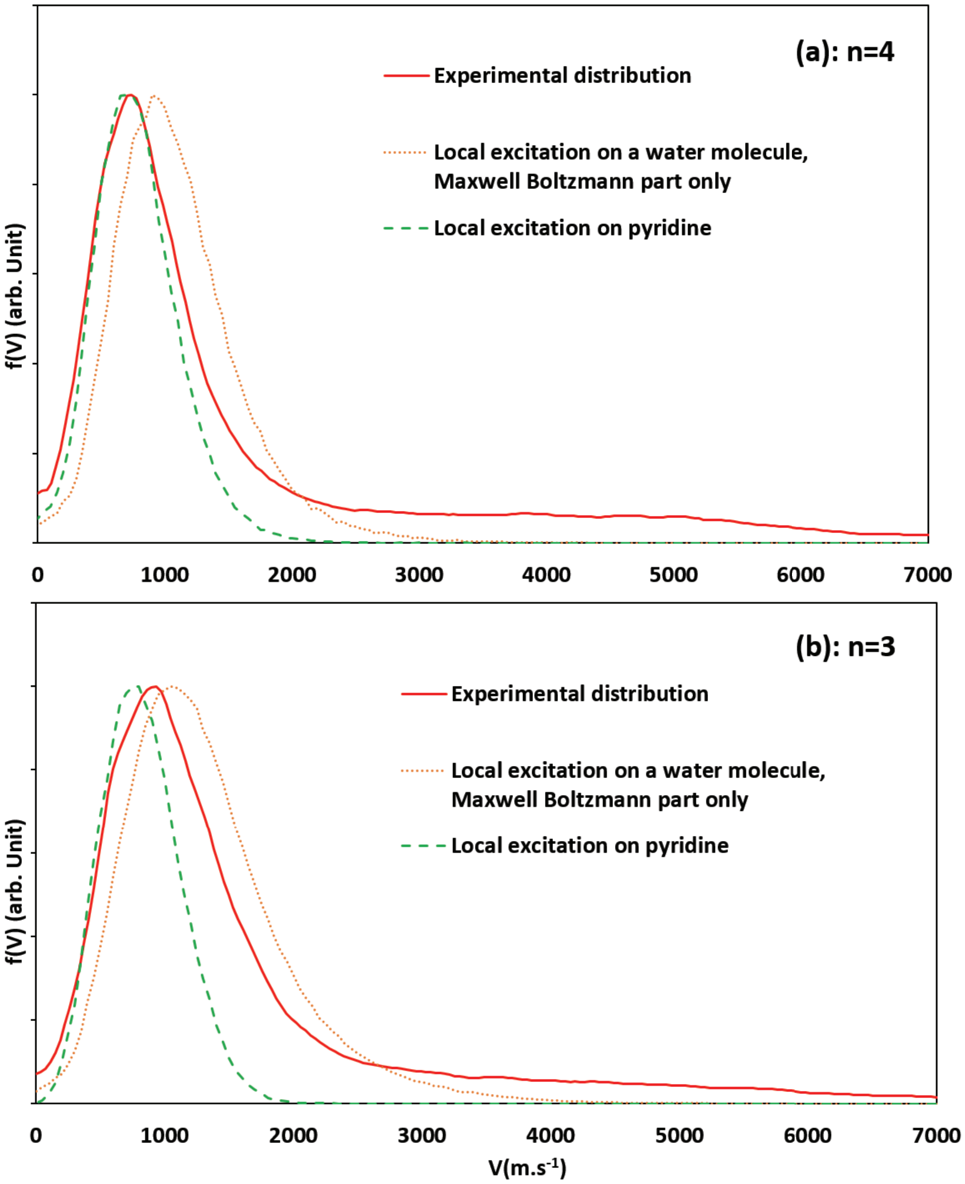

Figure 80: velocity distribution calculated with Monte-Carlo simulation from the SMD calculated distribution for the evaporation of a single molecule: evaporation of three molecules for n= 4 (a) and for n=3 (b). Full red line: experimental data, dashed green line: simulation from local excitation on pyridine, orange line: simulation from local excitation on a single water molecule.

All distributions are normalized at their maximum and plotted with a global shift of -250m.s^{-1}. As for the evaporation of a single and two molecules, the local excitation on water has a wider distribution and the maximum is higher than that is observed for local excitation on pyridinium molecular ion.

b) Fit of the low velocity part

We use the distributions calculated above to fit the experimental distributions. We proceed as for the evaporation of one and two molecules. The width of the Maxwell-Boltzmann function is the one of the distribution calculated in the previous paragraph. The difference of the average value of the two

MB functions will be the calculated value. However, we use a global shift of the calculated distribution as done previously. We adjust both contribution proportions to fit our experimental distribution as:

$$Exp\ distribution = a \times contribution\ \ pyridine + b\ \times contribution\ water \tag{21}$$

Where “Exp distribution” is the experimental velocity distribution, “contribution pyridine”: is the Maxwell-Boltzmann function corresponding to the local excitation on pyridine, “contribution water” is the Maxwell-Boltzmann function corresponding to the local excitation on a water molecule and a+b=1.

The results are shown in Figure 81 with in red the experimental distribution, in dashed green line the distribution corresponding to a local excitation on pyridine and in dashed orange line a local excitation on a water molecule from $PyrH^+(H_2O)_4$. The blue line is the sum of the orange and green lines. The x-axis is the velocity and the y-axis, the velocity distribution: f(V).

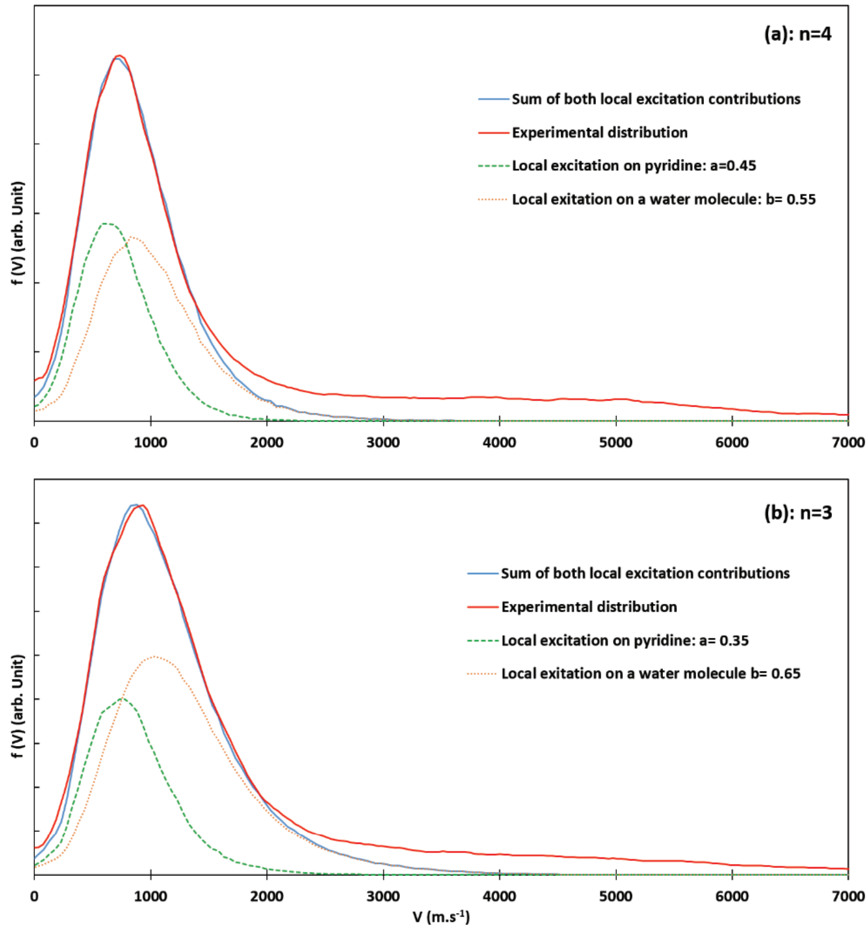

Figure 81: Fit of the experimental distribution with two Maxwell-Boltzmann functions, from the contribution of two local excitations: local excitation on a single water molecule (orange) and local excitation on pyridine (green) for the evaporation of three molecules from n=4 (a) or from n=3 (b). The blue line is the sum of both contributions and the red line is the experimental distribution.

From the SMD calculation, the width of the green curve is fixed at 720 $m.s^{-1}$ for n=4 and at 783 $m.s^{-1}$ for n=3. The width of the orange curve is fixed at 928 $m.s^{-1}$ for n=4 and at 1150 $m.s^{-1}$ for n=3. And the difference of the average value between them is fixed at 300 $m.s^{-1}$ for n=4 and at 457 $m.s^{-1}$ for n=3. We apply a global shift for both contributions of -320 $m.s^{-1}$.

The low velocity parts of the experimental distributions are well fitted and most of the experiment events are in the sum of both contributions. Both contributions have almost the same importance even if the local excitation on a water molecule is slightly higher. The value of a and b obtained for the evaporation of one, two and three molecules will be discussed in the next paragraph

The results obtained here assuming sequential evaporation demonstrates that the velocity distribution measured for the evaporation of several molecules can be quantitatively reproduced from the velocity distribution corresponding to the evaporation of a single molecule.

This leads to confirm that differently from what was observed for protonated water clusters, the low velocity part of the velocity distributions still remains information from the excitation process. The two Maxwell-Boltzmann shapes which are involved in the measured distributions show that evaporation of a water molecule occurs after energy redistribution in the water part of the cluster but before complete energy redistribution in the entire cluster.

2) Relative contribution of local excitation of the pyridine molecule and local excitation of a water molecule

i. Pyridine excitation and water excitation in the low velocity part of the distribution

The proportion of each local excitation over the number of events in the low velocity part of the distribution is directly extracted from the a and b values resulting from the fit of the experimental distributions. The results are presented in Figure 82: in green, the number of events associated with local excitation of pyridine over the total number of events in the low velocity part of the experimental distribution, in orange, the number of events associated with local excitation of a water molecule over the total number of events in the low velocity part of the experimental distribution with in full line (full circle) m=1 , in dashed line (full square) m=2 and dotted line (full triangle) m=3.

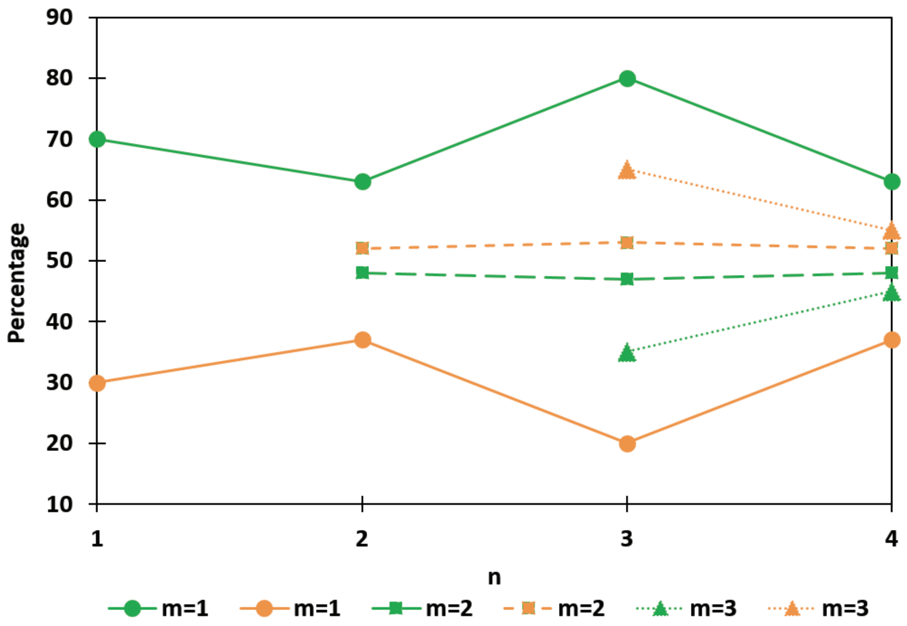

Figure 82: Comparison of the number of events associated with local excitation of pyridine (in green) and the number of Maxwell-Boltzmann events associated with local excitation of a single water molecule (orange) over the total number of events in the low velocity part of the experimental distribution for the evaporation of a single molecule (m=1, full line, round marker), of two molecules (m=2, dashed line, square marker) and of three molecules (m=3, dotted line, triangle marker).

Considering evaporation of a single molecule, the results shows that the local excitation on pyridine has a dominant contribution. Differently for the evaporation of several molecules local excitation of a water molecule dominates. For the evaporation of one molecule (m=1), the percentage of events after local excitation on pyridine are 63% for n=4, 80% for n=3, 63% for n=2 and 70% for n=1. For the evaporation of several water molecules, it is the opposite: the percentage of events for local excitation on pyridine is lower than for the local excitation on water but the difference between them is lower. In the case of local excitation on pyridine, for the evaporation of two molecules (m=2), the percentages are 48%, 47% and 48% for n=4-2 and for the evaporation of three molecules (m=3): 45% and 35% for n=4-3.

To explain the inversion, after a local excitation of pyridine, the time to transfer the energy in the entire cluster can be longer and therefore the evaporation of single water molecules dominates. On the other hands, the local excitation on a water molecule leads to fast partial equilibrium in the water part of the cluster and favors the evaporation of several molecules.

v. Proportion of Maxwell-Boltzmann and non-ergodic event among all the events associated with a given number of evaporated molecules

We compare the number of events in the low velocity part of the distribution (Maxwell-Boltzmann events) and the number of non-ergodic events for the experimental distribution. We consider as Maxwell-Boltzmann events, all the events which are in the sum of the local excitation on pyridine and on water (the blue lines in Figure 77, Figure 79 and Figure 81). The non-ergodic events are all the other events at higher velocity. The results are presented in Figure 83: in red, the number of Maxwell-Boltzmann events over the total number of events in the experimental distribution, in blue, the number of non-ergodic events over the total number of events in the experimental distribution with in full line (full circle) m=1, in dashed line (full square) m=2 and dotted line (full triangle) m=3.

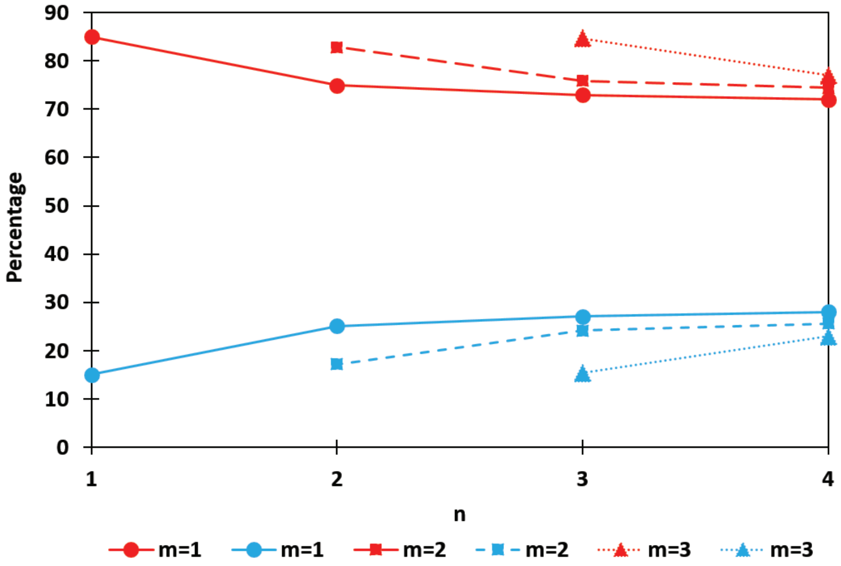

Figure 83: Comparison of the number of Maxwell-Boltzmann events (in red) and the number of non-ergodic (NE) events (blue) over the total number of events in the experimental velocity distribution for the evaporation of a single molecule (m=1, full line, round marker), of two molecules (m=2, dashed line, square marker) and of three molecules (m=3, dotted line, triangle marker).

The number of Maxwell-Boltzmann events is always higher than the non-ergodic events, and is almost independent of the cluster size n. The percentage of Maxwell-Boltzmann events for the evaporation of one molecule is around 70% with: 72% for n=4, 73% for n=3, 75% for n=2 and 85% for n=1. For the evaporation of 2 molecules, the percentage of Maxwell-Boltzmann events is a little bit higher with 74% for n=4, 76% for n=3 and 82% for n=2. And the evaporation of three molecules gives even higher Maxwell-Boltzmann events with 77% and 85% for n=4-3.

The Maxwell-Boltzmann events are a majority: more evaporated molecules come from a thermalisation of the cluster rather than a fast evaporation before energy redistribution.

vi. Proportion of pyridine excitation and water excitation among all the events associated with a given number of evaporated molecules

In Figure 82, we compared the proportion of each local excitation in the experimental velocity distribution for the low velocity part of the distribution. But according to the SMD calculation the local excitation on a water molecule has another component at high velocity. Moreover, the SMD calculations show that only local excitation on a water molecule gives non-ergodic events. We will now take into account these non-ergodic events as a contribution of local excitation of a water molecule. The results are presented in Figure 84: in green, the number of events associated with local excitation of Pyridine over the total number of events in the experimental distribution, in orange, the number of events associated with local excitation of a water molecule over the total number of events in the experimental distribution with in full line (full circle) m=1, in dashed line (full square) m=2 and dotted line (full triangle) m=3.

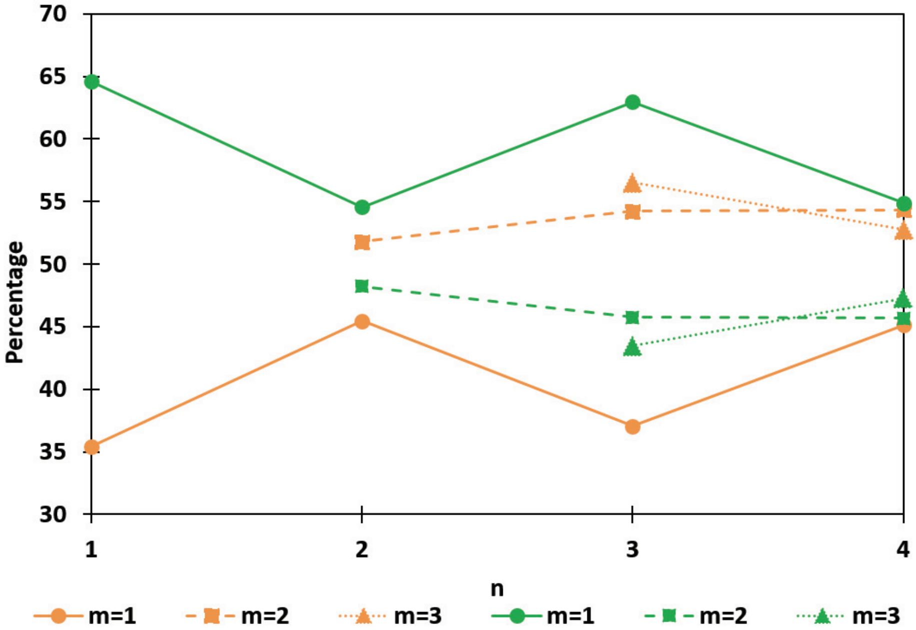

Figure 84: Comparison of the number of events associated with local excitation of pyridine (in green) and the number of Maxwell-Boltzmann events associated with local excitation of a single water molecule (orange) over the total number of events in the experimental distribution for the evaporation of a single molecule (m=1, full line, round marker), of two molecules (m=2, dashed line, square marker) and of three molecules (m=3, dotted line, triangle marker).

Compared with Figure 82, only the evaporation of a single molecule mainly changes: from 60%-80% to 55%-65%. The percentage of local excitation on a water molecule increases because non-ergodic events are possible only in the situation where the excitation is localized in a single water molecule. From the SMD calculations, we obtained that for the evaporation of one molecule, the number of non-ergodic events is high. On the other hand, the number of non-ergodic events is low in the case of the evaporation of two and three water molecules, for which the percentage of local excitation on pyridine is 45%-48% and 43%-47% respectively.

vii. Percentage of non-ergodic events in the measured and the SMD distributions among the events associated with local excitation of water.

In the SMD calculations, only the local excitation on a water molecule produces non-ergodic events. We compared in Figure 85 the number of non-ergodic events for the events associated with local excitation of water between the SMD calculation and the experimental result.

The result is shown in Figure 85: in red, the number of non-ergodic events in the experimental distribution over the total number of events associated to local excitation of a water molecule, in blue, the number of non-ergodic events in the SMD calculation over the total number of events associated to local excitation of a water molecule with in full line (full circle) m=1, in dashed line (full square) m=2 and dotted line (full triangle) m=3.

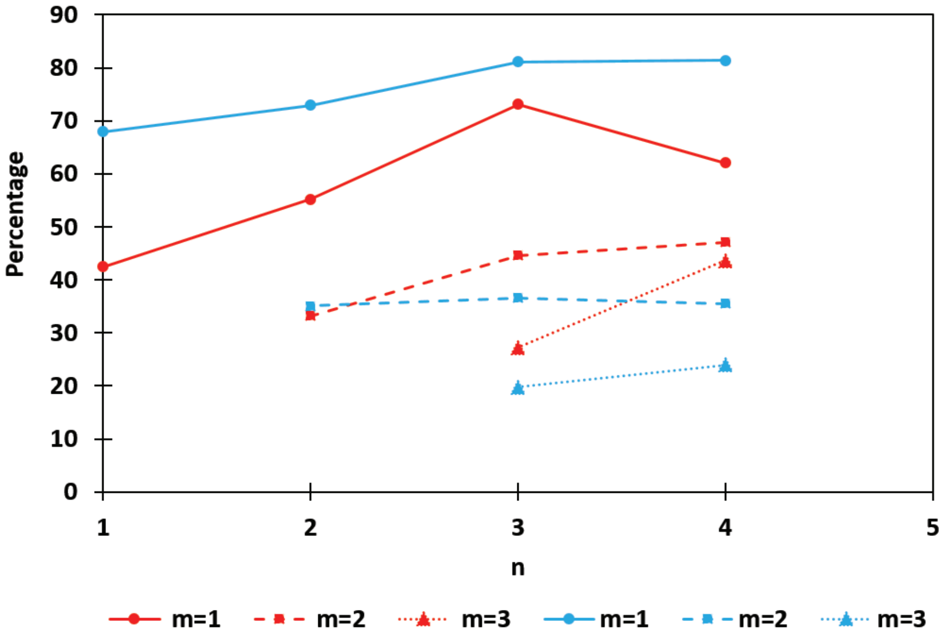

Figure 85: Comparison of the number of non-ergodic (NE) events in the experimental velocity distribution (in red) and in the SMD calculations (in blue) over the total number of events in the local excitation of a single water molecule for the evaporation of a single molecule (m=1, full line, round marker), of two molecules (m=2, dashed line, square marker) and of three molecules (m=3, dotted line, triangle marker).

For m=1, the number of non-ergodic events is higher in the SMD calculation: the experimental distribution range from 42% for n=1 to 62% for n=4 and the SMD calculation from 67% for n=1 to 81% for n=4. In the case of the evaporation of several molecules, the experimental number of non-ergodic events is higher than the SMD number of non-ergodic events. It ranges from 33% to 47% for the evaporation of two molecules and from 27% to 44% for the evaporation of three molecules against 35% and 19% - 24 % respectively for the SMD calculation. The number of non-ergodic events increases with n, but seems to saturate for n=3-4. This phenomenon is more clearly seen in the experimental data.

The number of non-ergodic events is decreasing with m, the number of evaporated molecule. The non-ergodic events are produced when the energy is not well redistributed in the cluster, after the water is evaporated, it takes most of the energy. There is not enough energy available for the evaporation of other molecules. This phenomenon is exaggerated in the SMD calculations in which the percentage of non-ergodic events is divided by two for the evaporation of two molecules.

Conclusion

This chapter was dedicated to the DIAM set-up and to the experiment of collision induced dissociation of mass selected PyrH$^+$(H$_2$O)$_{n=1-4}$ cluster ions. We presented the experimental set-up DIAM which produces a beam of energy and mass selected cluster ions. The detection system mounted after the collision zone couples the COINTOF detector and a DLA line detector and allows the measurement event-by-event of the arrival time and the position of each fragment (neutral and charged). The unfolding method calculates the velocity distribution of the evaporated water molecule using the radial distribution of the neutral detected fragment.

We presented the results of the velocity distribution of the single evaporated molecule induced by collision of 8 keV- $PyrH^+(H_2O)_{n=1-4}$ cluster ions with argon atoms. We observed two components: a peak at low velocity which was fitted with a Maxwell-Boltzmann distribution and a longer tail at high velocity. The Maxwell-Boltzmann events come from an evaporation after energy redistribution in all the degrees of freedom of the molecules. The long tail events are associated with non-ergodic events for which a water molecule is evaporated with a high velocity before complete energy redistribution. We compared our results on protonated pyridine water cluster with those on protonated water cluster. The width and the average value of the low velocity part of the distribution were decreasing with the cluster size n and saturate at high n, but they were always higher for the protonated water cluster. The protonated water cluster is distributing the energy overall every degree of freedom faster and more efficiently than for protonated pyridine water cluster. However, we saw that for protonated pyridine water cluster, the Maxwell-Boltzmann distribution could not fit well the event at higher velocity in the low velocity part while it fitted perfectly the measured distribution from protonated water cluster.

The measured distributions were compared to the SMD calculation results made with three different kinds of excitations: global excitation, local excitation on a water molecule and local excitation on pyridine molecule. The low velocity part of all the distributions could be fitted with a Maxwell-Boltzmann and only for the excitation on a water molecule, we could observe some non-ergodic events. The width and the average value of the low velocity part of the distribution follow the same behavior and both are decreasing with the cluster size n and saturate at high n. The average values of the calculated distribution are systematically higher than for the measured distributions. The, local excitation on pyridine seems to reach a lower limit that the local excitation on a water molecule or a global excitation, which both tend to the same average value. Regarding the width of the distribution, the calculated and the measured distributions have similar value.

The low velocity part of the measured and SMD calculated velocity distributions of the evaporation of a single molecule has a continuous behavior and does not drastically change for a specific number of cluster size n.

Then we studied the evaporation of several molecules and presented the velocity distributions for the evaporation of two and three molecules from $PyrH^+(H_2O)_{n=1-4}$. As for the evaporation of a single molecule, we observed a low velocity part which could be fitted with a Maxwell-Boltzmann distribution and a high velocity part associated with non-ergodic events. The width and the average value of the distribution are decreasing with the number of evaporated molecule m as well as the number of molecule in the parent cluster n. However, for a fixed parent cluster size, the distance between the evaporation of m and m-1 molecules is decreasing with n. For high n, the width and the average value for the evaporation of any number molecule seem to reach the same value.

A Monte-Carlo simulation which represents the sequential evaporation of several molecules from the measured distribution of a single molecule, taking into account the recoil velocity of the daughter ions was used to calculate the velocity distribution of two and three water molecules. The simulated distribution did not correspond with the measured one, especially for small n. However, in the case of protonated water cluster, the simulated distribution corresponded very well to the measured distribution.

The SMD calculations were made with two kinds of local excitation and each of them gave a Maxwell-Boltzmann fit of the low velocity part of the velocity distribution with different width and average value. From there, we concluded that the experimental excitations were actually a contribution of two excitations and we used the theory as a tool to study their relative importance.

By summing two distributions with the characteristics of both local excitations, we could fit the measured distribution and find their relative importance. We found that for the evaporation of a single molecule, the local excitation on pyridine was always more important than for the local excitation on a water molecule for any cluster size n. In the case of the evaporation of two and three molecules, we used the Monte-Carlo simulation of sequential evaporation to calculate the velocity distribution from the distribution of a single evaporated molecule calculated with the SMD model. The contributions of both local excitations were very similar.

References:

[1] G. Bruny, "Production et caracterisation d agregats moleculaire protones contenant un nombre donne de molecules d eau aupres du dispositif DIAM," PhD thesis, Universite Claude Bermard - Lyon I, Lyon, 2011.

[2] J. Jiang, Y. Wang and H. Chang, "Infrared spectra of H+(H2O)5-8 clusters: Evidence for symmetric proton hydration," *J. Am. Chem. soc.,* vol. 122, no. 7, pp. 1398-1410, 2000.

[3] F. Berthias, "Thermalisation dans une nanogoutte d eau," Universite de Lyon, IPNL, Lyon, 2016.

[4] G. Bruny, S. Eden, S. Feil, R. Fillol, R. El Farkh, M. Harb, C. Teyssier, S. Ouaskit, H. Abdoul-Carime, B. Farizon, M. Farizon and T. Mark, "A new experimental setup designed for the investigation of irradiation of nanosystems in the gas phase: a high intensity mass-and-energy selected cluster beam," *Review of Scientifi Instruments,* vol. 83, p. 013305, 2012.

[5] C. Teyssier, R. Fillol and H. Abdoul-Carime, "« A novel “correlated ion and neutral time of flight” method: Event-by-event detection of neutral and charged fragments in collision induced dissociation of mass selected ions," *Rev. Sci. Instrum ,* vol. 85, no. 1, p. 15118, 2014.

[6] C. Teyssier, "Spectrométrie de masse COINTOF: Conception d’un analyseur à temps de vol et développement de la méthode d’analyse," PhD thesis, Universite Claude Bernard Lyon I, Lyon, 2012.

[7] V. Rybkin, O. Simakov and V. Bakken, "Insights into the dynamics of evaporation and proton migration in protonated water clusters from large-scale bornoppenheimer direct dynamics," *J.Comput.Chem,* vol. 34, no. 7, pp. 533-544, 2013.

[8] F. Berthias, L. Feketeova, H. Chermette, C. Morel, H. Abdoul-Carime, B. Farizon, M. Farizon and T. D. Mark, "Proton Migration in Protonated Pyridine Solvated by Water Molecules," *Chem. Phys. Chem,* vol. 16, no. 15, pp. 3151-3155, 2015.

[9] RoentDek, "MCP Delay Line Detector Manual version 11.0.1607.2," http://www.roentdek.com/manuals/MCP%20Delay%20Line%20manual.pdf.

[10] F. Berthias, L. Feketeova, R. Della Negra, T. Dupasquier, R. Fillol, H. Abdoul-Carime, B. Farizon, M. Farizon and T. Mark, "Measurement of the velocity of neutral frgments by the " correlated ion and neutral time of flight"," *Review of Scientific Instrument,* vol. 88, p. 083101, 2017.

[11] R. Brun and F. Rademarkers, "ROOT — An object oriented data analysis framework," *Nucl. Instrum. Methods Phys. Res. Sect. Accel. Spectrometers Detect. Assoc. Equip,* vol. 389, no. 1, pp. 81-86, 1997.

[12] H. Lee and M. Kim, "Excitation Mechanism in the Collision-Induced Dissociation of Methane Molecular Ion at Kiloelectronvolt Translational Energy," *The journal of physical chemistry,* vol. 100, no. 5, pp. 1459-1465, 1996.

[13] R. G. Cooks, "Special feature: Historical. Collision-induced dissociation: Readings and commentary," *Journal of Mass spectrometry,* vol. 30, pp. 1215-1221, 1995.

[14] U. Saalmann and R. Schmidt, "Excitation and Relaxation in Atom-Cluster Collisions," *Phys. Rev. Lett.,* vol. 80, pp. 3213-3216, 1998.

[15] G. Greetham, "PICNIC Network," [Online]. Available: http://www1.chem.leeds.ac.uk//PICNIC/home.htm. [Accessed 19 07 2017].

[16] B. Liu, S. B. Nielson, P. Hvelpung, H. Zettergren, H. Cederquist, B. Manil and B. Huber, "Collision-Induced Dissociation of Hydrated Adenosine Monophosphate Nucleotide Ions: Protection of the Ion in Water Nanoclusters," *Phys. Rev. Lett.,* vol. 97, p. 133401, 2006.

[17] M. Stockett, H. Zettergren, L. Adoui, J. Alexander, U. Berzins, T. Chen, M. Gatchell, N. Haag, B. Huber, p. Hvelplund, A. Johansson, H. Johansson, K. Kulyk, S. Rosen, P. Rousseau, K. Stochkel, H. Schmidt and H. Cederquist, "Nonstatistical fragmentation of large molecules," *Phys. Rev. A,* vol. 89, p. 032701, 2014.

[18] M. Cowan, B. Bruner, N. Huse, J. Dwyer, B. Chugh, E. Nibbering, T. Elsaesser and R. Miller, "Ultrafast memory loss and energy redistribution in the hydrogen bond network of liquid H2O," *Nature,* vol. 434, pp. 199-202, 2005.

[19] Z. Zhang, L. Piatkowski, H. J. Bakker and M. Bonn, "Ultrafast vibrational energy transfer at the water/air interface revealed by two-dimensional surface vibrational spectroscopy," *Nature Chemistry,* vol. 3, pp. 888-893, 2011.

[20] L. Chang, A. Samanta, G. Czako, J. Bowman and H. Reisler, "Experimental and Theoretical Investigations of Energy Transfer and Hydrogen-Bond Breaking in the Water Dimer," *J. Am. Chem. Soc,* vol. 134, p. 15430–15435, 2012.

[21] V. H. Wysocki, H. l. Kenttamaa and R. Cooks, "Internal energy distributions of isolated ions after activation by various methods," *International Journal of Mass Spectrometry and Ion Processes,* vol. 75, no. 2, pp. 181-208, 1987.

[22] Y. Ibrahim, R. Mabrouki, M. Meot-Ner and M. S. Ei-Shall, "Hydrogen Bonding Interactions of Pyridine•+ with Water: Stepwise Solvation of Distonic Cations," *J. Phys. Chem. A ,* vol. 111, pp. 1006-1014, 2007.

[23] M. J. Ryding, A. S. Zatula, P. U. Andersson and E. Uggerud, "Isotope exchange in reactions between D2O and size-selected ionic water clusters containing pyridine, H+(pyridine)m(H2O)n," *Physical Chemistry Chemical Physics ,* vol. 13, pp. 1356-1367, 2010.

[24] H. Abdoul-Carime, F. Berthias, L. Feketeova, M. Marciante, F. Calvo, V. Forquet, H. Chermette, B. Farizon, M. Farizon and T. D. Mark, "Velocity of a Molecule Evaporated from a Water Nanodroplet: Maxwell–Boltzmann Statistics versus Non-Ergodic Events," *Angewandte cover picture,* vol. 54, no. 49, p. 14685–14689, 2015.

[25] J. Laskin and C. Lifshitz, "Kinetic energy release distribution in mass spectrometry," *Journal of mass spectrometry,* vol. 36, pp. 459-478, 2001.

[26] R. Levine and R. Bernstein, Molecular reaction dynamics and chemical reactivity, New York: Oxford University Press, 1987.

[27] T. Baer, Unimolecular reaction dynamics, theory and experiments, New York: Oxford university press, 1996.

[28] Z. Shi, J. Ford, Castleman Jr. and S. Wei, "Water clusters: Contributions of binding energy and entropy to stability," *The journal of chemical physics,* vol. 99, p. 8009, 1993.

[29] C. Klots, "Kinetic methods for quantifying magic," *Z.Phys. D,* vol. 21, pp. 335-342, 1991.

[30] K. Hansen, P. Andersson and E. Uggerud, "Activation energies for evaporation from protonated and deprotonated water clusters from mass spectra," *The journal of chemical physics,* vol. 131, p. 124303, 2009.

[31] E. Bruzzie, R. Parajuli and A. Stace, "Binding energies determined from kinetic energy release measurements following the evaporation of single molecules from the molecular clusters H+(H2O)n, H+(NH3)n and H+ (CH3OH)n," *Int. J. Mass Spect,* Vols. 345-347, pp. 160-166, 2013.

[32] G. Douberly, R. Walters, J. Cui, K. Jordan and M. Duncan, "Infrared Spectroscopy of Small Protonated Water Clusters, H+(H2O)n (n = 2−5): Isomers, Argon Tagging, and Deuteration," *. Phys. Chem. A,* vol. 114, no. 13, p. 4570–4579, 2010.

[33] S. Natarajan, T. Morawietz and j. Behler, "Representing the potential-energy surface of protonated water clusters by high-dimensional neural network potentials," *Physical Chemistry Chemical Physics,* vol. 17, no. 13, pp. 8356-8371, 2015 .

[34] M. Hodges and A. Stone, "Modeling small hydronium–water clusters," *the journal of chemical physics,* vol. 110, no. 14, pp. 6766-6772, 1999.

[35] M. Hodges and D. Wales, "Global minima of protonated water clusters," *Chemical Physics Letters,* vol. 324, no. 4, pp. 279-288, 2000.

[36] M. Ryding, A. Zatula, P. Andersson and E. Uggerud, "Isotope exchange in reactions between D2O and size-selected ionic water clusters containing pyridine, H+(pyridine)m(H2O)nw," *Physical Chemistry Chemical Physics,* vol. 13, p. 1356–1367, 2010.

[37] Y. Ibrahim, R. Mabrouki, M. meot-Ner and M. EL-Shall, "Hydrogen Bonding Interactions of pyridine+ with water: stepwise solvation of distonic cations," *J. Phys. Chem. A ,* vol. 111, pp. 1006-1014, 2007.

[38] T. Wroblewski, L. Ziemczonek, E. Gazda and G. Karwasz, "Dissociation energies of protonated water clusters," *Radiation physics and chamistry,* vol. 68, pp. 313-318, 2003.

[39] T. Magnera, D. David and J. Michl, "The first twenty-eight gas-phase proton hydration energies," *Chem. Phys. Lett,* vol. 182, no. 3-4, pp. 363-370, 1991.

[40] K. Honma, L. Sunderlin and P. Armentrout, "Guided-ion beam studies of the reactions of protonated water clusters, H(H2O)n+ (n=1-4) with acetonitrile," *J. Chem. Phys,* vol. 99, no. 3, pp. 1623-1632, 1993.

[41] Y. Wang, C. Tsai, Y. Lee, H. Chang, J. Jiang, O. Asvany, S. Schlemmer and D. Gerlich, "Investigations of protonated and deprotonated water clusters using a low-temperature 22-pole ion trap," *American chemical society,* vol. 107, no. 21, p. 4217–4225, 2003.

[42] A. Cunningham, J. Payzant and P. Kebarle, "A Kinetic Study of the Proton Hydrate H+(H2O)n equilibria in the gas phase," *J. Am. Chem. Soc.,* vol. 94, no. 22, p. 7627–7632, 1972.

[43] P. Kebarle, S. Searles, A. Zolla, J. Scarborough and M. Arshadi, "The solvation of the hydrogen Ion by water molecules in the gas phase. Heats and entropies of solvation of individual reactions: H + (H2O)n− 1 + H2O − >H + (H2O)n," *J. Am. Chem. Soc,* vol. 89, p. 6393, 1967.

[44] M. Meot-Ner and F. Field, "Stability, association, and dissociation in the cluster ions H3S+.+-..nH2S, H3O+.+-..nH2O, and H3S+.H2O," *J. Am. Chem. Soc.,* vol. 99, no. 4, p. 998–1003, 1977.

[45] M. Meot-Ner and C. Speller, "Filling of solvent shells about ions. 1. Thermochemical criteria and the effects of isomeric clusters," *J. Phys. Chem,* vol. 90, no. 25, p. 6616–6624, 1986.

[46] Y. Lau, S. Ikuta and P. Kebarle, "Thermodynamics and kinetics of the gas-phase reactions H3O+(H2O)n-1 + water = H3O+(H2O)n," *J. Am. Chem. Soc.,* vol. 104, no. 6, p. 1462–1469, 1981.

[47] W. Davidson, J. Sunner and P. Kebarle, "Hydrogen bonding of water to onium ions. Hydration of substituted pyridinium ions and related systems," *American Chemical Society,* vol. 101, no. 7, pp. 1675-1980, 1978.

[48] M. Meot-Ner and L. W. Sieck, "The ionic hydrogen bond. 1. Sterically hindered bonds. Solvation and clustering of protonated amines and pyridines," *J. Am. Chem. Soc.,* vol. 105, no. 10, p. 2956–2961, 1983.

[49] F.Berthias, "Thermalisation dans une nanogoutte d eau," Universite de Lyon, IPNL, Lyon, 2016.

[50] G. Brancato and M. Tuckerman, "A polarizable multistate empirical valence bond model for proton transport in aqueous solution," *The Journal of Chemical Physics,* vol. 122, no. 22, p. 224507, 2005.

[51] M. Marciante and F. Calvo, "Modelling infrared action spectra of protonated water clusters," *molecular simulation,* vol. 40, p. 176–184, 2013.

[52] L. Ojamae, I. Shavitt and S. Singer, "Potential models for simulations of the solvated proton in water," *The Journal of Chemical Physics,* vol. 109, no. 13, p. 5547–5564, 1998.

[53] M. C. Sicilia, C. Munoz-Caro and A. Nino, "Theoretical Analysis of Pyridine Protonation in Water Clusters of Increasing Size," *ChemPhysChem,* vol. 6, p. 139 – 147, 2005.

[54] M. C. Sicilia, A. Nino and C. Munoz-Caro, "Mechanism of Pyridine Protonation in Water Clusters of Increasing Size," *J. Phys. Chem. A,* vol. 109, pp. 8341-8347, 2005.

[55] O. K. Rice and H. C. Ramsperger, "THEORIES OF UNIMOLECULAR GAS REACTIONS AT LOW PRESSURES. II," *J. Am. Chem. Soc,* vol. 50, no. 3, p. 617–620, 1928.

[56] L. S. Kassel, "STUDIES IN HOMOGENEOUS GAS REACTIONS I," *J.Phys.Chem,* vol. 32, no. 2, pp. 225-242, 1928.

[57] V. Weisskopf, "Statistics and Nuclear Reactions," *Phys. Rev.,* vol. 52, no. 4, p. 0295-0303, 1937.

Conclusion

The thesis contains two parts, both of which related to complementary work on the study of the relaxation processes of molecular cluster ions: the development of an ion beamline for the storage ring RICE in RIKEN and the analyses of experiments made with the DIAM set-up in IPNL, Lyon.

In the first part, the design of the ion trap beam line injection for the RICE ring was detailed. An electrospray ion source produces positive and negative clusters in gas-phase, different parameters influence the beam production such as the solution or the temperature of the capillary. The quadrupole mass filter is used to measure the mass spectrum, and different calibration methods were explained. One is a published calibrated solution, the other is a well-known spectrum of protonated water cluster. Then a radio frequency octupole ion trap is used to store, cool and bunch the ions. The trap is cool down to 5.2 K and helium is used as a buffer gas to allow continuous injection in the trap and to cool the ions. The extraction electrodes are used to shorten the ion bunch width down to 15 µs without losing any ions. The bunch is guided through octupole guides to the acceleration tube where they gain up to 20 keV in kinetic energy. Different lenses, an Einzel lens and a quadrupole doublet allow us to control the position and the focusing of the beam.

Then the beam is probed by a laser to measure an action spectrum. A laser collides the ion bunch after the acceleration tube. When a photon is absorbed, the cluster ion might dissociate, the charged fragments and the non-dissociated cluster ion are removed from the beam with a pair of quadrupole deflectors. The neutral fragments are detected on a MCP detector placed after the quadrupole toward the beam line. Then we can extract the signal induced by laser fragmentation. We controlled that the signal induced by laser fragmentation is independent of the laser and the ion beam intensity. By changing the laser wavelength, we measured an action spectrum for methylene blue cation and compared it to a spectrum measured in liquid phase. The measured action spectrum has a main peak around 650 nm corresponding to n-π* transitions and a shoulder at lower wavelength: 610 nm – 630 nm corresponding to vibronic transition 0-1. The liquid phase spectrum is shifted by 15 nm in the red.

The second part is dedicated to collision induced dissociation of mass selected $PyrH^+(H_2O)_{n=1-4}$ cluster ions. The experiment was performed with the DIAM set-up at the IPNL (Lyon) which provides a 8 keV beam of mass selected cluster ions. After a single collision with an argon atom at high velocity, a molecule of the cluster is electronically excited in a very short time scale (fs). This local electronic excitation rapidly relaxes in vibrational excitation of the molecule. The excitation energy is then transferred to the other molecules and during this relaxation process, evaporation of water molecules can occur. The detection system mounted after the collision zone combines the COINTOF technique and a velocity map imaging technique. The arrival time and the impact position of the evaporated molecules and of the residual molecular cluster ion are measured on an event-by-event basis. The resulting multiparametric data set allows the selection of cluster ions evaporating a given number of molecule and the measurement of the velocity distribution of the corresponding evaporated molecules.

The measured velocity distributions for the evaporation of a single molecule by $PyrH^+(H_2O)_{n=1-4}$ cluster ions exhibit two components: a peak at low velocity and a longer tail at high velocity. The long tail previously observed with protonated water clusters is associated with non-ergodic events. A water molecule is evaporated with a high velocity before complete energy redistribution in the cluster. The width and the average value of the low velocity part of the distribution decrease with the cluster size n and saturate at high n. This behavior is similar to the one observed for the evaporation from protonated water cluster but the values are always lower in the case of $PyrH^+(H_2O)_{n=1-4}$ cluster ions.

Assuming the fit of the low velocity part of the distribution with a Maxwell-Boltzmann distribution, the width of the distribution can be related to an equivalent temperature related to the translational degree of freedom. The k_bT values measured from the experimental velocity distributions for $PyrH^+(H_2O)_{n=1-4}$ and $(H_3O)^+(H_2O)_n$ are set in a correlation plot with the available calculated and measured values of the binding energy. The correlation plot shows that both the binding energy and the k_bT values are decreasing with the decrease of the number of molecules in the cluster. The limit for high n values appeared to be the same for protonated pyridine water cluster and protonated water cluster.

The measured distributions are compared to the SMD calculation results performed by F.Calvo with three different kinds of initial excitation: a global excitation of the entire cluster, a local excitation on a water molecule and a local excitation of the protonated pyridine molecular ion. The low velocity part of the calculated distributions can be fitted with a Maxwell-Boltzmann function but the width and average velocity depend on the initial excitation. Moreover, non-ergodic events are obtained, only for the excitation of a water molecule. The n dependency of the width and of the average value for the low velocity part of the calculated distributions is similar that of the experimental ones: they are both decreasing with the cluster size n and saturate at high n. The average value of the distribution for local excitation on a pyridine molecule is systematically lower than other kind of excitation, even for high n. The local excitation on a water molecule and the global excitation tend to the same limit at high n.

The velocity distribution for the evaporation of two and three molecules from $PyrH^+(H_2O)_{n=1-4}$ were measured and display two components as for the evaporation of a single molecule. A Monte-Carlo simulation is used to reconstruct the velocity distribution for the evaporation of several molecules from the distributions measured for the evaporation of a single molecule, assuming sequential evaporation and taking in account the recoil velocity of the daughter ions. Differently from the case of protonated water clusters, the resulting distributions do not reproduce the experimental ones in the case of protonated pyridine water cluster ions. Additionally, a Maxwell-Boltzmann function does not fit the low velocity part of the velocity distribution for the evaporation of a single molecule. This demonstrates that measured velocity distributions keep a trace of the initial excitation process.

These experimental facts and the SMD calculation results lead to analyze the experimental distributions considering the contribution of the two initial excitations: a local excitation on a water molecule and a local excitation on a pyridine molecular ion. The fit with two Maxwell-Boltzmann functions with the characteristic of the low velocity part of the calculated distributions gives an excellent agreement for the evaporation of a single molecule as well as that for the evaporation of two and three molecules. As supported by the SMD calculations, the measured velocity distributions reveal that evaporation of a water molecule occurs after redistribution of the energy between the water molecules but before the complete redistribution within the entire molecular cluster ion.

The proportion of the two different initial excitations for the evaporation of one, two or three molecule is extracted from the fit procedure. The local excitation on pyridine is dominant for the evaporation of a single molecule but the proportion is inverted for the evaporation of several molecules for which the local excitation on a water molecule is dominant. Considering the whole experimental velocity distribution which includes both kind of excitation, the number of Maxwell-

Boltzmann events is always higher than the non-ergodic events, and is almost independent of the cluster size n or of the number of water molecules evaporated.

The next step of my work will be to study the same molecular system with both experiments: in DIAM and with RICE. The first step is to inject ions from the trap beam line to the storage ring RICE. In the ring, molecular ions will be cooled further down and the internal energy distribution of the ion bunch reduced. As for DIAM, the study of solvated molecular ions will be done with a controlled number of water molecule attached. The first molecular systems to be studied will be pyridine and pyrimidine, two heterocyclic prebiotic molecules.

Appendix 1: Riken cryogenic storage ring: RICE

a. Beam injection into RICE

One of the advantages of electrostatic storage rings is to store an intense beam of heavy molecular ions for extended periods of time. The beam can either interacts with a laser, with other particles like residual gas or a neutral beam. The description of the storage ring RICE was described in [1] and an overall view of the RICE facility and the trap injection beam line is shown in Figure 86. The ions produced in the ESI source are cooled and bunched in the ion trap and accelerated to up to 20 keV. The beam is bent with a quadrupole deflector and is injected in the ring.

In the ring, the stored ions can be probed with a tunable laser as it has been performed similarly behind the trap, however, the event rate is expected to be much higher as the interaction volume is larger (~100 cm with merged beam experiments in the ring compared to ~1 cm in crossed beam experiments behind the trap). Furthermore, the noise in the ring is very low as the noise comes from collision with residual gas and the ring vacuum pressure is very low, around 10^{-13} mbar. The signal to noise ratio will be higher reducing the measurement time and thus systematic errors such as ion source fluctuations. Furthermore, ions that cannot be produced with a high intensity can be studied repeatedly in the ring.

After a laser shot, we measure the neutral rate each half turn and we can trace the decay of the excited molecules over time. Then we can easily measure the lifetime of the excited states. However, the lifetime must be in the measurement range of the ring, which is between a few µs to minutes. If the molecular ion is excited to a dissociative state with a short lifetime, the ions will dissociate rapidly and only a few neutrals will be detected in the next turn.

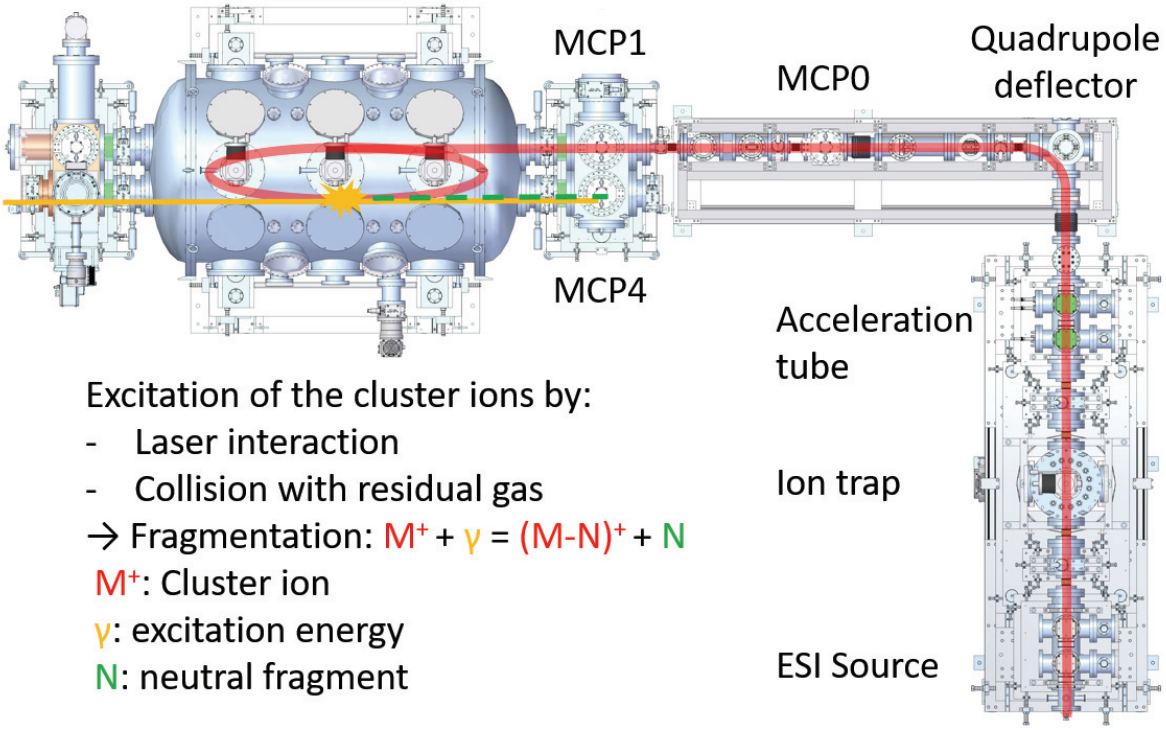

Figure 86: The RIken cryogenic storage ring RICE and the ion injection beam line. The beam line produces a bunch of cold ions that can be injected in the ring. Different movable MCP let us observe the beam and help us to optimize the ion bunch injection.

The first experiment performed in RICE was the study of a 15-keV Ne^+ beam for different ring temperatures [1]. The initial bunch was 5 µs long with around 10^6 ions and had a revolution frequency of 130 kHz in the ring. The storage ring lifetime was measured for different ring temperatures and the result is shown in Figure 87. The x-axis is the neutral counts at MCP4 in counts per second and the y-axis is the time after injection of the 15-keV Ne^+ beam in the RICE. The decay curves were observed for different ring temperatures: 25 K in red, 20 K in orange, 13 K in green, 10 K in cyan and 4.2 K in blue. Except for early times, all curves show a single exponential decay, which is mainly attributed to collisional loss of ions with residual gas in the vacuum. The number of ions N, is given by:

$$N(t) = N_O e^{-t/\tau} \qquad 22$$

And the lifetime, τ is defined as:

$$\tau = {}^{1}/_{\sigma_{col}\rho v}\,, \qquad 23$$

With σ_{col}, the collision cross-section, ρ the number density of the residual gas, and v the velocity of the ion beam. Thus, by measuring this lifetime τ, the vacuum pressure p in the ring can be determined. The decay curve of a 20 keV Ne^+ beam in the TMU E-ring measured at room temperature [2] is plotted in grey, the pressure could be obtained using normal vacuum gauges.

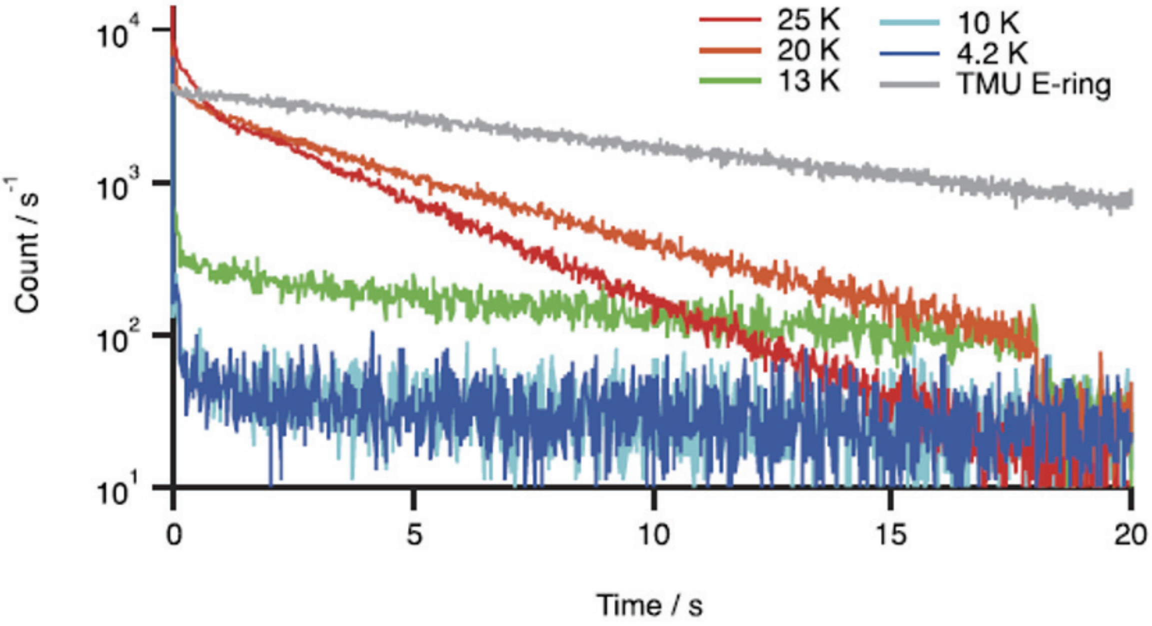

Figure 87: Neutral counts at MCP4 as a function of time after injection of the 15-keV Ne⁺ beam in the RICE. The decay curves were observed for different ring temperature: 25K in red, 20K in orange, 13K in green, 10K in cyan and 4.2K in blue. The measurements were compared with the decay curve of a 20-keV Ne⁺ beam in the TMU E-ring measured at room temperature [2]. (copied from [1]).

The storage lifetimes measured were: 3.05 s at 25 K, 4.91 s at 20 K and 17.3 s at 13 K. For the temperature lower than 10 K, the count rate is as low as the background and we could not measure the lifetime. The lifetime of the 15-keV beam at 4.2 K was measured by dumping the remaining ion beam on the detector at different storage times and was measured to be 780 s with an uncertainty of 35% from the fit error.

b. Ion injection in RICE

To inject ions in the ring efficiently, the beam needs to have a specific divergence. The storage ring and the beam line are shown in Figure 88 (figure directly copy from [1]). In the figure, the green arrow specified by ESI represents the trap beam line. Three movable detectors are used to observe the beam shape, in blue in Figure 88, called BPM as Beam Profile Monitor: BPM0, BPM1 and BPM2. They can be pull in and pull up of the beam as the trap MCP. We used as well a movable MCP which can be inserted anywhere in the beam line to observe the beam in between the beam profile monitor. The beam line from the quadrupole deflector to the ring is equipped with a beam steerer (ST), a quadrupole triplet lens (QL1), and a quadrupole doublet lens (QL2). Three 10 mm apertures (A1, A2 and A3) are used for differential pumping. In the ring, the beam can be non-destructively monitored by four pick-up detectors and destructively by two MCP detectors: BPM2 and BPM4. The beam is focused and defocused with quadrupoles (QF and QD) in the straight part of the ring.

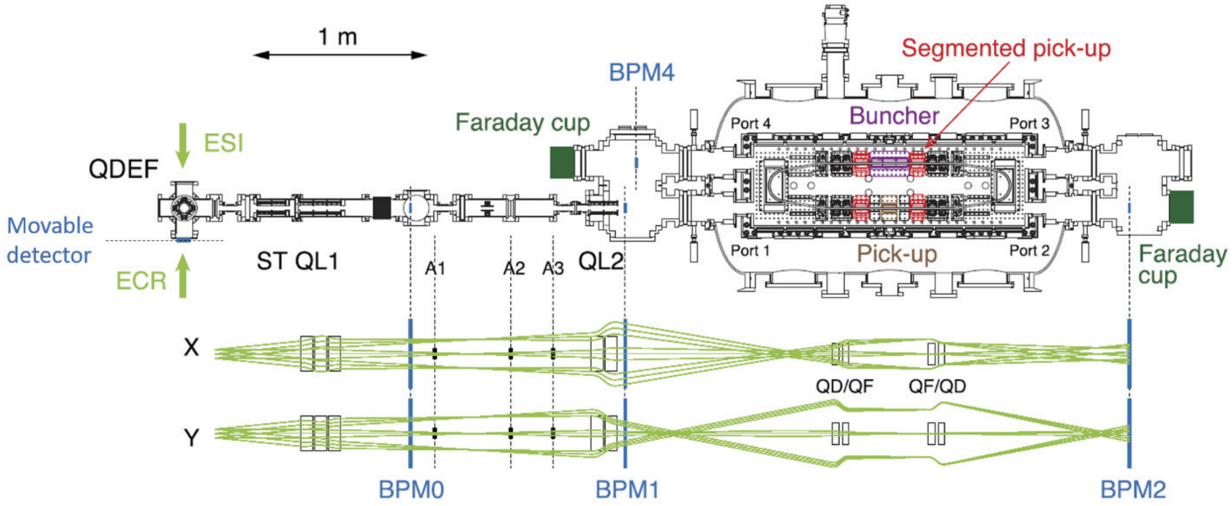

Figure 88: Schematic view of the RICE injection beamline and diagnosis system. The beamline consists of a 90° quadrupole deflector (QDEF), a beam steerer (ST), a quadrupole triplet lens (QL1), and a quadrupole doublet lens (QL2). Three sets of apertures (A1, A2 and A3) were installed for differential pumping of the beamline. For beam diagnosis, beam profile (BPM), pick up detectors, and Faraday cups were installed at the indicated locations. An example of the beam optics calculation for the X and Y beam envelopes is also shown with the positions and sizes of the electrostatic elements. (copied from [1]).

The lower part of Figure 88 shows the beam envelope calculated for x and y as well as the size and position of each electrostatic elements. An optimized beam would be in the center of the beamline with a diameter smaller than 10 mm at the positions of the different apertures.

As detailed in the thesis, the ion beam line produces a bunch of cold molecular ions. As they are internally cold, they are good candidates to be injected in the ring: the ion bunch energy distribution is narrow and the ions are in the electronic and vibrational ground states. An Einzel lense and a pair of quadrupole allow us to control the position and the focusing of the beam. It is very important to control the combinations of applied voltages and the beam shape precisely to inject ions in the ring.

Now we present the ion injection from the trap beam line into the ring. We used a pulsed bunch of methylene blue cation, accelerated at 10 keV. The size of the bunch was on purpose increased to 25 µs and all parameters of the beam line (trapping voltage, acceleration, focusing and beam position) were optimized to find the best beam shape and optimize the ion transmission until the ring.

Figure 89 shows the ion bunch at different positions: in red the bunch was measured with a MCP placed in the trap injection beam line, called Trap MCP, in green with the Movable detector placed straight after the quadrupole, and in blue at MCP0, placed in the beam line between the quadrupole deflector and the storage ring. To reach the MCP0, the ion beam needs to be bended at 90° in the quadrupole deflector. The bunch detected with the Trap MCP and the movable MCP have almost the same intensity, but shifted by 15 µs which corresponds to the time of flight of the 10 keV methylene blue ions. The distance between the Trap MCP and the movable detector is around 1.2 meters. It is noted that as we use two different MCPs, their gain is different and it is not straight forward to compare the intensities of the signals. The blue curve from MCP0 has an intensity about 5 times lower than the two others bunches and is shifted by around 30 µs which corresponds well to the distance between the Trap MCP and MCP0 of 2.4 meters. The length of the bunch is 30 µs for the bunch in red, 25 µs for the bunch in green and 20 µs for the bunch traced in blue.

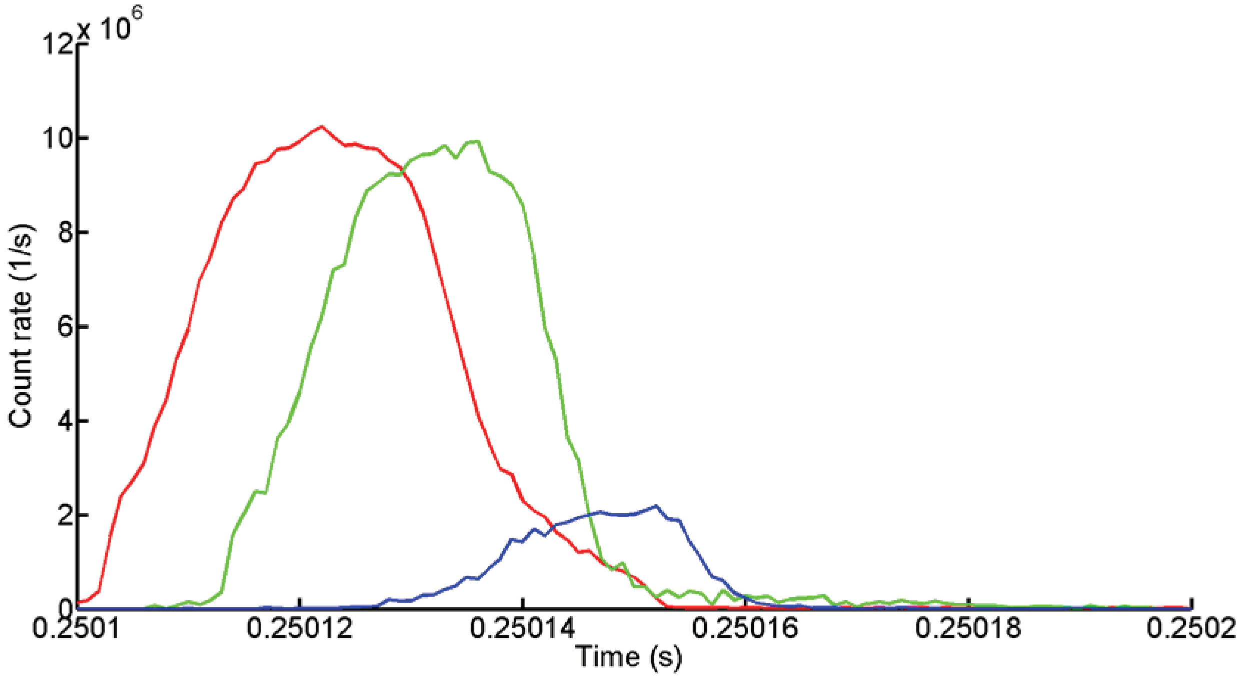

Figure 89: Ion injection in the ring with in red the ion bunch measured before the quadrupole deflector with the trap MCP. In green is the ion bunch observed straight after the quadrupole deflector and in blue is the bunch measured in the beam line by MCP0.

The bunch was also detected on MCP1, placed after MCP0 towards the beam line and situated just before the ring, and is shown in black in Figure 90. The bunch intensity is very low: about five times lower that the intensity on MCP0. Between both MCPs, the beamline has three small apertures of 10 mm diameter. From the fact that the beam is strongly reduced, it is consistent that our beam is not still in the center of the beam line and a better beam shape needs to be achieved. The optimization with these ions from the trap is more challenging compared to the atomic beam from the ECR ion source as these heavy molecular ions are produced with much lower intensity and the trap set-up can only be operated in a bunched ion mode.

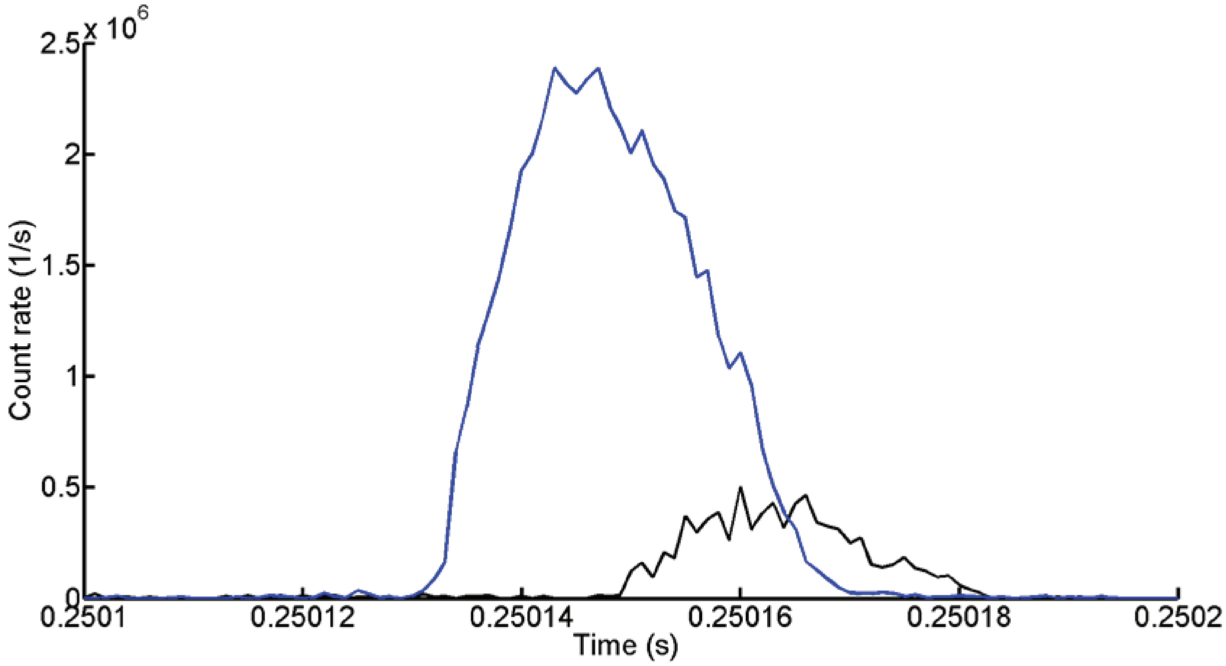

Figure 90: Ion injections in the ring with in blue the bunch detected with MCP0 and in black the bunch detected with MCP1.

To conclude, we prepared the ion beam for injection in the ring. The einzel lens and the quadrupole doublet mounted after the acceleration tube are used to change the beam shape and optimize the beam injection in the ring. The beam has been detected on different beam monitors in the beam line (MCP detectors). After the 90° deflector, most of the beam is lost and cannot reach MCP0. The optimization of the beam shape needs to be improved as the intensity of the beam drastically decreases in the injection beamline and only a few ions can be injected into the ring. The experiment of beam injection in the ring is still ongoing and simulations are made to find the suitable voltage combinations.

[1] Y. Nakano, Y. Enomoto, T. Masunaga, S. Menk, P. Bertier and T. Azuma, "Design and commissioning of the RIKEN cryogenic electrostatic ring (RICE)," *Review of Scientific Instruments,* vol. 88, no. 3, p. 033110, 2017.

[2] S. Jinno, "Storage of atomic/molecular ions in an electrostatic ring," Tokyo metropolitan University, PhD thesis, Tokyo, 2007.

Tables of figures: